Hybrid-PIC Modeling and Electrostatic Probe Survey of Hall Thrusters

by

John Michael Fife

Submitted to the Department of Aeronautics and Astronautics
in partial fulfillment of the requirements for the degree of

Doctor of Philospohy in Aeronautics and Astronautics

at the

MASSACHUSETTS INSTITUTE OF TECHNOLOGY

September 1998
[February, 1999]

Author_____
Department of Aeronautics and Astronautics
September 30, 1998

Certified by_____
Manuel Martinez-Sanchez
Professor
Thesis Supervisor

Certified by_____
Daniel E. Hastings
Professor

Certified by_____
Kenneth S. Breuer
Principal Research Scientist

Certified by_____
Ian H. Hutchinson
Professor

Certified by_____
John J. Deyst
Professor

Accepted by_____
Jaime Peraire
Chairman, Department Graduate Committee

Hybrid-PIC Modeling and Electrostatic Probe Survey of Hall Thrusters

by

John Michael Fife

Submitted to the Department of Aeronautics and Astronautics
on September 30, 1998, in partial fulfillment of the
requirements for the degree of
Doctor of Philospohy in Aeronautics and Astronautics

Abstract

In order to study the physics of the acceleration process in Hall thrusters, an evolved hybrid particle-in-cell (PIC) numerical model was developed. A set of quasi-one-dimensional fluid equations are used for electrons, and a particle-tracking Boltzmann solver is used for the heavy species. The two solutions are linked by charge neutrality. A novel statistical approach to particle creation and tracking is employed which reduces computational time. To provide boundary conditions for the numerical model, and to verify its accuracy, an extensive set of electrostatic probe measurements were performed in the plume of an SPT-70. Various probe geometries were used, including triple probes, to measure the time-averaged plasma parameters in the near-plume. Also, AC components of discharge current and floating potential were measured. The combined experimental and numerical results are used to examine phenomena such as the nature of low-frequency discharge oscillations, the interaction of the thruster walls with the plasma, the distribution of ion energies ejected from the thruster, and the effect on efficiency of facility background pressure. Performance results from the numerical model agree well with measurements. A formula for the change in measured efficiency versus facility pressure is also presented, based on numerical results. Widening of the ion distribution of energies is seen, and attributed to time variation of the electric field, due to oscillations. Measured low-frequency oscillations seem to be related to an ionization instability observed in the numerical model, but conclusive evidence is not found. Although the model predicts strong electric fields outside the acceleration channel, experiments do not. The discrepancy is believed to be due to localized anomalous electron conductivity caused by azimuthal asymmetry.

Thesis Supervisor: Manuel Martinez-Sanchez
Title: Professor

Acknowledgments

I would like to thank Professor Manuel Martinez-Sanchez for his patience and tolerance throughout this research project. He was able to keep me on track, while, at the same time, promoting an exciting atmosphere of discovery. He made my stay at MIT a pleasant and enlightening experience. Given any other advisor, I don't think I would have pursued my PhD.

Also, I would like to thank the Air Force Electric Propulsion Laboratory for providing the facilities and personnel necessary for the electrostatic probe experiments presented in this thesis report. Ron Spores and his entire group are first-rate. I am looking forward to working with them in the future.

Most of all, I want to acknowledge my parents, Linda and Harry Fife, for all their support, and my beautiful wife, Julianne. Julianne never complained when I had to stay up working all night. She never complained about her 9-5 job during the times when my schedule was flexible. She never complained about the years when we were squeaking by at the poverty level. She gave up warm, sunny, New Mexico mountains for cold, grey, Boston winters.

And some thanks go to our dog, Sancho, and the MIT Rugby Team for keeping things in perspective: long runs, tall beers, good friends, and good times never to forget.

Contents

List of Figures

Chapter 1

Introduction

1.1 Hall Thrusters – Overview

Hall thrusters are a class of electric space propulsion device operating at around 1600 s of specific impulse. They generally use noble gas propellants, such as xenon. The primary feature of a Hall thruster is an annular geometry with a radial magnetic field, as shown in Figure 1-1. The radial magnetic field is strong enough to reduce the Larmor radius of electrons to a small value compared with the size of the channel. This, coupled with the fact that the mean free path for electron collisions is very long, means their drift in an azimuthal direction is effectively closed. This results in high axial electron impedance, maintaining an electric field between the cathode and the anode. Neutral gas, injected at the anode, is ionized by collisions with the trapped electrons. The Larmor radius of the ions is large, so they experience very little curvature and stream directly out of the device, accelerating down the potential gradient. Figure 1-2 shows the engineering sketches of two models.

The operating characteristics of a typical Hall thruster (Fakel SPT-70) are given in Table 1.1. Thrust efficiency is superior to most forms of electric propulsion at the same specific impulse, but closely comparable to gridded ion engines. Lifetime is currently the most important issue for their continued development. Production models last approximately 7,000 hours, eventually degrading due to accelerator wall erosion from ion impact [14].

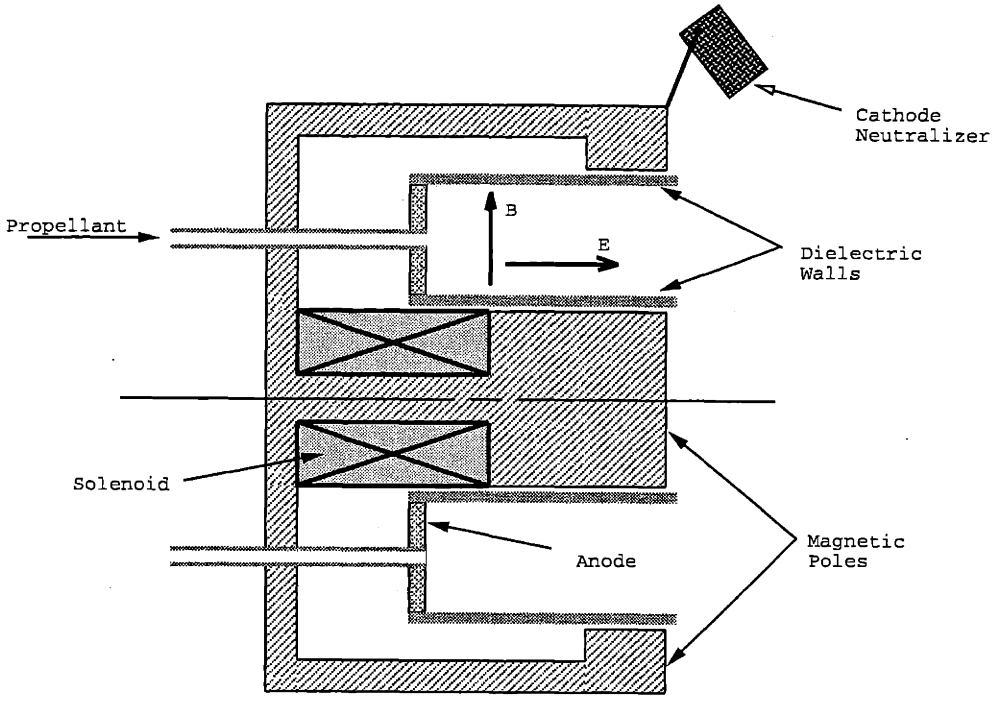

Figure 1-1: Basic Hall thruster diagram – side view.

Specific Impulse	1600 sec
Efficiency	43.3%
Thrust	37.2 mN
Mass Flow Rate	2.42 mg/sec
Anode Current	2.2 A
Discharge Voltage	300 V
Magnetic Field	180 $Gauss$
Service Life	$\sim$ 4000 $hours$
Power	700 W

Table 1.1: Fakel SPT-70 operating characteristics.

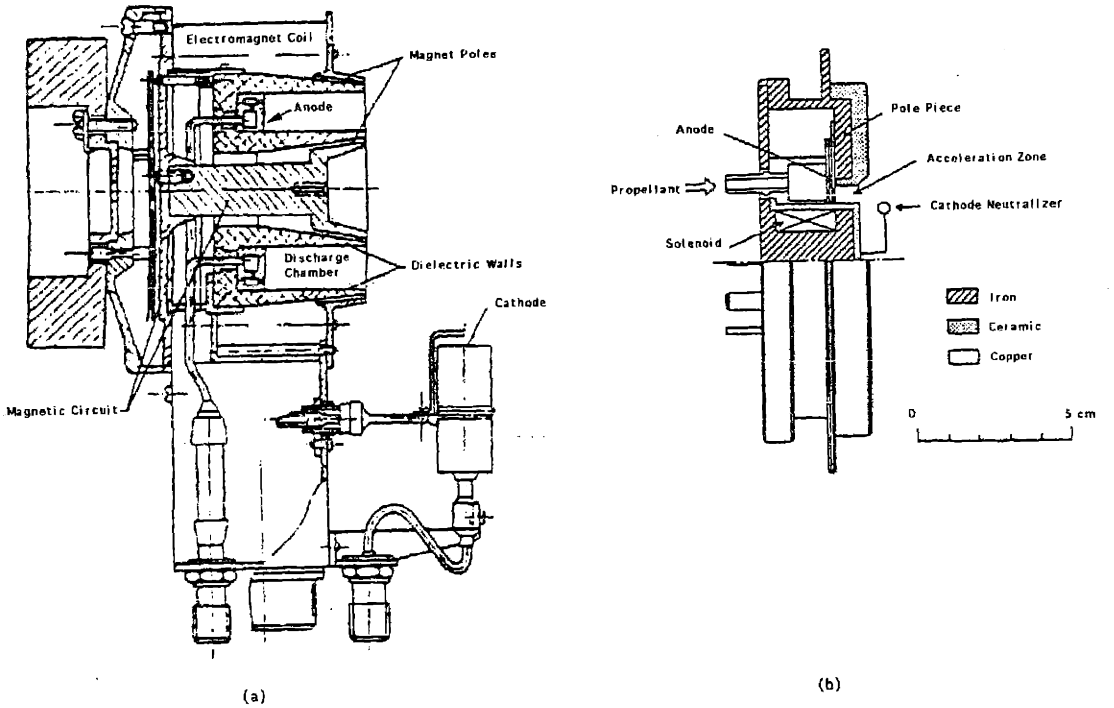

Figure 1-2: Two hall thrusters. (a) Russian SPT-100 [13]. (b) Japanese Type II [44].

1.2 Status of Hall Thruster Research

Hall thrusters were first developed experimentally in the United States by Brown and Pinsley [15] and later by Janes and Lowder [40]. However, severe plasma oscillations led to the abandonment of U.S. Hall thruster efforts. Russian experiments began in the early 1960's with a concept thruster designed by A. I. Morozov. Since then, experimental work has continued in Russia, resulting in papers by Morozov [53, 55, 56], Bugrova [17, 18], Smirnov [59], Bishaev [9, 10], Esipchuk [25], and Zubkov [62] to name a few. In addition to ground tests, over fifty Hall thrusters were launched on Soviet Meteor satellites for station keeping.

In 1992, Lentz [47] used a one-dimensional numerical model to accurately predict the operating characteristics and plasma parameters in the acceleration zone of a Japanese Type II Hall Thruster. The assumptions of the Lentz model included quasineutrality, Bohm diffusion across the magnetic field, constant ratio of ionization energy loss to total electron energy loss, and fixed magnetic field.

In 1995, Fife [30] extended the work of Lentz to two dimensions (z, r). That model assumed quasineutrality, Maxwellian electrons, and Bohm diffusion across the magnetic field lines. Heavy particles were simulated directly with a Particle-In-Cell (PIC) method, while electrons were modeled as a fluid continuum. A time-accurate electron energy equation was used to determine electron temperature, and a generalized Ohm's Law was used to determine the electric field strengths. Results indicated a strong correlation with experimental performance data for the SPT-100. The simulation was also able to accurately predict wall erosion rates, thrust, torque, power, and efficiency. Two-dimensional plasma distributions were similar to experiment, but did not match in all cases. In particular, the peak electron temperature was overpredicted by a factor of two.

Many experiments have been performed to characterize Hall thrusters' oscillatory behavior. These have been documented in many publications [26] [14]. Also, several theories about their physics have been put forth [26] [20]. Similar oscillations have been observed in Fife's numerical simulations [29], although it is unclear whether all the relevant physics were represented.

1.3 Overview of This Research

This reseach attempts to explore in detail the physics of the acceleration process in Hall thrusters. A combination of experimental measurements and numerical modeling will be used to examine phenomena such as the nature of the low-frequency discharge oscillations and the interaction of the thruster walls with the plasma.

Experimentally, an attempt is made to thoroughly characterize the near-field plume emissions from an SPT-70. This includes measuring time-averaged plasma parameters as well as oscillatory components. Data from these measurements are used to compare with analytical models governing the near-field plume region, and are also be used as boundary conditions for a numerical model of the complete plume-acceleration channel combination.

The numerical model is an evolved version of the previous work by Fife [30]. However, several important modifications are made. The use of a detailed wall interaction model limits the electron temperature to more reasonable levels. Furthermore, near-wall electron conductivity due to secondary electron emission is modeled. Also, second-degree ionization is implemented, as well as the capability to compute ion energy distribution functions emitted by the thruster. The effect of background pressure is also modeled, so that facility effects may be analyzed.

The governing equations and analytical model are detailed in Chapter 2. Chapter 3 describes the numerical method. Chapter 5 presents theory of electrostatic probes and a detailed explaination of the experimental set-up for measuring plasma parameters in the plume of an SPT-70. Chapter 5 shows the steady-state results from the probe experiments and numerical model. Chapter 6 contains an analysis of the dynamics of low-frequency discharge oscillations. Chapter 7 discusses the level of agreement between theory and data, both with respect to this work and also more generally. Conclusions and recommendations for future work are given in Chapter 8.

Chapter 2

Governing Equations

2.1 Two-Dimensional Approximation

Although Hall thrusters generally have three-dimensional axisymmetric cylindrical ($z-r-\theta$) geometries, some azimuthal variation in magnetic field and wall erosion have been reported [54]. Furthermore, it has been theorized that azimuthal drift waves may contribute to the anomalous electron diffusion [6]. Consistent with the goal of modeling only large-scale phenomenon, however, gradients in the θ-direction are not included in the simulation. The effects of azimuthal waves are accounted for by modification of the classical transport equations to include Bohm diffusion terms. This reduces the problem to two $(z-r)$ spatial dimensions for tractability.

2.2 Magnetic Field

The magnetic field vector, $\vec{B}$, is governed by Maxwell's equations,

$$\nabla \cdot \vec{B} = 0, \tag{2.1}$$

$$\nabla \times \vec{B} = \mu_0(\vec{j} + \epsilon_0 \frac{\partial E}{\partial t}). \tag{2.2}$$

In the plasma region, magnetic field variations due to plasma currents and changing electric fields are assumed to be small compared to the field produced by the electromagnet. From Ampere's law, the terms of interest are $\mu_0\vec{j}$, and $\mu_0\epsilon_0\frac{\partial \vec{E}}{\partial t}$. Measurements by Bugrova [18] approximate the azimuthal current density as $j_\theta \approx 2\times10^4\ A/m^2$. The electric field variation

may be estimated as $V_d/d/\triangle t \approx 6 \times 10^{11}\ V/m/s$, where d is the thruster length scale, and $\triangle t$ is the simulation timestep. Together,

$$\mu_0(\vec{j} + \epsilon_0 \frac{\partial \vec{E}}{\partial t}) \approx .02\ T/m, \tag{2.3}$$

which is small compared to magnetic field gradients due to electromagnets ($\sim 0.5\ T/m$). Ampere's law therefore reduces to,

$$\nabla \times \vec{B} = 0. \tag{2.4}$$

A magnetic potential function, σ, therefore exists where,

$$\vec{B} = \nabla\sigma. \tag{2.5}$$

Equation 2.5 identically satisfies Equation 2.4. Laplace's equation must be satisfied in the plasma region,

$$\nabla^2\sigma = 0. \tag{2.6}$$

Or, in cylindrical coordinates,

$$\frac{\partial^2\sigma}{\partial z^2} + \frac{\partial^2\sigma}{\partial r^2} + \frac{1}{r}\frac{\partial\sigma}{\partial r} = 0. \tag{2.7}$$

Also, since $\nabla \cdot \vec{B} = 0$, it is possible to define a magnetic stream function whose gradient is everywhere orthogonal to $\vec{B}$. One such stream function is λ, given by,

$$\frac{\partial\lambda}{\partial z} = r\frac{\partial\sigma}{\partial r} = rB_r, \tag{2.8}$$

$$\frac{\partial\lambda}{\partial r} = -r\frac{\partial\sigma}{\partial z} = -rB_z. \tag{2.9}$$

Therefore,

$$\nabla\lambda = r(B_r\hat{e}_z - B_z\hat{e}_r), \tag{2.10}$$

where $\hat{e}_z$ and $\hat{e}_r$ are unit vectors in the z- and r-directions. If $\hat{n}$ is the distance vector normal to the magnetic field lines, as shown in Figure 2-1, then one can write the derivatives with respect to the normal vector as derivatives with respect to λ:

$$\frac{\partial}{\partial\hat{n}} = \frac{\partial\lambda}{\partial\hat{n}}\frac{\partial}{\partial\lambda} = -rB\frac{\partial}{\partial\lambda}. \tag{2.11}$$

Equation 2.11 allows us to write spatial derivatives across magnetic field lines as derivatives with respect to values invariant along the lines. It will be particularly useful when integrating spatial derivatives along lines of force later in this chapter.

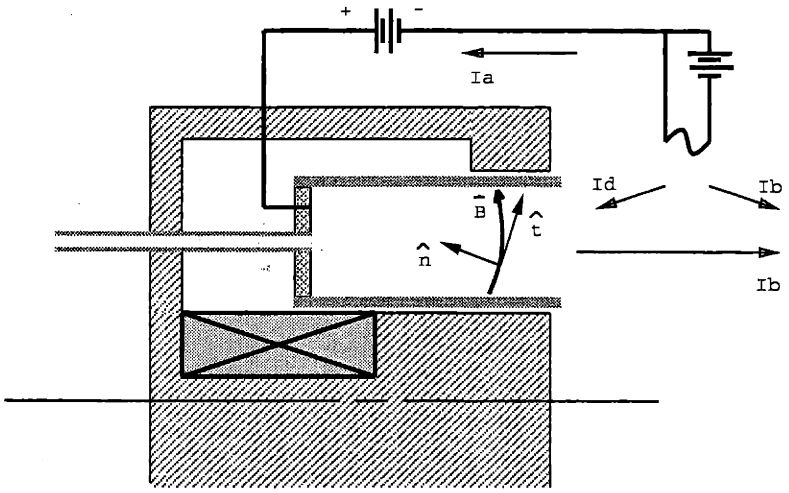

Figure 2-1: Hall thruster notational diagram: magnetic field lines and their associated curvilinear coordinates; current conventions.

2.3 Quasineutrality

The Debye length for a typical Hall thruster plasma ranges between .02 mm near the anode and .1 mm in parts of the plume. This is smaller than the spatial resolution we are attempting to model. Therefore, we ignore Poisson's equation and take the quasineutral approximation, $n_e = Zn_i$, where Z is the degree of ionization. For noble gas propellants such as argon and xenon, the only species to be considered are: neutral atoms, ions, and electrons. As a further simplification, we consider initially only $Z = 1$. Atoms with ionization degrees greater than one are ignored. The effect of second ions will be discussed in Section 2.6.5.

2.4 Electron Equations

The simplified electron equations consist of a generalized Ohm's law, a current conservation equation, and an electron temperature equation. Assuming a Maxwellian electron distribution, and given a particular ion field, these three equations are sufficient to yield electron current density, space potential, and electron temperature as a function of time.

Different assumptions are made along magnetic field lines versus across them. Figure 2-1 shows the notation used to describe coordinate directions with respect to magnetic field lines.

2.4.1 Momentum Equation Along Lines of Force

The diffusion coefficient of electrons along magnetic field lines is assumed to be much greater than the diffusion coefficient across them. Ignoring the magnetic mirror effect, a balance can be written between the pressure force and the electric force along magnetic field lines:

$$\frac{\partial(n_e k T_e)}{\partial \hat{t}} = e n_e \frac{\partial \phi}{\partial \hat{t}}, \tag{2.12}$$

which, assuming constant electron temperature along magnetic field lines, gives,

$$\phi - \frac{kT_e}{e}\ln(n_e) = \phi_0 - \frac{kT_e}{e}\ln(n_{e,0}). \tag{2.13}$$

Note that Equation 2.13 holds along magnetic field lines. The expression on the right hand side is therefore a constant for any given field line. We will call this constant ϕ^*. It may vary perpendicular to the magnetic field lines, and may be written as a function of λ:

$$\phi - \frac{kT_e}{e}\ln(n_e) = \phi^*(\lambda). \tag{2.14}$$

Equation 2.14 is also obtained as the equilibrium balance of a distribution of electrons in a conservative force field [11]. However, in that case it has a different meaning: given Maxwellian electrons at some point, P_0, with $T_{e,0}$, $n_{e,0}$, and potential ϕ_0, and ignoring collisions, the density at any other place with potential ϕ_1 would be given by,

$$\phi_1 - \frac{kT_{e,0}}{e}\ln(n_{e,1}) = \phi_0 - \frac{kT_{e,0}}{e}\ln(n_{e,0}). \tag{2.15}$$

Equation 2.15 applies only to situations where the electron distribution is initially Maxwellian at P_0. Furthermore, care must be taken when using Equation 2.15, since the electron temperature, $T_{e,0}$, is strictly meant to be the value at P_0.

A more rigorous approach would involve writing a steady-state energy equation for the variation of T_e along lines of force. This results in more complicated electron fluid equations, however, and is saved for the future. Instead, the isothermal momentum balance, Equation 2.14 will be used. The limit of adiabatic electrons is briefly examined in Section 7.4, and found to be less accurate.

2.4.2 Ohm's Law Across Lines of Force

Electron diffusion across the magnetic field is assumed to obey a Generalized Ohm's Law. In the lab frame the cross-field electron current density is,

$$j_{e,\hat{n}} = -en_e u_{e,\hat{n}} = \sigma_{e,\perp}\left(E_{\hat{n}} + \frac{1}{en_e}\frac{\partial p_e}{\partial \hat{n}}\right). \tag{2.16}$$

In terms of an effective electron mobility across the magnetic field lines, $\mu_{e,\perp}$,

$$u_{e,\hat{n}} = -\mu_{e,\perp}\left(E_{\hat{n}} + \frac{1}{en_e}\frac{\partial p_e}{\partial \hat{n}}\right). \tag{2.17}$$

Using $p = n_e k T_e$,

$$u_{e,\hat{n}} = -\mu_{e,\perp}\left(E_{\hat{n}} + \frac{kT_e}{en_e}\frac{\partial n_e}{\partial \hat{n}} + \frac{k}{e}\frac{\partial T_e}{\partial \hat{n}}\right). \tag{2.18}$$

Applying $\vec{E} = -\nabla\phi$,

$$u_{e,\hat{n}} = \mu_{e,\perp}\left(\frac{\partial \phi}{\partial \hat{n}} - \frac{kT_e}{en_e}\frac{\partial n_e}{\partial \hat{n}} - \frac{k}{e}\frac{\partial T_e}{\partial \hat{n}}\right). \tag{2.19}$$

An expression for $\frac{\partial \phi}{\partial \hat{n}}$ can be found by differentiating Equation 2.14 and rearranging:

$$\frac{\partial \phi}{\partial \hat{n}} = \frac{\partial \phi^*}{\partial \hat{n}} + \frac{kT_e}{en_e}\frac{\partial n_e}{\partial \hat{n}} + \frac{k\ln(n_e)}{e}\frac{\partial T_e}{\partial \hat{n}}. \tag{2.20}$$

Substituting into Equation 2.19,

$$u_{e,\hat{n}} = \mu_{e,\perp}\left(\frac{\partial \phi^*}{\partial \hat{n}} + \frac{k}{e}(\ln(n_e) - 1)\frac{\partial T_e}{\partial \hat{n}}\right). \tag{2.21}$$

Rewriting the derivatives using Equation 2.11,

$$u_{e,\hat{n}} = \mu_{e,\perp}\left(-rB\frac{\partial\phi^*}{\partial\lambda} - rB\frac{k}{e}(\ln(n_e)-1)\frac{\partial T_e}{\partial\lambda}\right). \tag{2.22}$$

Equation 2.22 expresses the electron velocity in the lab frame in terms on derivatives which are constant along lines of force. This will allow the derivatives to be moved outside any integral along lines of force.

2.4.3 Diffusion Coefficient

Classical cross-field mobility in the weakly ionized limit is given by [52],

$$\mu_{e,\perp} = \frac{\mu_e}{1+{\beta_e}^2}, \tag{2.23}$$

where $\mu_e = e/\nu_{en}m_e$ is the electron mobility, and $\beta_e = \omega_c/\nu_{en}$ is the electron Hall parameter. For the conditions of interest, $\beta_e >> 1$, and,

$$\mu_{e,\perp} \simeq \frac{\mu_e}{{\beta_e}^2} \sim \frac{1}{B^2}. \tag{2.24}$$

It is shown [40] that classical $1/B^2$ diffusion is not adequate to describe the high electron transport across lines of force in the presence of a strong magnetic field. Some previous work [12] has suggested that the discrepancy between measured and predicted mobility may be due to anomalous "Bohm" diffusion which goes as $1/B$:

$$D_{Bohm} \approx \frac{kT_e}{16eB}. \tag{2.25}$$

Here, the T_e/B dependence is fundamental, but the 1/16 factor is empirical, and actual values may vary between this and, perhaps, 1/4 of it. The effective Bohm mobility is,

$$\mu_{e,\perp} = \frac{1}{16B}. \tag{2.26}$$

Figure 2-2 shows a comparison between Bohm, classical, and empirical mobility using measurements of $\vec{B}$, n_e, V_p, T_e and j_e by Bishaev and Kim [9] in the acceleration channel of an SPT-100-type geometry. Neither classical nor Bohm models appropriately describe the high measured mobility near the anode or exit of the channel. It is believed that, in these

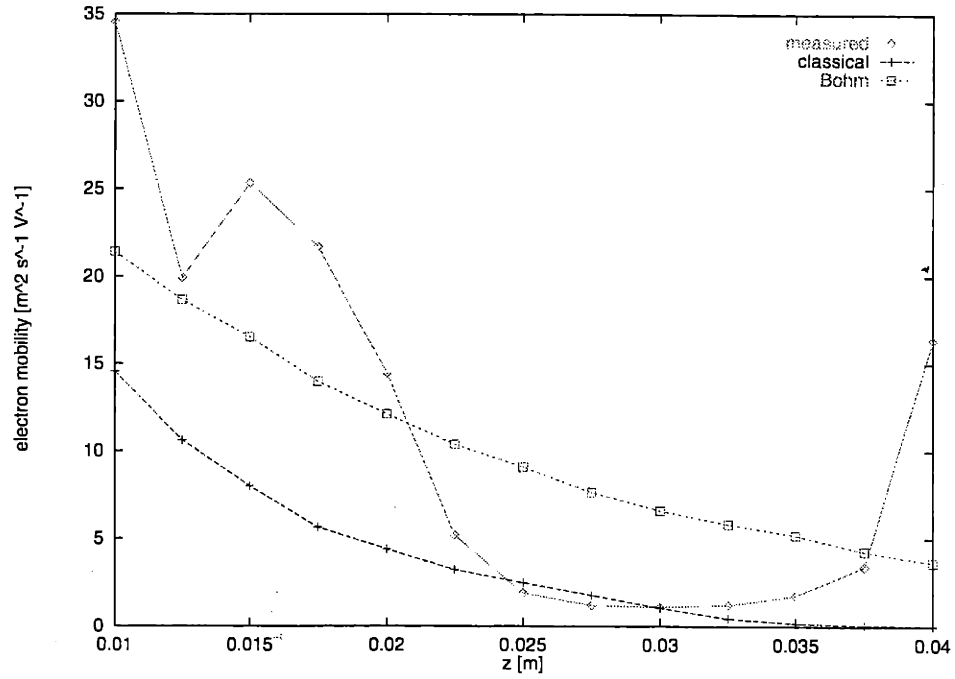

Figure 2-2: Comparison of measured, Bohm, and classical cross-field electron mobility, $\mu_{e,\perp}$, versus axial channel position. The anode is at $z = 0$ and the channel exit is at $z = 4$ cm.

regions, another mechanism, such as wall conductivity or wave transport, may dominate. In the interest of exploring the physics of the acceleration process, we use both classical and Bohm mobility here,

$$\mu_{e,\perp} = \frac{\mu_e}{\beta_e{}^2} + K_B \frac{1}{16B}, \tag{2.27}$$

and leave the coefficient, K_B, as an adjustable parameter between 0 and 1. Based on comparison with experimental data, the "best" K_B was found to be .15 for the SPT-70. With this choice, classical scattering contributes about 70% to the total cross-field mobility.

2.4.4 Current Conservation

Since quasineutrality is imposed, no space charge can accumulate, and current must be conserved for the whole device. Figure 2-1 shows the components of current for a typical Hall thruster. The cathode emits enough electrons (I_a) to neutralize the ion beam (I_b) as well as enough to initiate ionization in the acceleration zone (I_d). The current emitted by the cathode must also be equal to the current collected by the anode, or the entire thruster will charge. A conservation equation for current crossing any magnetic field line can be

written as,

$$I_a = I_i + I_e + I_w, \tag{2.28}$$

where I_i is the ion current, I_e is the electron current in the plasma region, and I_w is the total near-wall electron current. In terms of integrals along each magnetic field line,

$$I_a = -2\pi e \int_0^l n_i u_{i,\hat{n}} r ds + 2\pi e \int_0^l n_e u_{e,\hat{n}} r ds + I_w, \tag{2.29}$$

where ds is a differential length element along the line. Substituting Equation 2.22 into Equation 2.29,

$$\begin{aligned} I_a &= -2\pi e \int_0^l n_i u_{i,\hat{n}} r ds - 2\pi e \int_0^l n_e \mu_{e,\perp} r B \frac{\partial \phi^*}{\partial \lambda} r ds \\ &\quad -2\pi e \int_0^l n_e \mu_{e,\perp} r B \frac{k}{e} (\ln(n_e) - 1) \frac{\partial T_e}{\partial \lambda} r ds + I_w. \end{aligned} \tag{2.30}$$

Taking functions of λ outside the integrals,

$$\begin{aligned} I_a &= -2\pi e \int_0^l n_i u_{i,\hat{n}} r ds - 2\pi e \frac{\partial \phi^*}{\partial \lambda} \int_0^l n_e \mu_{e,\perp} B r^2 ds \\ &\quad -2\pi k \frac{\partial T_e}{\partial \lambda} \int_0^l n_e \mu_{e,\perp} B (\ln(n_e) - 1) r^2 ds + I_w. \end{aligned} \tag{2.31}$$

Rearranging,

$$\frac{\partial \phi^*}{\partial \lambda} = \frac{-I_a + I_w - 2\pi k \frac{\partial T_e}{\partial \lambda} \int_0^l n_e \mu_{e,\perp} B (\ln(n_e) - 1) r^2 ds - 2\pi e \int_0^l n_i u_{i,\hat{n}} r ds}{2\pi e \int_0^l n_e \mu_{e,\perp} B r^2 ds}. \tag{2.32}$$

2.4.5 Electron Energy Equation

Taking the first, second, and third moments of the Boltzmann Equation, the fluid conservation equations for electrons may be obtained:

$$\frac{\partial n_e}{\partial t} + \nabla \cdot (n_e \vec{u}_e) = \dot{n_e}, \tag{2.33}$$

$$\frac{\partial}{\partial t}(n_e m_e \vec{u}_e) + \nabla \cdot (n_e m_e \vec{u}_e \vec{u}_e) + \nabla \cdot \vec{\vec{p}}_e = \sum_r (\vec{M}_{re}), \tag{2.34}$$

$$\frac{\partial}{\partial t}(\frac{3}{2} n_e k T_e) + \nabla \cdot (\frac{3}{2} n_e \vec{u}_e k T_e + \vec{q}_e) + \vec{\vec{p}}_e : \nabla \cdot \vec{u}_e = \sum_r (E_{re} - \vec{u}_e \cdot \vec{M}_{re}) - S_i, \tag{2.35}$$

where S_i is the inelastic collision transfer term, and $\sum_r(\vec{M}_{re})$ and $\sum_r(E_{re} - \vec{u}_e \cdot \vec{M}_{re})$ are the elastic collision transfer terms. We will call the latter S_e. The term $\vec{q}_e$ in Equation 2.35 is the thermal conduction vector,

$$\vec{q}_e = -K_e \nabla T_e, \tag{2.36}$$

where K_e is the heat conduction coefficient. The right hand sides of Equations 2.34 and 2.35 represent the net momentum and energy transfer rates to the electrons, respectively. Assuming the pressure dyad reduces to a scalar pressure term, $n_e k T_e$,

$$\frac{\partial}{\partial t}\left(\frac{3}{2} n_e k T_e\right) + \nabla \cdot (\frac{5}{2} n_e k T_e \vec{u}_e + \vec{q}_e) - \vec{u_e} \cdot \nabla(n_e k T_e) = S_e - S_i. \tag{2.37}$$

The source terms, S_e and S_i, will be discussed in later sections.

2.4.6 Electron Thermal Conductivity

A fundamental assumption of this analysis is that heat and mass diffuse by the same mechanism. Concerning ourselves only with the direction perpendicular to the magnetic field, one can then write the mathematical relation,

$$\frac{D_{h,\perp}}{D_{m,\perp}} = 1, \tag{2.38}$$

where $D_{h,\perp}$ and $D_{m,\perp}$ are the heat and mass diffusion coefficients, respectively. These are given by,

$$D_{h,\perp} = \frac{K_{e,\perp}}{c_p \rho} = \frac{2K_e}{5 n_e k}, \tag{2.39}$$

where $K_{e,\perp}$ is the thermal conductivity, and,

$$D_{m,\perp} = k T_e \mu_{e,\perp} e. \tag{2.40}$$

Substituting, we find that,

$$K_{e,\perp} = \frac{5 n_e k^2 T_e \mu_{e,\perp}}{2e}. \tag{2.41}$$

As mentioned in Section 2.4.1, diffusion in the direction parallel to the magnetic field is assumed to be much higher than perpendicular to it:

$$D_{e,\parallel} \gg D_{e,\perp}. \tag{2.42}$$

This gives rise to the assumption of constant electron temperature along lines of force, which we used before.

2.4.7 Elastic Collision Energy Terms

The electron energy source due to collisions with other specie may be written as,

$$S_e = \sum_r m_e \nu_{er} n_e \left[(\vec{u}_r - \vec{u}_e)^2 + \frac{2}{m_r} \frac{3}{2} k (T'_r - T'_e) \right], \tag{2.43}$$

where ν_{er} is the average momentum transfer collision frequency of electrons with species r, $\vec{u}_r$ is the mean velocity of species r, and T'_e and T'_r are the temperatures associated with random velocities with respect to the mean velocity of species r. Considering only electron-neutral and electron-ion collisions, Equation 2.43 may be written as,

$$\begin{aligned} S_e &= m_e \nu_{en} n_e (\vec{u}_n - \vec{u}_e)^2 + m_e \nu_{ei} n_e (\vec{u}_i - \vec{u}_e)^2 + & (2.44) \\ & m_e \nu_{en} n_e \frac{2}{m_n} \frac{3}{2} k (T'_n - T'_e) + m_e \nu_{ei} n_e \frac{2}{m_i} \frac{3}{2} k (T'_i - T'_e). & (2.45) \end{aligned}$$

For the conditions of interest, u_i can be of the same order as u_e, but since $\nu_{ie} << \nu_{en}$, the first term dominates the second. Also, $\vec{u_n}$ is negligible in comparison to $\vec{u_e}$. The magnitude of the thermal component of elastic collision transfer (last two terms) is on the order of 10^3 times larger than the mean components, and is ignored. Therefore,,

$$S_e = \frac{j_e^{\,2}}{\sigma_e}, \tag{2.46}$$

where $\vec{j_e} = -e n_e \vec{u}_e$ is the electron current density, and σ_e is the electrical conductivity,

$$\sigma_e = \frac{e^2 n_e}{m_e \nu_{en}}. \tag{2.47}$$

A vector form of the electron momentum balance may be written as,

$$\vec{j_e} + \vec{j_e} \times \vec{\beta} = \sigma_e \left(\vec{E}' + \frac{\nabla p_e}{e n_e} \right), \tag{2.48}$$

where,

$$\vec{\beta} = \frac{e\vec{B}}{m_e \nu_{en}}, \tag{2.49}$$

and since $\vec{u_n} \approx 0$,

$$\vec{E'} = \vec{E} + \vec{u}_n \times \vec{B} = \vec{E}. \tag{2.50}$$

Using these relations, Equation 2.46 may be written as,

$$S_e = \vec{j}_e \cdot \vec{E} - \vec{u_e} \cdot \nabla p_e. \tag{2.51}$$

2.4.8 Inelastic Losses

Considerable energy is lost to electronic excitation of neutral atoms. The net energy cost for producing a singly-charged ion, φ, can be expressed as the sum of the energy required for ionization, plus the energy lost to excitation of neutral atoms. This is justified, because the gas is optically thin, and excitation energy lost by radiation is not recovered by the electrons through quenching collisions.

$$\varphi = E_i + \frac{\sum_j \langle Q_j(u_e) u_e \rangle E_j}{\langle Q^+(u_e) u_e \rangle}, \tag{2.52}$$

where E_i is the first ionization energy, $Q_j(u_e)$ is the cross section for excitation from the ground state to energy level E_j, and $Q^+(u_e)$ is the cross section for ground state ionization. A complicated analytical expression for φ is derived by Dugan et. al. [24]. The result can be fitted closely as,

$$\varphi' = Ae^{-\frac{B}{z}} + C, \tag{2.53}$$

where φ' and z are normalized ion production cost and dimensionless electron kinetic temperature,

$$\varphi' = \frac{\varphi}{E_i}, \tag{2.54}$$

$$z = \frac{kT_e}{E_i}. \tag{2.55}$$

The constants A, B, and C are given in Table 2.1, and φ' is plotted in Figure 2-3 versus dimensionless electron kinetic temperature, $z = \frac{kT_e}{E_i}$. Using the normalized ion production cost, the volumetric electron energy loss rate can then be given as,

$$S_i = \dot{n}_e \varphi' E_i. \tag{2.56}$$

	A	B	C
Argon	0.188	0.624	1.75
Xenon	0.254	0.677	2.00

Table 2.1: Constants to fit the Dugan ion production cost model.

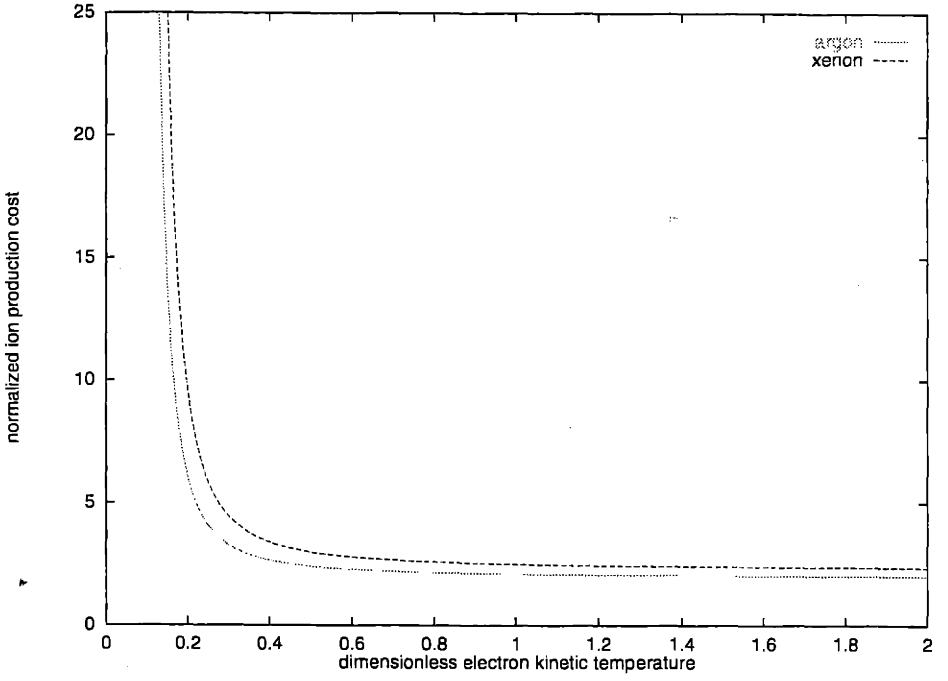

Figure 2-3: Normalized ion production cost, $\varphi' = \frac{\varphi}{E_i}$, versus dimensionless electron kinetic temperature, $z = \frac{kT_e}{E_i}$, for argon and xenon.

This model only considers excitations and ionizations from inelastic collisions of free electrons with ground state neutral atoms. It is estimated that inelastic losses due to electron-ion collisions are two orders of magnitude smaller than those due to electron-neutral collisions, and are ignored.

2.4.9 Electron Energy Summary

Now that all bulk energy sources have been defined, we are in a position to summarize the electron energy equation with one simplification. The elastic collision energy source model, derived in Section 2.4.7, contains a term, $\vec{u_e} \cdot \nabla p_e$, representing heating due to internal pressure gradients. It will cancel with the identical term in Equation 2.37, giving,

$$\frac{\partial}{\partial t}\left(\frac{3}{2}n_e k T_e\right) + \nabla \cdot (\frac{5}{2}n_e k T_e \vec{u}_e + \vec{q}_e) = S_h - S_i, \tag{2.57}$$

where,

$$S_h = \vec{j}_e \cdot \vec{E}, \tag{2.58}$$

$$S_i = \dot{n}_e \varphi' E_i. \tag{2.59}$$

Equation 2.57 is the form for conservation of internal energy we will use when describing the numerical method in the next chapter.

2.4.10 Wall Losses, Simple Analysis

The insulator walls of a Hall thruster absorb energy from the electron population in the channel. To quantify this loss, one approach is to set the net current to the insulator wall to zero and simply balance the flux of electrons with the flux of ions ($\Gamma_e = \Gamma_i$). In this case the wall acts as a third body, on which electrons and ions recombine. For a wall potential (with respect to the plasma) of ϕ_w, the net energy flux to the wall is,

$$q_w = \Gamma_i(2kT_e - e\phi_w). \tag{2.60}$$

More correctly, energetic electrons which make it to the wall may cause a secondary electron to be emitted from the wall surface. To be exact, secondary electron emission by ion impact should also be included, but this effect is believed to be small by comparison, and is ignored.

If δ is used to represent the secondary electron emission yield (fraction of electron impacts that results in a secondary electron being emitted), then the balance becomes,

$$\Gamma_i = \Gamma_{e,primary}(1-\delta), \tag{2.61}$$

where $\Gamma_{e,primary}$ represents the electron flux coming from outside the sheath. For the case where δ is invariant with electron energy [47],

$$q_w = n_e\sqrt{\frac{kT_e}{2\pi m_e}}e^{\frac{-e\phi_w}{kT_e}}(2kT_e - e\phi_w + \delta e\phi_w). \tag{2.62}$$

For boron nitride, δ is around 0.6 for electron energies around 10 eV [16]. The potential drop at the sheath may be found by balancing the electron and ion fluxes. For $T_i << T_e$, conventional sheath theory requires ions to be supersonic ($v_i = v_{Bohm} = \sqrt{\frac{kT_e}{m_i}}$) at the sheath edge. Balancing the ion flux with the electron flux reduced by Boltzmann factor, ϕ_w is found to be,

$$\phi_w = \frac{kT_e}{e}\ln\left[\frac{e^{-1/2}}{(1-\delta)}\sqrt{\frac{2\pi m_e}{m_i}}\right], \tag{2.63}$$

which is usually negative. Equation 2.63 is not exactly correct for ions with some initial velocity toward the wall. In that case, the potential drop in the plasma region (accelerating ions to v_{Bohm}) may be smaller. From measurements and simulations, the normal component of the ion velocity near the channel wall has been found to be subsonic, so the potential drop in the sheath region must actually be somewhere between $\frac{kT_e}{2e}$ and zero. This discrepancy is small compared to the total sheath drop, ϕ_w, which, for xenon, is about 10 times larger. As a simplification, the initial velocity of ions normal to the wall will be taken to be zero for computing electron losses.

2.4.11 Wall Losses, Detailed Analysis

Previous models [30] using the simple wall models presented in the previous section predicted the electron energy flux to the wall to be small. Predictions of T_e just outside the accelerator channel, in those cases, were high. The following theory is a more detailed approach, parts of which have been published before. In Russian literature [33], a short description of the resulting behavior is presented, but without a detailed derivation. Katz et. al. [41] present an analogous theory for computation of charging rate on geosynchronous spacecraft, except

in that case, current collection is orbit-motion-limited, and the mean electron energies are in kiloVolts. They find that the charging rate depends strongly on the form of the secondary emission yield as a function of electron energy. In the case of Hall thruster wall loss, we will show that the same is true.

Experimental data show that the ratio of secondary to primary electrons, δ, is a function of electron energy. For many ceramic insulators, δ exceeds unity at a few tens of eV. At low ($< 100eV$) energies, an exponential fit can be used to closely approximate $\delta(E)$:

$$\delta(E) = \frac{secondaries}{primaries} \approx AE^B, \tag{2.64}$$

where E is the monoenergetic electron energy in eV. Based on experimental data by Bugeat and Koppel [16], $A = 0.141$ and $B = 0.576$ for boron bitride.

Ion-Attracting Sheath

We start by making the approximation that an ion attracting sheath is present whenever $\phi_w < 0$ (not quite true for small ϕ_w). The freestream electron number density is adjusted for the wall potential ϕ_w, arriving at a Maxwell-Boltzman distribution in the sheath:

$$n_e = n_{eo} \exp \frac{e\phi_w}{kT_e}. \tag{2.65}$$

The primary electron distribution function is Maxwellian with temperature T_e and density as given by Equation 2.65:

$$f_e(w) = n_e(\frac{m_e}{2\pi kT_e})^{\frac{3}{2}} \exp \frac{-mw^2}{2kT_e}. \tag{2.66}$$

The primary electron flux to the wall is

$$\Gamma_{e,primary} = \frac{n_e \bar{c_e}}{4}, \tag{2.67}$$

where $\bar{c_e}$ is the electron mean thermal speed,

$$\bar{c_e} = \sqrt{\frac{8kT_e}{\pi m_e}}. \tag{2.68}$$

Denoting the primary primary electron velocity component normal to the wall as $w_\perp$, the integral,

$$\Gamma_{e,secondary} = \int w_\perp f_e(w) \delta d^3 w, \tag{2.69}$$

yields the secondary electron flux, $\Gamma_{e,secondary} = \Gamma_{e,primary} \delta_{eff}$, and the effective secondary emission coefficient, δ_{eff}, in the form (using Equation 2.64):

$$\delta_{eff} = \Gamma[2+B] A (kT_e/e)^B, \tag{2.70}$$

where $\Gamma[x]$ is Euler's Gamma function.

By imposing wall neutrality, including the fluxes of ions and of primary and secondary electrons, it can be shown that,

$$\phi_w = \frac{-kT_e}{e} \ln[(1-\delta_{eff}) e^{\frac{1}{2}} \frac{\bar{c}_e}{4v_b}], \tag{2.71}$$

where v_b is the Bohm velocity given by $v_b = \sqrt{\frac{kT_e}{m_i}}$. Once again, this assumes the mean ion velocity normal to the wall to be zero. The sheath potential, ϕ_w, remains negative for T_e below the value which makes $[(1-\delta_{eff}) e^{\frac{1}{2}} \frac{\bar{c}_e}{4v_b}] = 1$. For xenon and boron nitride, this happens at $T_e = 16.55eV$ and $\delta_{eff} = 0.997$. Above this T_e, the sheath potential turns positive.

For the remainder of this discussion, we will use 16.55 eV as the break-point. Other insulator-propellant combinations will have a different value.

It is interesting to note that, for the case of the ion-attracting sheath, an analogy exists with charging of spacecraft. Hastings and Garrett [37] give a thorough discussion of this topic. For the case of geosynchronous (GEO) spacecraft, the total charging rate is dependent upon the balance between ions, primary electrons, secondary electrons, and backscattered electrons. Resulting potentials have been observed between 2 and 20 kV below the ambient plasma. Katz et. al. [41] used a detailed model of the high energy ($> 5keV$) portion of the secondary electron yield function to accurately predict charging rate for several surface materials. In the analysis presented here, the electrons are much colder, and only the low energy portion of the yield function is modeled. This is more like the case of a low-earth-orbit (LEO) spacecraft, where floating potentials may reach a few hundreds of volts below the plasma potential. In all three cases (LEO, GEO, Hall Thrusters), the result is strongly

dependent on $\delta(E)$.

Ion-Repelling Sheath

It is assumed here that an ion-repelling sheath exists, and is monotonic. For that case, the neutrality condition requires that $\delta_{eff} \approx 1$. Since secondaries must now overcome the sheath barrier to escape into the plasma, the (slightly positive) wall potential is,

$$\phi_w = \frac{kT_{sec}}{e} \ln [\Gamma[2+B]A(kT_e/e)^B], \tag{2.72}$$

and $T_e > 16.64$ eV. This is of order T_{sec}, i.e. no more than $\sim 1eV$.

Energy Flux to the Walls

An equation for electron energy lost to the wall and sheath is obtained by integrating the primary and secondary electron energy fluxes across Maxwellian distributions:

$$q_w = \int w_\perp f_e(w)(\frac{1}{2}m_e w^2)d^3w - \int w'_\perp f_e(w')(\frac{1}{2}m_e w'^2)d^3w', \tag{2.73}$$

where w' is the velocity of the secondary electrons assumed to be Maxwellian at temperature T_{sec}. The integral yields:

$$q_w = \Gamma_{e,primary}[(2kT_e - e\phi_w) - \delta_{eff}(2kT_{sec} - e\phi_w)]. \tag{2.74}$$

Thus,

$$\frac{q_w}{\bar{\Gamma}_e} \approx \begin{cases} \exp\frac{e\phi_w}{kT_e}[2k(T_e - \delta_{eff}T_{sec}) - (1-\delta_{eff})e\phi_w] & T_e < 16.5eV \\ 2k(T_e - T_{sec}) & T_e > 16.5eV \end{cases}, \tag{2.75}$$

where $\bar{\Gamma}_e = \frac{n_{e0}\bar{c}_e}{4}$. Graphs of these functions are shown in Figure 2-4. Notice the sharp change in the character of these curves in the region around $T_e \approx 16eV$. The sheath reaches a maximum negative voltage of about $50eV$ at $T_e \approx 13eV$, but collapses to zero by $T_e \approx 16.5eV$. There is little heat loss for $T_e < 16eV$, but q_w develops rapidly beyond this.

As the electron temperature along any magnetic streamline approaches or exceeds $16.55eV$, wall losses increase dramatically, pulling the electron temperature back down. Because we assume infinite electron mobility along magnetic streamlines, this limits the

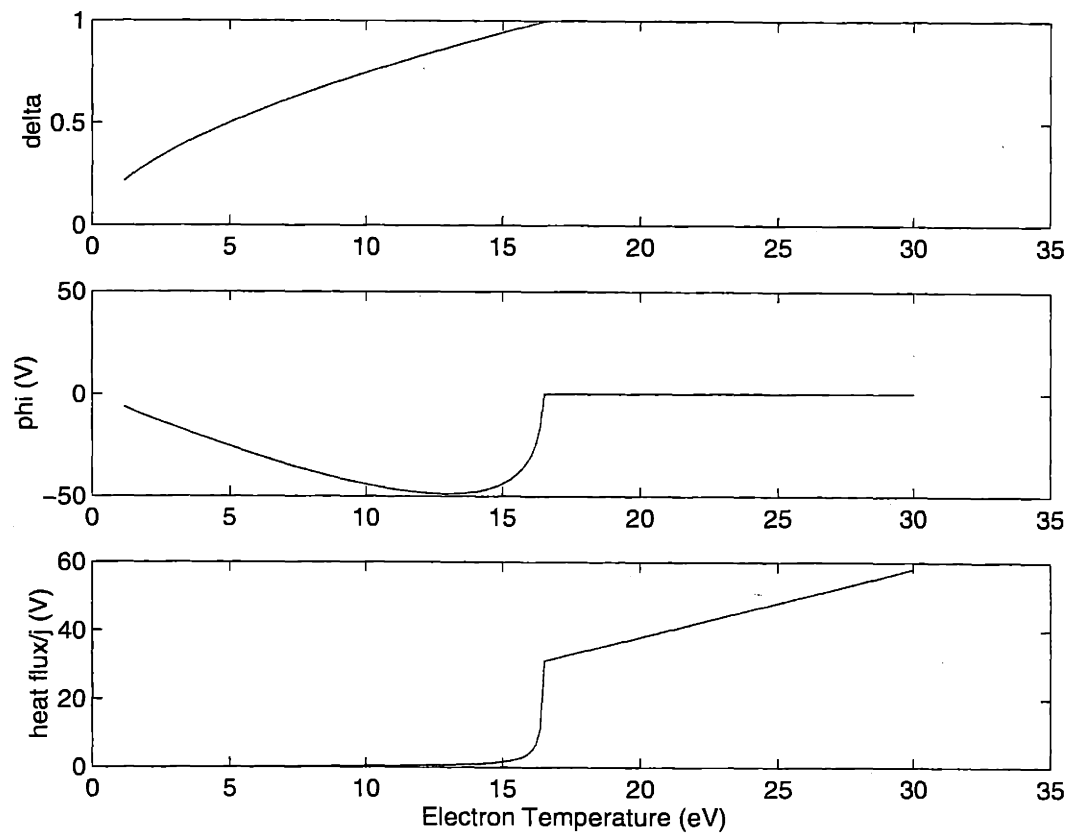

Figure 2-4: Secondary emission coefficient δ_{eff}, wall potential ϕ_w, and normalized heat flux q_w vs. T_{e^*}[eV]

electron temperature to $16.55eV$.

It should be noted that all of the fluxes derived so far in this section assume the magnetic field lines intersect the wall perpendicularly. To account for some intersection angle, θ, which is not 90°, the fluxes should be multiplied by a factor of $\sin(\theta)$.

Near-Wall Cross-Field Electron Transport

The secondary emission coefficient is also important when considering cross-field electron transport near the wall. The low-energy secondary electrons are considered to start from rest at the wall in crossed electric and magnetic fields. For collisionless trajectories, the electron velocities in the axial and azimuthal directions will be, respectively:

$$u_z = -\frac{E}{B}\sin\omega_c t, \tag{2.76}$$

$$u_\theta = -\frac{E}{B}(1-\cos\omega_c t). \tag{2.77}$$

The time to complete one Larmor cycle is

$$t = \frac{2\pi}{\omega_c}. \tag{2.78}$$

Referring to Figure 2-5, the guiding center of this motion is located $\Delta\hat{n}$ closer to the anode than the initial emission point:

$$\Delta\hat{n} = \frac{E}{B\omega_c}. \tag{2.79}$$

Thus, the secondary electrons "step" toward the anode with a step size of $\Delta z = \frac{\Delta\hat{n}}{\sin(\theta)}$. It takes the secondary electrons one quarter Larmor cycle to travel this distance. This amounts to increased electron mobility in the axial direction near the wall.

The excess flux is localized to a distance, Δr, from the insulator wall, which is the distance traveled by a secondary electron before Larmor motion is initiated. This distance is determined by the mean ejection velocity normal to the wall, u_r, and the time, Δt, required to execute the first Larmor quarter cycle:

$$\Delta r = \Delta t u_r \approx \frac{1}{4}\frac{2\pi}{\omega_c}u_r, \tag{2.80}$$

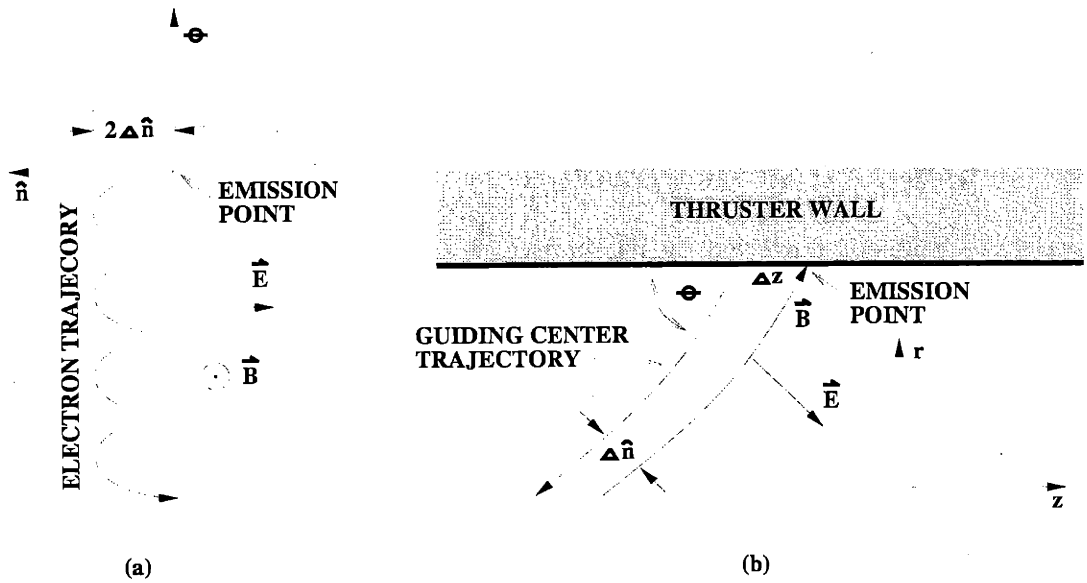

Figure 2-5: Secondary electron trajectory in the (a) $z-\theta$ plane and in the (b) $z-r$ plane.

where,

$$u_r = \begin{cases} \sqrt{\frac{2e\phi_w}{m_e}} & T_e < 16.5eV \\ \frac{\bar{c}_e(T_{sec})}{4} = \sqrt{\frac{kT_{sec}}{2\pi m_e}} & T_e > 16.5eV \end{cases} . \tag{2.81}$$

The total number of secondary electrons per second crossing an axial plane beginning at the wall and ending at Δr will be equal to the number of secondary electrons per second emitted in the wall area extending Δz downstream in the axial direction. Thus we estimate the mean axial flux in the wall region to be:

$$\Gamma_{e,z} = \Gamma_e \delta_{eff} \frac{2\pi r \Delta z}{2pir\Delta r} = \Gamma_e \delta_{eff} \frac{\Delta z}{\Delta r}, \tag{2.82}$$

Writing flux as the product of E times a "mobility," μ_{wall},

$$\Gamma_{e,z} = \mu_{wall} E n_e, \tag{2.83}$$

and averaging over the cross section, including emission from both walls separated by a

distance, h, we can say:

$$\mu_{wall} = \begin{cases} \frac{\bar{c}_e}{2B\omega_c h \sin(\theta)} \delta_{eff} e^{\frac{e\phi_w}{kT_e}} & T_e < 16.5eV \\ \frac{\bar{c}_e}{2B\omega_c h \sin(\theta)} \delta_{eff} & T_e > 16.5eV \end{cases} . \tag{2.84}$$

This is equivalent to ordinary collisions with molecules at frequencies:

$$\nu_{wall} = \begin{cases} \frac{\bar{c}_e}{2h \sin(\theta)} \delta_{eff} e^{\frac{e\phi_w}{kT_e}} & T_e < 16.5eV \\ \frac{\bar{c}_e}{2h \sin(\theta)} \delta_{eff} & T_e > 16.5eV \end{cases} , \tag{2.85}$$

which is proportional to $\bar{c}/h$, which is the mean time required for electrons to travel between walls.

Plotting μ_{wall} versus T_e in Figure 2-6, and comparing with the classical and Bohm values from Figure 2-2, it can be seen that wall transport is comparable, especially in regions of high T_e, to the Bohm value. It is believed that the high-temperature regions are concentrated downstream of the ionization layer. In the longer region between the anode and the ionization layer, where T_e is low, near-wall transport plays no role according to Figure 2-6.

Instead of accounting for the localized effects of near-wall electron current, a total electron current will be computed and used in the electron continuity equation, Equation 2.32.

Total Near-Wall Electron Current

A total near-wall electron current, I_w, across a line of force can be computed by similar logic. The total number of secondary electrons per second which cross an axial plane is simply the flux that are emitted from the wall times the area of the "strip" of wall with axial distance Δz:

$$I_w = e\Gamma_e \delta_{eff} \left(\frac{2\pi r \Delta z}{\sin(\theta)} \right) = \Gamma_e \delta_{eff} \left(\frac{2\pi r E m_e}{B^2 \sin(\theta)} \right) . \tag{2.86}$$

The additional electron conductivity gained by the near-wall term may account for some of the "anomalous" conductivity, as proposed by Morozov [56]. The wall conductivity here is found to be $\sim 1/B^2$ instead of $\sim 1/B$. This is in accordance with the analogy that has been put forth before [17] that the wall functions like a molecule, with $\frac{1}{B^2}$ collisionality with

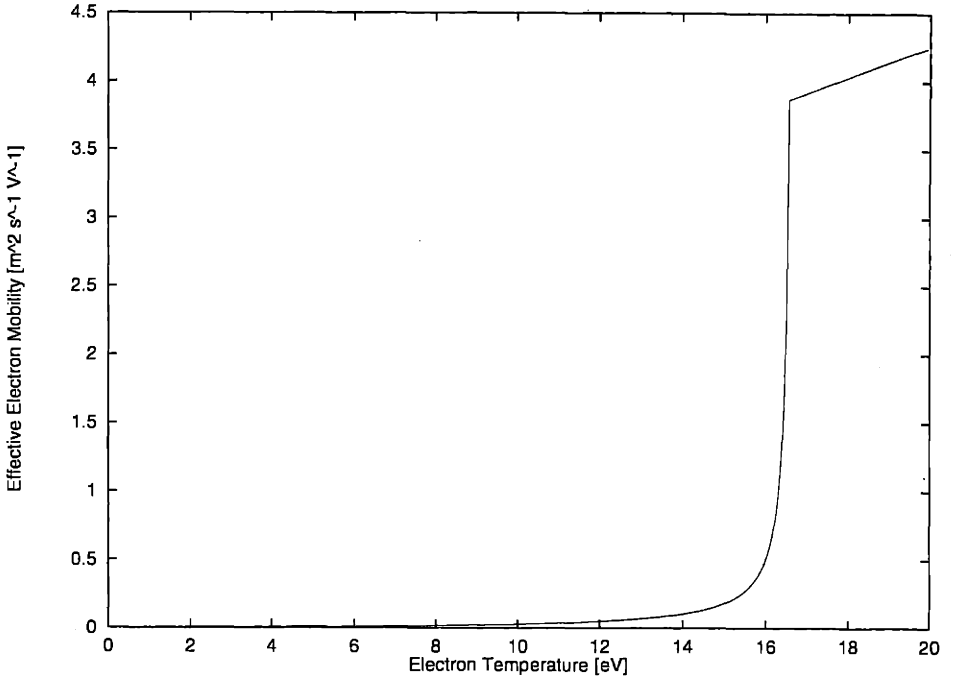

Figure 2-6: Effective electron mobility due to wall transport, $h = 2\ cm$, $B = .01\ Tesla$, $\theta = 0$.

electrons.

2.5 Heavy Species

The equations of motion for particles in cylindrical coordinates are,

$$\frac{d}{dt}\begin{bmatrix} r \\ \theta \\ z \\ \dot{r} \\ \dot{\theta} \\ \dot{z} \end{bmatrix} = \begin{bmatrix} \dot{r} \\ \dot{\theta} \\ \dot{z} \\ \frac{F_r}{m} + r\dot{\theta}^2 \\ \frac{1}{r}(\frac{F_\theta}{m} - 2\dot{r}\dot{\theta}) \\ \frac{F_z}{m} \end{bmatrix}. \tag{2.87}$$

Due to the assumption of spatial uniformity in the azimuthal direction, the θ-component of position can be ignored, and a 2-D 3-V approach is taken. Furthermore, it will be advantageous to represent the azimuthal velocity in terms of angular momentum per unit

2.6.2 Charge Exchange

From Rapp and Francis [58], the charge exchange cross section for Xe and Xe^+ is between 1×10^{-18} and 4×10^{-19} m^2 for relative velocities between 100 and 15,000 m/s. Near the anode, where the ion velocity is low, the neutral density is approximately 1×10^19 m^{-3}, giving a mean mean free path of 10 cm. Although this is comparable to the channel width (1.5 cm), charge exchange is neglected here. In the plume, the ion velocity is high, and the neutral density drops by a factor of 10, giving a mean free path of 2.5 m. For considering larger distances away from the thruster, charge exchange may be important in generating slow ions. These could be more easily turned back toward thruster, increasing wall loss and conductivity. However, this model focuses on the near-field physics, so charge exchange in the plume is neglected as well.

2.6.3 Bulk Recombination

The bulk three-body electron recombination rate can be written as,

$$\frac{dn_e}{dt} = -\alpha n_e n_i, \tag{2.91}$$

where α is a macroscopic recombination rate. According to Mitchner [52], α can be approximated as,

$$\alpha = 1.09 \times 10^{-20} n_e T^{-9/2} \ m^3/s, \tag{2.92}$$

which, for $T = 3000°K$ and $n_e = n_i = 1 \times 10^{18}$ gives $\frac{dn_e}{dt} = 2 \times 10^{18}$ $m^{-3}s^{-1}$. This is much less than the characteristic ionization rate (1×10^{23} $m^{-3}s^{-1}$), so bulk recombination is ignored.

2.6.4 Bulk Ionization Rate

The ionization rate, $\dot{n}_i$, is the rate at which ions are created per unit volume. In this model, it is assumed that only electron-neutral collisions can produce ions. Furthermore, only singly-ionized atoms are treated (for reasons discussed in Section 2.6.5):

$$\dot{n}_i = \dot{n}_e. \tag{2.93}$$

	β_1	β_2	$Q[m^3 s^{-1}]$
Argon	0.82	1.00	2.77×10^{-13}
Xenon	1.00	0.80	4.13×10^{-13}

Table 2.3: Constants for the Drawin ionization model with Maxwellian electrons.

Considering only random kinetic energy, the ion production rate is given by,

$$\dot{n_i} = n_n \int_0^\infty f_e {c_e}^3 4\pi \sigma_i(c_e) dc_e, \tag{2.94}$$

where $\sigma_i(c_e)$ is the ionization cross section, and f_e is the Maxwellian electron velocity distribution function,

$$f_e = n_e \left(\frac{m_e}{2\pi k T_e} \right)^{3/2} e^{-\frac{m_e c_e^2}{2kT_e}}. \tag{2.95}$$

The ionization cross section is approximated according to Drawin [52] as a function of electron energy,

$$\sigma_i = 2.66\pi a_0^2 \beta_1 \left(\frac{\epsilon_i^H}{\epsilon_i} \right)^2 \xi g(u), \tag{2.96}$$

where,

$$g(u) = \frac{u-1}{u^2} \ln(1.25\beta_2 u). \tag{2.97}$$

Here $u = \epsilon/\epsilon_i$ is the nondimensional electron energy, ϵ_i^H is the ionization energy of hydrogen, ϵ_i is the first ionization energy of the heavy species, ξ is the number of equivalent electrons in the outer shell, and β_1 and β_2 are adjustable constants of order unity. Comparing with empirical data, β_1 and β_2 can be found iteratively, and are given in Table 2.3. Substituting Equations 2.95 and 2.97 into Equation 2.94 [47],

$$\dot{n_i} = n_e n_n Q \beta_1 \frac{I(\theta)}{\theta^{\frac{3}{2}}}, \tag{2.98}$$

where,

$$I(\theta) = \int_1^\infty e^{-\frac{u}{\theta}} \frac{(u-1)}{u} \ln(1.25\beta_2 u) du. \tag{2.99}$$

Here $\theta = kT_e/\epsilon_i$, and Q is a constant shown in Table 2.3. The ionization rate may then be written as,

$$\dot{n_i} = \varsigma(T_e) n_e n_n, \tag{2.100}$$

where, from Equation 2.98,

$$\varsigma(T_e) = Q\beta_1 \frac{I(\theta)}{\theta^{\frac{3}{2}}}. \tag{2.101}$$

The quantity ς is plotted versus electron temperature in Figure 2-8 for xenon.

2.6.5 Second-Degree Ionization

Following an approach similar to the one used in Section 2.6.4, we can write the bulk rate of creation of Xe^{++} ions as,

$$\dot{n_i}^{++} = \varsigma^{0\rightarrow II}(T_e) n_e n_n + \varsigma^{I\rightarrow II} n_e^2. \tag{2.102}$$

Mathur and Badrinathan [51] give cross-section data for double ionization of Xe atoms by electron impact. For electron energies less than 80 eV, this can be fitted in the Drawin form (Equation 2.96) with $\epsilon_i = 33.3\ eV$, $\xi = 3$, $\beta_1 = 1.0$ and $\beta_2 = 0.8$.

No data have been found for the partial ionization cross-section of Xe^+, so an educated guess will be taken. Referring again to the Drawin form, we will use $\epsilon_i = 21.2\ eV$, $\xi = 5$, $\beta_1 = 1.0$ and $\beta_2 = 0.8$. The threshold energy, ϵ_i, is the threshold energy of Xe^{++} (33.3 eV) minus the threshold energy of Xe^+ (12.1 eV).

Figure 2-7 shows a comparison between the ionization cross sections used here.

Integrating both cross-sections over Maxwellian electron distributions, the rate parameters are found. Figure 2-8 shows a comparison between the rate parameters $\varsigma^{0\rightarrow I}$, $\varsigma^{I\rightarrow II}$ and $\varsigma^{0\rightarrow II}$. Since $\frac{n_e n_n}{{n_e}^2} \sim 100$ for Hall thrusters, and noticing that $\varsigma^{I\rightarrow II} < \varsigma^{0\rightarrow II}$, $Xe^+ \rightarrow Xe^{++}$ will be small. However, due to $Xe \rightarrow Xe^{++}$ at electron temperatures above 15 eV, $\frac{\dot{n_i}^{++}}{\dot{n_i}}$ may be around .1.

2.7 Anode

The anode, like any other surface in contact with the plasma, will modify conditions in its vicinity. It can be expected that a sheath will begin at the anode and extend into the plasma a distance of the order of λ_D. Applying classical electrode theory in the thin-sheath collisionless limit, and assuming a potential drop to the anode, the current emitted is [38],

$$I_a = A_a e n_e \left[e^{\frac{e\phi_a}{kT_e}} \sqrt{\frac{kT_e}{2\pi m_e}} - e^{-1/2} \sqrt{\frac{kT_e}{m_i}} \right], \tag{2.103}$$

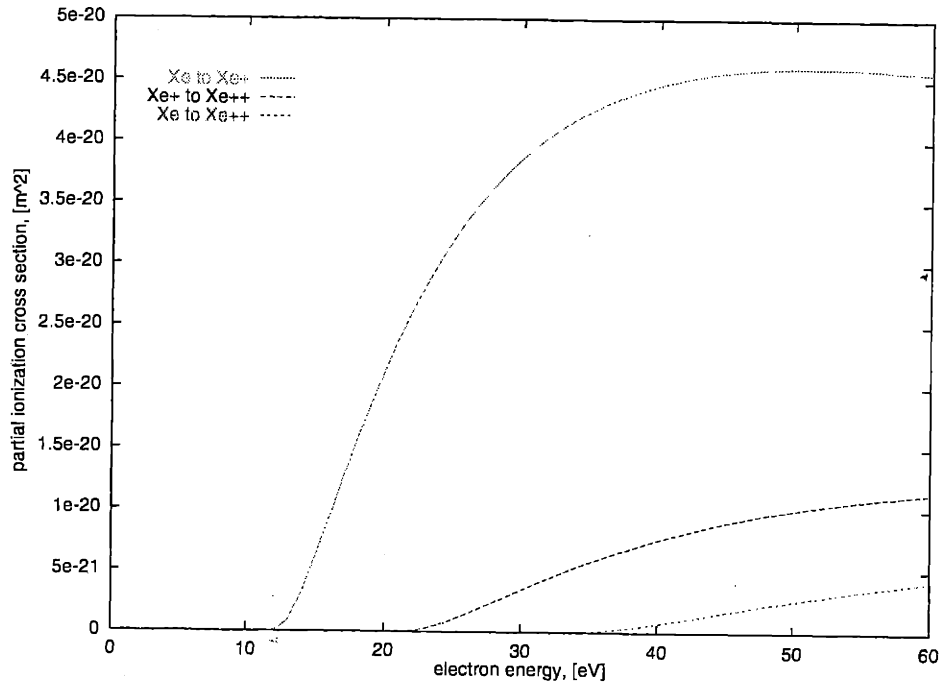

Figure 2-7: Ionization cross sections for $Xe \rightarrow Xe^{+}$, $Xe^{+} \rightarrow Xe^{++}$, and $Xe \rightarrow Xe^{++}$, by electron impact. Propellant: xenon. $[m^2]$.

where, ϕ_a is the potential of the anode with respect to the plasma, and A_a is the anode area. The magnitude of the expected potential drop is, therefore,

$$\phi_a = -\frac{kT_e}{e} \ln \left[\frac{I_a}{A e n_e \sqrt{\frac{kT_e}{2\pi m_e}}} + e^{-1/2} \sqrt{\frac{2\pi m_e}{m_i}} \right]. \tag{2.104}$$

This estimate becomes invalid as ϕ_a nears zero, or when the anode current is nearly equal to the random electron current ($\frac{e n_e \bar{c}}{4}$). However, most previous measurements and computations of conditions near the anode imply that the random electron current is much larger than I_a, so we will use Equation 2.104.

2.8 Cathode

Rigorously, the detailed properties of the cathode should be included, but this is beyond the scope of this work. Instead, it is modeled simply as a perfect current source with constant ϕ and T_e just outside.

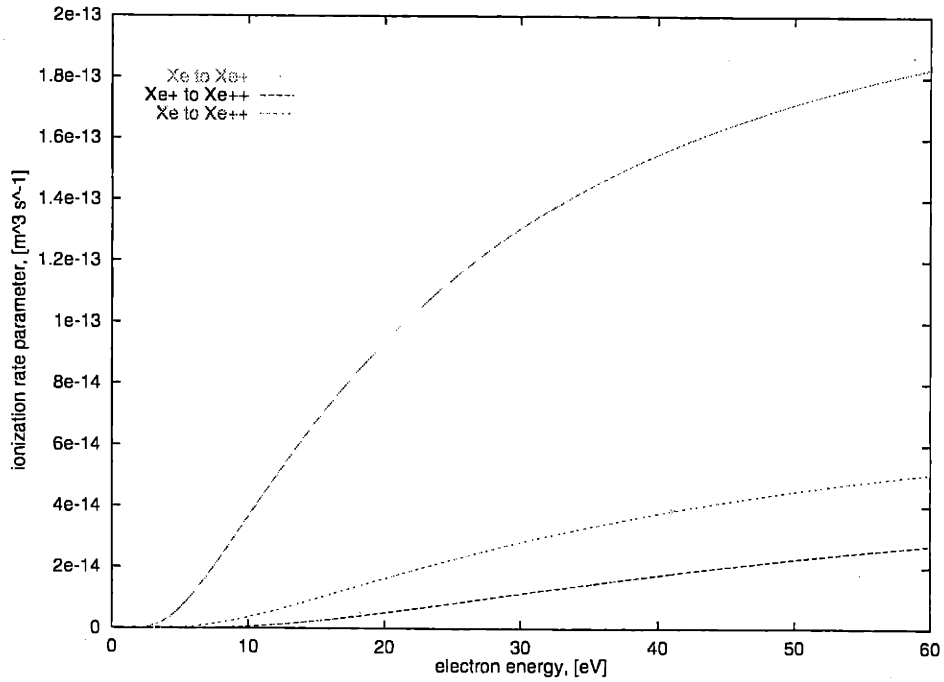

Figure 2-8: Comparison of ionization rate parameter, $\varsigma^{0\to I}$, $\varsigma^{I\to II}$ and $\varsigma^{0\to II}$, for ionization of Xe to Xe^{+}, Xe^{+} to Xe^{++}, and Xe to Xe^{++}, respectively, by electron impact. Propellant: xenon. $[m^3 \cdot s^{-}1]$

2.9 Summary of Governing Equations

Below is a summary of the governing equations developed in this chapter:

2.9.1 Magnetic Field

$$\vec{B} = \nabla\sigma \tag{2.105}$$

$$\nabla^2\sigma = 0 \tag{2.106}$$

$$\begin{aligned} \frac{\partial\lambda}{\partial z} &= r\frac{\partial\sigma}{\partial r} = rB_r & (2.107)\\ \frac{\partial\lambda}{\partial r} &= -r\frac{\partial\sigma}{\partial z} = -rB_z & (2.108) \end{aligned}$$

2.9.2 Electron Equations

Along Lines of Force

$$\phi - \frac{kT_e}{e}\ln(n_e) = \phi^*(\lambda) \tag{2.109}$$

$$T_e = T_e(\lambda) \tag{2.110}$$

Across Lines of Force

$$u_{e,\hat{n}} = \mu_{e,\perp}\left(-rB\frac{\partial\phi^*}{\partial\lambda} - rB\frac{k}{e}(\ln(n_e)-1)\frac{\partial T_e}{\partial\lambda}\right) \tag{2.111}$$

$$\mu_{e,\perp} = \frac{\mu_e}{{\beta_e}^2} + K_B\frac{1}{16B} \tag{2.112}$$

$$\frac{\partial\phi^*}{\partial\lambda} = \frac{-I_a + I_w - 2\pi k\frac{\partial T_e}{\partial\lambda}\int_0^l n_e\mu_{e,\perp}B(\ln(n_e)-1)r^2ds - 2\pi e\int_0^l n_i u_{i,\hat{n}}rds}{2\pi e\int_0^l n_e\mu_{e,\perp}Br^2ds} \tag{2.113}$$

$$\frac{\partial}{\partial t}\left(\frac{3}{2}n_e kT_e\right) + \nabla\cdot\left(\frac{5}{2}n_e kT_e\vec{u}_e + \vec{q}_e\right) = S_h - S_i \tag{2.114}$$

$$\begin{aligned} S_h &= \vec{j}_e\cdot\vec{E} & (2.115)\\ S_i &= \dot{n}_e\varphi' E_i & (2.116) \end{aligned}$$

Wall Effects

$$\frac{q_w}{\overline{\Gamma}_e} \approx \begin{cases} \exp\frac{e\phi_w}{kT_e}[2k(T_e - \delta_{eff}T_{sec}) - (1-\delta_{eff})e\phi_w] & T_e < 16.5eV \\ 2k(T_e - T_{sec}) & T_e > 16.5eV \end{cases} \tag{2.117}$$

$$I_w = e\Gamma_e\delta_{eff}\left(\frac{2\pi r\Delta z}{\sin(\theta)}\right) = \Gamma_e\delta_{eff}\left(\frac{2\pi rEm_e}{B^2\sin(\theta)}\right). \tag{2.118}$$

Anode and Cathode

$$\phi_a = -\frac{kT_e}{e}\ln\left[\frac{I_a}{Aen_e\sqrt{\frac{kT_e}{2\pi m_e}}} + e^{-1/2}\sqrt{\frac{2\pi m_e}{m_i}}\right] \tag{2.119}$$

$$\phi_c = Constant \tag{2.120}$$

$$T_{e,c} = Constant \tag{2.121}$$

2.9.3 Heavy Particle Equations

$$\frac{d}{dt}\begin{bmatrix} r \\ z \\ \dot{r} \\ h \\ \dot{z} \end{bmatrix} = \begin{bmatrix} \dot{r} \\ \dot{z} \\ \frac{F_r}{m} + \frac{h^2}{r^3} \\ \frac{rF_\theta}{m} \\ \frac{F_z}{m} \end{bmatrix} \tag{2.122}$$

$$\dot{n_i} = \varsigma(T_e)n_en_n \tag{2.123}$$

$$\dot{n_i}^{++} = \varsigma^{0\to II}(T_e)n_en_n + \varsigma^{I\to II}n_e^2 \tag{2.124}$$

Chapter 3

Numerical Method

3.1 Overall Scheme

The governing equations are solved time-accurately by separating the slow time scale (ion and neutral) motion from the fast time scale (electron) motion, and iterating successively. Individual ion and neutral atoms are simulated using a Particle-In-Cell method as described in Section 3.5. The electron motion is modeled as a fluid continuum with the equations derived in Section 2.4.

3.2 Grid Generation

In order to accommodate any contiguous axisymmetric geometry, and to simplify boundary conditions, a nonuniform spatial grid is used. The dimensions are adjustable, but runs presented in this paper use $47 - by - 22$, as shown in Figure 3-1. The grid is generated with (z, r)-coordinates which contour the walls of the acceleration zone and parts of the plume. This grid maps directly to a uniform computational grid in (ξ, η)-space, such that the inner boundary of the device is always at $\eta = 0$, the left boundary (anode) is always at $\xi = 0$, and the top boundary is always at $\eta = \eta_{max}$. The right hand side of the grid contacts the downstream region, which is not modeled. For simplicity, the distance between nodes in computational space is set to unity in each direction.

As mentioned in Section 2.1, rotational symmetry is assumed. Therefore, only a meridional section of the Hall thruster acceleration zone is modeled.

Grid spacing is determined by the timestep of the simulation. It is set to the smallest

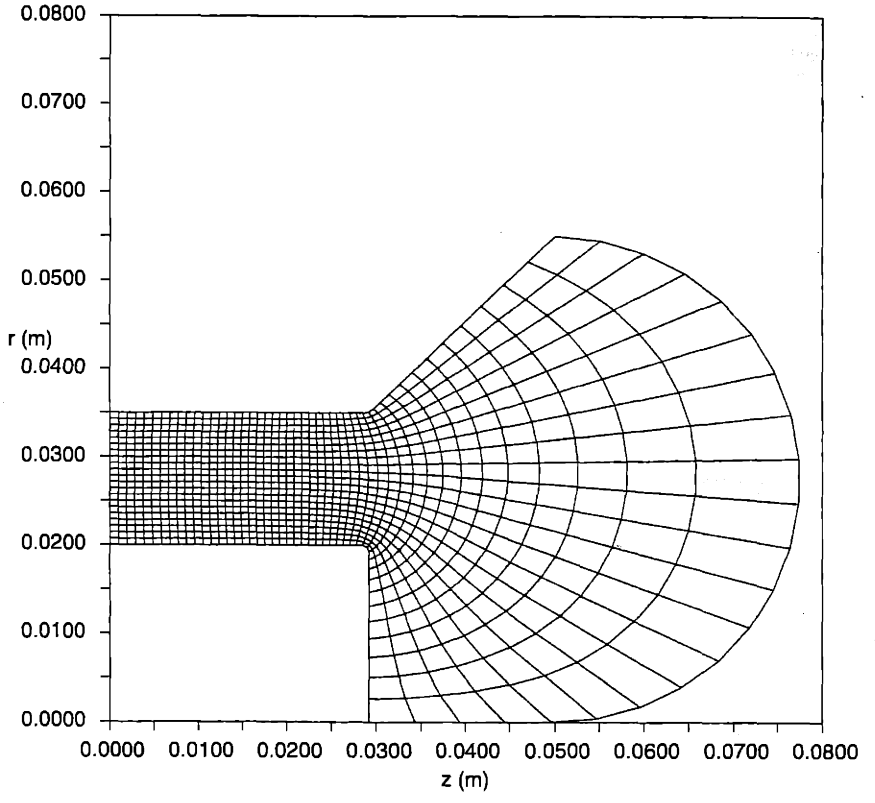

Figure 3-1: Spatial grid for the SPT-70 geometry.

value which is larger than the maximum distance traveled by an ion partice in one timestep.

Grid generation is accomplished by selecting the boundary nodes and solving an elliptic partial differential equation iteratively for the interior node locations. This method, commonly used in computational fluid dynamics, generates a smooth grid which contours the boundaries.

3.3 Magnetic Field Solution

The magnetic field is generated by specifying the thruster geometry, assuming infinite permeability of the iron poles, and solving Laplace's equation on the regions exterior to the poles. The coils are assumed to be perfect solenoids, so the problem reduces to that of potential flow, with each pole piece set to a given magnetic potential.

The solution of Laplace's equation is performed using the method of red-black ordering, which works as follows. A uniform grid is divided into alternating "red" and "black" nodes, as shown in Figure 3-2. During each iteration, the following two steps are performed:

- Red nodes are updated using a central four-point stencil of black nodes.
- Black nodes are updated using a central four-point stencil of red nodes.

Boundary nodes in the iron core have a fixed potential and are not updated during iteration.

This method is simple to implement and accepts any geometry that can be represented on a uniform grid. Convergence is slow, but the computation is considered preprocessing, and is only performed when the thruster geometry changes. A different, finer, "pre-processing" grid is also used. Results are then interpolated to the simulation grid (Figure 3-1) using bicubic splines. With a 400×400 pre-processing rectangular grid, three hours on a DEC 5000 is adequate for reasonable accuracy.

Once σ is known, Equation 2.5 can be used to find the magnetic field,

$$B_z = \frac{\partial \sigma}{\partial z}, \tag{3.1}$$

$$B_r = \frac{\partial \sigma}{\partial r}. \tag{3.2}$$

Likewise, the magnetic stream function, λ may be found from Equation 2.9,

$$\frac{\partial \lambda}{\partial z} = r B_r, \tag{3.3}$$

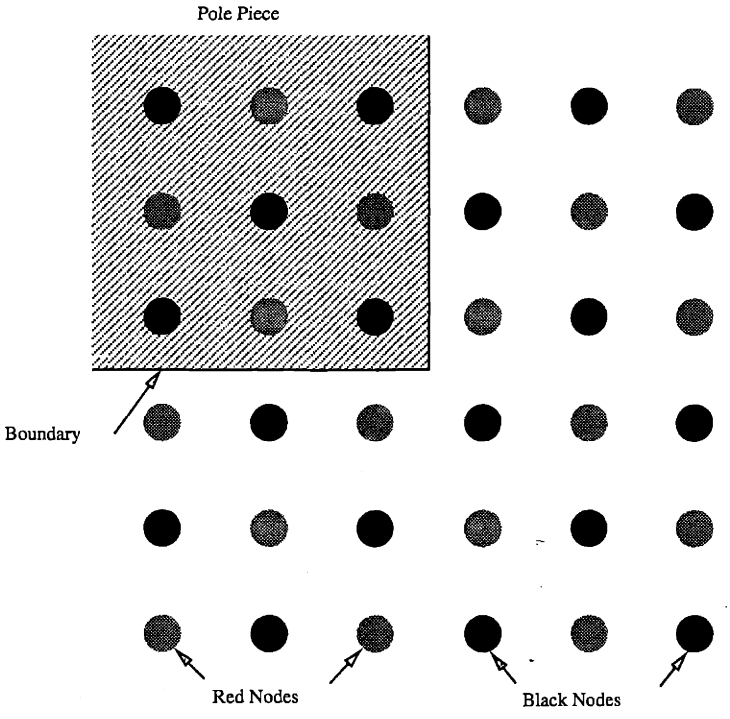

Figure 3-2: Graphical representation of the method of red-black ordering.

$$\frac{\partial \lambda}{\partial r} = -rB_z. \tag{3.4}$$

Equations 3.1 through 3.4 are discretized directly using central differences. Then, σ and λ are determined in one pass. Additionally, the magnetic field strength is found by,

$$B = \sqrt{B_z^2 + B_r^2}. \tag{3.5}$$

Once all of the relevant magnetic field parameters are determined for the geometry in question, the values are transferred to the nonuniform spatial grid (Figure 3-1) using bilinear interpolation. Finally, all magnetic field parameters are normalized by a constant to give a specified magnetic field strength at a control point in the acceleration zone.

3.4 Integration of the Electron Equations

The motion of heavy-particles is slow compared to the electrons. For computational efficiency, the electrons and heavy particles are moved on different timesteps. Figure 3-3 shows the scheme. First, the heavy particles are advanced through Δt. Then the electrons are advanced through the same time period, but using a shorter timestep on the order of $\frac{\Delta t}{100}$. During the electron integration from t_0 to $t_0 + \Delta t$, the local density of heavy particles is slowly varying compared to electron parameters. Therefore, the particle densities and fluxes are held constant at the midpoint $(t_0 + \frac{\Delta t}{2})$ value.

Since T_e does not vary along magnetic field lines ($T_e = T_e(\lambda)$), it will be possible to reduce the electron energy equation (Equation 2.57) to a quasi-one-dimensional form:

$$\bar{A}(\lambda)\frac{\partial T_e}{\partial t} + \bar{B}(\lambda)T_e + \bar{C}(\lambda)\frac{\partial T_e}{\partial \lambda} + \cdots = S(\lambda). \tag{3.6}$$

Such a partial differential equation may then be approached using standard methods. A time-accurate solution will then be valid, within the limits of the assumption of slowly-varying heavy particle density.

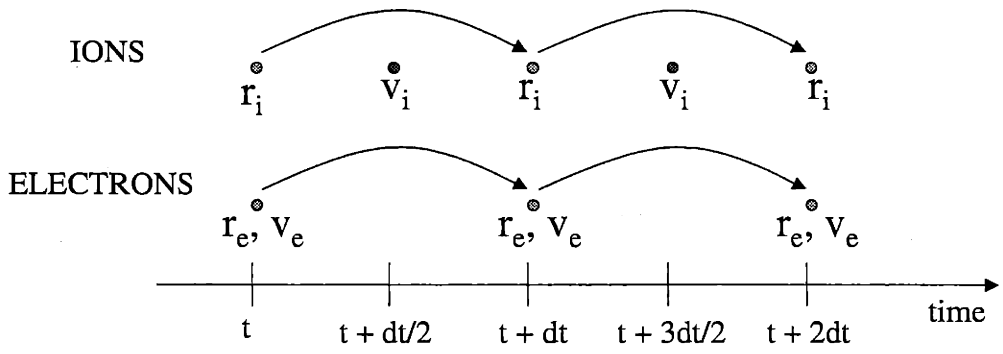

Figure 3-3: Graphical representation of the leap-frog particle integrator scheme.

3.4.1 Quasi-One-Dimensional Electron Energy Equation

The electron energy equation (Equation 2.37) is,

$$\frac{\partial}{\partial t}\left(\frac{3}{2}n_e k T_e\right) + \nabla \cdot (\frac{3}{2}n_e k T_e \vec{u}_e + \vec{q}_e) + \nabla \cdot (n_e k T_e \vec{u}_e) = S_h - S_i. \tag{3.7}$$

Alternately,

$$\frac{3}{2}n_e k \frac{\partial T_e}{\partial t} + \frac{3}{2}k T_e \frac{\partial n_e}{\partial t} + \nabla \cdot (\frac{5}{2}n_e k T_e \vec{u}_e + \vec{q}_e) - S_h + S_i = 0. \tag{3.8}$$

Since this must hold at all points in the plasma region, so must its volume integral. We choose a volume element, D, which is an axisymmetric ring bounded by two lines of force and the insulator wall, as shown in Figure 3-4. Integrating Equation 3.8 over region D:

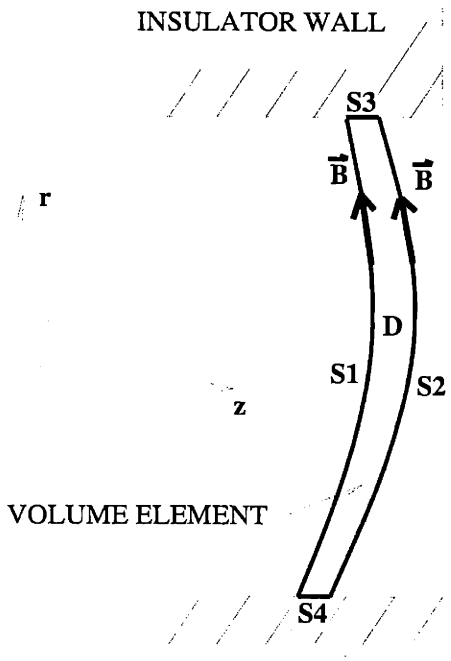

Figure 3-4: Volume element, D, and bounding surfaces, $S1$, $S2$, $S3$, and $S4$.

$$\iiint_D \frac{3}{2}n_e k \frac{\partial T_e}{\partial t} dV + \iiint_D \frac{3}{2}k T_e \frac{\partial n_e}{\partial t} dV + \iiint_D \nabla \cdot (\frac{5}{2}n_e k T_e \vec{u}_e) dV$$

$$+ \iiint_D \nabla \cdot \vec{q}_e dV - \iiint_D S_h dV + \iiint_D S_i dV = 0. \tag{3.9}$$

Consistent with finite volume techniques, we will now assume that the electron temperature is constant over the entire volume element, D. The next task is to extract the powers and differentials of T_e from the terms in Equation 3.9 and arrive at a form like Equation 3.6.

3.4.2 Expansion in Terms of Electron Temperature

The approach here will be first to expand the necessary electron continuity equations from Sections 2.4.2 and 2.4.4. Then, we will successively expand each term of Equation 3.9.

Continuity

Starting with Equation 2.22, we have,

$$u_{e,\hat{n}} = e_1 \frac{\partial \phi^*}{\partial \lambda} + e_2 \frac{\partial T_e}{\partial \lambda}, \tag{3.10}$$

where,

$$e_1 = -\mu_{e,\perp} r B, \tag{3.11}$$

$$e_2 = -\mu_{e,\perp} r B \frac{k}{e} (ln(n_e) - 1). \tag{3.12}$$

Now, looking at Equation 2.32,

$$\frac{\partial \phi^*}{\partial \lambda} = \frac{-I_a + I_w - 2\pi k \frac{\partial T_e}{\partial \lambda} \int_0^l n_e \mu_{e,\perp} B (\ln(n_e) - 1) r^2 ds - 2\pi e \int_0^l n_i u_{i,\hat{n}} r ds}{2\pi e \int_0^l n_e \mu_{e,\perp} B r^2 ds}, \tag{3.13}$$

we see the need to express the dependency of I_w on T_e. Looking at Equation 2.86, we can see that I_w is not a simple function of T_e. Therefore, we will make the assumption that the secondary electron flux, $\Gamma_{sec} = \Gamma_e \delta_{eff}$, is only a function of λ. In other words, I_w is constant over one timestep. This is a good approximation for the general situation where T_e varies slowly. A more accurate approach is saved for the future. Expanding the electric field term in Equation 2.86 using Equation 2.20, we have,

$$I_w = f_1 \frac{\partial \phi^*}{\partial \lambda} + f_2 T_e + f_3 \frac{\partial T_e}{\partial \lambda}, \tag{3.14}$$

where, taking into account the inner (1) and outer (2) walls,

$$f_1 = \left(-\frac{m_e 2\pi r^2 \Gamma_e \delta_{eff}}{B}\right)_1 + \left(-\frac{m_e 2\pi r^2 \Gamma_e \delta_{eff}}{B}\right)_2, \tag{3.15}$$

$$f_2 = \left(\frac{m_e 2\pi r \Gamma_e \delta_{eff} k}{B^2 e n_e}\frac{\partial n_e}{\partial \hat{n}}\right)_1 + \left(\frac{m_e 2\pi r \Gamma_e \delta_{eff} k}{B^2 e n_e}\frac{\partial n_e}{\partial \hat{n}}\right)_2, \tag{3.16}$$

$$f_3 = \left(-\frac{m_e 2\pi r^2 \Gamma_e \delta_{eff} k \ln(n_e)}{eB}\right)_1 + \left(-\frac{m_e 2\pi r^2 \Gamma_e \delta_{eff} k \ln(n_e)}{eB}\right)_2. \tag{3.17}$$

Using this expansion in Equation 3.13, we have,

$$\frac{\partial \phi^*}{\partial \lambda} = h_1 + h_2 \frac{\partial T_e}{\partial \lambda} + h_3 T_e, \tag{3.18}$$

where,

$$h_1 = \frac{-I_a - 2\pi e \int_0^l n_i u_{i,\hat{n}} r ds}{2\pi e \int_0^l n_e \mu_e B r^2 ds - f_1}, \tag{3.19}$$

$$h_2 = \frac{f_3 - 2\pi k \int_0^l n_e \mu_{e,\perp} B (\ln(n_e) - 1) r^2 ds}{2\pi e \int_0^l n_e \mu_{e,\perp} B r^2 ds - f_1}, \tag{3.20}$$

$$h_3 = \frac{f_2}{2\pi e \int_0^l n_e \mu_{e,\perp} B r^2 ds - f_1}. \tag{3.21}$$

Going back to Equation 3.10 and using Equation 3.18,

$$u_{e,\hat{n}} = j_1 + j_2 \frac{\partial T_e}{\partial \lambda} + j_3 T_e, \tag{3.22}$$

where,

$$j_1 = e_1 h_1, \tag{3.23}$$

$$j_2 = e_1 h_2 + e_2, \tag{3.24}$$

$$j_3 = e_1 h_3. \tag{3.25}$$

The perpendicular component of the electric field is given by Equation 2.20,

$$\frac{\partial \phi}{\partial \hat{n}} = \frac{\partial \phi^*}{\partial \hat{n}} + \frac{k T_e}{e n_e}\frac{\partial n_e}{\partial \hat{n}} + \frac{k \ln(n_e)}{e}\frac{\partial T_e}{\partial \hat{n}}, \tag{3.26}$$

which can be written as,

$$\frac{\partial \phi}{\partial \hat{n}} = k_1 + k_2 \frac{\partial T_e}{\partial \lambda} + k_3 T_e, \tag{3.27}$$

where,

$$k_1 = -rBh_1, \tag{3.28}$$

$$k_2 = -rB\left(h_2 + \frac{k \ln n_e}{e}\right), \tag{3.29}$$

$$k_3 = -rBh_3 + \frac{k}{en_e}\frac{\partial n_e}{\partial \hat{n}}. \tag{3.30}$$

Note also here that the tangential component of the electric field is,

$$\frac{\partial \phi}{\partial \hat{t}} = \frac{\partial \phi^*}{\partial \hat{t}} + \frac{kT_e}{en_e}\frac{\partial n_e}{\partial \hat{t}} + \frac{k \ln(n_e)}{e}\frac{\partial T_e}{\partial \hat{t}}, \tag{3.31}$$

which, according to our assumptions, reduces to,

$$\frac{\partial \phi}{\partial \hat{t}} = \frac{kT_e}{en_e}\frac{\partial n_e}{\partial \hat{t}}. \tag{3.32}$$

Energy

Starting with the first term of Equation 3.9,

$$\iiint_D \frac{3}{2} n_e k \frac{\partial T_e}{\partial t} dV = \frac{3}{2} k \frac{\partial T_e}{\partial t} \iiint_D n_e dV = \bar{A}_1(\lambda)\frac{\partial T_e}{\partial t}, \tag{3.33}$$

where,

$$\bar{A}_1(\lambda) = \frac{3}{2} k \iiint_D n_e dV. \tag{3.34}$$

The second term of Equation 3.9 gives,

$$\iiint_D \frac{3}{2} kT_e \frac{\partial n_e}{\partial t} dV = \frac{3}{2} kT_e \iiint_D \frac{\partial n_e}{\partial t} = \bar{A}_2(\lambda) T_e, \tag{3.35}$$

where,

$$\bar{A}_2(\lambda) = \frac{3}{2} k \iiint_D \frac{\partial n_e}{\partial t} dV. \tag{3.36}$$

Here, $\frac{\partial n_e}{\partial t}$ is computed by finite differencing as,

$$\frac{\partial n_e}{\partial t} = \frac{n_{e,t_0+\Delta t} - n_{e,t_0}}{\Delta t}. \tag{3.37}$$

The third term in Equation 3.9 can be rewritten using the divergence theorem,

$$\iiint_D \nabla \cdot (\frac{5}{2} n_e k T_e \vec{u}_e) dV = \iint_R \frac{5}{2} n_e k T_e \vec{u}_e \cdot d\vec{S}, \tag{3.38}$$

where R is the closed surface surrounding volume element D. Referring to Figure 3-4, the surface, R, is composed of two surfaces, $S1$ and $S2$, which contour the magnetic field, and two surfaces, $S3$ and $S4$, which border the wall. Expanding the surface integral into these components,

$$\begin{aligned}\iiint_D \nabla \cdot (\frac{5}{2} n_e k T_e \vec{u}_e) dV = & \iint_{S1} \frac{5}{2} n_e k T_e u_{e,\hat{n}} dS - \iint_{S2} \frac{5}{2} n_e k T_e u_{e,\hat{n}} dS \\ & + \iint_{S3} \frac{5}{2} n_e k T_e u_{e,3} dS + \iint_{S4} \frac{5}{2} n_e k T_e u_{e,4} dS.\end{aligned} \tag{3.39}$$

Here, the last two terms represent the internal energy lost to the wall. We will call this $\dot{E}_w$ and treat it separately later in this section. Using the expansion for $u_{e,\hat{n}}$,

$$\begin{aligned}\iiint_D \nabla \cdot (\frac{5}{2} n_e k T_e \vec{u}_e) dV &= \iint_{S1} \frac{5}{2} n_e k T_e (j_1 + j_2 \frac{\partial T_e}{\partial \lambda} + j_3 T_e) dS \\ &\quad - \iint_{S2} \frac{5}{2} n_e k T_e (j_1 + j_2 \frac{\partial T_e}{\partial \lambda} + j_3 T_e) dS \\ &= \bar{L}_1 T_{e,S1} + \bar{L}_2 T_{e,S2} \\ &\quad + \bar{L}_3 T_{e,S1} \left(\frac{\partial T_e}{\partial \lambda}\right)_{S1} + \bar{L}_4 T_{e,S2} \left(\frac{\partial T_e}{\partial \lambda}\right)_{S2} \\ &\quad + \bar{L}_5 T_{e,S1}^2 + \bar{L}_6 T_{e,S2}^2 + \dot{E}_w,\end{aligned} \tag{3.40}$$

where,

$$\bar{L}_1(\lambda) = \iint_{S1} \frac{5}{2} n_e k j_1 ds, \tag{3.41}$$

$$\bar{L}_2(\lambda) = - \iint_{S2} \frac{5}{2} n_e k j_1 ds, \tag{3.42}$$

$$\bar{L}_3(\lambda) = \iint_{S1} \frac{5}{2} n_e k j_2 ds, \tag{3.43}$$

$$\bar{L}_4(\lambda) = -\iint_{S2} \frac{5}{2} n_e k j_2 ds, \tag{3.44}$$

$$\bar{L}_5(\lambda) = \iint_{S1} \frac{5}{2} n_e k j_3 ds, \tag{3.45}$$

$$\bar{L}_6(\lambda) = -\iint_{S2} \frac{5}{2} n_e k j_3 ds \tag{3.46}$$

By applying a similar approach to the fourth term in Equation 3.9,

$$\iiint_D \nabla \cdot \vec{q}_e dV = \bar{M}_1 T_{e,S1} \left(\frac{\partial T_e}{\partial \lambda} \right)_{S1} + \bar{M}_2 T_{e,S2} \left(\frac{\partial T_e}{\partial \lambda} \right)_{S2}, \tag{3.47}$$

where,

$$\begin{aligned} \bar{M}_1 &= \iint_S K'_{e,\perp} B r dS, \\ \bar{M}_2 &= -\iint_S K'_{e,\perp} B r dS. \end{aligned} \tag{3.48}$$

The electron thermal conductivity, $K'_{e,\perp}$, is computed using Equation 2.41.

The third term in Equation 3.9 is the source due to Ohmic heating. Using the form derived in Section 2.4.7,

$$-\iiint_D S_h dV = \iiint_D \vec{j}_e \cdot \vec{E} dV \tag{3.49}$$

$$= -\iiint_D e n_e u_{e,\hat{n}} \frac{\partial \phi}{\partial \hat{n}} dV. \tag{3.50}$$

Rigorously, the contribution due to tangential gradients in ϕ must also be included. However, due to the assumption of tangential equilibrium, the gradients in ϕ are small for the conditions of interest. Using Equations 3.22 and 3.26,

$$-\iiint_D S_h dV = \bar{N}_1 + \bar{N}_2 T_e + \bar{N}_3 \frac{\partial T_e}{\partial \lambda} + \bar{N}_4 \left(\frac{\partial T_e}{\partial \lambda} \right)^2 + \bar{N}_5 T_e \frac{\partial T_e}{\partial \lambda} + \bar{N}_6 T_e^2, \tag{3.51}$$

where,

$$\bar{N}_1(\lambda) = -e \iiint_D n_e(j_1 k_1) dV, \tag{3.52}$$

$$\bar{N}_2(\lambda) = -e \iiint_D n_e(j_1 j_3 + j_3 k_1) dV, \tag{3.53}$$

$$\bar{N}_3(\lambda) = -e \iiint_D n_e(j_1 k_2 + j_2 k_1) dV, \tag{3.54}$$

$$\bar{N}_4(\lambda) = -e \iiint_D n_e(j_2 k_2) dV, \tag{3.55}$$

$$\bar{N}_5(\lambda) = -e \iiint_D n_e(j_2 k_3 + j_3 k_2) dV, \tag{3.56}$$

$$\bar{N}_6(\lambda) = -e \iiint_D n_e(j_3 k_3) dV. \tag{3.57}$$

The inelastic loss term in Equation Equation 3.9 is,

$$\iiint_D S_i dV = \iiint_D \dot{n}_e \varphi'(T_e) E_i dV = \iiint_D \varsigma(T_e) n_e n_n \varphi'(T_e) E_i dV. \tag{3.58}$$

The functions $\varsigma(T_e)$ and $\varphi'(T_e)$ have been tabulated prior to running the code, so,

$$\iiint_D S_i dV = \bar{P}_1 \varsigma(T_e) \varphi'(T_e), \tag{3.59}$$

where,

$$\bar{P}_1(\lambda) = E_i \iiint_D n_e n_n dV. \tag{3.60}$$

Returning to the problem of computing the internal energy flux to the wall, Equation 2.75 gives an analytical form normalized by random electron current density,

$$\frac{q_w}{\bar{\Gamma}_e} \approx \begin{cases} \exp \frac{e\Phi_w}{kT_e} [2k(T_e - \delta_{eff} T_{sec}) - (1 - \delta_{eff}) e\Phi_w] & T_e < 16.5eV \\ 2k(T_e - T_{sec}) & T_e > 16.5eV \end{cases} . \tag{3.61}$$

Using this in tabulated form, we can write the total energy flux lost to the cell as,

$$\dot{E}_w = q'_w(T_e) \frac{\bar{c}_e}{4} (n_{e,S3} A_{S3} + n_{e,S4} A_{S4}), \tag{3.62}$$

where $q'_w = q_w/j_e$, $n_{e,S3}$ and $n_{e,S4}$ are the plasma densities at the inner and outer walls, and A_{S3} and A_{S4} are the areas of the cell in contact with the inner and outer walls, as shown in Figure 3-4.

Collecting Terms

By substituting the volume integrals derived above into Equation 3.9 and grouping like terms, a consolidated electron energy equation may be written as,

$$\begin{aligned}
&\frac{\partial T_e}{\partial t} + C_I \frac{\partial T_e}{\partial \lambda} + C_J T_e + C_K T_{e,S1} + C_L T_{e,S2} \\
&+C_M T_{e,S1} \left(\frac{\partial T_e}{\partial \lambda}\right)_{S1} + C_N T_{e,S2} \left(\frac{\partial T_e}{\partial \lambda}\right)_{S2} + C_O T_{e,S1}^2 \\
&+C_P T_{e,S2}^2 + C_Q + C_R \left(\frac{\partial T_e}{\partial \lambda}\right)^2 + C_S T_e \frac{\partial T_e}{\partial \lambda} \\
&+C_T T_e^2 + Q_{wall}(T_e) + Q_{inelastic}(T_e) = 0,
\end{aligned} \tag{3.63}$$

where,

$$C_I = (\bar{N}_3)/\bar{A}_1, \tag{3.64}$$

$$C_J = (\bar{A}_2 + \bar{N}_2)/\bar{A}_1, \tag{3.65}$$

$$C_K = (\bar{L}_1)/\bar{A}_1, \tag{3.66}$$

$$C_L = (\bar{L}_2)/\bar{A}_1, \tag{3.67}$$

$$C_M = (\bar{L}_3 + \bar{M}_1)/\bar{A}_1, \tag{3.68}$$

$$C_N = (\bar{L}_4 + \bar{M}_2)/\bar{A}_1, \tag{3.69}$$

$$C_O = (\bar{L}_5)/\bar{A}_1, \tag{3.70}$$

$$C_P = (\bar{L}_6)/\bar{A}_1, \tag{3.71}$$

$$C_Q = (\bar{N}_1)/\bar{A}_1, \tag{3.72}$$

$$C_R = (\bar{N}_4)/\bar{A}_1, \tag{3.73}$$

$$C_S = (\bar{N}_5)/\bar{A}_1, \tag{3.74}$$

$$C_T = (\bar{N}_6)/\bar{A}_1, \tag{3.75}$$

$$Q_{wall}(T_e) = q'_w(T_e)\frac{\bar{c}_e}{4}(n_{e,S3}A_{S3} + n_{e,S4}A_{S4})/\bar{A}_1, \tag{3.76}$$

$$Q_{inelastic}(T_e) = \bar{P}_1 \varsigma(T_e)\varphi'(T_e)/\bar{A}_1. \tag{3.77}$$

Equation 3.63 is now in a form which may be integrated by standard methods.

3.4.3 FTCS Method

The solution of Equation 3.63 is accomplished by using a modified Forward Time Centered Space (FTCS) method [4]. The basic explicit FTCS method is obtained by applying forward-time and centered-space differencing to the equation. For instance, the linearized Burgers' Equation,

$$\frac{\partial u}{\partial t} + A\frac{\partial u}{\partial x} = \frac{\partial^2 u}{\partial x^2}, \tag{3.78}$$

gives,

$$\frac{u_j^{n+1} - u_j^n}{\Delta t} + c\frac{u_{j+1}^n - u_{j-1}^n}{2\Delta x} = \mu\frac{u_{j+1}^n - 2u_j^n + u_{j-1}^n}{(\Delta x)^2}. \tag{3.79}$$

Here, j is the spatial index and n is the time index. In our case, Equation 3.63 gives,

$$\begin{aligned} T_{e,j+1}^{n+1} = T_{e,j}^n - \Delta t[&C_{I,j}(T_{e,j+1}^n - T_{e,j-1}^n)/2/\Delta\lambda + C_{J,j}T_{e,j}^n + C_{K,j}(T_{e,j+1}^n + T_{e,j}^n)/2 \\ &+C_{L,j}(T_{e,j}^n + T_{e,j-1}^n)/2 + C_{M,j}(T_{e,j}^n + T_{e,j-1}^n)/2(T_{e,j}^n - T_{e,j-1}^n)/\Delta\lambda \\ &+C_{N,j}(T_{e,j+1}^n + T_{e,j}^n)/2(T_{e,j+1}^n - T_{e,j}^n)/\Delta\lambda + C_{O,j}(T_{e,j+1}^n + T_{e,j}^n)(T_{e,j+1}^n + T_{e,j}^n)/4 \\ &+C_{P,j}(T_{e,j}^n + T_{e,j-1}^n)(T_{e,j}^n + T_{e,j-1}^n)/4 + C_{Q,j} + C_{R,j}(T_{e,j+1}^n - T_{e,j-1}^n)^2/(\Delta\lambda)^2 \\ &+C_{S,j}T_{e,j}^n(T_{e,j+1}^n - T_{e,j-1}^n)/2/\Delta\lambda + C_{T,j}(T_{e,j}^n)^2 \\ &+q_w'(T_{e,j}^n)\frac{\bar{c_e}}{4}(n_{e,S3}A_{S3} + n_{e,S4}A_{S4}) + \bar{P}_1\varsigma(T_{e,j}^n)\varphi'(T_{e,j}^n)] \end{aligned} \tag{3.80}$$

3.4.4 Timestep

For the linearized Burgers' equation,

$$\frac{\partial u}{\partial t} + c\frac{\partial u}{\partial x} = \mu\frac{\partial^2 u}{\partial x^2}, \tag{3.81}$$

the FCTS method requires [4],

$$\frac{c^2\Delta t}{(\Delta x)^2} \leq \mu. \tag{3.82}$$

This does not apply directly to Equation 3.63 due to the additional terms. Therefore, the Burgers' criterion was used as a starting point for an iterative search for a stable timestep. Successive runs for identical conditions were executed with different timesteps. The timestep selected corresponded to the case where the solution was stable and unchanging for smaller

timesteps. This was found to be 5×10^{-11} seconds for most operating conditions.

3.4.5 Space Potential

Once the electron temperature is determined by integrating Equation 3.63, ϕ^* may be found by integrating Equation 3.18 using the Trapezoidal rule. Then, using Equation 2.13, ϕ may be found on the entire domain by,

$$\phi = \phi^*(\lambda) + \frac{kT_e}{e} \ln(n_e). \tag{3.83}$$

3.5 Particle-In-Cell Method for Heavy Species

The standard particle-in-cell method [8] is a direct simulation technique which models a gas as discrete particles. Collisions are usually accounted for by a Monte Carlo technique, which computes a probability of collision for each particle for each timestep. Typically, both ions and electrons are modeled with PIC, and Poisson's equation is solved to find the space potential.

In this simulation, heavy species are modeled time-accurately using a modified Particle-In-Cell (PIC) method. Although based on the standard PIC method, this method has several unique features which enhance performance for the specific problem of simulating a Hall thruster plasma with a nonuniform grid.

3.5.1 Standard PIC Method

To use the standard PIC method in two dimensions, the domain is divided into uniform cells, as shown in Figure 3-5. Then, some initial guess of particle locations and velocities is taken. After initialization, an iterative method begins. In each timestep,

- The particle equations of motion are integrated
- The field vectors are computed

A flow diagram is shown in Figure 3-6.

The particle densities and current densities are found at the nodes by weighting – usually first order area weighting. The electromagnetic fields are then computed at the nodes using these values.

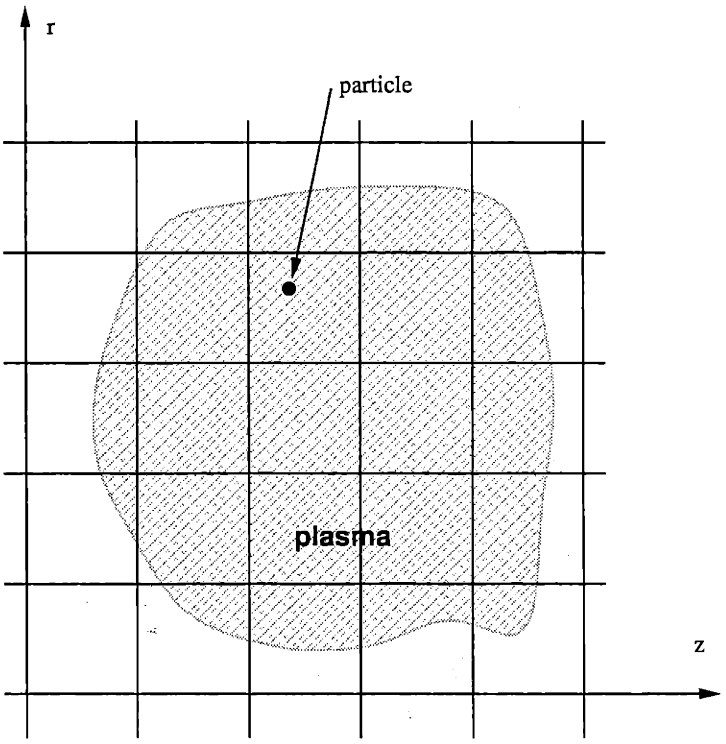

Figure 3-5: Uniform PIC grid for density, current, and field computations [8].

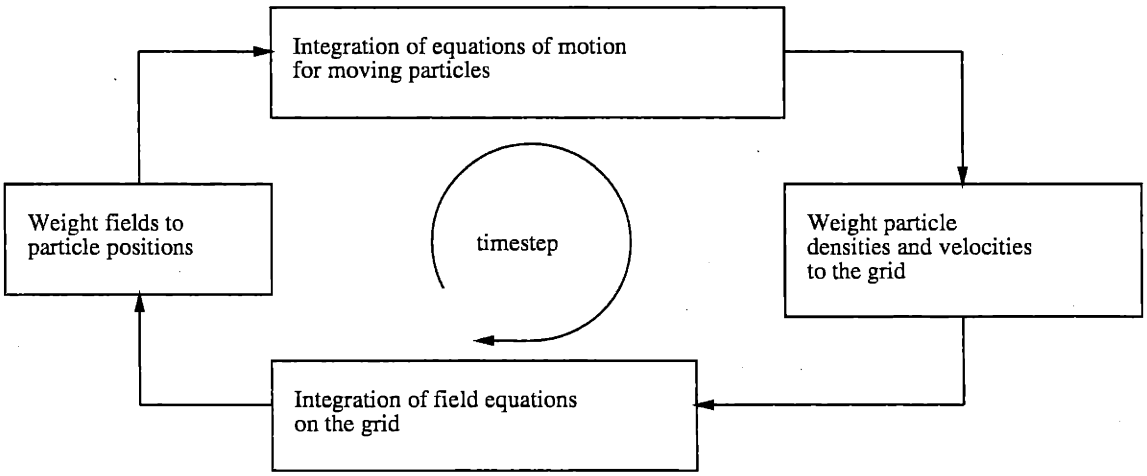

Figure 3-6: PIC computational cycle [8].

The particle equations of motion are integrated independently, resulting in new positions and velocities. To apply the field vectors at the nodes to particles inside the cell, an inverse-weighting scheme is used. Typically, a leap-frog integration scheme is used for the particle motion equations, so the position and velocity are offset by one half timestep.

3.5.2 Quasineutral Approximation – Hybrid PIC

With conventional PIC methods, both electrons and heavy species are modeled with discrete particles. However, since the Hall thruster plasma is assumed to be quasineutral, Poisson's equation is not used to find the space potential (except in its limiting form to impose $n_e = n_i$, where n_i comes from the ion tracking). Instead, ions and neutrals are modeled with PIC, and the electrons are modeled as a fluid continuum. The space potential is a result of imposing Ohm's Law across magnetic field lines, and of an isothermal momentum balance along them, as described in Section 2.4. For this reason, the method is called "hybrid-PIC."

3.5.3 Weighting Function: Connection Between Grid and Particle Quantities

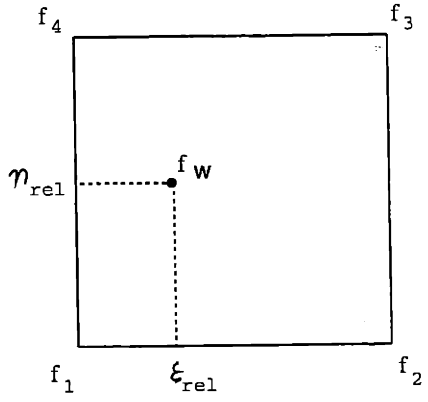

Figure 3-7: First order particle weighting scheme.

A first order weighting function, f, is used to relate values at the grid notes to the particles positioned somewhere within a cell [8]. Such a function is used to compute $\vec{E}$ at a particualr particle's location, for example. It is written in terms of the four grid nodes at

the corners of the cell containing the particle:

$$f_w(\xi_{rel}, \eta_{rel}) = f_1(1-\xi_{rel})(1-\eta_{rel}) + f_2\xi_{rel}(1-\eta_{rel}) + f_3\xi_{rel}\eta_{rel} + f_4(1-\xi_{rel})\eta_{rel}, \quad (3.84)$$

where ξ_{rel} and η_{rel} are distances, in computational space, from the particle to the lower left node (see Figure 3-7). An inverse relationship is also used to relate a particle's value, f_w, to the grid nodes around the cell containing the particle:

$$f_1 = f_w(1-\xi_{rel})(1-\eta_{rel}), \quad (3.85)$$

$$f_2 = f_w\xi_{rel}(1-\eta_{rel}), \quad (3.86)$$

$$f_3 = f_w\xi_{rel}\eta_{rel}, \quad (3.87)$$

$$f_4 = f_w(1-\xi_{rel})\eta_{rel}. \quad (3.88)$$

This inverse weighting is used to compute n_i at the grid nodes, for example. Other weighting functions may also be used, but this formulation is a good compromise between speed and accuracy for this application.

3.5.4 Particle Follower for Nonuniform Grids

Typically, PIC methods employ a uniform grid with dimensions normalized to one unit distance per cell. This simplifies the weighting scheme and the integration of the equations of motion. For nonuniform grids, such as the one used in this simulation, several modifications to the standard PIC method must be made. The mapping between physical space and computational space becomes nontrivial. The transformation from the physical domain (z, r) to the computational domain, (ξ, η) must be tabulated for each node as,

$$\begin{Bmatrix} d\xi \\ d\eta \end{Bmatrix} = \begin{bmatrix} \xi_z & \xi_r \\ \eta_z & \eta_r \end{bmatrix}_{j,k} \begin{Bmatrix} dz \\ dr \end{Bmatrix}, \quad (3.89)$$

where the indices, j and k, refer to nodes in the ξ and η direction, respectively.

The forces on the particles are known in terms of physical (z, r) coordinates, and the equations of motion contain second derivatives of position in z, r coordinates. One approach to the problem would be to recast the equations of motion and the forces in terms of $\xi - \eta$ coordinates. This poses many problems, including loss of accuracy due to the transforma-

tion. Instead, a novel algorithm was devised to perform integrations in terms of spatial $(z-r)$ coordinates, while maintaining computational coordinates for each particle.

For each particle in the simulation, a record is kept with the following information:

- $z-r$ coordinates
- $\xi-\eta$ coordinates
- $z-r$ velocity (and angular momentum for neutrals)
- mass
- charge

At each iteration, the particles are moved in $z-r$ space to preserve accuracy. Then, an estimate is made of the new coordinates in $\xi-\eta$ space. This estimate is checked against a predicted value based on their known $z-r$ coordinates. If the error is greater than some bound, the $\xi-\eta$ coordinates are refined with an error-minimizing algorithm.

STEP 1: MOVE PARTICLES

A particle is moved in $z-r$ space distances Δz and Δr using the leap-frog method described in Section 3.4. The fields used in the leap-frog scheme are computed at the particle's position using the weighting function, Equation3.84.

STEP 2: ESTIMATE ξ and η

An estimate is then made of its new $\xi-\eta$ coordinate using Equation 3.89:

$$\xi_{est} = \xi_z \Delta z + \xi_r \Delta r, \tag{3.90}$$

$$\eta_{est} = \eta_z \Delta z + \eta_r \Delta r. \tag{3.91}$$

STEP 3: CHECK ERROR

The error between z and r, and the estimated weighting function values for z and r may be written (in vector form) as,

$$\{F\} = \left\{ \begin{array}{c} F_1 \\ F_2 \end{array} \right\} = \left\{ \begin{array}{c} z(\xi_{rel}, \eta_{rel}) - z_w(\xi_{est}, \eta_{est}) \\ r(\xi_{rel}, \eta_{rel}) - r_w(\xi_{est}, \eta_{est}) \end{array} \right\}, \tag{3.92}$$

where $z_w(\xi_{est}, \eta_{est})$ and $r_w(\xi_{est}, \eta_{est})$ are the weighting functions for z and r evaluated at ξ_{est} and η_{est}. If this error is greater than some bound, STEP 4 must be performed. Otherwise, the particle's movement is finished. In runs presented in this research, the bound on error is set to one-tenth of the smallest cell width.

STEP 4: UPDATE ξ AND η IF NECESSARY

The algorithm uses Newton's method to refine ξ and η based on the particle's known $z - r$ coordinates. Newton's method for nonlinear systems is given by the vector form of the first two terms of the Taylor series expansion. For our problem,

$$[J] \left\{ \begin{array}{c} \Delta\xi_{rel} \\ \Delta\eta_{rel} \end{array} \right\} = -\{F\}, \tag{3.93}$$

where $[J]$ is the Jacobian matrix,

$$[J] = \left[\begin{array}{cc} \frac{\partial F_1}{\partial \xi_{rel}} & \frac{\partial F_1}{\partial \eta_{rel}} \\ \frac{\partial F_2}{\partial \xi_{rel}} & \frac{\partial F_2}{\partial \eta_{rel}} \end{array} \right]. \tag{3.94}$$

An analytical expression for the derivatives can be found in this case by fixing z_{rel} and r_{rel}, and differentiating Equation 3.84. Then, a single Newton iteraton is performed to find $\Delta\xi$ and $\Delta\eta$ by inverting Equation 3.93.

Despite this work to maintain accurate values of ξ and η, it is z and r that are used as the starting conditions for the next integration of the equations of motion. ξ and η are used only for relating to values to and from the grid.

3.5.5 Variable Particle Mass

PIC methods do not simulate the motion of every atom or molecule. They lump a large number of them into "superparticles" in order to reduce the number of computations. These superparticles, which we simply call "particles," generally all have the same mass.

In the Hall thruster simulation, however, this restriction has been eliminated, to give an extra degree of freedom which is used in setting the rate of generation of particles per cell. The masses of the ion particles created are not necessarily identical, although their charge-to-mass ratio is. This gives control of the statistics be allowing generation of "just enough"

particles for statistical significance, without overburdoning the CPU. Computer power is thereby distributed evenly to all cells, and it is found that simulation of dynamic ionizing plasmas is greatly improved by this method. Otherwise, cells with low density would have correspondingly low particle numbers and bad statistics. This is particularly important when a region of low ion density experiences the beginnings of ionization instability.

In addition, this method allows neutral particles to have a mass different than ions. This is extremely important in the Hall thruster simulation, since the neutral density is orders of magnitude higher than the ion density in most regions. All of the computational power would be spent moving a multitude of slow neutrals. With variable mass, however, the ratio of ion to neutral particle masses may be adjusted to achieve a reasonable total number of particles without bogging down the CPU.

The simulation is run with approximately 60,000 ion particles and 60,000 neutral particles. This gives roughly 60 ion and neutral particles per grid cell for a 47×22 compuational grid.

3.5.6 2-D 2-V and 2-D 3-V

Neutrals, which have azimuthal velocity comparable to their axial and radial velocities, require integration of the full cylindrical equation set, Equation 2.88. However, ions have azimuthal velocities much less than their axial and radial velocities. The equations of motion can then be approximated as,

$$\frac{d}{dt}\begin{bmatrix} r \\ z \\ \dot{r} \\ \dot{z} \end{bmatrix} = \begin{bmatrix} \dot{r} \\ \dot{z} \\ \frac{F_r}{m} \\ \frac{F_z}{m} \end{bmatrix}, \tag{3.95}$$

and reflections made at the centerline. This introduces little error, as can be seen in Figure 3-8 for a typical initial condition.

3.5.7 Ionization

Once per PIC timestep, the ionization rate is computed and new ions are created. The ionization rate is given by Equation 2.100 using a tabulated function for $\varsigma(T_e)$.

The number of ion particles created per cell per timestep is fixed at between .30 and .85 per timestep, depending on the operating conditions. The particle's position in the cell is

determined randomly. The particle mass is determined by weighting the ionization rates at the four corners of the cell to the particle using Equation 3.84. The initial velocity of the particle is computed by sampling all three components from Maxwellian distributions at $1000°K$ using the acceptance-rejection method [7], and adding the mean velocity of neutrals.

For mass conservation, some neutral mass must be removed. A fraction of each neutral's mass is deducted, based on the local weighted ionization rate:

$$\Delta M_n = -\frac{M_{n,0}\ \Delta t\ \dot{n}_{e,weighted}}{n_n}, \tag{3.96}$$

where $M_{n,0}$ is the original mass of the neutral particle.

A similar approach is taken for production of doubly-charged ions. For $Xe \rightarrow Xe^{++}$, Xe^{++} ions are created at each cell, and mass is deducted from neutrals proportional to $\dot{n}_i{}^{0\rightarrow II}$. For $Xe^{+} \rightarrow Xe^{++}$, new Xe^{++} ions are created at each cell, and mass is deducted from each singly-charged ion proportional to $\dot{n}_i{}^{I\rightarrow II}$.

3.5.8 Background Pressure

In order to compare numerical results with measured data, it is necessary to also model the facility background pressure, which, in some cases may be on the order of the mean neutral density inside the acceleration channel. This is done similarly to wall recombination by setting a fractional number of ionizations per boundary node per timestep. The mass of each neutral created is then set to give a total cross-plane flux of, $\frac{n_{n,b}\bar{c}}{4}$, where $n_{n,b}$ is the background number density. The initial velocity is taken as the mean thermal speed at $300°K$ with random direction.

3.6 Boundary Conditions and Wall Interactions

The electron boundary conditions are handled by directly fixing T_e at the cathode, and by imposing a zero-slope condition ($\frac{\partial T_e}{\partial \lambda} = 0$) at the anode. Fixing T_e at the cathode represents the direct one-way injection of electrons from the cathode at a given energy. The Neumann condition there is chosen as the limiting case of infinite diffusion at the anode, which agrees with measurements for most operating conditions.

At each PIC iteration, checks are made for ions and neutrals which have fallen outside the boundaries. Ions are eliminated, neutrals are reflected back into the domain, and neutrals

are created at the walls to account for recombination.

Neutral particles which impact the wall experience diffuse scattering. That is, the angle of incidence of the particle leaving is selected from a uniform random distribution. Its velocity is taken to be the mean thermal speed of the neutral after accommodation with the wall. The accommodation coefficient and wall temperature are fixed at .8 and 900 $degK$, respectively. The wall temperature is based on experimental data [60].

A neutral particle is not created in place of each ion that recombines at the wall. Instead, neutral particles are created at the walls based on a recombination probability at that point. This allows the recombined neutrals to have a much higher mass than the recombined ions. Again, this prevents the accumulation of neutrals, and allows the user to adjust the number of neutrals created at the wall. The recombination probability is proportional to the ion flux, such that the total neutral flux is equal to the ion flux, when averaged over time.

Like the scattered neutrals, the recombined neutrals are generated with random (diffuse) trajectories. Their velocity is also the mean thermal speed after wall accommodation.

The boundary conditions at the injector also include the introduction of particles from the propellant feed. These particles are placed randomly within the injector region, and take random trajectories corresponding to a half-range Maxwellian at a temperature of $1000°K$. The number of particles created at the injector per timestep is set by the user to a value around 6.

3.7 Anode and Cathode

An effective cathode is defined as the line of force which exactly intersects the actual cathode. This is modeled as a discontinuity, upstream of which, the standard electron equations hold, and downstream of which, a simpler relationship is imposed. Upstream, a Dirichlet boundary condition on T_e is used at the cathode, based on experimental measurements, with a value around 5 eV. Downstream, a point is chosen to be effective GND. T_e is set to .1 eV, and ϕ^* is computed there. At all points between the effective cathode and the effective GND, T_e and ϕ^* are computed by linear interpolation.

Direct measurements showed the potential of the cathode to be approximately 20 V below GND. Using the convention that all voltages are with respect to GND, the anode voltage will be $V_d - 20\ V$.

The drop in plasma potential at the anode is given by Equation 2.104,

$$\phi_a = -\frac{kT_e}{e} \ln \left[\frac{I_a}{Aen_e \sqrt{\frac{kT_e}{2\pi m_e}}} + e^{-1/2} \sqrt{\frac{2\pi m_e}{m_i}} \right]. \tag{3.97}$$

However, since this drop occurs over a length of the order of λ_D, it is not directly modeled. Instead, the true anode potential is found by deducting ϕ_a from the computed space potential at the anode. Therefore, the maximum plasma potential with respect to GND will be $V_d - 20\ V + \phi_a$.

3.8 Execution Sequence

The execution sequence is shown in Figure 3-9. First, three pre-processes are executed: a nonuniform grid is generated, the magnetic field is computed, and initial guesses are made. The initial guess is usually a solution from previous run. The actual iteration involves two primary tasks: integration of the electron equations and integration of the heavy particle equations. Also at each time step, the heavy particles are created and destroyed based on such conditions as local ionization rate. Lastly, the results are saved, and post-processing may be performed.

3.9 Convergence

Since the method is time-accurate, there is no guarantee that the system will converge to a steady state solution. Two types of instabilities may prevent convergence:

- Plasma instabilities due to ionization, convection, and diffusion of electrons and ions
- Numerical "noise" due to the limitations of the PIC method in simulating a continuum of heavy particles

Nevertheless, a solution is considered complete when the fluctuations reach a regular frequency and amplitude, and have repeated several periods. Or, if there is no discernable pattern to the fluctuations, the parameters are averaged over a long time scale, and iteration is stopped when the averages reach a constant value. The time it takes for convergence is assumed to be, at the very minimum, the time for convection of slow neutrals along the length of the gridded volume.

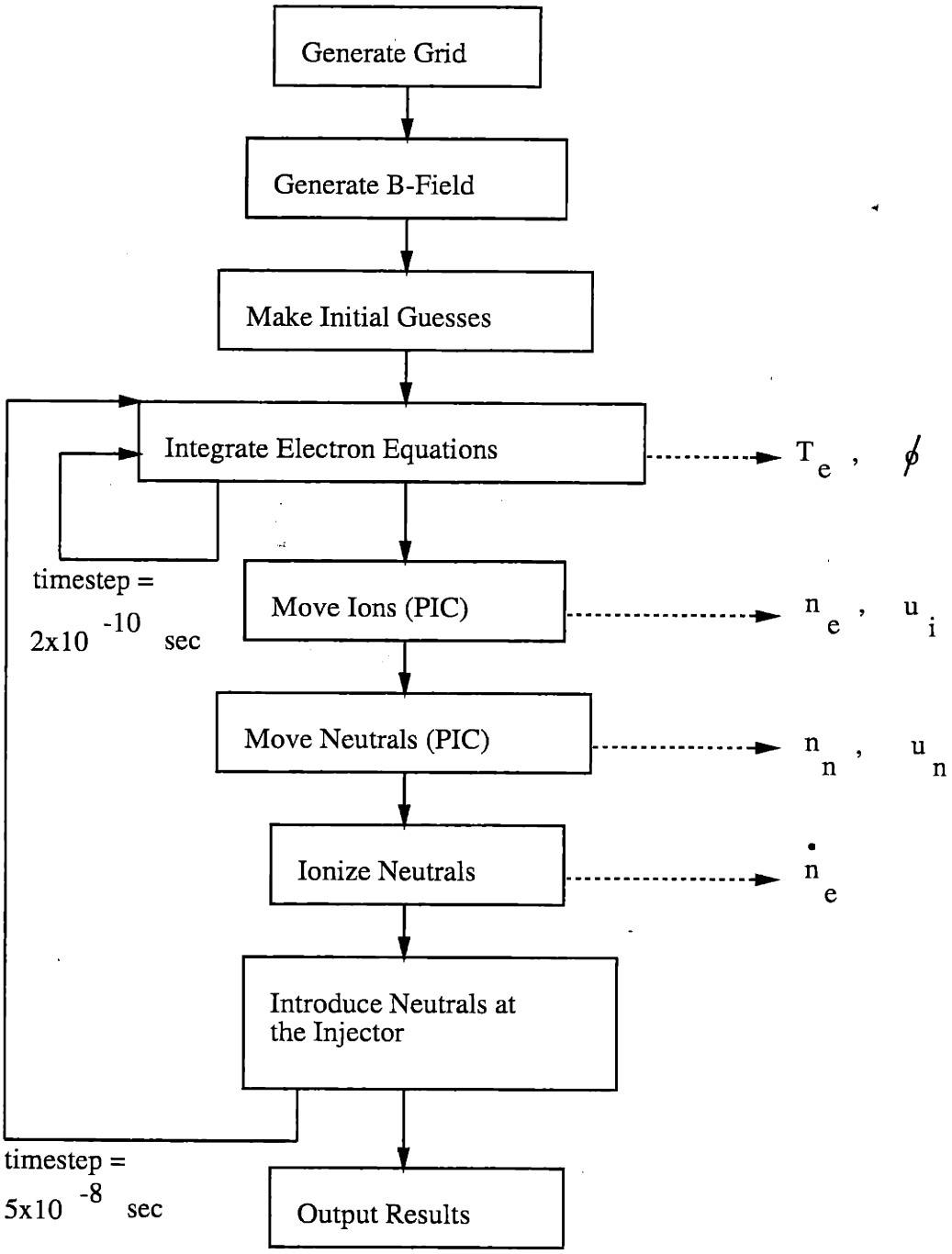

Figure 3-9: Execution sequence of the numerical simulation.

3.10 Computing Cost

The numerical simulation involves four phases: pre-processing, running, averaging, and post-processing. Once the geometry is specified, the magnetic field is computed in the pre-processing phase. Then, operating parameters are set to nominal conditions, and execution begins. One case takes approximately, 8 hours to converge on a DEC AlphaStation 200. or 4 Hours on an SGI Octane. The Octane can run two cases simultaneously in the same time period using twin processors. Select cases are then run again in "average mode", which accumulates parameters at each timestep, and divides by the number of timesteps upon completion. Post-processing involves computation of thrust, torque, wall erosion rates, etc. from the averaged data set.

The bulk of the CPU time is split almost equally between two primary tasks: ionization and movement of the heavy particles, and integration of the electron equations. Approximately 30% of the work of the integration of the electron equations is used in simply weighting the values to points on evenly-spaced lines of force. Indeed, transfer of information between grids, lines of force, and particles accounts for probably 80% of the total computing cost.

3.11 Verification

Extensive efforts were undertaken to verify the results of the numerical model. In addition to plasma parameters, the simulation produces numeric breakdowns which are used to check conservation of mass, charge, momentum and energy in several different ways. Furthermore, one-dimensional data sets are generated which are useful for checking the validity of the solutions, especially those of the electron integrator. Each new segment of code was tested and compared with hand calculations before the next segment was begun. In this way, the techniques of "top-down design" and "step-wise refinement" were used to make sure bugs were kept to a minimum. Finally, the complete simulation has been executed for three different geometries. In each case, some experimental data was available to compare results. Disparities between numerical results and emperical data were carefully examined as possibly due to bugs in the code. The simulation does not necessarily generate a perfectly realistic picture of Hall thruster physics, but, according to all indications, it accurately solves the governing equations presented here.

Chapter 4

Electrostatic Probe Experiments

4.1 Overview

In order for the numerical model to be useful, the boundary conditions must be set to realistic values and the results must be verified by some independent experiment. Several sets of experimental data are available and may be used for this purpose. Bishaev and Kim [9] [10] published the most complete sets of data for plasma inside the acceleration channel of an SPT-100-type Hall thruster at a single operating condition. They limited their studies to time-averaged results, however. Komurasaki et. al. also present data from measurements taken inside laboratory hall thruster models [44]. However, a complete set of AC and DC data for various operation conditions, including specific details on the thruster geometry, is not available. Collection of such data is one goal of this research.

The Air Force Electric Propulsion Laboratory at Edwards Air Force Base, California, supplied facilities, equipment, and a Fakel SPT-70 to be used in electrostatic probe experiments. These experiments involved measurement of thruster operating conditions as well as plasma parameters in the immediate plume region. Both DC and AC signal components were recorded.

4.2 Electrostatic Probes in Supersonic Plasmas

A simple model of an insulated cylindrical probe is shown in Figure 4-1. It consists of a metallic wire insulated except for a short length at the tip. By biasing the electrode to various voltages, V, a current, I, may be collected. The current-voltage characteristics of the

electrode may then be related to the plasma properties near the tip, allowing determination of such parameters as T_e, ϕ, and n_e.

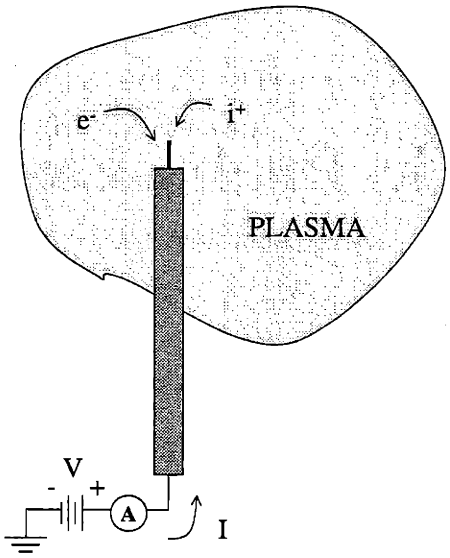

Figure 4-1: Single electrostatic probe – simplified view.

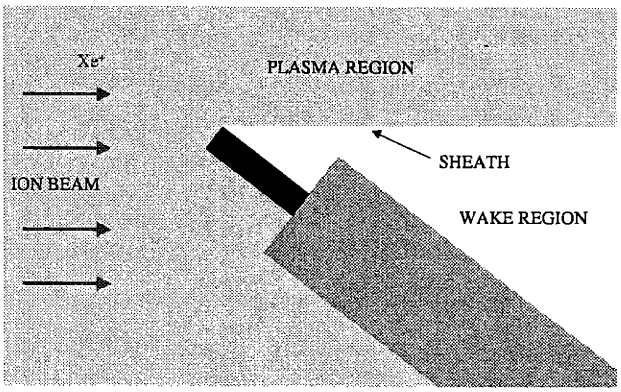

Figure 4-2: Cylindrical electrostatic probe perpendicular to a supersonic plasma beam.

The problem of determining plasma parameters from electrostatic probe measurements has been studied before [38] [21]. For quiescent collisionless plasmas, the current-voltage

characteristics can be numerically computed. This computation has been done by Laframboise [45].

Laframboise assumed the plasma to be quiescent, stationary, and collisionless. The plasma in the plume region of the SPT-70 is collisionless but flowing. The Mach number ($M = v_i/v_{Bohm}$) is believed to be greater than 3. Since this plasma does not meet the criteria of the Laframboise model, a different approach must be taken. Strict treatment would require the solution of the trajectories of ions and electrons self-consistently with Poisson's equation. We will not undertake that problem here. Instead, we will use theory presented by de Boer [23] which he applied to the study of ion engine plumes.

The magnitude of the probe bias will be less than 50 V, much less than the expected ion energy of 300 V. Therefore, in the absence of potential barriers in the sheath, the probe bias is not sufficient to significantly modify the density of ions near the probe. So we may assume, on the beam-impinging side of the probe, the density of ions to be constant from the plasma to the electrode surface. On the downstream side of the probe, a wake region will exist where the ion density is near zero. Figure 4-2 is a representation of such a probe.

At the interface between the wake region and the unperturbed ion beam, there will be a thin sheath region of electrons. The thickness of the sheath will be on the order of λ_D, and will act to prevent electrons from entering the wake. For the conditions of interest, λ_D will be around 60 μm. This is smaller than the probe radius by a factor of 6, so we will assume the wake region to be devoid of electrons.

The ion current to the probe is given by the product of the ion charge flux times the probe area projected on a plane perpendicular to the flow direction, S_i, plus additional ion collection due to expansion of the sheath:

$$I_i = en_e v_i S_i + I_{i,s}. \tag{4.1}$$

by measuring the voltage-current characteristic at ion-saturation (see Figure 5-1 for a typical result), it was found that $I_{i,s}$ was linear with the probe bias with respect to the plasma $(V_p - V)$. The slope of the characteristic was found to obey,

$$\frac{\partial I_{i,s}}{\partial (V_p - V)} = M_s \lambda_D e n_e v_i S_i, \tag{4.2}$$

reasonably well at most points in the plume with M_s approximately 143 $V^{-1}m^{-1}$. This

is smaller than predicted by thin-sheath theory [38] by a factor of 10. It is believed that this difference is due to the effects of the supersonic beam. Therefore, to avoid a detailed analysis of the perturbed ion trajectories in the near-plume region, we will use the first order estimate,

$$I_{i,s} = en_e v_i S_i f_s, \tag{4.3}$$

where,

$$f_s = M_s \lambda_D (V_p - V). \tag{4.4}$$

For electron-repelling probes ($V < V_p$), the electron current is straightforward. In this case, regardless of geometry, and assuming a Maxwellian velocity distribution, the electron current will be,

$$I_e = e\frac{n_e \bar{c}}{4} e^{\frac{e(V-V_p)}{kT_e}} S_e = en_e \sqrt{\frac{kT_e}{2\pi m_e}} e^{\frac{e(V-V_p)}{kT_e}} S_e, \tag{4.5}$$

where S_e is the area for electron collection. Since electrons arrive from all directions (except on the wake side), S_e differs from S_i by a factor of $\pi/2$ for cylindrical probes perpendicular to the flow.

Some cases may exist where the electrons also have a mean velocity component. Drifting electrons in Hall thrusters, for instance, may reach velocities on the order of the mean thermal speed. In these cases, the the impinging distribution will be a shifted Maxwellian. Electron-repelling probes will adjust potential so that the net current of electrons balances with the ions. Therefore, once can expect the floating potential to be lower by mean electron drift energy, $\frac{\sqrt{m_e(E/B)^2/2}}{e}$, which, for Hall thruster plumes, is about 3 V. This can be taken to represent error in the measured plasma potential.

For electron-attracting probes ($V > V_p$), the electron current is not easily determined. If the ion density is truly constant at all points around the probe, then no intervening effective barriers of potential will exist, and none of the electrons at infinity will be excluded from reaching the probe on the basis of energy considerations alone. The resulting current corresponds to the limit of infinitely thick sheath around the probe and is called the orbit motion limit (OML) [21]. For spherical geometry, the current is then linear with potential:

$$I_e = e\frac{n_e \bar{c}}{4} \left(1 + \frac{e(V - V_p)}{kT_e}\right) S_e. \tag{4.6}$$

However, for probes in flowing plasmas which are not aligned with the beam, the presence

of a wake region downstream of the probe may cause a potential barrier. For those cases, a more complicated approach must be taken which is beyond the scope of this work.

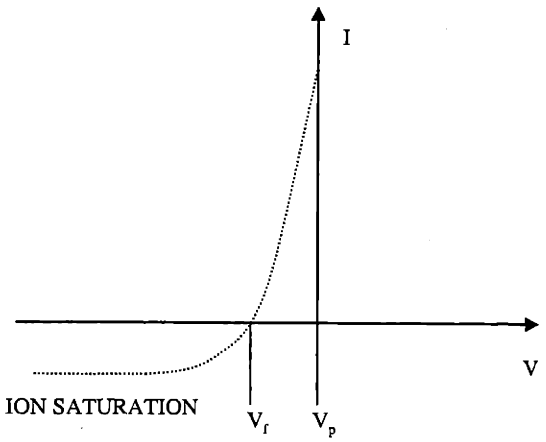

Figure 4-3: Voltage-current characteristic of a single electrostatic probe.

Figure 4-3 shows a typical voltage-current characteristic for a single electrode. Considering only the electron-repelling part ($V < V_p$), the total current collected by the probe is,

$$I = en_e \left(v_i S_i (1 + f_s) - \sqrt{\frac{kT_e}{2\pi m_e}} e^{\frac{e(V-V_p)}{kT_e}} S_e \right). \tag{4.7}$$

At ion saturation ($V - V_f << \frac{-kT_e}{e}$), the exponential term is negligible. Ignoring $I_{i,s}$, knowing the projected area gives the ion beam flux $n_e v_i$. If it is possible to predict v_i based on, perhaps, discharge voltage, V_d, then some estimate of n_e may also be made. In this paper, we will use,

$$v_i = \sqrt{\frac{2eV_d\eta_e}{m_i}}. \tag{4.8}$$

Here, η_e is the beam energy efficiency, taken to be .88 [13]. From the exponential growth portion of the characteristic, T_e and V_p may be determined by numerous methods, including regression.

To uniquely determine n free parameters in the current-voltage model, a minimum of n measurements on the characteristic curve are required. By sweeping V over a broad range while measuring I, many measurements may be taken to reduce the statistical uncertainty of the final estimates. However, to measure the variation in plasma parameters with time

requires a sweep rate much faster than any high-amplitude variations.

4.3 Triple Probes

One method which does not require sweeping probe voltages involves the use of multiple electrodes, each biased to a different value. By simultaneously measuring the current collected by each electrode, multiple points on the characteristic may be found. Experiments have shown that a triple probe is useful for instantaneously measuring T_e, V_p, and n_e in collisionless, Maxwellian, two-temperature plasmas [19]. The theory presented here will be similar, but modified to use our model for current collected by an electrode in a supersonic plasma, Equation 4.7.

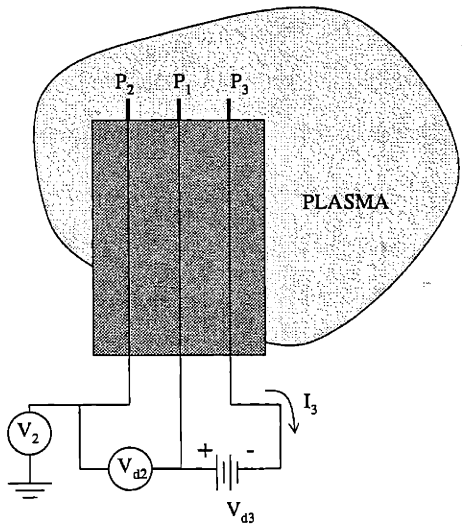

Figure 4-4: Triple electrostatic probe circuit – simplified view.

Figure 4-4 is a simplified diagram of a triple probe circuit. P_2 is allowed to remain at the floating potential, V_f. The other two are biased V_{d3} apart. V_1 will be above V_f, while V_3 will be below V_f.

By fixing V_{d3} and measuring V_2, V_{d2}, and I_3, it is possible to find three separate points on the characteristic, as shown in Figure 4-5. These three points are observations of the current-voltage relationship. Assuming the thickness of the ion sheath is smaller than the

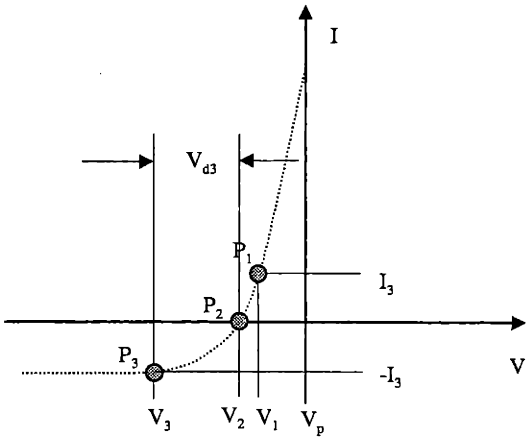

Figure 4-5: Triple probe determination of the characteristic.

separation between the probes, so that electrode interaction effects are negligible, we can use the current-voltage model, Equation 4.7. We now have three nonlinear equations with three unknown plasma parameters, n_e, T_e, and V_p:

$$\begin{aligned} I_1 &= en_e\left(v_i S_{i,1}(1+f_s) - \sqrt{\frac{kT_e}{2\pi m_e}} e^{\frac{e(V_1-V_p)}{kT_e}} S_{e,1}\right) \\ I_2 &= en_e\left(v_i S_{i,2}(1+f_s) - \sqrt{\frac{kT_e}{2\pi m_e}} e^{\frac{e(V_2-V_p)}{kT_e}} S_{e,2}\right) \\ I_3 &= en_e\left(v_i S_{i,3}(1+f_s) - \sqrt{\frac{kT_e}{2\pi m_e}} e^{\frac{e(V_3-V_p)}{kT_e}} S_{e,3}\right). \end{aligned} \tag{4.9}$$

This system may be solved by Newton's method, given an appropriate initial guess.

4.4 Description of the Experiment

The experimental work was carried out in the near plume of a Fakel SPT-70 Hall thruster, operating at the Air Force Electric Propulsion Laboratory in Edwards, California. EP Lab Chamber 6 was used. It is a 255 ft^3 chamber capable of pumping 27,000 l/s of xenon at STP. An ADP 22-inch cryo-pump is mounted at one end. Along the sides are 4 $18-by-32-inch$ $20°K$ panels cooled by ADP HC-8C1 compressors. Around the panels are D-shaped $150°K$ thermal shrouds cooled by a Polycold PFC1100. At nominal operating conditions for the SPT-70, the base pressure is 8×10^{-6} $Torr$, measured by a MKS Type

290C charge rate ion gauge.

The thruster was affixed to a steel mount located on the centerline of the chamber and pointed axially, as shown in Figure 4-6. Below the plume region of the thruster was placed an optics table, to the top of which was fastened a two-axis translation table. Motion was in the horizontal plane and had a throw of 25 cm in both directions. Probes were mounted to the top of the translation table and moved with respect to the thruster using commands issued from a Gateway 2000 computer via a Compumotor stepper motor controller unit.

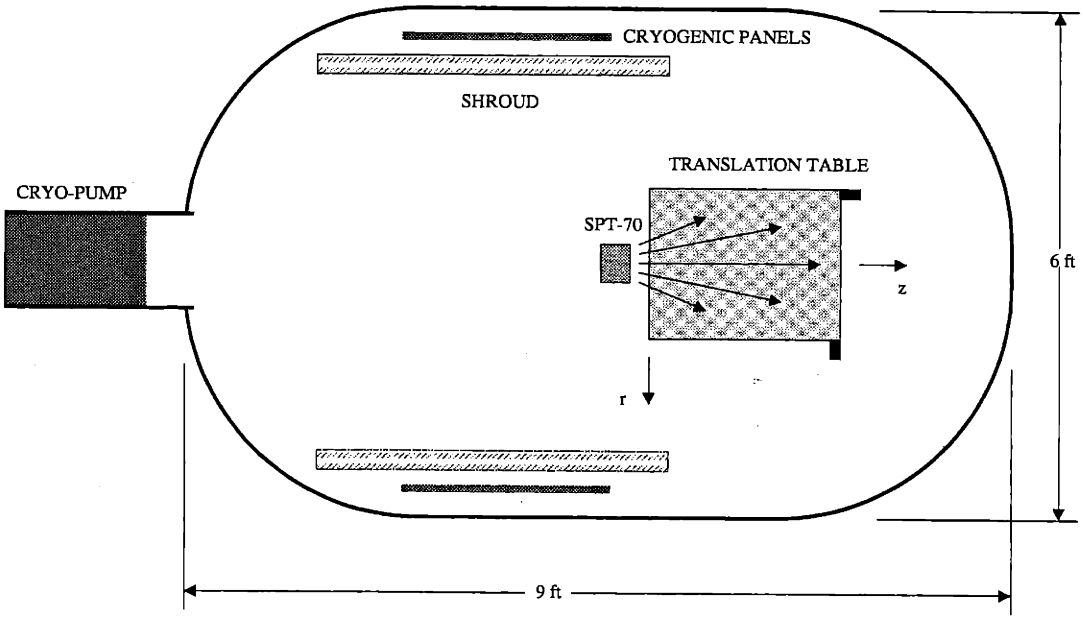

Figure 4-6: Vacuum chamber layout.

The thruster was connected with a power circuit shown in Figure 4-7. The resistor R_0 is set to 10 Ω, limiting the closed-circuit current through the power supply circuit to 30 A. The coupling with capacitor C_0 (100 μF) gives a discharge time constant of 1 ms. R_1 (60 $k\Omega$) is a safety feature for open-circuit discharge of C_0. R_i limits current to the ignitor, and is set to 2 $k\Omega$. The ignitor voltage, V_i, was 30 V. Cathode heater current was 12.5 A,

used only at startup. Discharge voltage was controlled from the primary power supply, V_0, and read directly on a Fluke multimeter. Discharge current was measured with a Tektronix Model A6303 Hall-effect current probe with an AM503 amplifier.

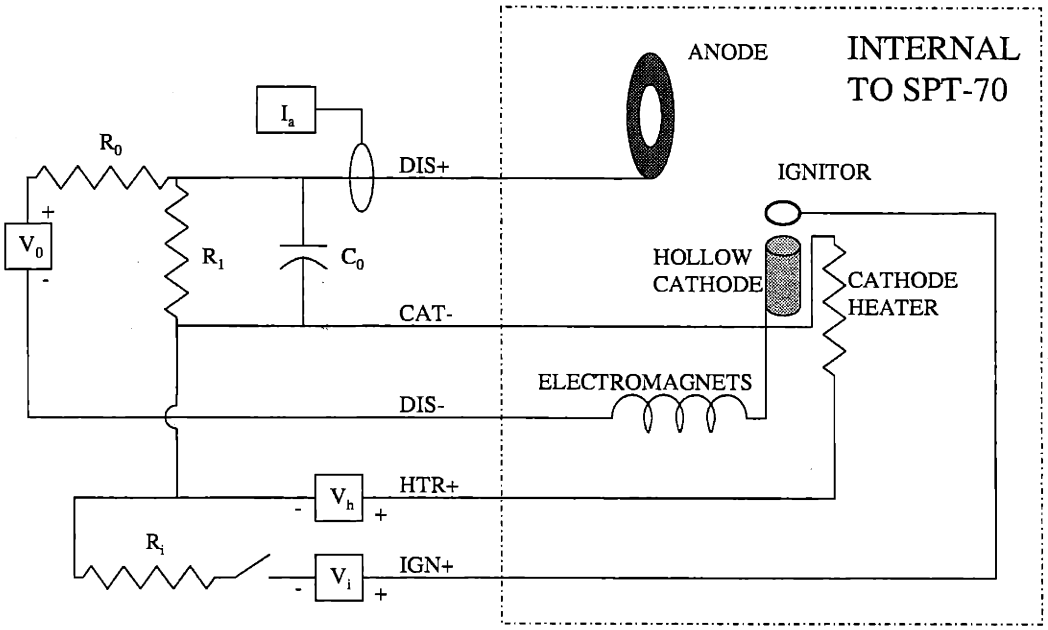

Figure 4-7: Power processing circuit.

The propellant feeds for the thruster discharge and hollow cathodes were controlled by Unit UFC-8160 flow controllers calibrated for xenon to within .3% for the range of operating conditions used in this experiment.

Data was acquired using Tektronix digital oscilloscope models DSA 601 and TDS 684B, each with 1 GHz sample rates. (The maximum sample rate used was $10MHz$). The TDS 684B has four separate digitizers, enabling simultaneous 4-channel sampling. Data from the oscilloscopes were downloaded to the Gateway 2000 computer via a IEEE 488.2 standard interface. Software was written in National Instruments LabVIEW for autonomous probe positioning, and data acquisition from the oscilloscope.

4.4.1 Thruster Selection and Geometry

The Fakel SPT-70 was chosen as a test article because of its intermediate size and ready availability. The width of the acceleration channel is 1.5 cm. Probes can be constructed small enough ($\sim$ 1 mm) to measure gradients in the SPT-70 plume with reasonable accuracy up to the exit of the acceleration channel itself.

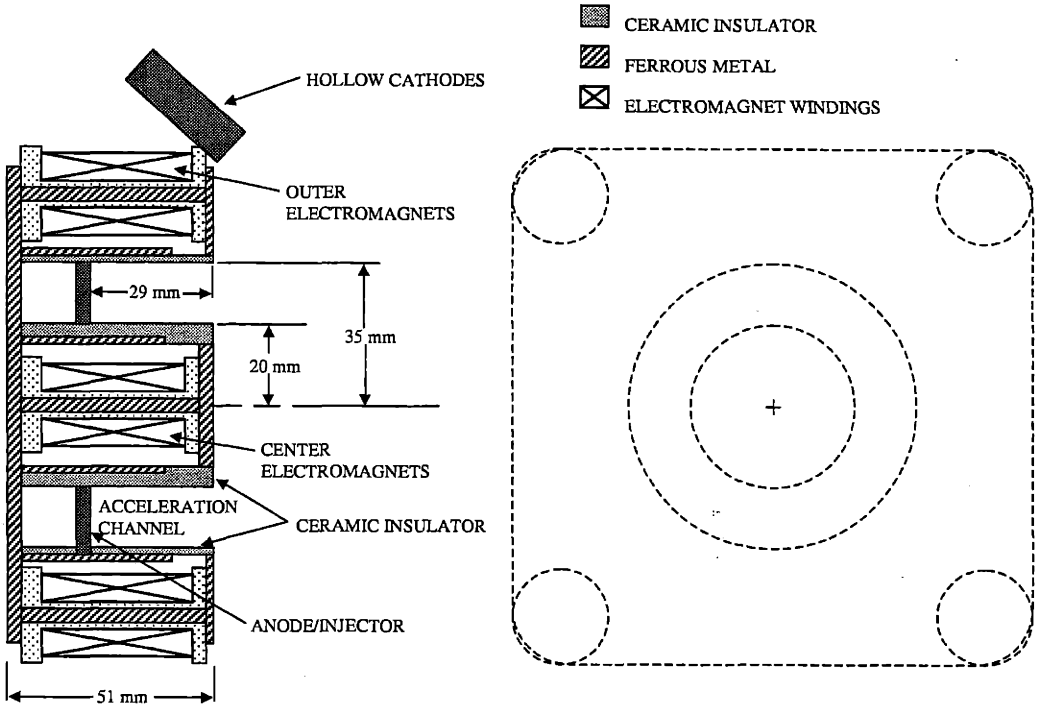

Figure 4-8: Simplified diagram of the SPT-70 geometry.

Referring to Figure 4-8, the SPT-70 has five electromagnet coils. Four are located outside the acceleration channel and one is at the centerline. Two hollow cathodes are attached above the thruster and canted toward the centerline. The metallic outer surfaces of the thruster, including the front pole pieces, are electrically connected. When mounted in the chamber, these surfaces, as well as the chamber walls, are at GND.

4.4.2 Determination of Probe Projected Area

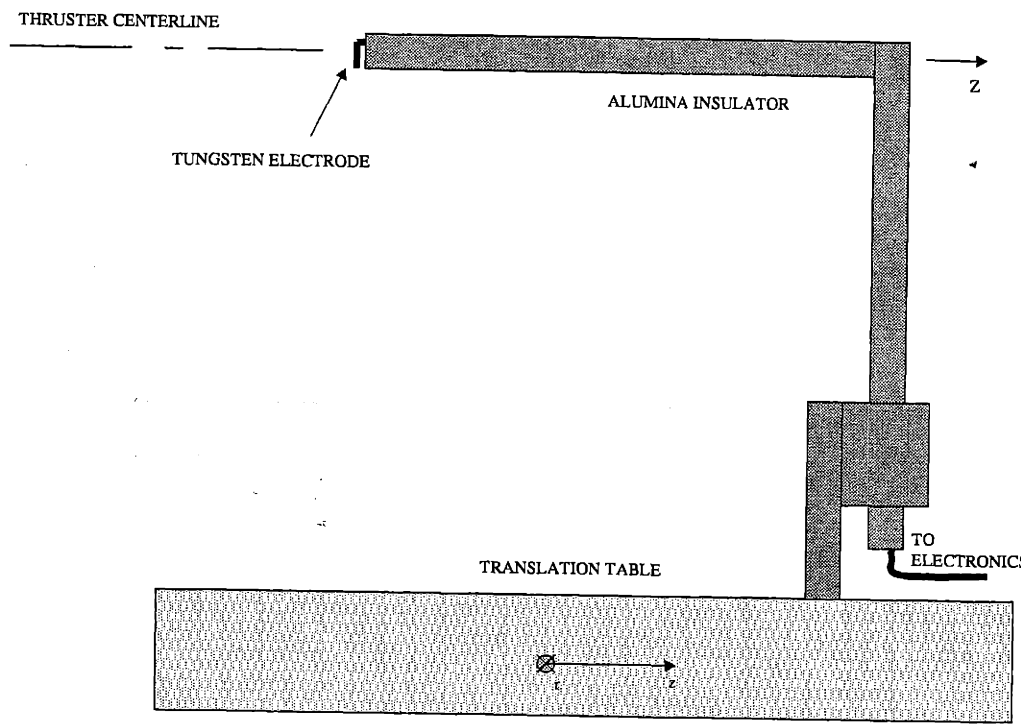

Figure 4-9: Probe orientation.

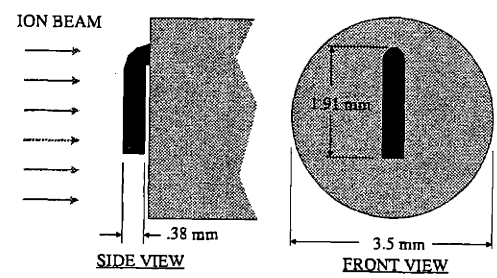

Figure 4-10: Tip dimensions of the ion flux probe.

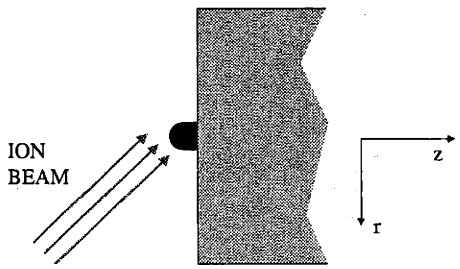

Figure 4-11: Top view of the ion flux probe showing the invariance of collection area with beam incidence angle.

For reasons described in the next section, we would like to use triple probes which are aligned axially. When the axial probe is moved to different points in the plume, its projected area, S_i, with respect to the ion beam, will change. This presents a problem. We must know S_i at all points in the plume, but we do not know the ion beam vector a priori, so we cannot calculate S_i by geometry. Furthermore, for axial probes, the relationship between the ion collection area and beam incidence angle may be complicated by end effects [21]. Fortunately, a method was found which experimentally determines $S_i(z,r)$.

Two separate probe measurements were performed. First, A cylindrical probe was constructed which has invariant projected area with beam incidence angle. Referring to Figures 4-9 through 4-11, its longitudinal axis was normal to the $z-r$ plane. .015 *in* diameter tungsten wire was used, insulated from the plasma by two 6 *in* lengths of 3.5 *mm* diameter alumina tubing joined with ceramic adhesive to form an "L" shape. The angle of incidence of the beam was always 90° from the electrode longitudinal axis, so end effect could be ignored. We denote the known projected area of this probe $S_\perp$. Second, the axial probe was used, with the unknown projected area, S_i. The near plume was scanned with both probes operating at ion saturation. Since, for a given electrode, the ratio of projected area to saturation current is constant,

$$S_i = S_\perp \frac{I_{sat}}{I_{sat,\perp}}. \tag{4.10}$$

Here, $S_\perp$ is the directly-measurable geometric projected area of the ion flux probe, simply the product of its length and diameter. Thus, Equation 4.10 gives a method for determining

$S_i(z,r)$ by measuring $I_{sat}(z,r)$ and $I_{sat,\perp}(z,r)$.

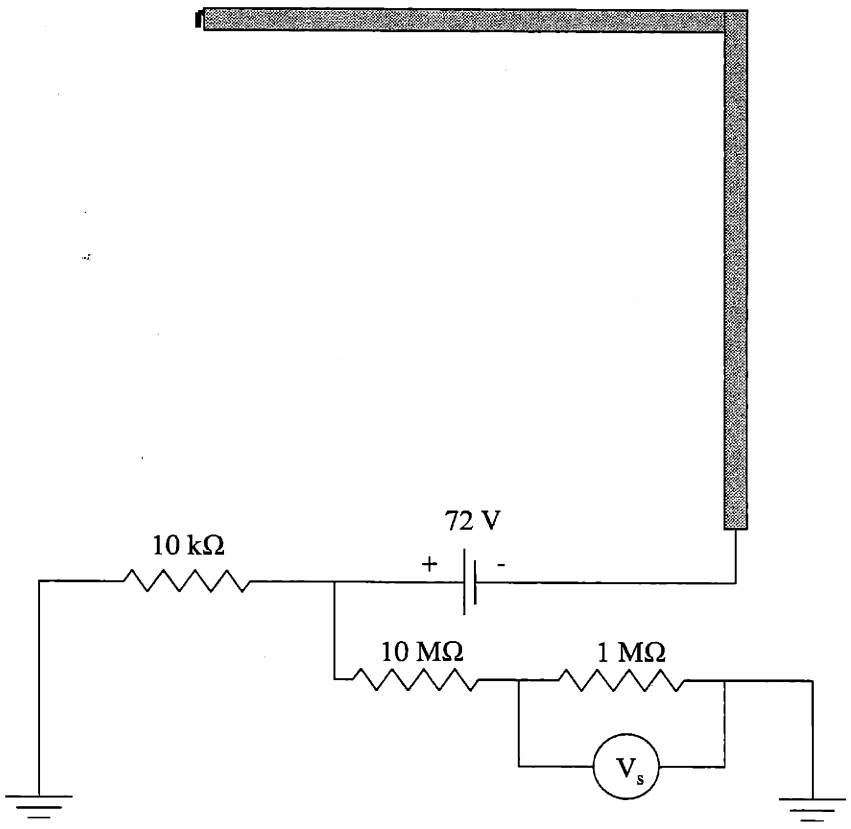

Figure 4-12: Circuit for ion saturation current measurement.

A shunt circuit was assembled to measure the ion saturation current collected by the probe, as shown in Figure 4-12. The applied bias voltage was determined by computing the expected voltage at ion saturation. Referring to Figure 4-3, this is the floating potential minus the exponential decay constant for electron collection. To determine the floating potential, Equation 4.7 is solved for zero current to get $V_f - V_p$. For xenon and $T_e = 10\ eV$ (worst case), $V_f - V_p$ is around $-34\ V$. Since V_p is greater than $20\ V$ with respect to GND,

V_f must be greater than $-14\ V$. Accounting for exponential decay of electron collection at $T_e = 10\ eV$, we must choose a voltage bias less than $-24V$. For additional margin, a probe bias of $-72\ V$ was selected and provided by a single high-voltage battery. The 10 $M\Omega$ resistor helps isolate the measurement equipment, while the bulk of the current flows through the 10 $k\Omega$ resistor to ground. An oscilloscope is used to measure V_s. From this, the voltage and current may be found by:

$$V = 11V_s - 72, \tag{4.11}$$

$$I = \frac{11V_s}{1 \times 10^4}. \tag{4.12}$$

The Gateway 2000 computer was programmed to scan a 2-D $(z-r)$ grid in the plume. At each point, the TDS 684B oscilloscope was triggered to begin sampling V_s and I_a. After completing a 2 s sample, the PC downloaded the data sets via the IEEE standard interface, saved the information on the hard disk, and instructed the translation system to continue to the next point. For grids of dimension 15-by-21, the entire process took approximately 20 minutes.

4.4.3 DC Triple Probe

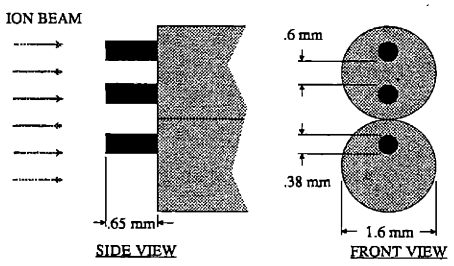

Figure 4-13: Tip dimensions of the triple probe.

Triple probes were constructed using .015 in diameter tungsten wire. Figure 4-13 details the tip. The three electrodes were pointed axially and positioned at equal $z-r$ coordinates, spaced .6 mm apart azimuthally. This orientation was selected based on the assumption of low gradients in the azimuthal direction, so that the plasma conditions at each electrode would be as similar as possible. It was constructed similar to the ion flux probe, but by

using four smaller alumina tubes instead of two. Like the ion flux probe, the triple probe was "L"-shaped and joined with ceramic adhesive. It was mounted as shown in Figure 4-9.

To prevent interaction between the electrodes, the spacing between them, r_s, was chosen as the minimum which still satisfies $r_s > \lambda_D$. For conditions of interest, the worst case is $T_e = 10\ eV$ and $n_e = 2 \times 10^{17}\ m^{-3}$, which gives $\frac{r_s}{\lambda_D} = 11$.

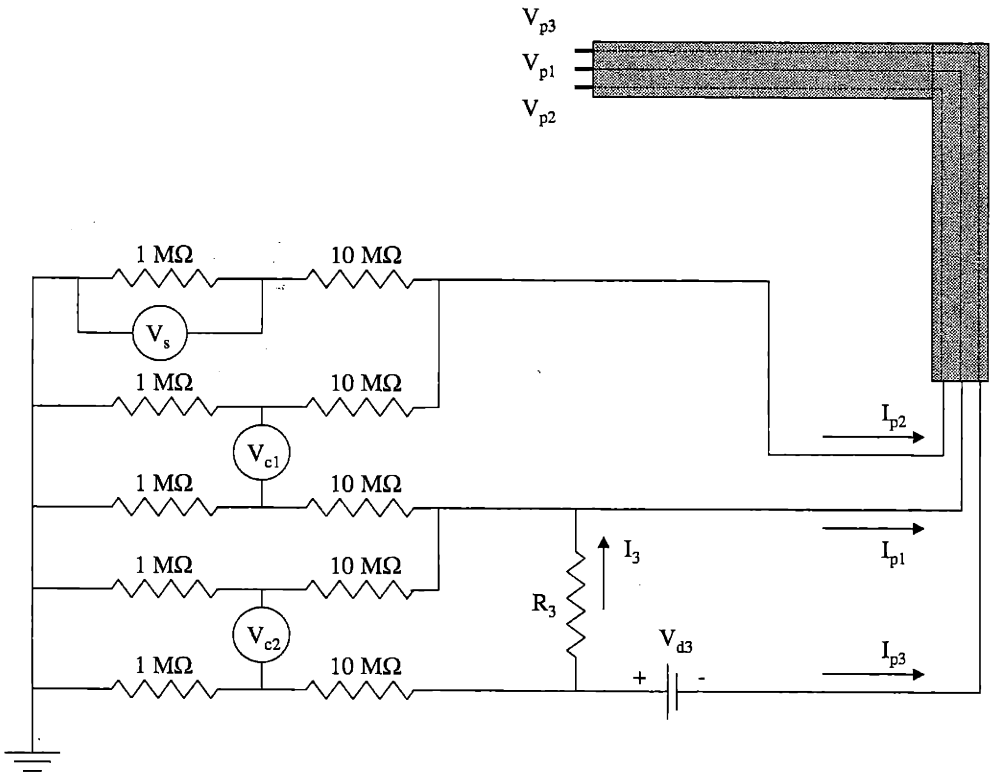

Figure 4-14: DC triple probe circuit.

The triple probe circuit, shown in Figure 4-14, was used during the tests. The 10 $M\Omega$ resistors help isolate the measurement equipment. Several values of R_3 and V_{d3} were used during various trials, with 15 $k\Omega$ and 27 V being most common. V_{c1} and V_{c2} were measured using Tektronix ADA400A differential preamplifiers. Grids were mapped autonomously as described in the ion flux probe experiment. The four channels of the TDS 684B oscilloscope were used to record V_{c1}, V_{c2}, V_s, and I_a simultaneously. Applying the standard methods of circuit analysis to Figure 4-14, it is possible to determine the electrode voltages and the

currents they emit:

$$V_{p1} = 11(V_{s1} + V_{c1}) \tag{4.13}$$

$$V_{p2} = 11V_{s1} \tag{4.14}$$

$$V_{p3} = 11(V_{s1} + V_{c1} + V_{c2}) - V_{d3} \tag{4.15}$$

$$I_{p1} = \frac{(V_{p3} + V_{d3} - V_{p1})}{R_3} - \frac{2V_{p1}}{11 \times 10^6} \tag{4.16}$$

$$I_{p2} = -\left(\frac{2V_{s1}}{1 \times 10^6}\right) \tag{4.17}$$

$$I_{p3} = -\left(\frac{(V_{p3} + V_{d3} - V_{p1})}{R_3} + \frac{(V_{p3} + V_{d3})}{11 \times 10^6}\right) \tag{4.18}$$

4.4.4 AC Probes

Electrostatic probes were also operated in an AC mode which allowed time resolution of fast fluctuations of the plasma parameters. For these experiments, the oscilloscope was operated in AC mode with either the a simple floating potential probe or an ion saturation current probe. In both cases, no 10 $M\Omega$ resistors were used in-line. Computing the input impedance of the measurement system at the frequencies of interest (higher than 10 kHz) gives negligible attenuation.

4.4.5 Azimuthal Rake

An azimuthal rake experiment was carried out in an attempt to detect waves traveling azimuthally. It consisted of three single electrodes, each pointing axially toward the thruster (in the $-z$ direction), as shown in Figure 4-15. Construction was similar to probes described above, made of .015 in diameter tungsten 1 mm long. The three electrodes were placed at three azimuthal locations: 0°, 74°, and 106°. Separate trials measuring V_f and ion saturation current were performed. In each case, the parameters at each electrode were recorded simultaneously with I_a. The oscilloscope was set to AC mode for all cases.

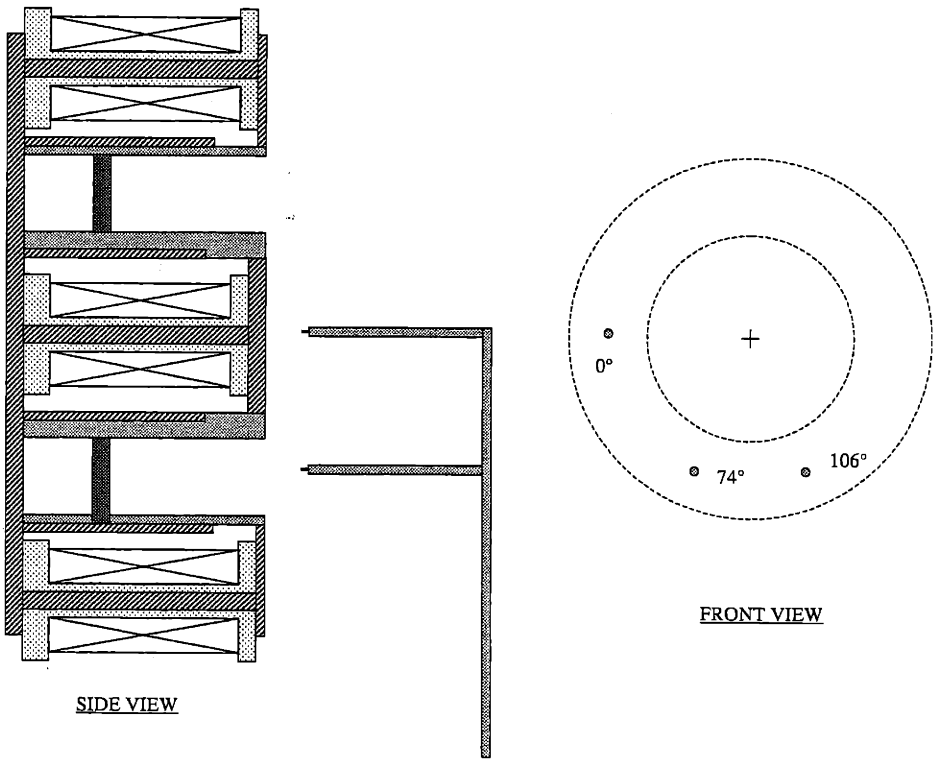

Figure 4-15: Orientation of the azimuthal rake.

Chapter 5

DC Results

During operation of the SPT-70 thruster, discharge current oscillations were observed in the $10 - 60\ kHz$ range with RMS amplitudes up to 100% of the DC value. This chapter describes results obtained by time-averaging measurements over periods greater than $2\ s$. Chapter 6 addresses the oscillatory components of those signals.

5.1 Experiment

Several trials were executed with the DC experimental apparatus described in Sections 4.4.3 and 4.4.2. Local sweeps of the voltage-current characteristic were performed. A two-dimensional $(z - r)$ survey was performed at the nominal operating conditions, and several axial one-dimensional scans were performed at various operating conditions.

All z-coordinates shown in experimental data are with respect to the exit of the acceleration channel. All r-coordinates are with respect to the centerline. Unless otherwise noted, the operating conditions at the time of the measurement were $V_d = 300\ V$, $\dot{m} = 2.34\ mg/s$.

5.1.1 Shape of the Characteristic

Using the triple probe apparatus with a 100 V power supply, sweeps of the voltage-current characteristic were made at various points in the plume. Figure 5-1 is the result of plotting measured voltages (with respect to tank GND) and currents for all three electrodes parametrically for a $10 - second$ sweep. An exponential rise can be seen, as predicted by the electron collection model, with a constant of approximately 7 eV. The ion saturation current continues to increase as voltage is reduced further due to enlargement of the ion

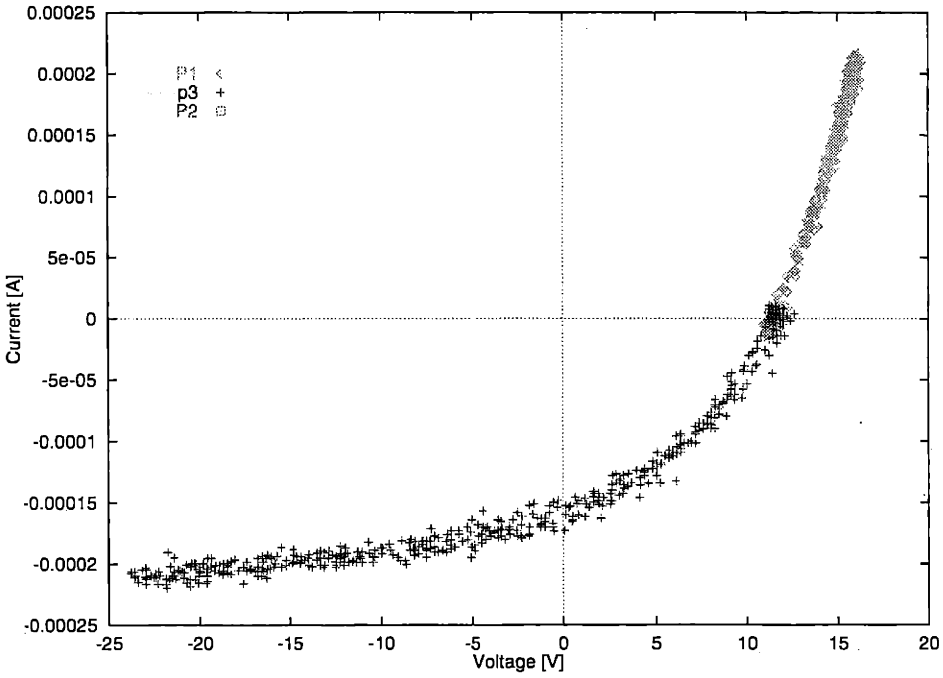

Figure 5-1: Triple probe sweep at $z = .01\ m$ from the exit of the acceleration channel, $r = .03\ m$ radially outward from the centerline.

collection area of the probe.

Figure 5-2 shows the current collected during a voltage sweep with a single probe, biased directly with respect to GND. Notice the greatly expanded scale, compared to Figure 5-1. For a quiescent thin-sheath plasma above the plasma potential, an electron saturation current should be reached with a value approximately equal to the random electron flux times the surface area of the probe, $en_eS_e\sqrt{\frac{kT_e}{2\pi m_e}}$. For the conditions of interest here, the value would be approximately 9 mA. The results show no tendency toward electron saturation. Even in trials where the probe voltage exceeded 100 V, the characteristic remained linear. This implies, as discussed in the previous chapter, that the electron collection for $V > V_p$ may be orbit motion limited.

5.1.2 Two-Dimensional Near Plume Survey

Probe scans in the $z-r$ plane of the SPT-70 plume were performed for $z = 5$ to 40 mm (from the front of the thruster) and radially out from $r = 0$ to 50 mm. Increments were 2.5 mm in each direction. Operating conditions of the SPT-70 were near nominal: $\dot{m} = 2.34\ mg/s$,

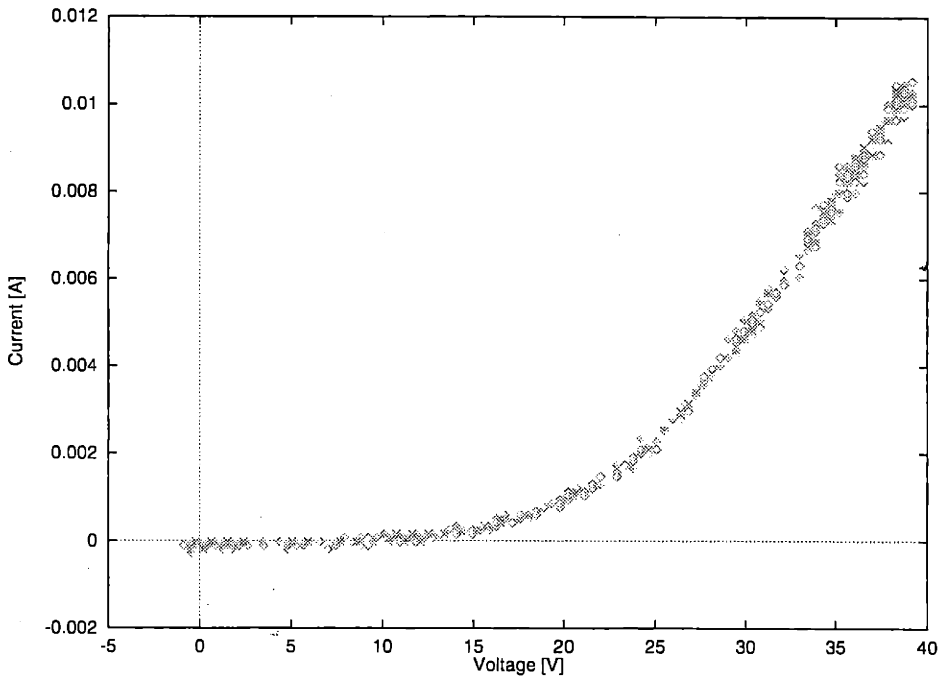

Figure 5-2: Single probe sweep at $z = .04\ m$, $r = .0275\ m$.

and $V_d = 300\ V$. The electromagnets were connected in series with the discharge, as shown in Figure 4-7. It is expected that the peak radial magnetic field, although not directly measured, is close to that of the SPT-100, which was measured at NASA Lewis to be .0143 T [27].

Determination of Probe Projected Area

As described in Section 4.4.2, measurement of $S_i(z,r)$ required two experiments: a plume scan using the ion flux probe (with known projected area, $S_\perp$) biased to $-72\ V$, and a plume scan using the triple probe with each electrode biased to $-72\ V$, each with respect to GND. Then, Equation 4.10 was applied to compute the projected areas for ion collection,

$$S_i = S_\perp \frac{I_{sat}}{I_{sat,\perp}}. \tag{5.1}$$

Results for electrode 1 are shown in Figure 5-3. The ion collection area goes to zero near the thruster at wide radial locations. In these regions, it is believed that the plasma consists of slow ions from the plume which travel back toward the thruster. Due to this negative

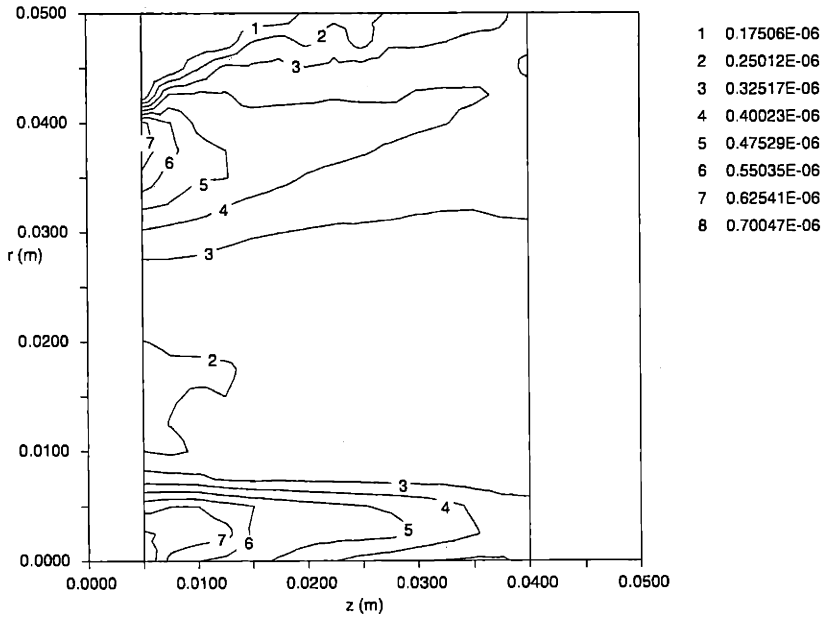

Figure 5-3: Effective probe area, S_i $[m^2]$, for ion collection by triple probe electrode P_1.

axial velocity component, the electrode is shadowed by the insulating part of the probe. The regions where S_i is highest correspond to regions where the ion beam is expected to be perpendicular to the triple probe. There, S_i is approximately equal to the sideways projected area, ld. When the probe is aligned with the flow, the effective area for collection may exceed the tip area because of additional collection along the sides of the electrode. This "end effect" is apparent in the data, where the minimum S_i is computed to be approximately 3 times the tip area.

Consistent with the supersonic flowing plasma model, the area for electron collection by an electrode is assumed to be simply the portion of surface area impacted by ions (not in the wake region – see Figure 4-2). For axial probes, the area is constant throughout the plume, and is half the surface area of the probe:

$$S_e = \frac{ld\pi}{2}. \tag{5.2}$$

Once again, this is not exactly correct as the probe becomes exactly aligned with the beam. At perfect alignment, the collection area for electrons will become the total surface area of the cylindrical probe, $ld\pi$. Since the beam angle with respect to the electrode is

not determined, no compensation for end effect can be made. A sensitivity analysis was performed to measure the effect of this assumption on the final plasma parameters. The parameter most sensitive to S_e is V_p. Doubling S_e resulted in changes of T_e, V_p, and n_e of .1%, 14%, and -6%, respectively. Overall, the triple probe solutions were found to be repeatable. For two separate experiments, using two different triple probes, the results were in agreement to within 20%.

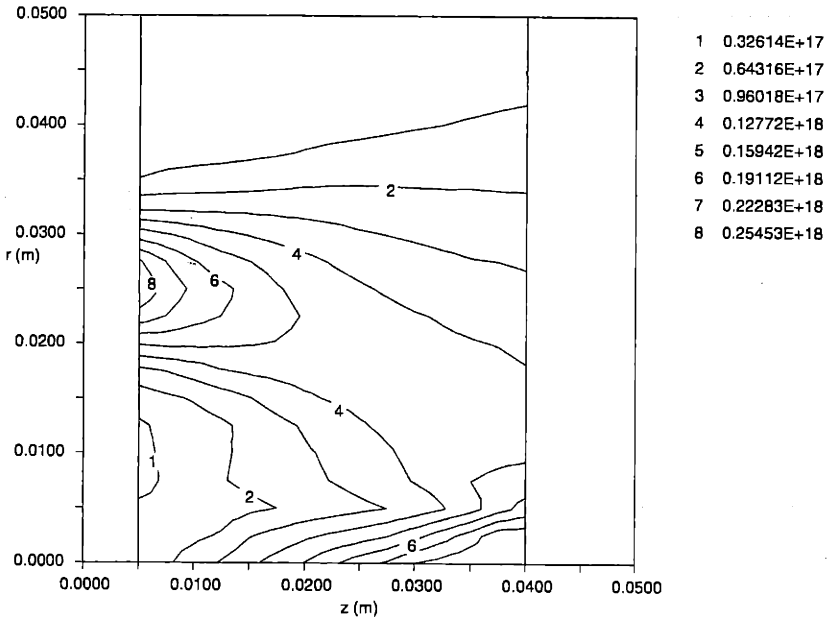

Figure 5-4: Plasma density, n_e $[m^3]$, from triple probe measurements.

To calculate the two-dimensional DC plasma parameters in the plume, $2-second$ time-averaged measurements were made of V_{p1}, V_{p2}, V_{p3}, I_{p1}, I_{p2}, and I_{p3} using the triple probe apparatus described in the previous section. The system of nonlinear equations (Equation 4.9) was then solved for T_e, V_p and n_e using Newton's method. Actually, ion flux, $n_e v_i$, is measured. As mentioned in Section 4.2, the computation of n_e is only an estimate, subject to the assumption,

$$v_i = \sqrt{\frac{2eV_d\eta_e}{m_i}}. \tag{5.3}$$

Results will show, however, that most of the acceleration of ions takes place inside the acceleration channel, and that the total measured thrust is in agreement with mean ion velocities close to those given by Equation 5.3.

Figure 5-4 shows the ion density computed by triple probe measurements. The triple probe provides a measure of beam current density. To find n_e, we have assumed a mean ion velocity based on Equation 4.8. A check on accuracy may be performed by computing the total beam current near the channel exit. Integrating radially,

$$I_{b,meas} = e \int_0^\infty n_e v_{i,z} 2\pi r dr \tag{5.4}$$

Above, $n_e v_{i,z}$ is the axial component of the ion beam flux, which we will estimate using a point of origin of the ion beam (z_0, r_0). With $z = 5\ mm$, $z_0 = -10\ mm$, $r_0 = 25\ mm$, we get $I_{b,meas} = 1.67\ A$. To compare with known values for this type of thruster, we can construct a beam current by knowing the utilization fraction and fraction of doubly charged ions. If f^{++} is the fraction of doubly charged ions emitted in the beam, then the total beam current is,

$$I_b = (1 + f^{++}) I_{b,Aeq}, \tag{5.5}$$

where $I_{b,Aeq}$ is the total rate of ejection of ions, in Aeq. Then, using the utilization fraction, $\eta_u = I_{b,Aeq}/I_{\dot{m}}$,

$$I_b = (1 + f^{++}) \eta_u I_{\dot{m}}, \tag{5.6}$$

where $I_{\dot{m}}$ is the propellant flow rate in $Amperes$. For $f^{++} = .04$ and $\eta_u = .95$, $I_b = 1.76\ A$. This shows the probe measurements of beam current agree well with expected values, to within 6%.

The high-density conical region near the centerline represents the effect of a radially converging rarefied annular ion beam, giving $n_e \sim \frac{1}{r}$. The exiting beam of neutrals which escaped ionization also converge at the centerline. Therefore, neutral excitations ($\sim n_n n_e$) and ion excitations ($\sim n_e^2$) are both proportional $\frac{1}{r^2}$ at constant T_e. The resulting emitted light is a well-defined cone extending a distance 1 m downstream from the thruster and is easily visible with the naked eye.

Figures 5-5 and 5-6 show T_e and V_p from the triple probe experiment. The black lines on Figure 5-7 are a plot of magnetic field lines computed with a Laplace solver. The computed magnetic field was comparable in both profile and magnitude to that measured at NASA Lewis on an SPT-100 [27].

T_e peaks at 7.8 eV 15 mm downstream from the exit of the acceleration channel. This is

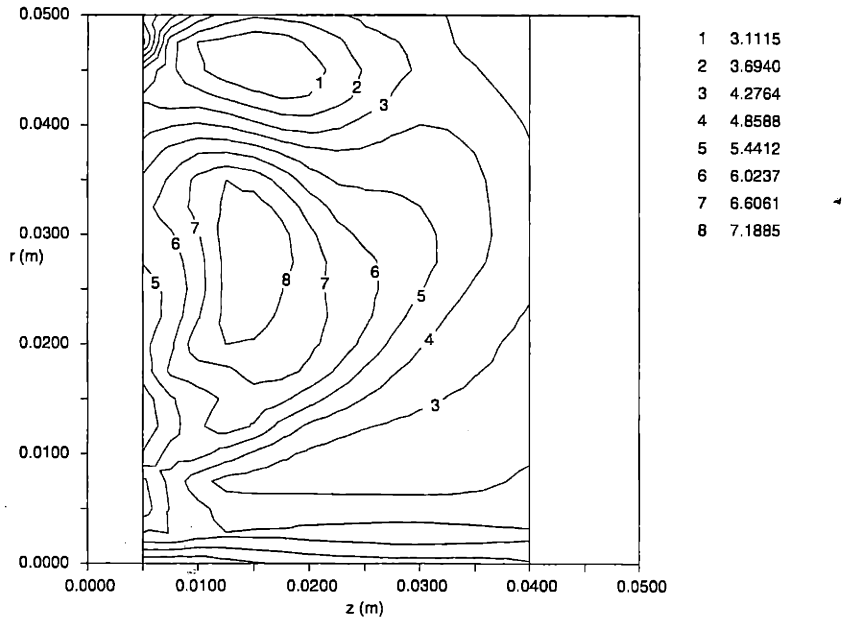

Figure 5-5: Electron temperature, T_e $[eV]$, from triple probe measurements.

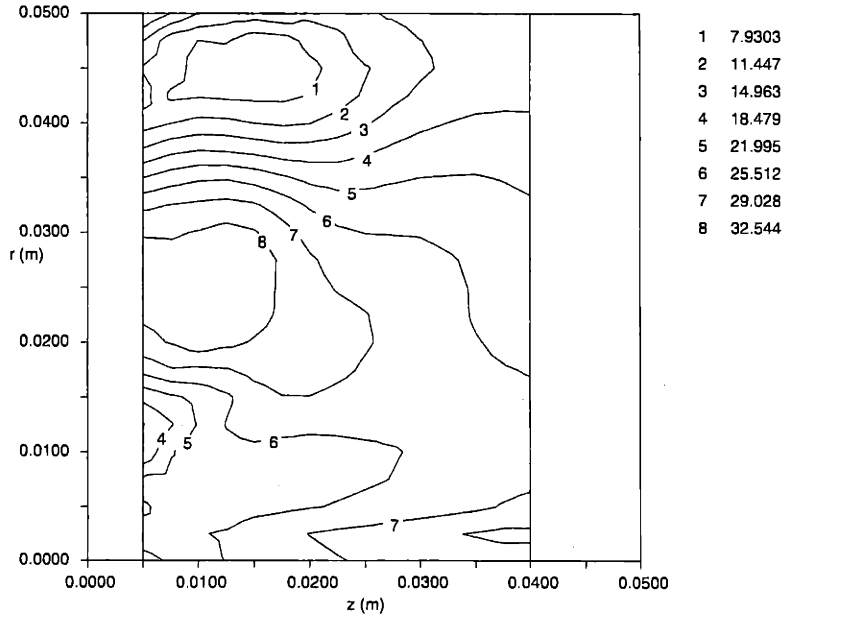

Figure 5-6: Plasma potential, V_p $[V]$, from triple probe measurements, measured with respect to tank GND. The metallic thruster body is also at GND.

in fairly good agreement with measurements by Kim [43] which show T_e peaking at $8.75eV$ 10 mm from the exit of an SPT-100. Kim's measurements also show T_e at $6eV$ 25 mm from the channel exit, which also agrees well with the data presented here.

Closer to the channel exit, measurements of T_e drop to 70% of their peak value 5 mm from the channel exit. Cooling appears to take place near the B-field line which forms the interface between the metallic front pole piece and the ceramic channel walls (marked with a "*" on Figure 5-7). Rotating this curve azimuthally forms a surface which we will call the "metal-insulator transition surface." It is believed that near this surface, electron mobility drops abruptly from some enhanced ("anomalous") value outside the channel. This is discussed in detail in the next chapter.

The contours of T_e can be seen to roughly follow the magnetic field lines. However, along any given B-field line, T_e does varies slightly. The assumption of isothermal electrons along lines of force does not seem to apply. The variation in measured T_e is small, however, and limited to less than about 3 eV along any line. Nevertheless, either the measurements were in error, or the isothermal electron model is not applicable in this region. It is also possible that the variation may be due to a geometric effect. The peak electron temperatures along each line of force correspond with axial alignment of probe with the beam. Measured electron temperature drops off as the probe angle with respect to the thruster axis deviates from zero. This is simply an observation, however, and it is not immediately known how this may effect measurement of T_e.

As can be seen by comparing Figures 5-4 and 5-6, T_e drops with n_e and ϕ, which reinforces the possiblity that a different equilibrium relationship (besides isothermal) holds. Some possibilities will be explored in Chapter 7. For now, to quantify the deviation from isothermal equilibrium in the entire plume, Figure 5-8 shows a plot of $V_p - V_{p,0} - \frac{kT_e}{e} \ln \frac{n_e}{n_{e,0}}$, where $V_{p,0}$ and $n_e e, 0$ are taken at the point $z = 15\ mm$, $r = 35\ mm$. Deviation from zero is limited to about $\pm 1\ V$ in the near-exit of the thruster, but varies greatly at the radial extremum.

From Figures 5-7 and 5-6 an area of minimum plasma potential and electron temperature can be observed near the outlet of the cathode ($r \simeq 45\ mm$). It is believed that this area consists mainly of colder electrons emitted by the cathode, which was measured to be $-20\ V$ with respect to GND.

To verify the consistency of the 2-D results presented here, some simple relationships

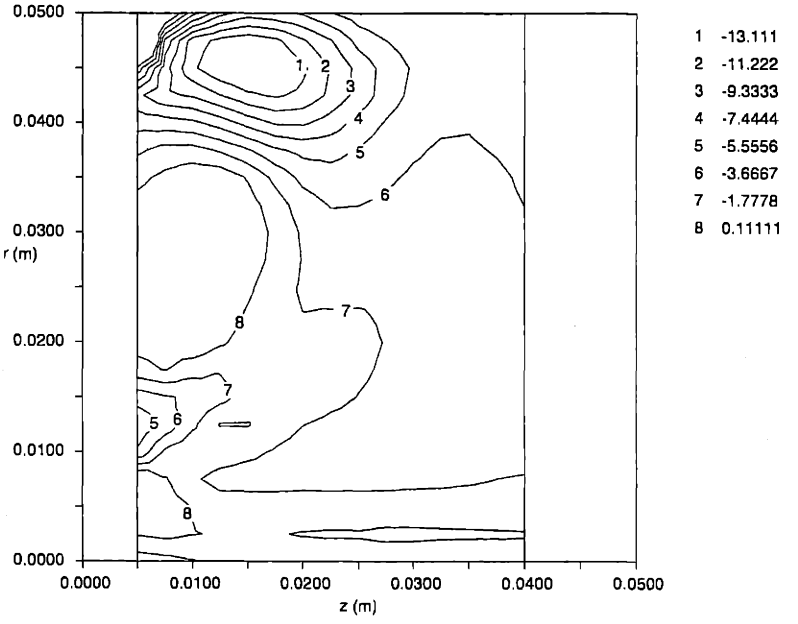

Figure 5-8: Deviation from isothermal, normalized at $z = 15\ mm$, $r = 35\ mm$, $[Volts]$.

can be tested. Electrons in the interior region have higher density and energy and must be confined by a potential difference. For negligible net current across the interface,

$$\frac{\bar{c_e}}{4} e^{-\frac{e\phi}{kT_e}} = 0.61 v_{Bohm}, \tag{5.7}$$

where ϕ is the potential drop between the regions. This gives $\phi = 5.77 T_e[eV]$. For $T_e = 6\ eV$, the potential drop must be 35 V, which is slightly more than what is shown in the data.

The interior regions of the plume have higher electron temperature due to the $\sim 28\ V$ rise from the cathode region. However, based on a convective energy relationship alone, $T_e[eV]$ should rise by $\frac{2}{5}\phi = 11.2\ eV$. Actually, it rises to only 7 eV. Power lost in the plume is, therefore, $\frac{5}{2}(11.2 - 7) I_a = 21\ W$.

Heat lost to diffusion may be checked with the following calculation. For an assumed parabolic T_e distribution with mean value $\bar{T_e}$, width l, and axial area A, the amount of heat conducted away is,

$$Q_{cond} = \frac{1}{12} K_e \bar{T_e} \frac{A}{l}. \tag{5.8}$$

The Bohm-controlled cross-field thermal conductivity is,

$$K_e = (\frac{kT_e}{16eB})(\frac{5}{2}kn_e), \tag{5.9}$$

and using $\bar{T_e} = 7\ eV$, $B = .004\ T$, $n_e = 1.5 \times 10^{17} m^{-3}$, we find $K_e \simeq 0.009\ W/m/^\circ K$. The temperature peak for the case in Figure 5-7 has $l \simeq 1\ cm$, and area $A \simeq 2.4 \times 10^{-3} m^2$. This yields $Q_{cond} = 14\ W$. Thus, diffusive losses explain most of the 21 W deficit. The rest appears to be related to wall losses to the metallic surface, which are discussed in the next chapter.

5.1.3 Variation with Operating Parameters

A separate set of triple probe measurements was performed to examine the variation of plasma parameters with thruster operating conditions. During these experiments, axial scans were performed at $r = 27.5\ mm$, corresponding to the annular channel's centerline. The range of z was 0 to 20 mm, with 1 mm between data points. No data points were measured inside the channel ($z < 0\ mm$) because of excessive probe heating. The test matrix consisted of $\dot{m} = 2.34$, 1.76, and 1.17 mg/s, and $V_d = 300$, 250, and 200 V. The propellant flow rates were chosen as 100%, 75%, and 50% of nominal.

Figures 5-9, 5-10, and 5-11 show electron temperature measured with the triple probe at 100%, 75%, and 50% of nominal propellant flow rate, respectively. The peak at $z = 15\ mm$, described in the 2-D $(z - r)$ results, is clearly seen in he curve labeled 300 V in Figure 5-9. At the lower propellant flow rates, the hump appears to move inward. In each case, higher discharge voltage produced higher electron temperatures, as expected.

Figures 5-12, 5-13, and 5-14 show a plasma potential that is fairly flat, reaching a maximum of only 40 V with respect to GND (the chamber wall and thruster body), suggesting most of the acceleration occurs inside the channel. This is reinforced by the qualitative observation of the onset of catastrophic heating of the probe just inside the channel at $z = -2\ mm$. At that point, T_e must become large rapidly.

Writing the steady-state electron energy equation, and neglecting the diffusive term,

$$\nabla \cdot (\frac{5}{2} n_e k T_e \vec{u}_e) = \vec{j_e} \cdot \vec{E} - \dot{E}_l, \tag{5.10}$$

Where $\dot{E}_l$ is a volumetric loss term collectively representing any electron energy sink. Ex-

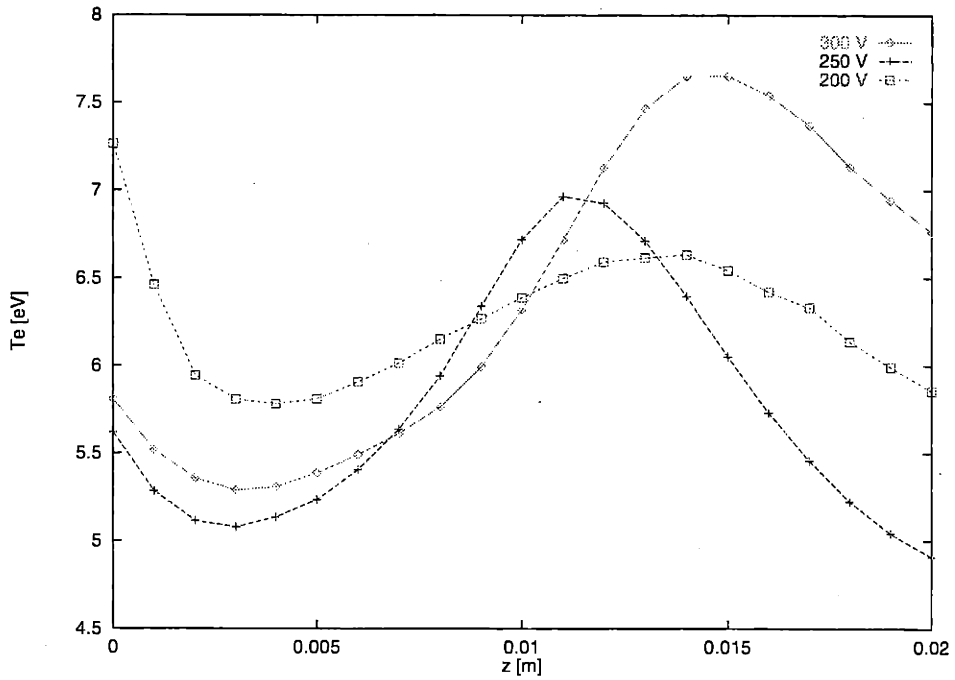

Figure 5-9: Electron temperature, T_e $[eV]$, from triple probe measurements. $\dot{m} = 2.34$ mg/s, $r = .0275$ m.

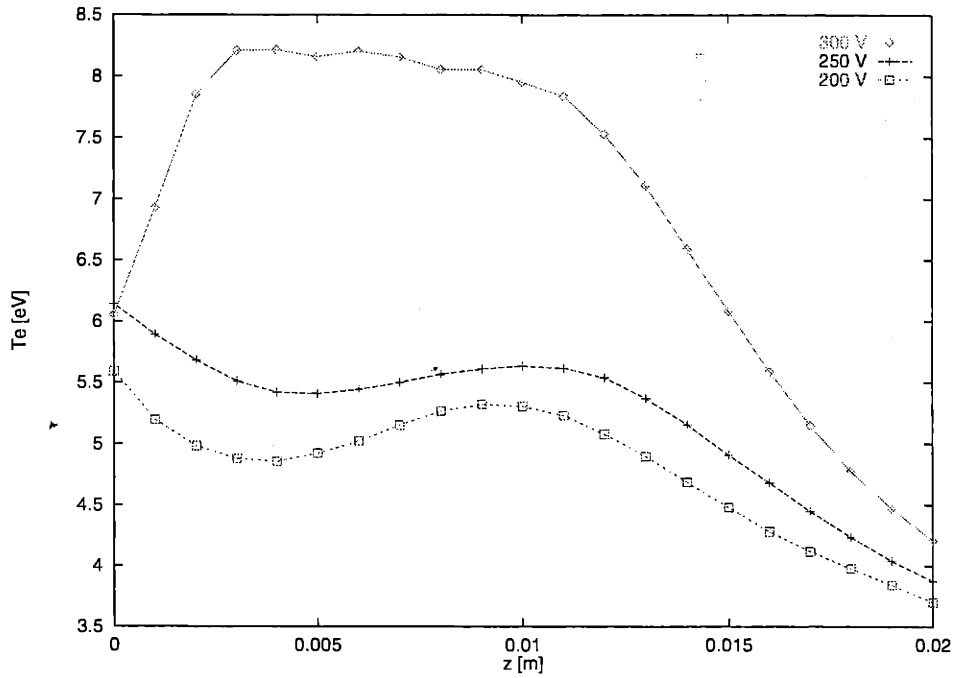

Figure 5-10: Electron temperature, T_e $[eV]$, from triple probe measurements. $\dot{m} = 1.76$ mg/s, $r = .0275$ m.

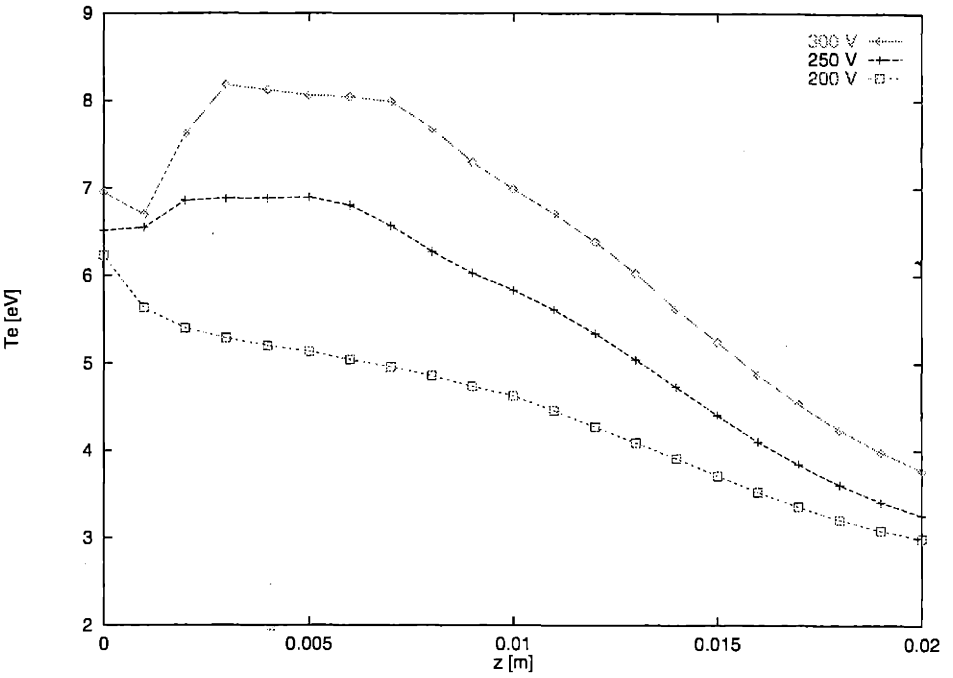

Figure 5-11: Electron temperature, T_e $[eV]$, from triple probe measurements. $\dot{m} = 1.17$ mg/s, $r = .0275$ m.

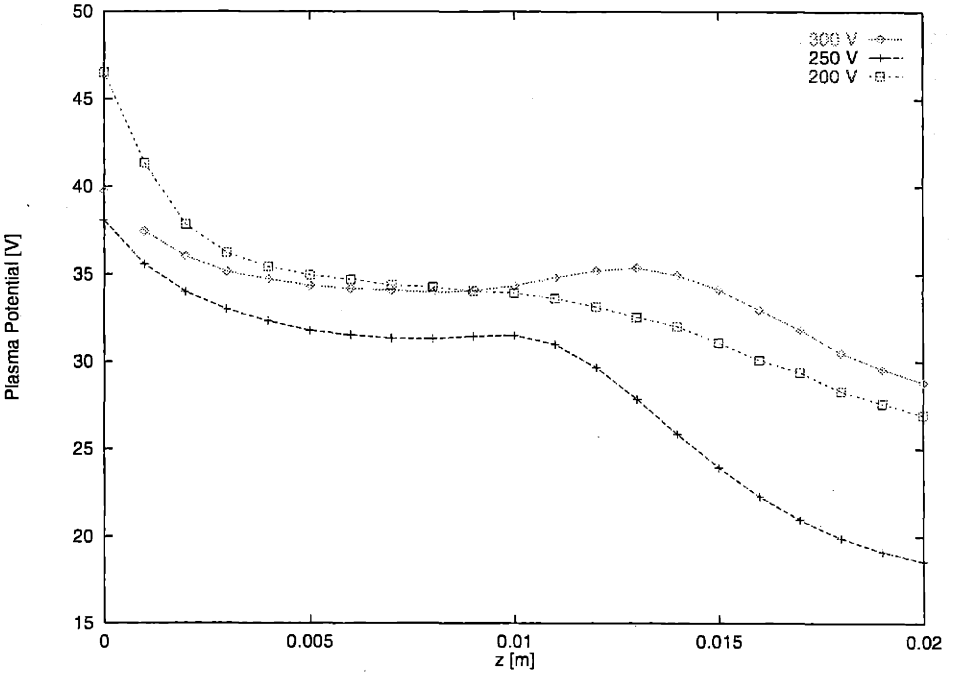

Figure 5-12: Plasma Potential, V_p $[V]$, from triple probe measurements. $\dot{m} = 2.34$ mg/s, $r = .0275$ m.

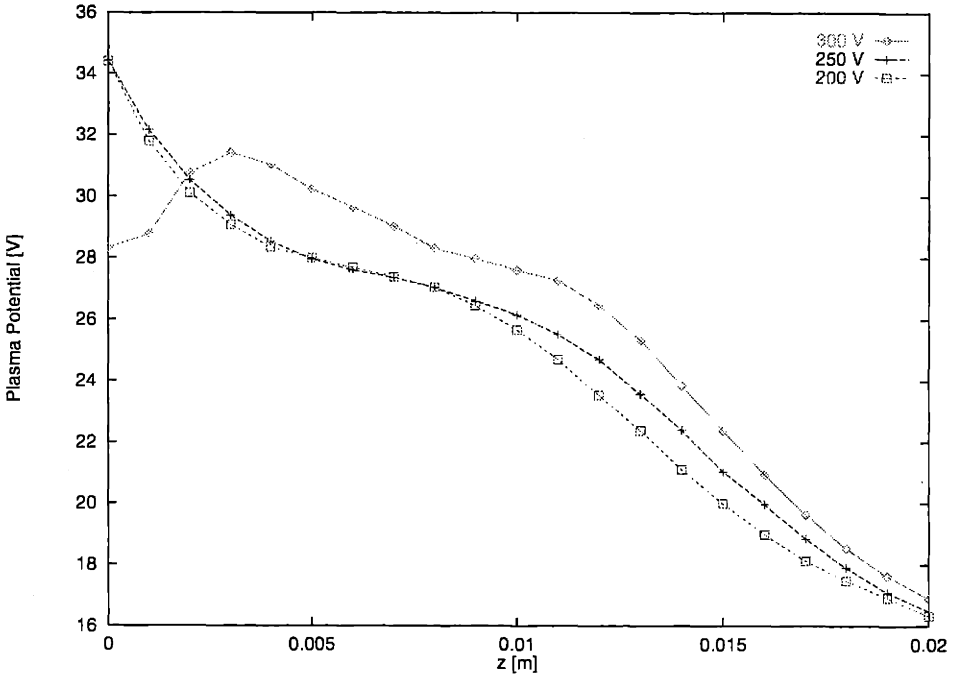

Figure 5-13: Plasma Potential, V_p $[V]$, from triple probe measurements. $\dot{m} = 1.76$ mg/s, $r = .0275$ m.

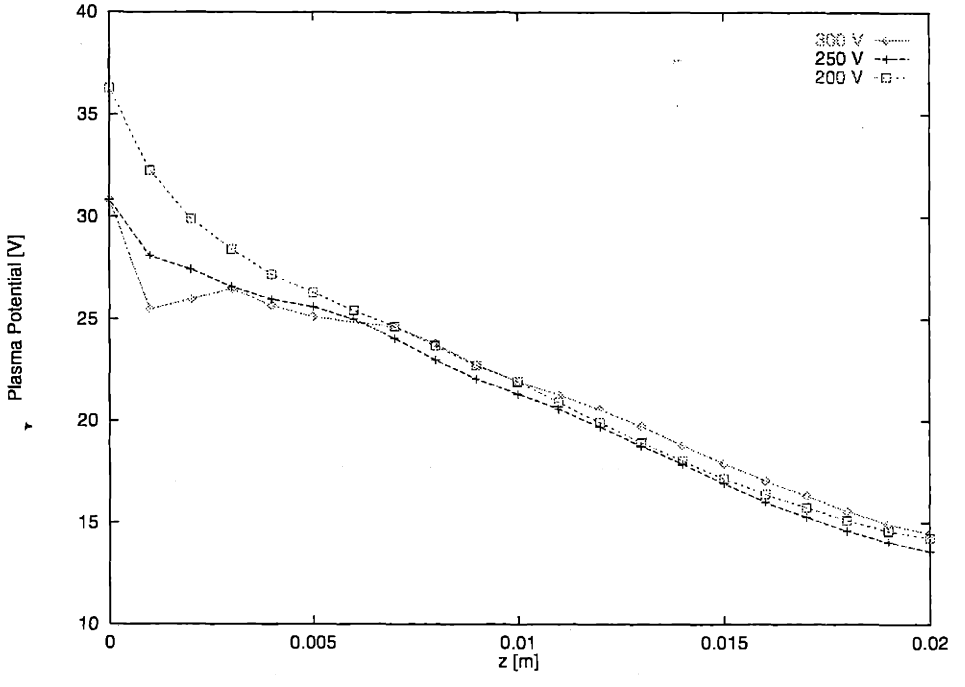

Figure 5-14: Plasma Potential, V_p $[V]$, from triple probe measurements. $\dot{m} = 1.17$ mg/s, $r = .0275$ m.

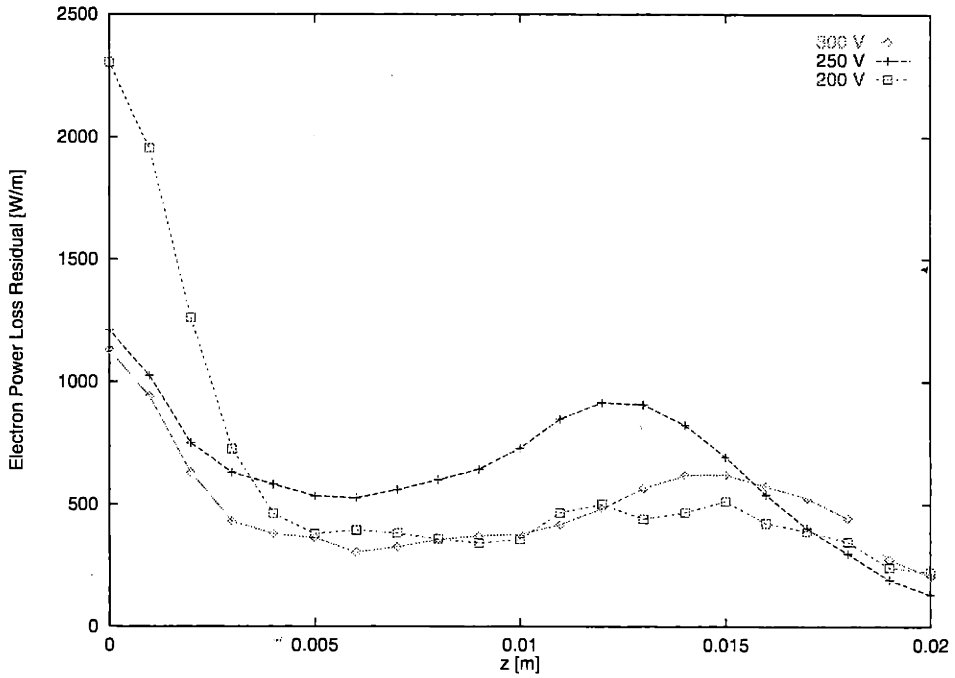

Figure 5-15: Electron energy loss residual, $\dot{L}A$, $[W/m]$, $\dot{m} = 2.34\ mg/s$, $r = .0275\ m$.

panding the divergence term, using continuity, and neglecting ionization,

$$\vec{j_e} \cdot [\frac{5}{2}\frac{k}{e}\nabla T_e + \vec{E}] = \dot{E}_l. \tag{5.11}$$

Assuming T_e and $\vec{E}$ and $\dot{E}_l$ invariant along lines of force, and integrating over the area, A, of a flux surface,

$$I_a(1-\eta_a)[\frac{5}{2}\frac{k}{e}\frac{dT_e}{dz} + E_z] = \dot{E}_l A, \tag{5.12}$$

where $\eta_a = I_i/I_a$ is the acceleration efficiency. The left hand side of Equation 5.12 can be computed from the probe data. It is plotted in Figure 5-15 for the case of nominal flow rate and $\eta_a = .67$. Positive values indicate power lost due to inelastic collisions and wall interaction. A sharp rise can be seen to begin near the metal-insulator transition surface which intersects at approximately $z = 4\ mm$. This may be due to a change in loss to the wall or inelastic collision rate. Integrating $\dot{E}_l A$ along z, the total power amounts to approximately 15 W. This, in part, verifies the existence of 21 W plume losses described in the previous section.

Figures 5-16, 5-17, and 5-18 show the drop in ion density due to the expanding rarefied

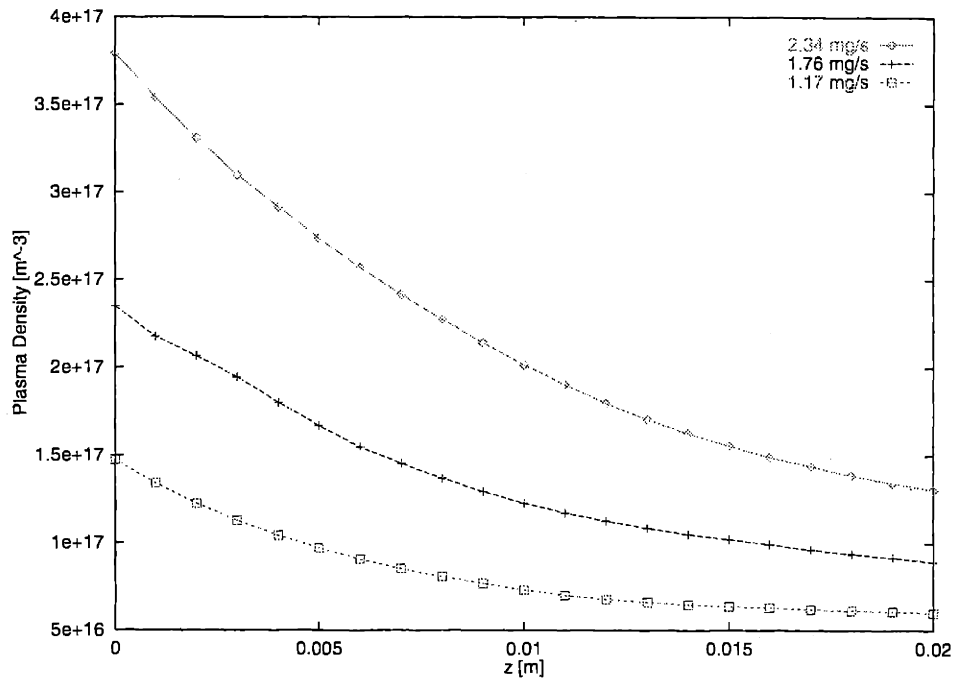

Figure 5-16: Plasma Density, n_e $[m^{-3}]$, from triple probe measurements. $V_d = 300\ V$, $r = .0275\ m$.

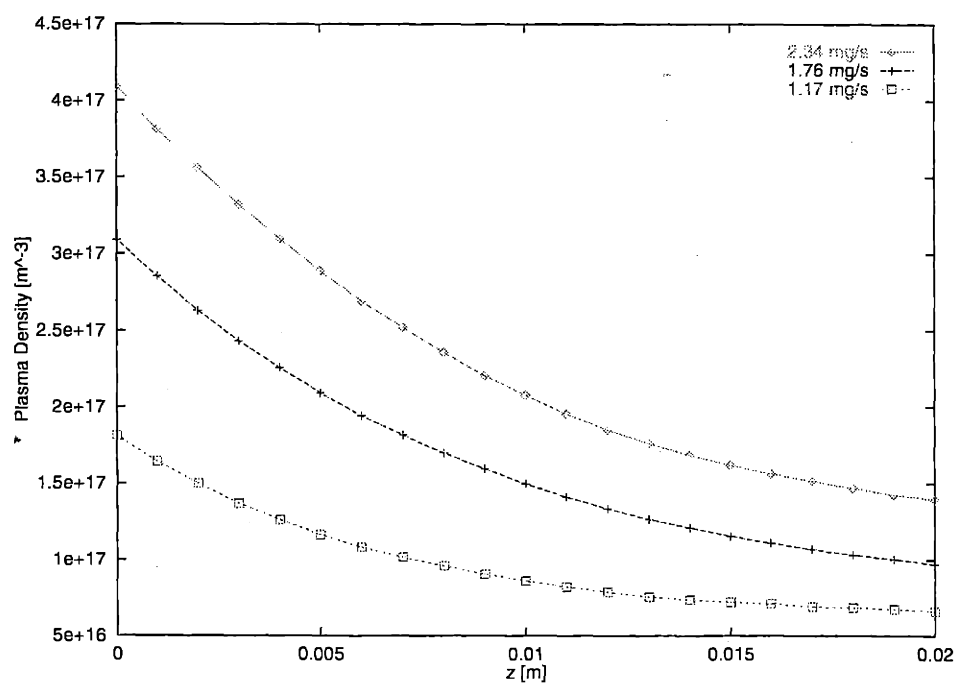

Figure 5-17: Plasma Density, n_e $[m^{-3}]$, from triple probe measurements. $V_d = 250\ V$, $r = .0275\ m$.

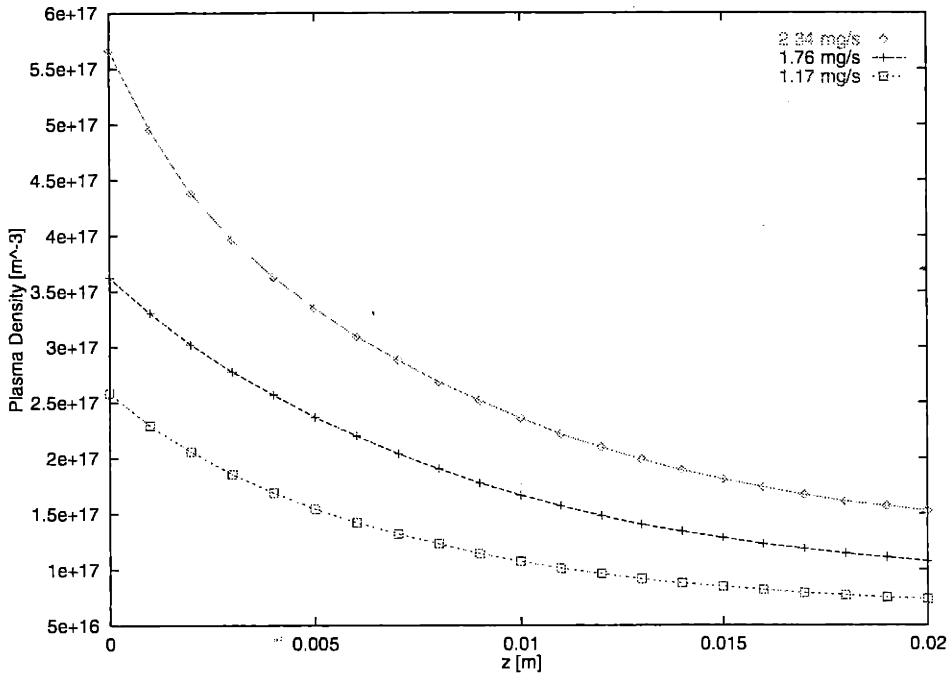

Figure 5-18: Plasma Density, n_e $[m^{-3}]$, from triple probe measurements. $V_d = 200\ V$, $r = .0275\ m$.

beam. Note that these figures are each plotted for a single voltage so that the variation in density with flow rate may be compared. The magnitudes are approximately proportional to the flow rate, as expected. For constant flow rate, density decreases with increasing discharge voltage. This is due to conservation of particle flux: $\nabla \cdot (en_i\vec{u_i}) \approx 0$ at constant flow rate, where $\vec{u_i}$ is decreasing with V_d.

5.1.4 Performance

Measurements of thrust were performed using a NASA-Lewis-type inverted pendulum thrust balance [34] calibrated from 0 to 47 mN using discrete weights. Figure 5-19 shows thrust measured at a variety of operating conditions. Thrust can be seen to increase at a rate greater than the square root of discharge voltage, due to an increase in thrust efficiency with discharge voltages. Figure 5-20 shows the variation in discharge current, I_a, measured simultaneously with thrust using a Tektronix Model A6303 Hall-effect current probe. That instrument was zeroed to $\pm.001A$ but not calibrated with known current sources. The data suggest that the thruster is operating at nearly full propellant utilization for the entire

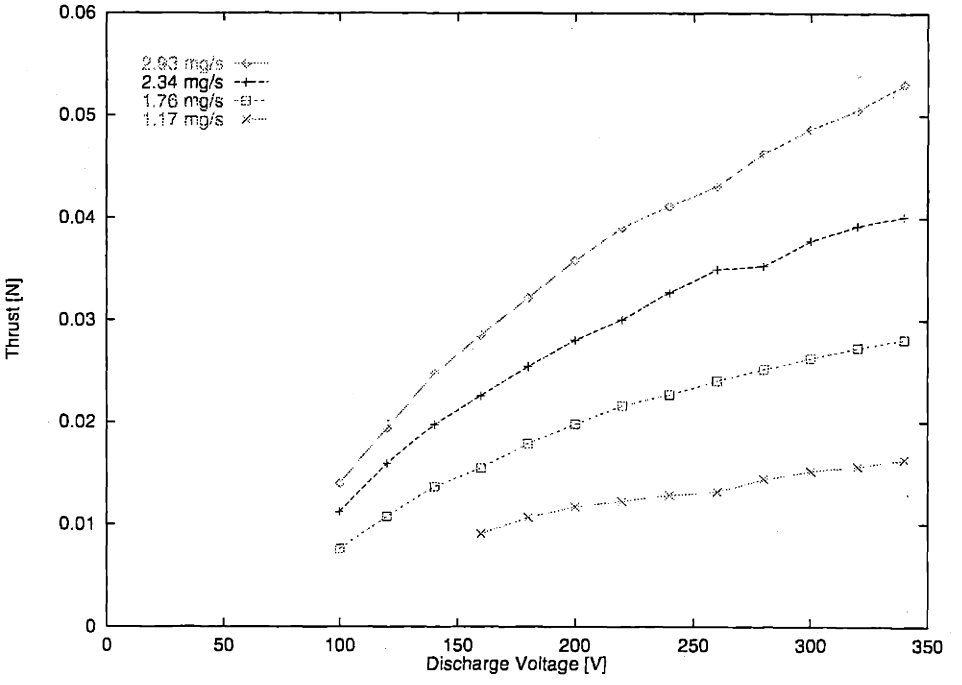

Figure 5-19: Measured thrust at various operation conditions, [N].

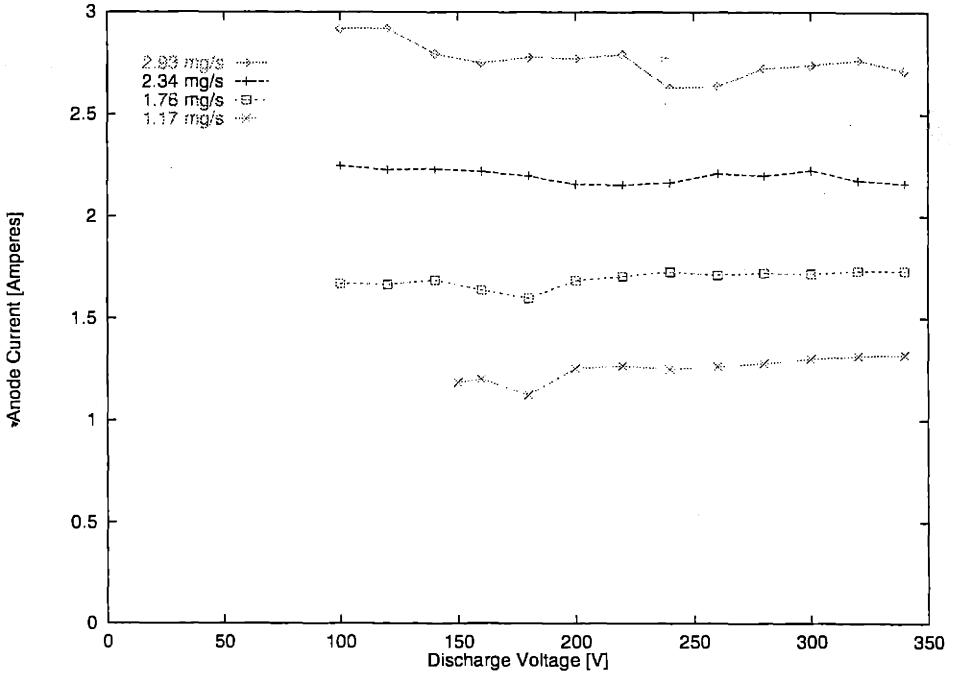

Figure 5-20: Measured discharge current at various operation conditions, [A].

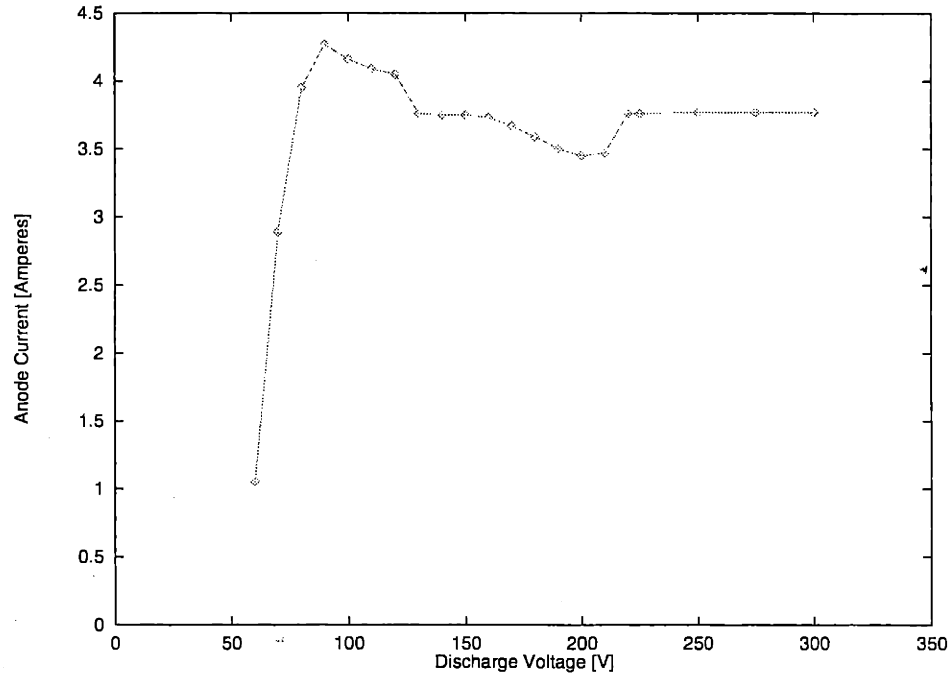

Figure 5-21: Measured discharge current for the SPT-100 [A]. $\dot{m} = 4.1\ mg/s$, $V_d = 305\ V$.

range of operating parameters tested here. This is in agreement with measurements taken at NASA Lewis using an SPT-100. Figure 5-21 shows the discharge current measured in that experiment at nominal operating conditions.

Figures 5-22 and 5-23 show thrust efficiency and specific impulse directly computed using data from the previous figures. The drop in efficiency at lower voltages has been reported before [10]. The SPT-100 data shown on the same figures are were taken at constant discharge current by Brophy [14]. The flow rate was $5.52 \pm .05\ mg/s$, and is the design value for that thruster. All efficiencies have been computed strictly based on power to the discharge and magnet coils, excluding the cathode.

5.1.5 Effects of Aging

As will be seen in the next chapter, the character of plasma fluctuations changes over the thruster lifetime. The DC measurements presented in this chapter were performed between 40 and 60 hrs from Beginning Of Life (BOL). Unfortunately, no quantitative measurements were made of the variation of DC parameters with lifetime. This may be important to understanding the changes that take place over time, and is saved for future experiments.

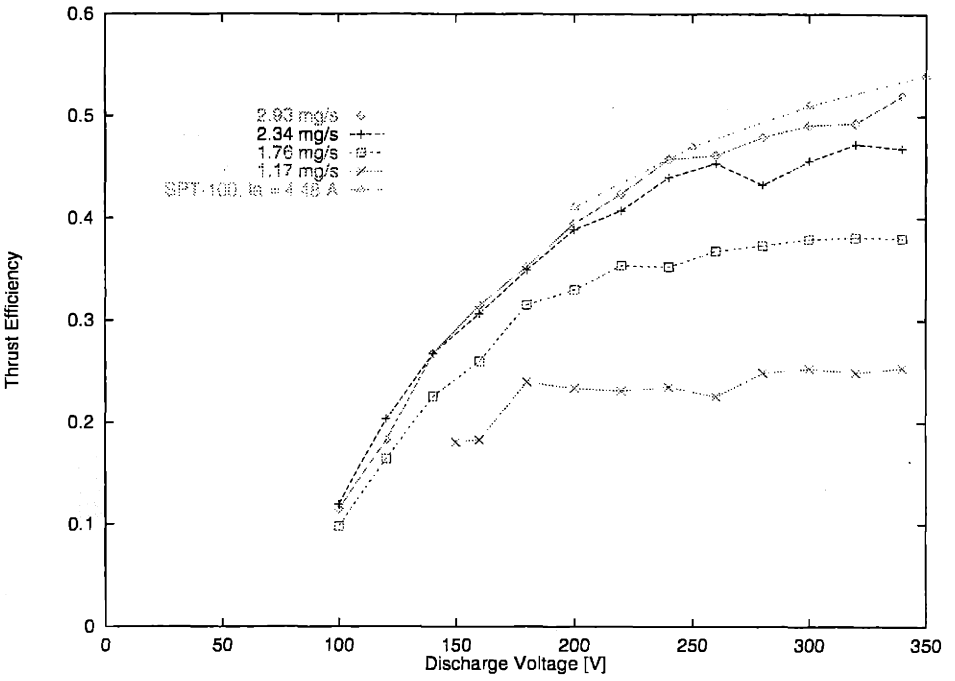

Figure 5-22: Measured thrust efficiency, η, at various operation conditions.

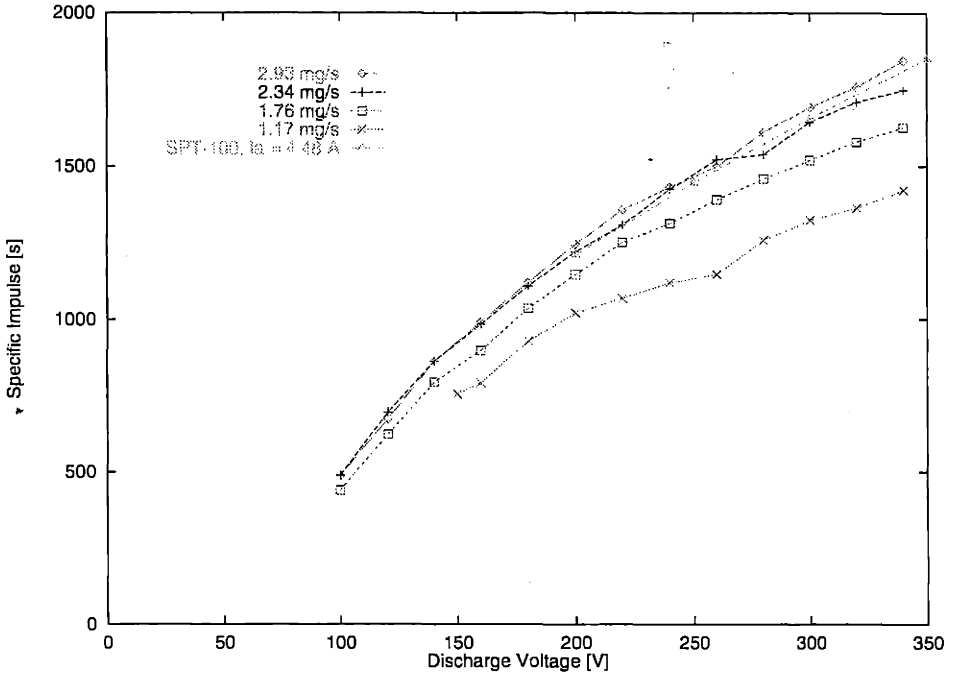

Figure 5-23: Measured specific impulse, I_{sp} [s] at various operation conditions.

5.2 Numerical Model

As described in Section 3.10, the numerical simulation involves four phases: pre-processing, running, averaging, and post-processing. Once the geometry is specified, the magnetic field is computed in the pre-processing phase. Then, operating parameters were set to nominal conditions, and execution begins. One case takes approximately, 8 hours to converge on a DEC AlphaStation 200. or 4 Hours on an SGI Octane. The Octane can run two cases simultaneously in the same time period using twin processors. Select cases are then run again in "average mode", which accumulates parameters at each timestep, and divides by the number of timesteps upon completion. Post-processing involves computation of thrust, torque, wall erosion rates, etc. from the averaged data set.

5.2.1 Magnetic Field

To compute the magnetic field, Laplace's equation is solved on the vacuum region, as described in Section 3.3. The dimensions of the iron poles of the SPT-70 were taken by external inspection. Therefore, some dimensions, such as the internal thicknesses, are assumed. Also, it is assumed that the inner and outer magnet coils have a 2-to-1 ratio of Ampere-turns. This ratio was determined to give a magnetic field profile most similar to the measured value for an SPT-100. The two magnetic screens on either side of the acceleration channel serve to effectively reduce the magnitude of the field near the anode. The outer screen is visible on the SPT-70. The inner one is assumed, and it's length is chosen to give a similar magnetic profile as measured in the SPT-100. Figure 5-24 shows the computed magnetic potential contours, normalized such that $|\vec{B}| = 1\ T$ at $z = .029\ m$, $r = .0275\ m$ in the acceleration channel.

The magnetic field parameters are shown on the computational domain in Figures 5-25 through 5-28. Since no magnetic field data are available for the SPT-70, we will compare with SPT-100 data. Figure 5-29 shows SPT-100 magnetic field data collected by Fife with a Hall-effect probe. The peak radial field on the centerline of the channel was measured to be .0143 $Tesla$. Scaling laws suggest that B should scale as $\sim \frac{1}{l}$ to preserve electron gyro radius similarity, where l is a scale length of the thruster. Applying this law gives a B-field magnitude of .0204 $Tesla$ for the SPT-70.

The computed magnetic field vectors for the SPT-70 do not correlate exactly with the

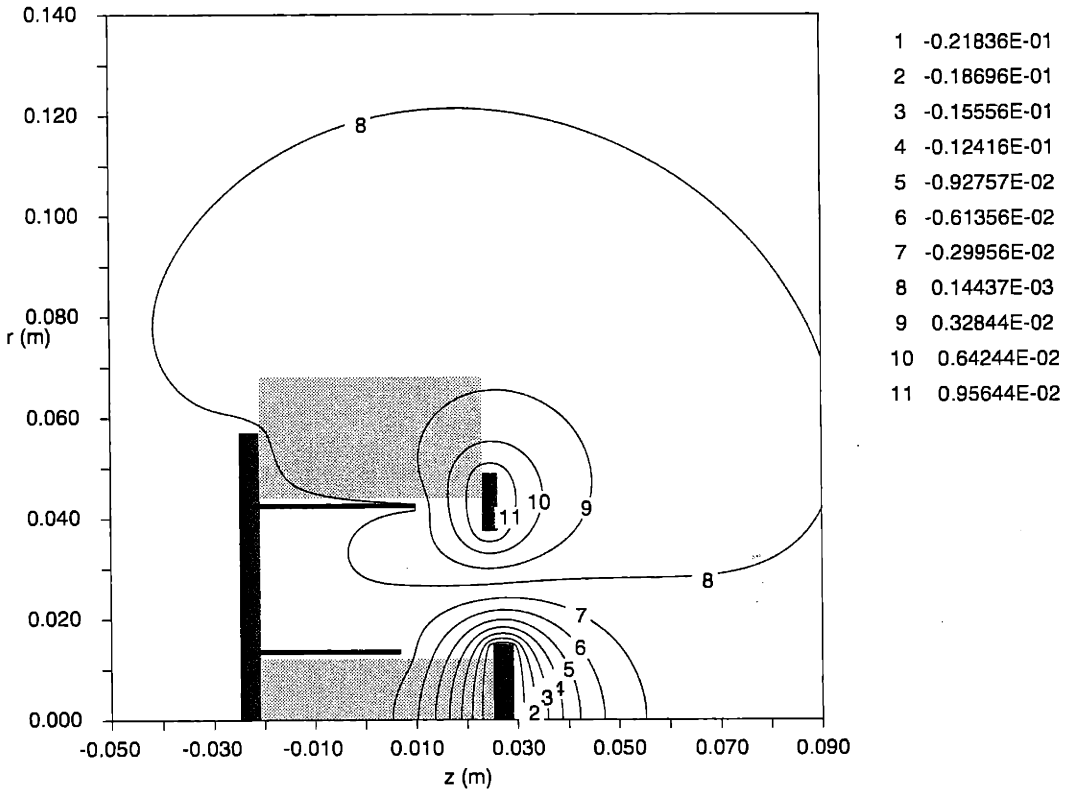

Figure 5-24: Computed magnetic potential contours, σ $[T \cdot m]$, computed for the SPT-70 geometry. The contour numbers correspond to the values of σ listed in the key.

measured SPT-100 values. Although the radial magnetic field strength has been matched, the contours of magnetic flux vary slightly. This is likely due to differences in geometry, as well as to the assumptions of infinite permeability and ideal solenoid used in the numerical model.

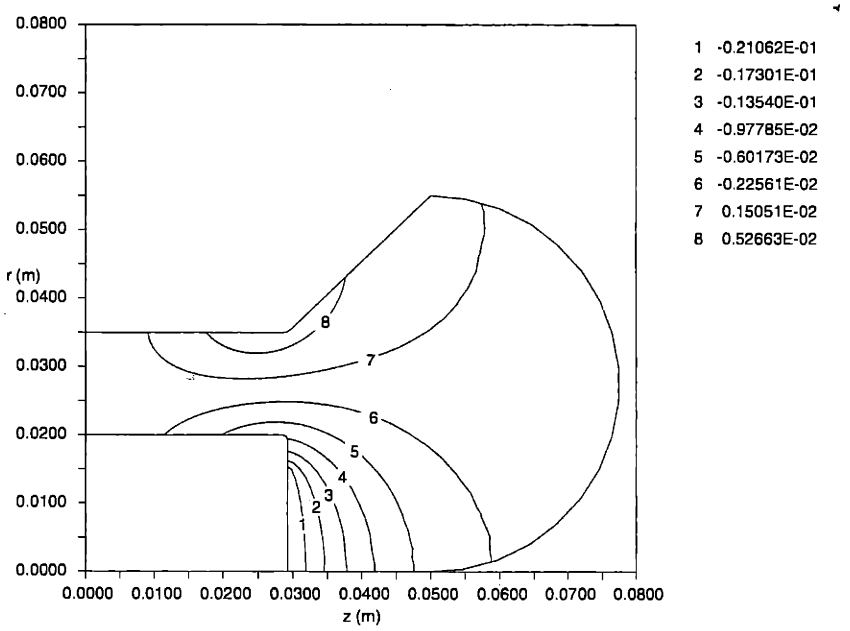

Figure 5-25: Normalized magnetic potenial contours, σ $[T \cdot m]$, computed for the SPT-70 geometry.

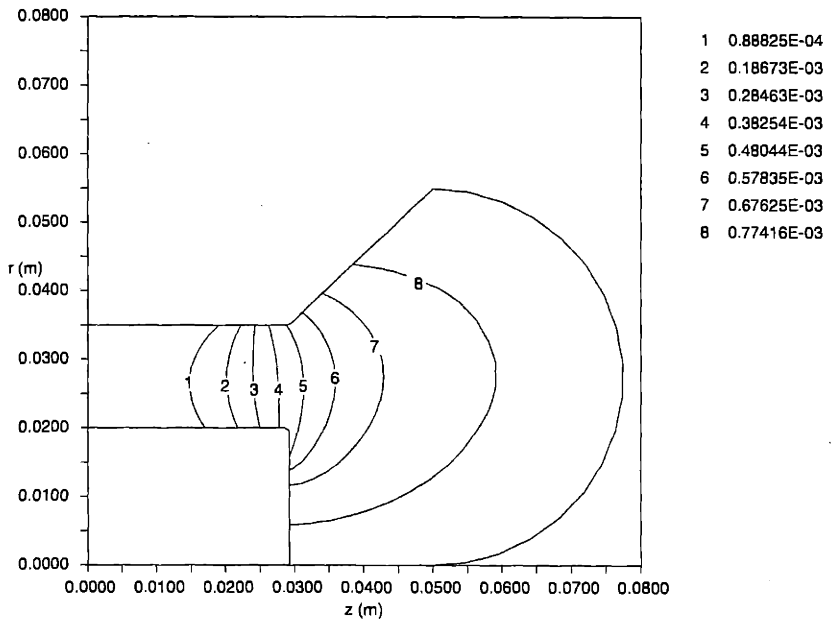

Figure 5-26: Normalized magnetic stream contours, λ $[T \cdot m^2]$, computed for the SPT-70 geometry.

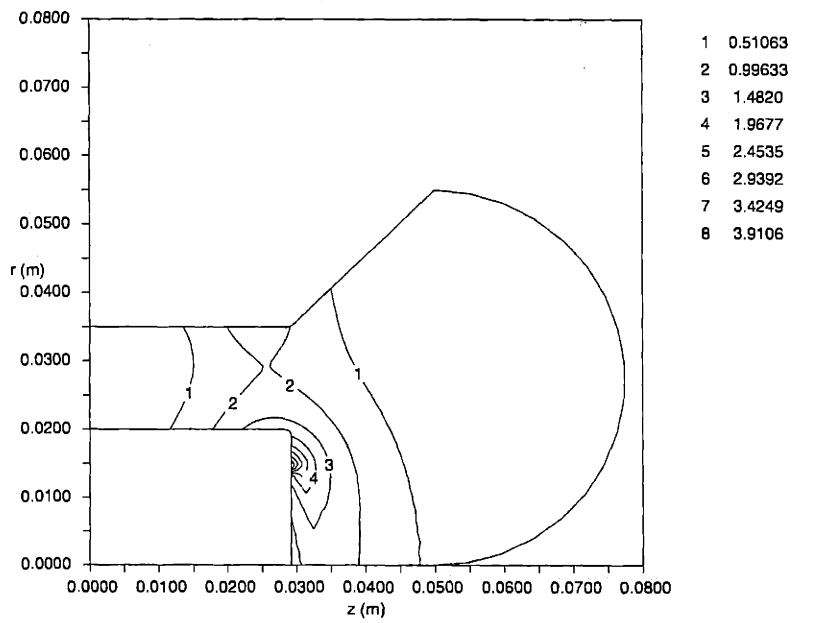

Figure 5-27: Normalized magnitude of the magnetic field, B $[T]$, computed for the SPT-70 geometry.

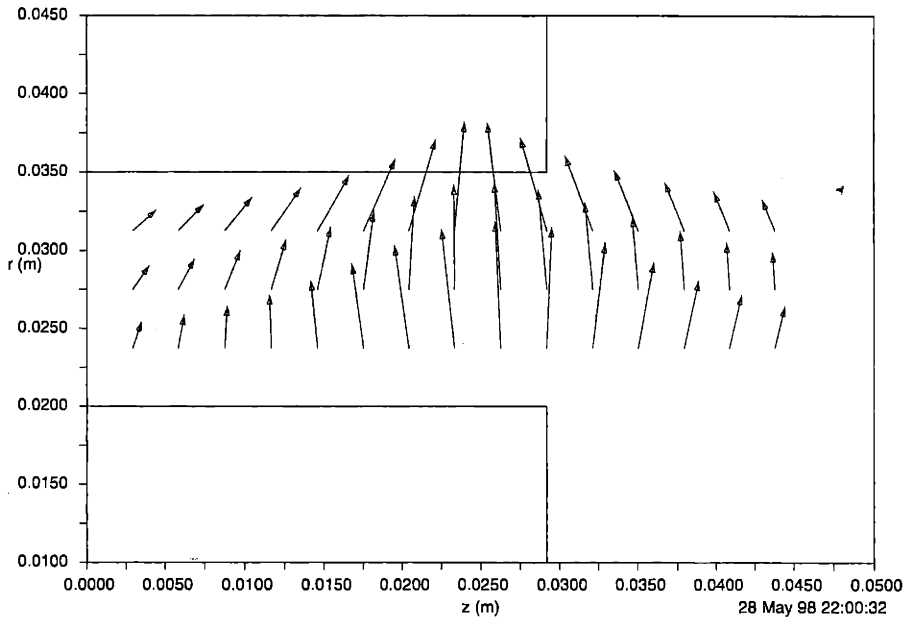

Figure 5-28: Vector plot of the magnetic field, B $[T]$, computed for the SPT-70 geometry.

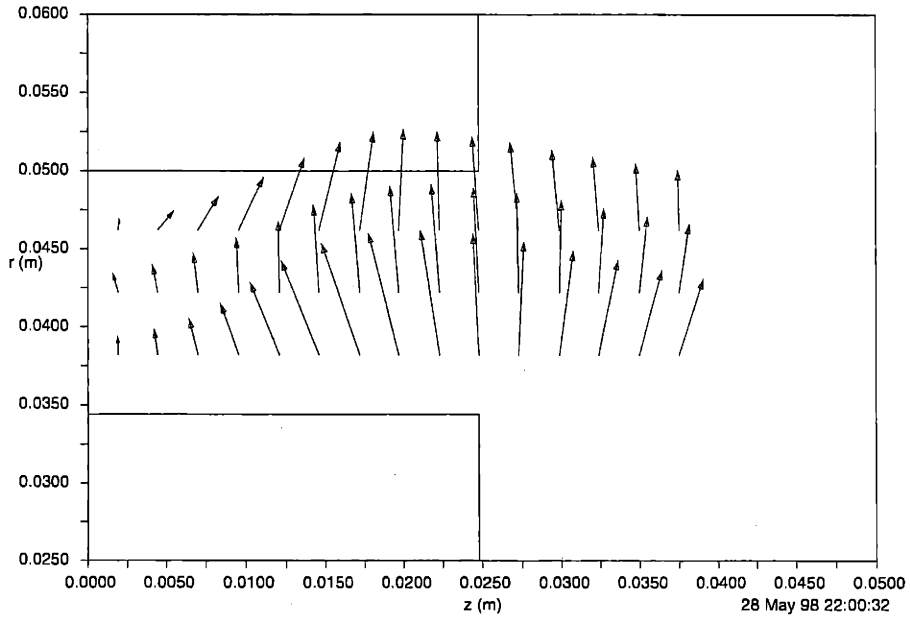

Figure 5-29: Vector plot of the magnetic field, B $[T]$, measured in the channel of an SPT-100.

5.2.2 Two-Dimensional Plasma Parameters

	CASE 1	CASE 2
propellant	xenon	xenon
$\dot{m}$	$2.34 mg/s$	$2.34 mg/s$
V_d	$300\ V$	$300\ V$
K_B	0.15	0.15
$T_{e,bp}$	$23\ eV$	$23\ eV$
P_b	0	0
cathode position	$z = 3\ cm$ downstream	$z = 5\ mm$ downstream
wall interaction	anode to exit: insulator exit to cathode: metallic	insulator

Table 5.1: Inputs to the numerical simulation, CASE 1 and CASE 2.

The simulation was executed for several cases, the first of which had operating parameters at the nominal settings shown in Table 5.1. Boundary conditions at the cathode were taken directly from the experimental measurements 3 cm downstream of the channel exit. The breakpoint temperature, $T_{e,bp}$, above which wall losses dominate, was set by adjusting the secondary electron emission function described in Section 2.4.11. After convergence, the data were saved and used as a starting conditon for a second run of 250 μs. The results from the second run were averaged over that time period and are shown in Figures 5-30 through 5-35.

The results from CASE 1 show almost all acceleration taking place outside the acceleration zone. This is inconsistent with the electrostatic probe data, which shows the plasma potential in the plume reaching a value of only about 30 V. Therefore, a second case (CASE 2) was run, with the effective cathode moved inward to the metal-insulator transition surface, 5 mm downstream from the channel exit. Boundary conditions there were taken, again, from the experimental results. Downstream of the effective cathode, the electrons are isothermal along lines of force, with T_e and ϕ^* decreasing linearly to zero across them. Figures 5-36 through 5-41 show the time-averaged solution for CASE 2.

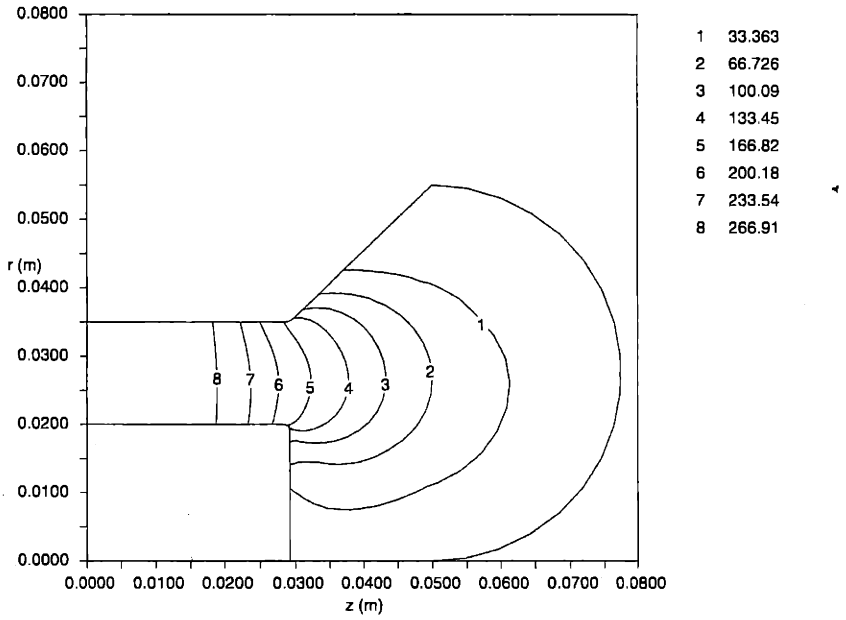

Figure 5-30: Plasma potential, V_p $[V]$, from numerical computation CASE 1.

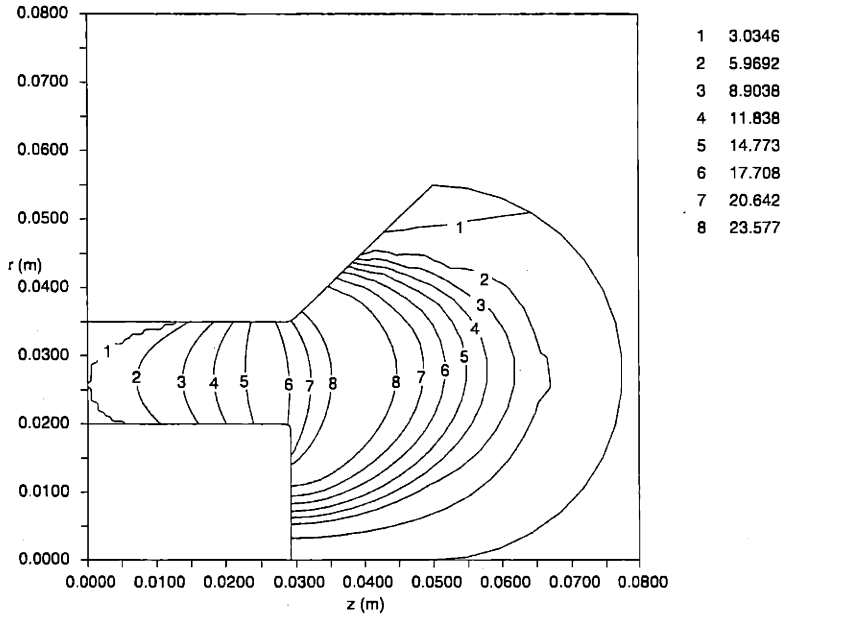

Figure 5-31: Electron Temperature, T_e $[eV]$, from numerical computation CASE 1.

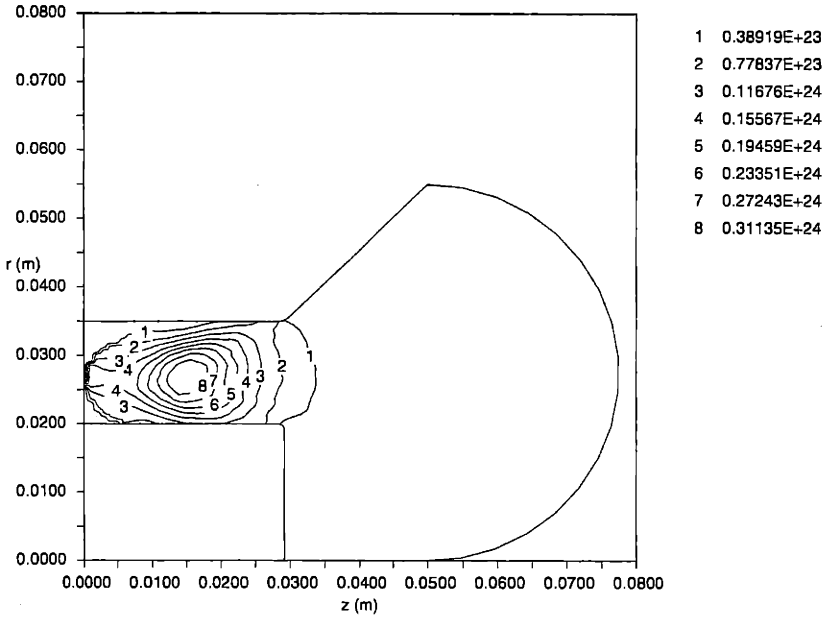

Figure 5-32: Bulk ionization rate, ni_i $[m^{-3}s^{-1}]$, from numerical computation CASE 1.

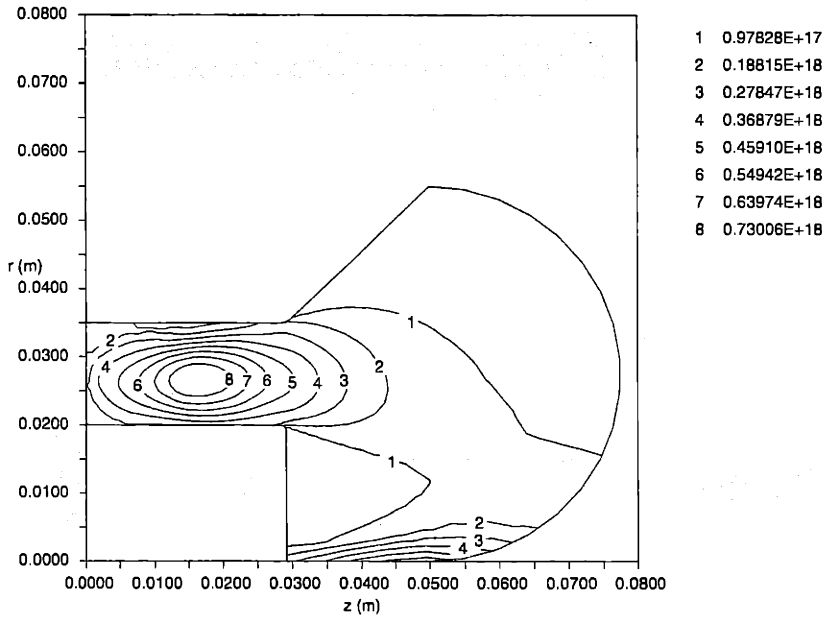

Figure 5-33: Plasma density, n_e $[m^{-3}]$, from numerical computation CASE 1.

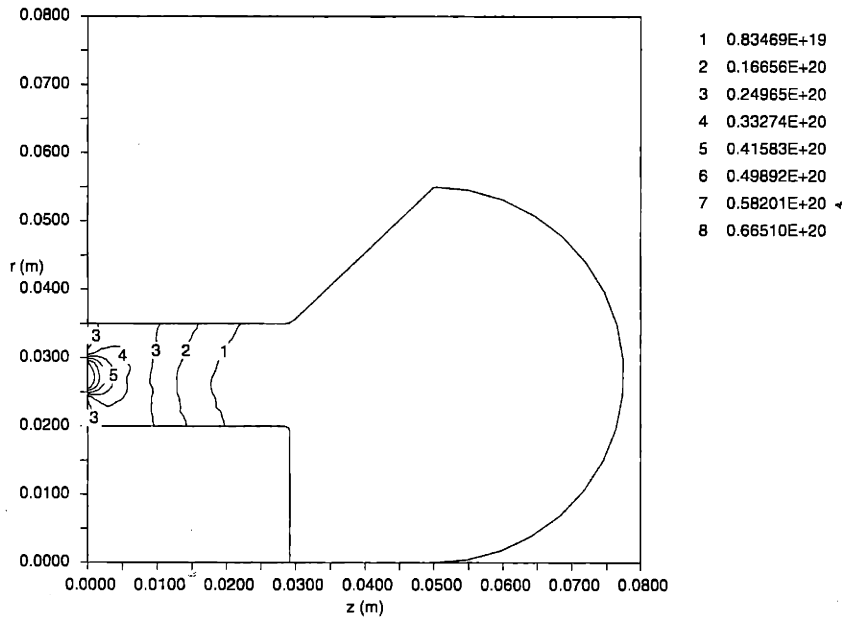

Figure 5-34: Neutral atom density, n_e $[m^{-3}]$, from numerical computation CASE 1.

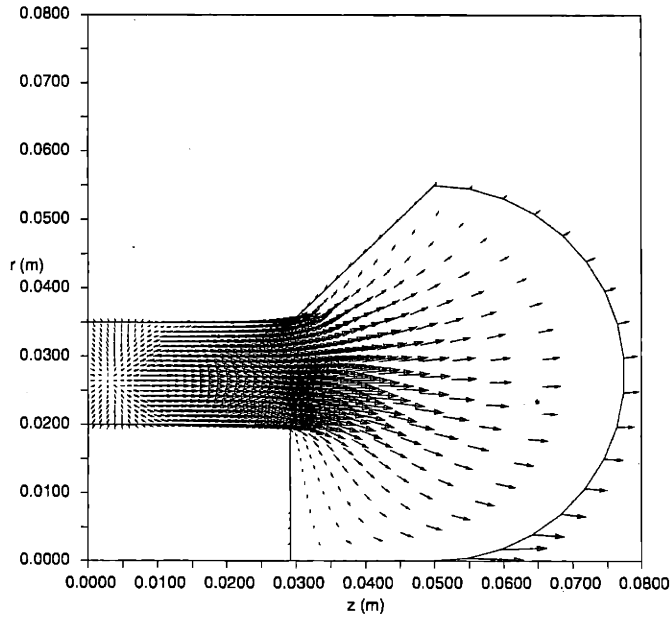

Figure 5-35: Ion current density, $\vec{j_i}$ $[A/m^2]$, from numerical computation CASE 1. The reference vector marked "*" is 237 A/m^2.

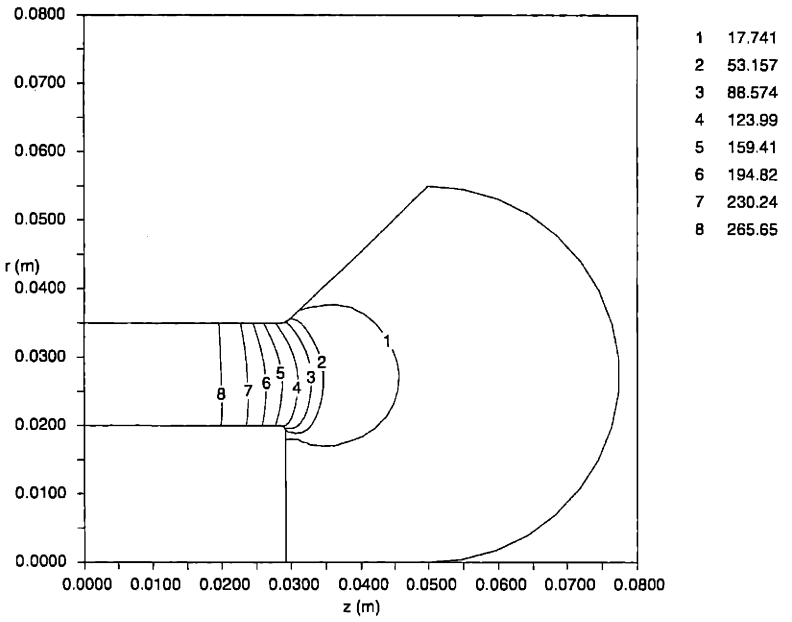

Figure 5-36: Plasma potential, V_p $[V]$, from numerical computation CASE 2.

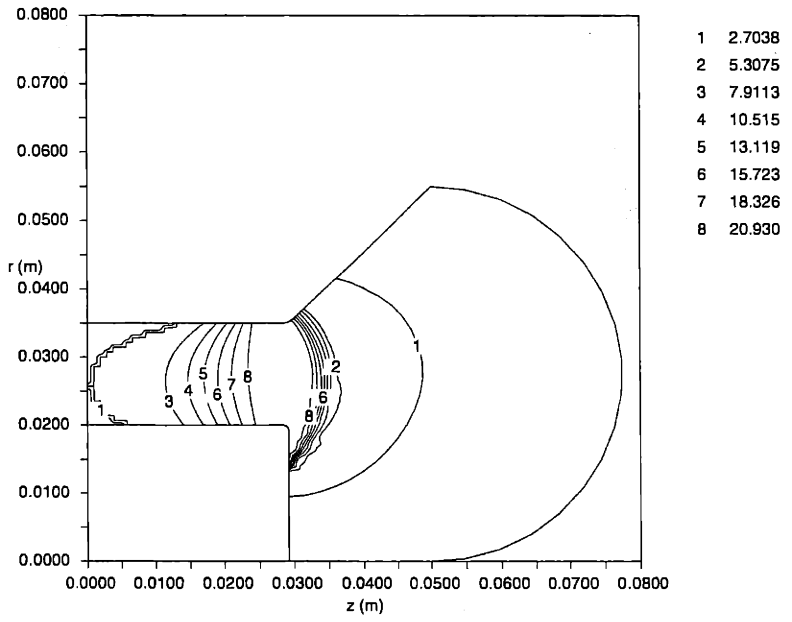

Figure 5-37: Electron Temperature, T_e $[eV]$, from numerical computation CASE 2.

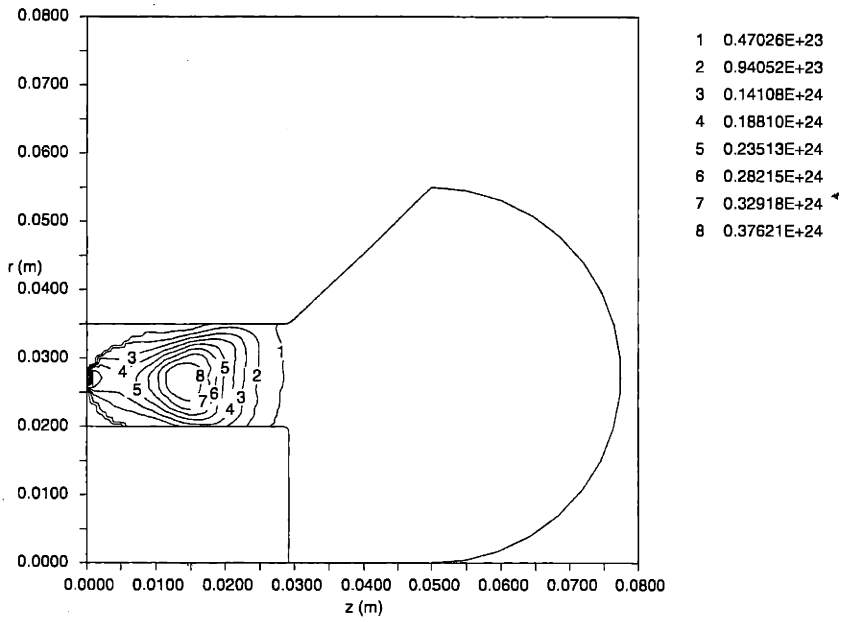

Figure 5-38: Bulk ionization rate, $\dot{n}_i$ $[m^{-3}s^{-1}]$, from numerical computation CASE 2.

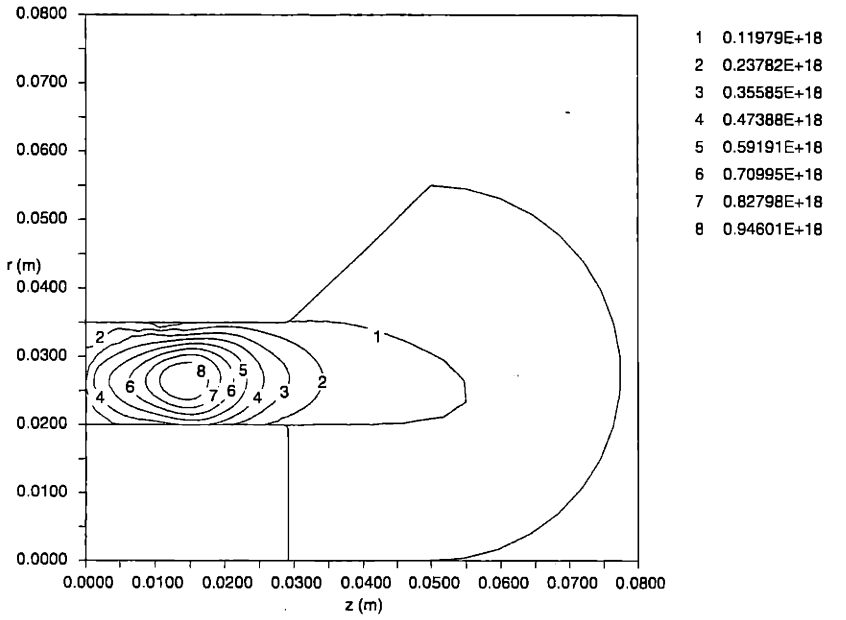

Figure 5-39: Plasma density, n_e $[m^{-3}]$, from numerical computation CASE 2.

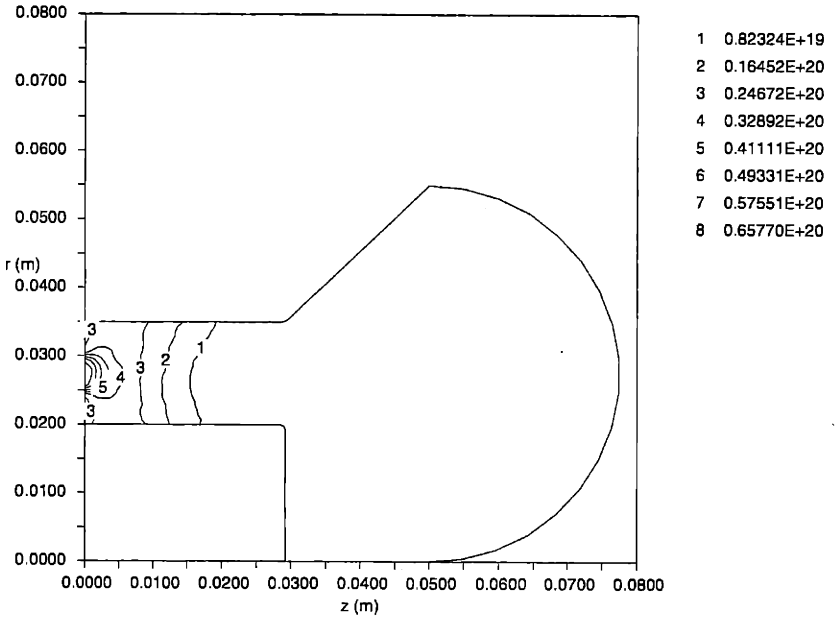

Figure 5-40: Neutral atom density, n_e $[m^{-3}]$, from numerical computation CASE 2.

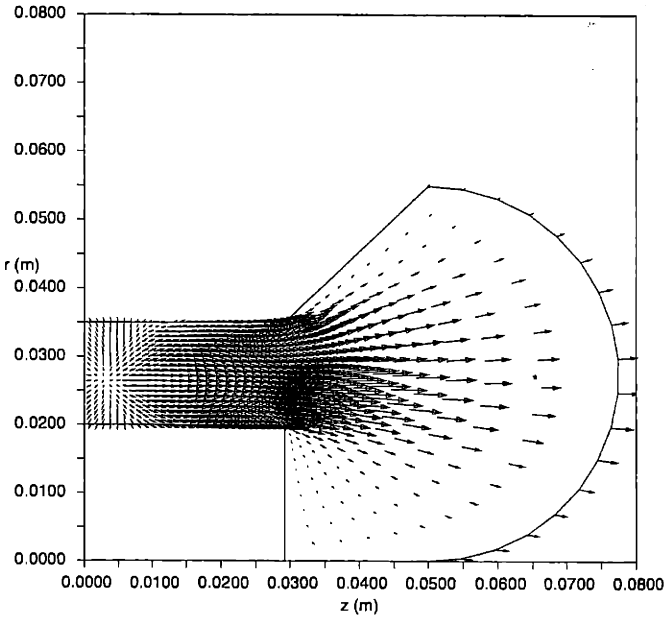

Figure 5-41: Ion current density, $\vec{j_i}$ $[A/m^2]$, from numerical computation CASE 2. The reference vector marked "*" is 303 A/m^2.

	Experimental	CASE 1	CASE 2
I_a $[A]$	2.23	1.98	2.47
$\dot{m}_i$ $[A_{eq}]$	1.61	1.57	1.57
I_{sp} $[s]$	1644	1489	1803
F $[mN]$	37.8	34.2	41.4
η_u	.936	.913	.913
η_a	.720	.793	.636
η_e	.677	.581	.852
η	.456	.421	.494
I_{wall} $[A]$	$\sim .5$	.303	.385
ξ_s $[\times 10^{-9}\ m/s]$	7.0	4.6	3.6
$Torque/(F \cdot r_{mean})$	.02	.0216	.0200

Table 5.2: Performance results from the numerical simulation, CASE 1 and CASE 2, not including cathode power or propellant supplied to the cathode.

5.2.3 Performance

Electric thruster performance is based primarily on two figures: specific impulse, I_{sp}, and thrust efficiency, η. I_{sp} is simply the thrust per propellant consumption rate, normalized by the gravitational constant to put it in universal units of seconds: $I_{sp} = F/\dot{m}g$. Thrust efficiency, η, is given as,

$$\eta = \frac{F^2}{2\dot{m}I_a V_d}, \tag{5.13}$$

where I_a is the discharge current, and V_d is the discharge potential. The overall efficiency can be broken down into three components [44],

$$\eta = \eta_u \eta_a \eta_e, \tag{5.14}$$

where η_u is the propellant utilization efficiency, η_a is the acceleration efficiency, and η_e is the beam energy efficiency. These are given by,

$$\eta_u = \frac{\dot{m}_i}{\dot{m}}, \tag{5.15}$$

$$\eta_a = \frac{e\dot{m}_i}{mI_a}, \tag{5.16}$$

$$\eta_e = \frac{V_b}{V_d}, \tag{5.17}$$

where $\dot{m}_i$ is the ion beam mass flow rate, and V_b is the mean axial beam energy in $Volts$.

Table 5.2 shows a comparison between measured and simulated performance corresponing to nominal operating conditions ($\dot{m} = 2.34\ mg/s$, $V_d = 300\ V$). For the experimental column, $\dot{m}_i$ was set to 1.61 A_{eq}, based on the triple probe measurements and $f^{++} = .04$. None of the efficiency numbers shown include power or propellant supplied to the cathode.

The simulation values in Table 5.2 were averaged over 250 μs. The beam flow rate, $\dot{m}_i$, was computed by summation of the total mass of ionized particles exiting the simulation grid. Their velocities were also saved and averaged to get V_b. Thrust was then computed as $\dot{m}_i\sqrt{2eV_b/m}$. The torque on the device can be written as the sum of the azimuthal moments on the ions in each grid cell as,

$$T = \sum 2\pi r^2 A_{cell} e n_i \vec{u}_i \times \vec{B}. \tag{5.18}$$

It is shown in Table 5.2 nonimensionalized by dividing by the thrust and the mean radius. For the SPT-100, this value is reported to be around .02 [49]. Using the $B \sim \frac{1}{l}$ scaling, the SPT-70 should have a similar thrust ratio. Back of the envelope calculations, using $B = .01\ T$ for 5 cm, give .02, as measured.

The discrepancy between simulated and measured performance is small for both cases. In CASE 1, acceleration happens outside the channel, where the lines of force are highly curved, producing beam divergence. This shows up as low beam energy efficiency, η_e. In CASE 2, the acceleration happens across lines of force which are more radially straight, producing a beam with better collimation and increasing η_e.

Performance was also computed for a range of operating conditions. Figures 5-42 and 5-43 show the variation in thrust efficiency and specific impulse. These may be compared with the measured values (Figures 5-22 and 5-23). Agreement is fairly good for both η and I_{sp}, although the simulated I_{sp} is slightly higher. The drop in simulated efficiency with voltage is primarily due to a reduction in propellant utilization fraction from incomplete ionization.

5.2.4 Ion Wall Impingement

From the numerical simulation, average wall impingement current is calculated to be around .35 A. According to Bishaev and Kim [9], ion loss to the walls is approximately 1.0 A for SPT-100-class devices. Scaling based on area, the expected wall current for the SPT-70 is

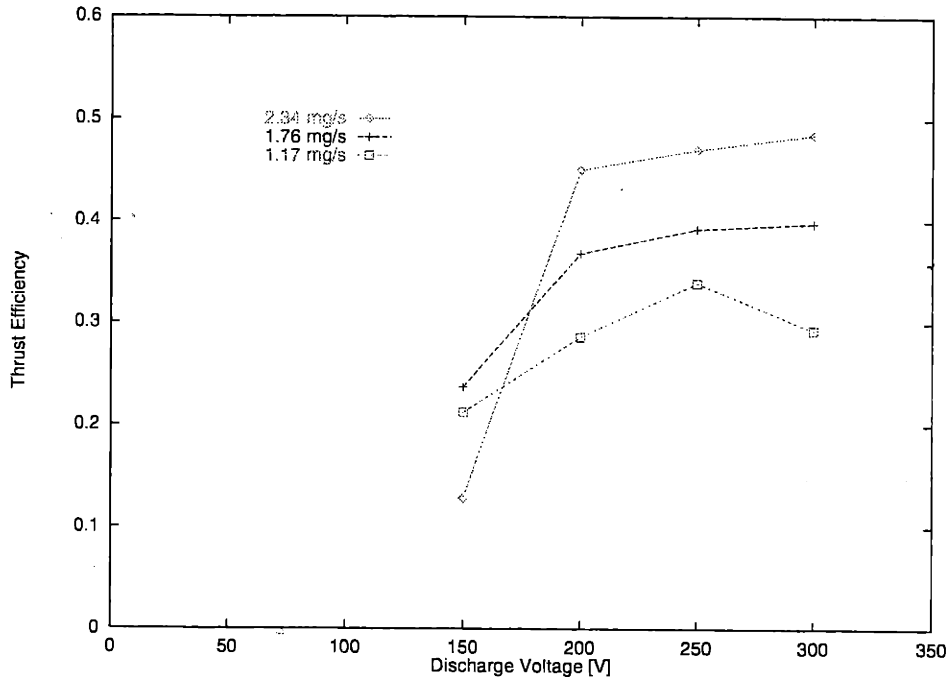

Figure 5-42: Computed thrust efficiency, η, at various operation conditions with $K_B = 0.15$, cathode 5 mm downstream of the channel.

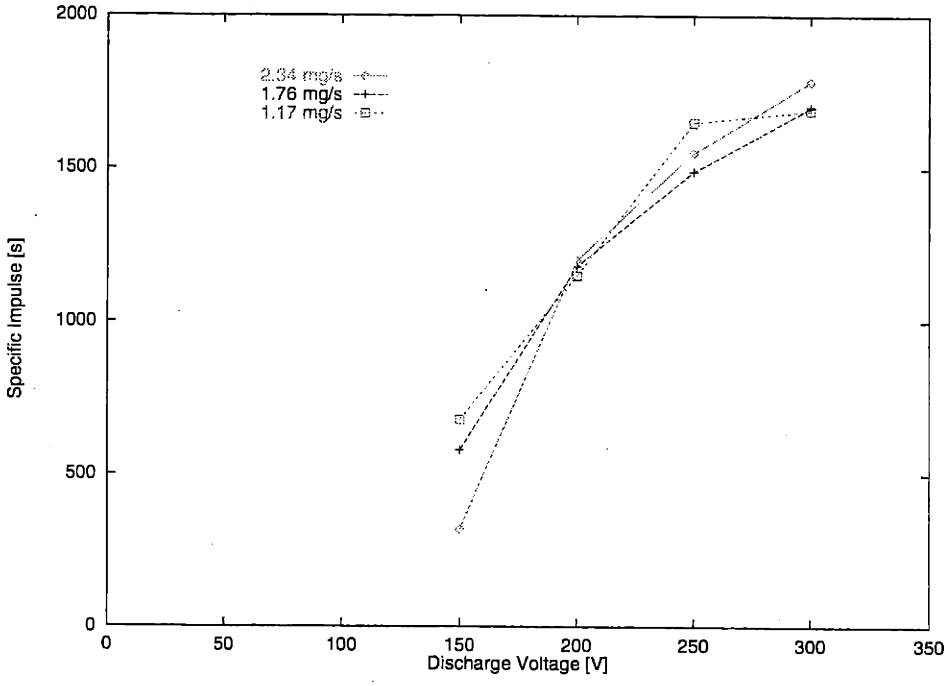

Figure 5-43: Computed specific impulse, I_{sp} [s] at various operation conditions with $K_B = 0.15$, cathode 5 mm downstream of the channel.

.5 A.

The SPT insulator wall is known to sputter most near the acceleration zone exit [32] where both the ion current density and mean ion energies are high. At the exit of the acceleration channel, the ion current density is 45 A/m^2 normal to the inner wall for CASE 2. A comparison of wall sputtering rate can be made by using the relation,

$$\xi_s = j_{i,w} S_v, \tag{5.19}$$

where ξ_s is the wall reduction rate in m/s, $j_{i,w}$ is the normal component of the ion current density, and S_v is the volumetric sputtering coefficient. Abgaryan et. al. [2] measured the sputtering properties of borosil, the dielectric wall material used in SPTs. They found that $S_v \approx .08\ (mm)^3/C$ for ion energies of 33 eV at an 80 degree angle of incidence. Using CASE 2, this gives us,

$$\xi_s \approx 3.6 \times 10^{-9} m/s. \tag{5.20}$$

At the inner insulator wall, the initial sputtering rate is 7×10^{-9} m/s from experiments by Garner et. al. [32]. Our estimate is half that, but the mean ion energy we compute there is much higher than 33 eV, around 100 eV.

5.2.5 Ion Distribution of Energies

Figure 5-44 and 5-45 shows a bivariate distribution of ions accumulated as they leave the simulation grid for CASE 1 and CASE 2. They have been sorted by energy and angle of off-axis travel. The distribution was divided by the solid angle ($2\pi sin(\theta)$) so that the relative magnitudes would be comparable to those measured by a device with constant area, such as a retarding potential analyzer (RPA) in the far field. Re-multiplying by the solid angle and integrating over the entire energy and angle domain gives the total ion current in A_{eq}. The bulk of the ions are ejected within 30 deg of axial at energies of around 285 V. There are some low-energy ions which are produced in the plume downstream of the acceleration zone. A population of double ions can also be seen at around 550 eV.

In CASE 1, substantial beam divergence can be seen, contributing to lower axial thrust. Much of this is belived to be due to acceleration taking place outside the channel, where the lines of force are curved. Also noticeable in CASE 1 is widening of the distribution, with a considerable number of ions escaping with energies greater than V_d. This is an

effect of discharge oscillations, and will be discussed in the next chapter. Absalamov [3] used an energy analyzer and electrostatic probe to map the ion beam flux emitted from an SPT-100. His results agree quite well with CASE 2, but show a distribution with slightly more widening at higher energies, and with a peak around 270 V. In addition, he detects a distinctive peak at around 20 eV, which may be due to charge exchange (not modeled in this simulation).

5.2.6 Doubly-Charged Ions

Figure 5-46 shows the distribution of double ions by total energy for CASE 2. By integrating the distribution over all energies, the total rate of emission of doubly charged ions may be computed. For this case, $\dot{m}_i^{++} = .0618\ A_{eq}$, giving the fraction $f^{++} = .039$.

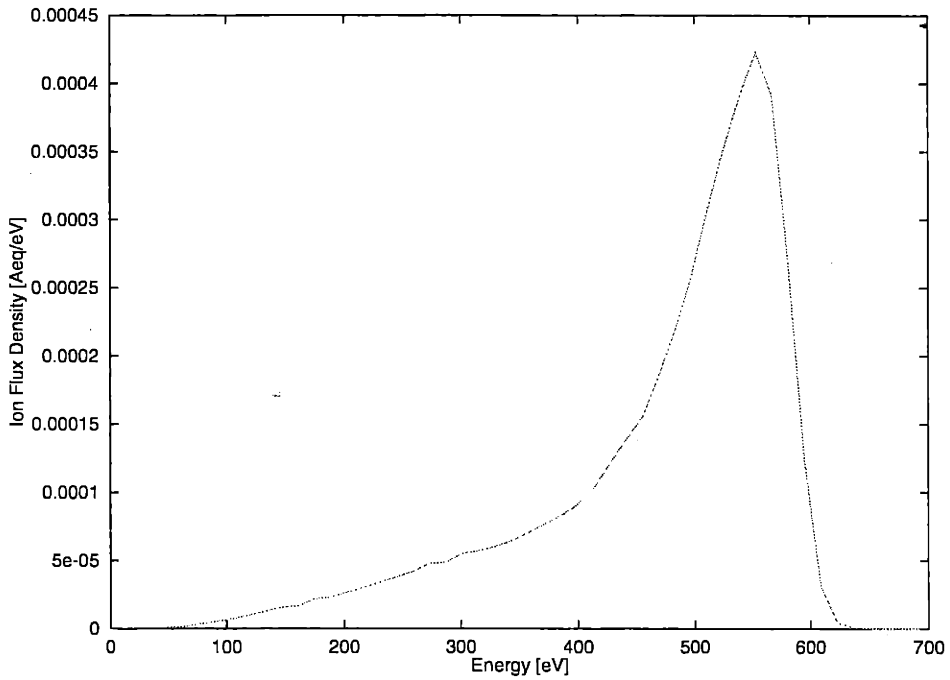

Figure 5-46: Ion distribution of energies $[A_{eq}/eV/deg]$, CASE 2.

The low-energy double ions were created at lower potentials and, therefore, did not gain as much energy by the time they reached end of the grid. By plotting the bulk ionization rates for the processes (Figures 5-47 and 5-48), it is possible to observe the origins of the double ions. Integrating over the computational volume, we find rates of creation of double ions from neutrals and single ions to be .0418 and .0237 A, respectively. The excess generated over emitted, 5.6%, are lost to the wall.

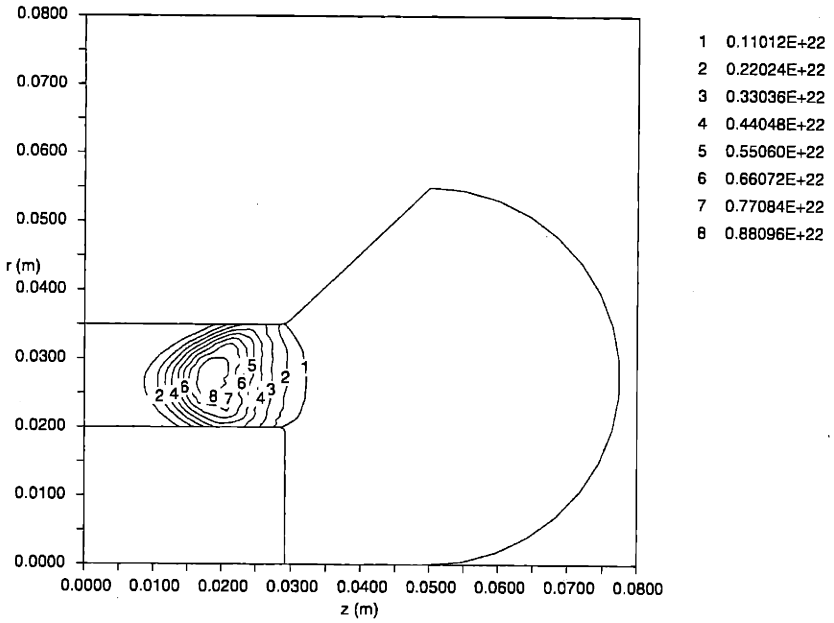

Figure 5-47: Bulk ionization rate, $\dot{n_i}^{++}$ $[m^{-3}s^{-1}]$, by the process $Xe \rightarrow Xe^{++}$, from numerical computation CASE 2.

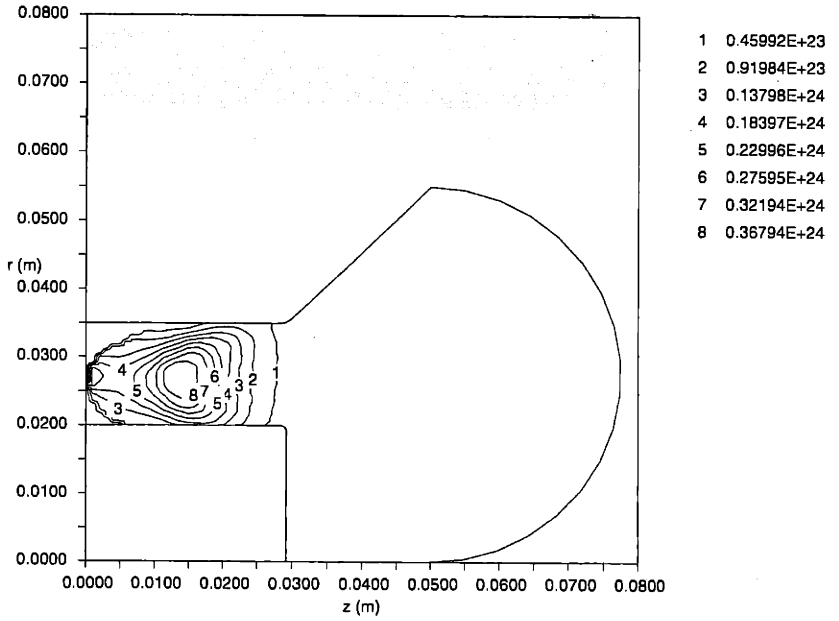

Figure 5-48: Bulk ionization rate, $\dot{n_i}^{++}$ $[m^{-3}s^{-1}]$, by the process $Xe^{+} \rightarrow Xe^{++}$, from numerical computation CASE 2.

	Experimental	CASE 2	CASE 3	CASE 4
P_c $[Torr]$	1×10^{-5}	0	1×10^{-5}	2×10^{-4}
I_a $[A]$	2.23	2.47	2.51	2.67
$\dot{m}_i$ $[A_{eq}]$	1.61	1.57	1.60	1.83
I_{sp} $[s]$	1644	1803	1830	2003
F $[mN]$	37.8	41.4	42.0	46.0
η_u	.936	.913	.930	1.06
η_a	.720	.636	.637	.685
η_e	.677	.852	.844	.774
η	.456	.494	.500	.564
I_{wall} $[A]$	~ 0.5	0.303	.393	.485
ξ_s $[\times 10^{-9}\ m/s]$	7.0	3.6	3.6	3.3
$Torque/(F \cdot r_{mean})$	.02	.0200	.0196	.0194

Table 5.3: Performance results from the numerical simulation, varying P_b.

5.2.7 Computed Efficiency Variation with Background Pressure

Typical background chamber pressures of $P_b = 5 \times 10^{-5}\ Torr$ correspond to atom number densities of $1.6 \times 10^{18}\ m^{-3}$ at ambient temperatures. This is approximately on the order of the atom density in parts of the acceleration channel, according to computations. It is natural to believe, then, that P_b may have an effect on thruster performance. To examine this possibility, numerical experiments were performed to examine the effect of various background pressures on the operation of the SPT-70.

Three cases were run:

$$\begin{aligned} &\text{CASE 2} \quad P_b = 0\ Torr \\ &\text{CASE 3} \quad P_b = 1 \times 10^{-5}\ Torr \\ &\text{CASE 4} \quad P_b = 2 \times 10^{-4}\ Torr \end{aligned}$$

Each case has operatational parameters set identical to CASE 2 (Table 5.1), except for the variation in P_b. CASE 2 was chosen as the background pressure in experiments presented here, and CASE 3 has the background pressure in experiments by Bishaev and Kim [9].

Table 5.3 shows the performance values for CASE 2, 3 and 4 compared to experiment. Background pressure has the effect of increasing measured efficiency. This is because neutrals from the background are ingested into the thruster channel, where they are used as propellant. In fact, when background pressure is high enough, the calculated utilization efficiency exceeds unity, as in CASE 4. A model for the increase in efficiency with background

pressure may be expressed as,

$$\eta_u' = \frac{\dot{m}_i + C_b m_i \frac{n\bar{c}}{4} A}{\dot{m}}, \tag{5.21}$$

or,

$$\eta_u' = \eta_u + \frac{C_b m_i \frac{n\bar{c}}{4} A}{\dot{m}}, \tag{5.22}$$

where η_u' represents efficiency measured in a chamber at P_b, and A is the annular area of the acceleration channel. For the data of CASE 2 and CASE 4, we find $C_b \approx 1.72$. This is peculiar, since it implies that a number greater than $\frac{n\bar{c}}{4} A$ from the background are being ionized. One possibility is that some are ionized outside the channel. This would be reflected by η'/η being less than η_u'/η_u, since the ions created outside the channel would not contribute much to thrust. For this case, $\eta'/\eta = 1.105$ and $\eta_u'/\eta_u = 1.16$, which suggests that, some of the background ions are formed outside the channel. Another possibility for $C_b > 1$ is that the ionization of background neutrals increases plasma density near the exit, and promotes further ionization of escaping fed propellant. This hypothesis is difficult to check with the data available, however.

It is also interesting to note that the number of ions neutralized at the walls increases with background pressure. These additional ions are created outside the thruster and impact the metallic face. Such additional ion flux may have the detrimental effect of increasing the loss rate of electrons to the metallic wall outside the channel by increasing the local density there.

Chapter 6

Transient Results

This chapter focuses on oscillatory components of the SPT-70 plasma plasma parameters. Both experimental and numerical data are presented.

6.1 Experiment

Several trials were executed with the AC experimental apparatus described in Sections 4.4.3 and 4.4.2. The spectrum of AC oscillations of floating potential at a single point is examined for various operating conditions. Two-dimensional $(z-r)$ surveys were performed at two operating conditions.

All z-coordinates shown in experimental data are with respect to the exit of the acceleration channel. All r-coordinates are with respect to the centerline.

One notable observation is that the discharge current oscillation spectra have changed with total thruster operating time. Therefore, results will be distinguished by the approximate time from Beginning Of Life (BOL) at which the raw measurements were taken.

6.1.1 Power Spectral Density

Time histories of discharge current, I_a, and floating potential, V_f, in the plume were measured. The power spectral densities (PSDs) were then computed numerically via fast Fourier transform (FFT). Several cases of particular interest will given here. The complete set of PSDs computed for a variety of operating conditions is given in Appendix A.

Early in the thruster lifetime, measurements of discharge current showed abrupt switching between quiet and oscillatory modes near the nominal flow condition, as shown in

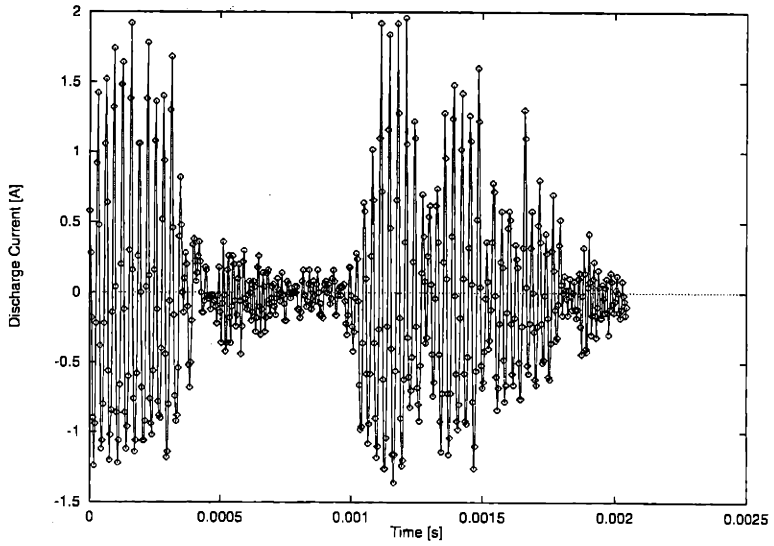

Figure 6-1: AC component of discharge current, I_a, $[A]$, $\dot{m} = 2.34\ mg/s$, $V_d = 330\ V$, 20 hrs from BOL.

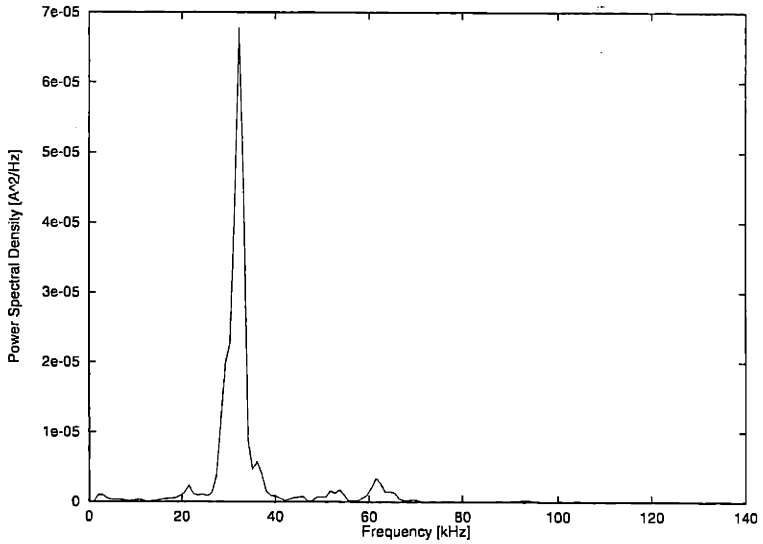

Figure 6-2: Power spectral density $[A^2/Hz]$ of I_a, $\dot{m} = 2.34\ mg/s$, $V_d = 330\ V$, 20 hrs from BOL.

Figure 6-1. (Note that early AC measurements were performed at the slow rate of $250kHz$, but later ones were done at $2.5MHz$.) Figure 6-2 shows the power spectral density (PSD) for that data set. The values are A^2/Hz, normalized such that integrating the PSD over the frequency domain gives the mean square amplitude of the signal:

$$\int_0^\infty S_{II}(f)df = \frac{1}{T}\int_0^T I_a(t)^2 dt, \tag{6.1}$$

where S_{II} is the PSD shown in the figures. A strong mode at 32 kHz is most obvious, as seen in Figure 6-2. RMS amplitude around that frequency is approximately .022 A. Also, a harmonic at 64 kHz is slightly discernable. This is believed to be due to a non-sinusoidal signal shape.

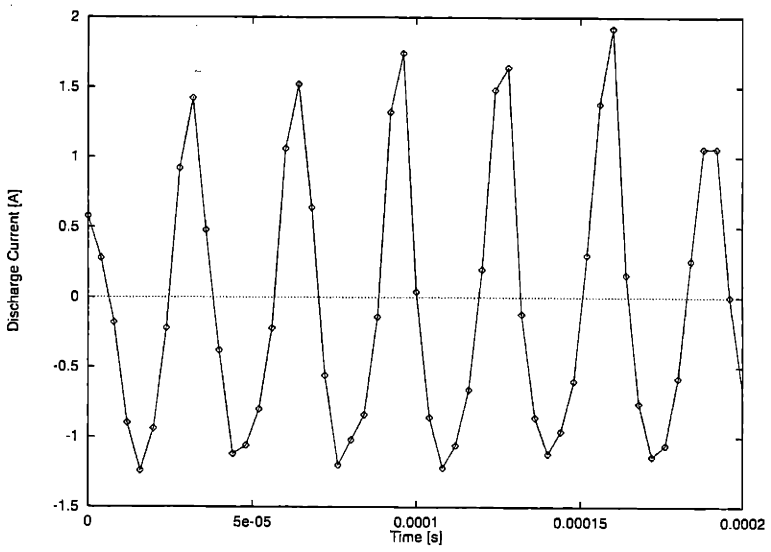

Figure 6-3: AC component of discharge current, I_a, $[A]$, $\dot{m} = 2.34\ mg/s$, $V_d = 330\ V$, 20 hrs from BOL.

Figure 6-3 shows a magnification of the high-amplitude 32 kHz mode. It is distinguished from a sinusoid by its sharp peaks and rounded valleys. Such a signal may be constructed using two superimposed harmonics, as shown in Figures 6-4 and 6-5. The phase difference between the first and second harmonics in the data are found to be approximately zero. Therefore, it is believed that either two harmonic frequencies are present and synchronized, or the nature of a single oscillation produces the distinct curve shown in Figure 6-3.

Figure 6-6 shows the PSD of the AC component of the discharge current 80 hrs from

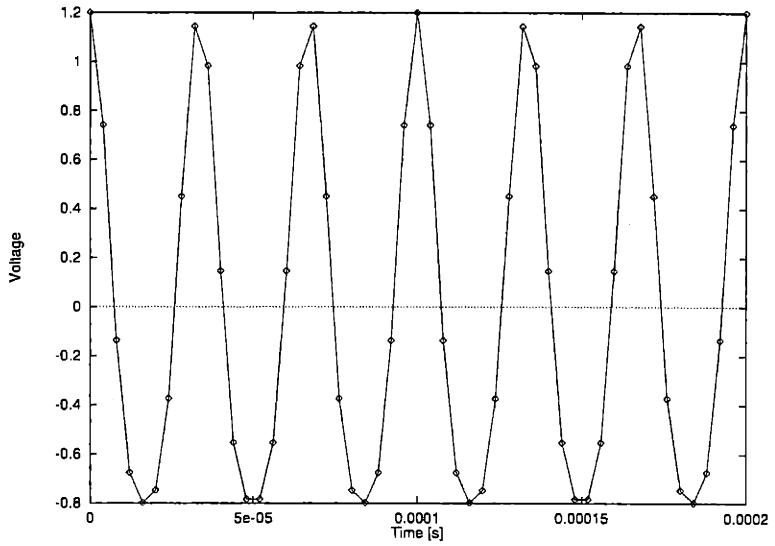

Figure 6-4: Test signal: $cos(\omega t) + .2cos(2\omega t)$ $[V]$, $\omega = 30\ kHz$.

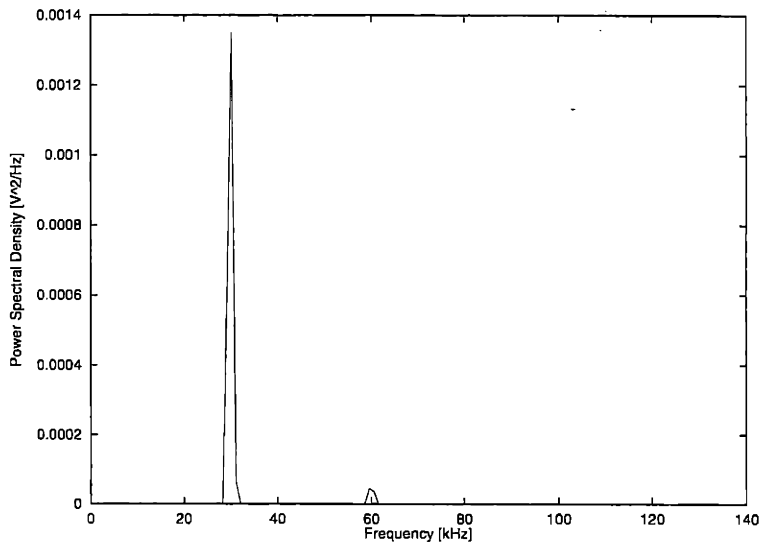

Figure 6-5: Power spectral density of test signal $cos(\omega t) + .2cos(2\omega t)$ $[V^2/Hz]$, $\omega = 30\ kHz$.

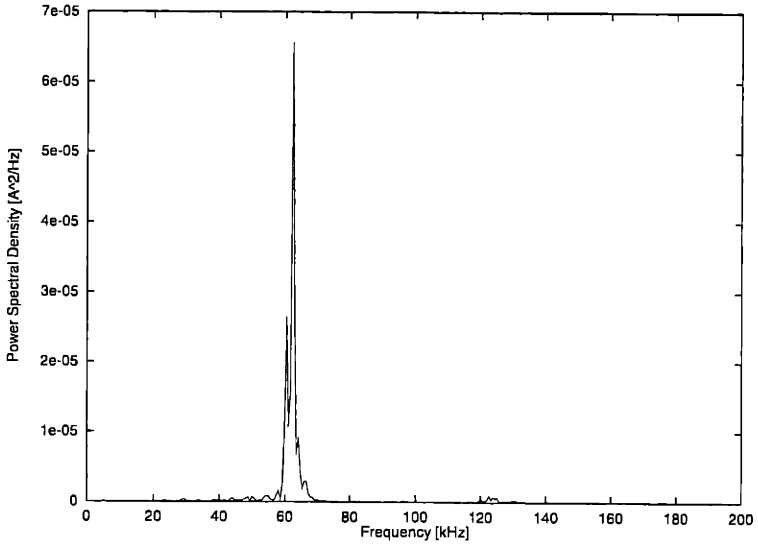

Figure 6-6: Power spectral density $[A^2/Hz]$ of I_a, $\dot{m} = 2.34\ mg/s$, $V_d = 300\ V$, 80 hrs from BOL.

BOL at nominal conditions. Clearly, a single high-amplitude mode exists at $f_n = 60\ kHz$ with no observable harmonics. In addition, the signal is closely sinusoidal, with no activity at $3f_n$, and only a weak component at $2f_n$. Signal power between 58 and 68 kHz comprises most of the total mean square amplitude of the signal (.13 A^2). The RMS amplitude is therefore .36 A, or 16% of the mean DC value. This mode is much stronger than at 20 hrs from BOL, where it was only 1% of the DC value.

As noted, the thruster was approximately 80 hrs from BOL at the time the data in Figure 6-6 were measured. At earlier times, the dominant frequency was lower, and the oscillation was smaller in magnitude, and less stable in time. Figure 6-7 shows the PSD for discharge current measured for the same thruster at approximately 40 hrs from BOL. The facility background pressure differed slightly for the cases: $6.8 \times 10^-6\ Torr$ at 40 hrs and $8.7 \times 10^-6\ Torr$ at 80 hrs. The RMS amplitudes at 40 and 80 hrs were approximately .1 and .4 A, respectively. At 40 hrs, the oscillations were spread in a band between 50 and 60 kHz, while at 80 hrs, the frequencies were confined to a narrow region around 61 kHz.

Figure 6-8 shows the PSD for a lower-power operating condition. This case was selected because of the pronounced 28 kHz mode. Again, no harmonics are visible and the dominant signal component is sinusoidal. This mode existed at 40 hrs at approximately the same frequency.

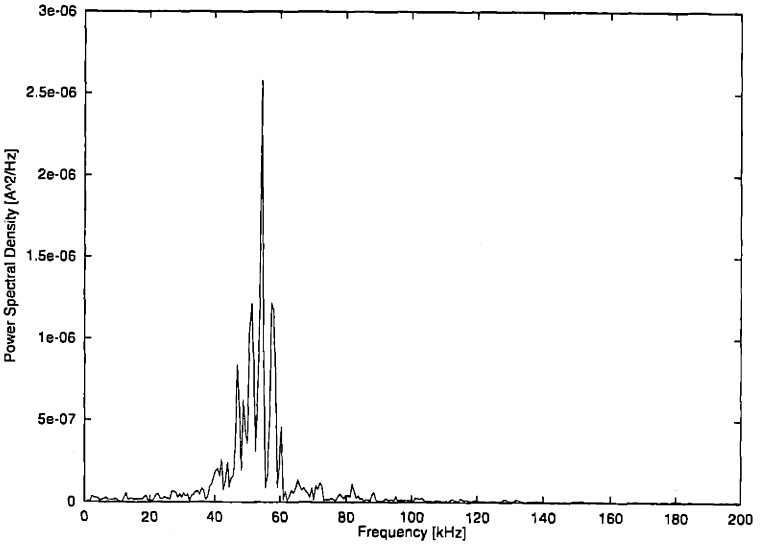

Figure 6-7: Power spectral density $[A^2/Hz]$ of I_a, $\dot{m} = 2.34\ mg/s$, $V_d = 300\ V$, 40 hrs from BOL.

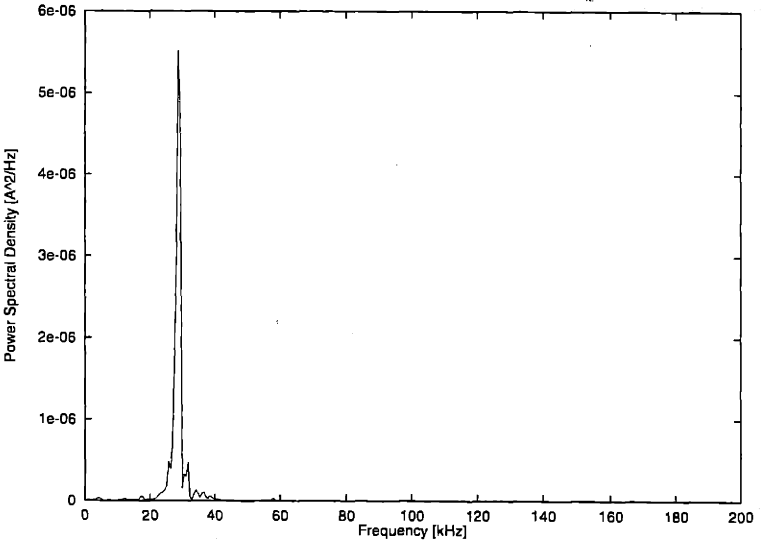

Figure 6-8: Power spectral density $[A^2/Hz]$ of I_a, $\dot{m} = 1.17\ mg/s$, $V_d = 200\ V$, 80 hrs from BOL.

	$1.17 mg/s$	$1.76\ mg/s$	$2.34\ mg/s$	$2.93\ mg/s$
$100V$	extenguished	f_n=6.10kHz, P_n=1.3·10$^{-4}A^2/Hz$ P_t=.41A	f_n=4.88kHz, P_n=2.2·10$^{-5}A^2/Hz$ P_t=.33A	f_n=5.48kHz, P_n=2.1·10$^{-5}A^2/Hz$ P_t=.45A
$150V$	extenguished	f_n=13.4kHz, P_n=3.1·10$^{-6}A^2/Hz$ P_t=.075A	f_n=15.3kHz, P_n=6.2·10$^{-6}A^2/Hz$ P_t=.17A	f_n=11.6kHz, P_n=9.0·10$^{-6}A^2/Hz$ P_t=.21A
$200V$	f_n=28.6kHz, P_n=5.5·10$^{-6}A^2/Hz$ P_t=.12A	f_n=19.5kHz, P_n=8.1·10$^{-7}A^2/Hz$ P_t=.075A	f_n=16.5kHz, P_n=2.3·10$^{-6}A^2/Hz$ P_t=.15A	f_n=17.7kHz, P_n=2.0·10$^{-6}A^2/Hz$ P_t=.15A
$250V$	f_n=39.1kHz, P_n=2.2·10$^{-6}A^2/Hz$ P_t=.092A	f_n=100kHz, P_n=1.6·10$^{-6}A^2/Hz$ P_t=.14A	f_n=50.0kHz, P_n=3.8·10$^{-5}A^2/Hz$ P_t=.22A	f_n=43.9kHz, P_n=1.2·10$^{-4}A^2/Hz$ P_t=.37A
$300V$	f_n=46.4kHz, P_n=2.4·10$^{-7}A^2/Hz$ P_t=.019A	f_n=63.5kHz, P_n=2.9·10$^{-7}A^2/Hz$ P_t=.079A	f_n=62.3kHz, P_n=6.6·10$^{-5}A^2/Hz$ P_t=.36A	f_n=51.9kHz, P_n=3.1·10$^{-5}A^2/Hz$ P_t=.51A
$350V$	f_n=99.5kHz, P_n=2.5·10$^{-7}A^2/Hz$ P_t=.069A	f_n=46.4kHz, P_n=1.4·10$^{-7}A^2/Hz$ P_t=.055A	f_n=64.7kHz, P_n=3.7·10$^{-5}A^2/Hz$ P_t=.40A	f_n=53.1kHz, P_n=5.2·10$^{-5}A^2/Hz$ P_t=.48A

Table 6.1: Matrix summary of the AC part of I_a including the dominant mode frequency (f_n) and amplitude (P_n), and total RMS amplitude (P_t) at various propellant flow rates and voltages, 80 hrs from BOL.

The I_a PSDs were computed for a variety of operating conditions from $\dot{m} = 1.17$ to 2.93 mg/s and $V_d = 100$ to 350 V. Those data are given in complete form separately in Appendix A. Table 6.1 shows a summary of the dominant mode frequency and power density, as well as the total RMS amplitude for many operating points. No obvious trend is noticeable, except for a weak tendency for f_n to increase with V_d.

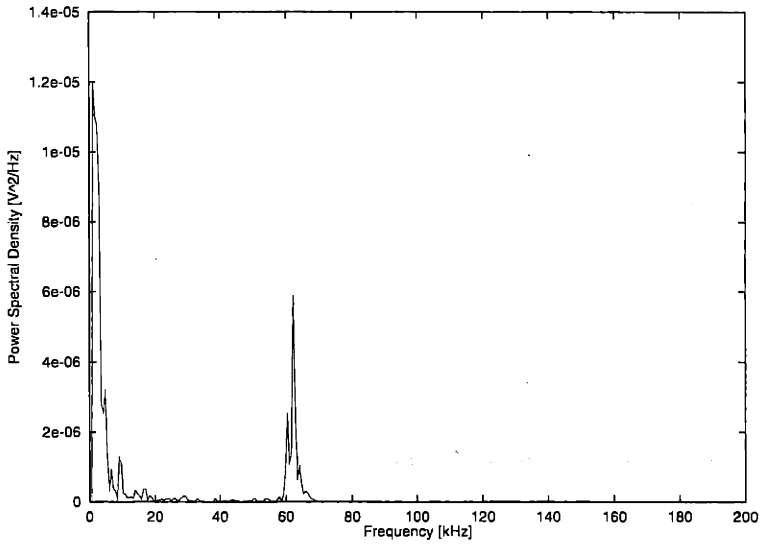

Figure 6-9: Power spectral density $[V^2/Hz]$ of V_f, $\dot{m} = 2.34$ mg/s, $V_d = 300$ V, 80 hrs from BOL.

Figure 6-9 shows the PSD of the floating potential signal measured by a single electrostatic probe positioned in front of the acceleration channel at $z = 1$ cm, $r = 2.75$ cm. The data were measured at nominal operating conditions simultaneously with the discharge current shown in Figure 6-6. Considerable power can be seen at frequencies lower than 10 kHz which does not appear in the PSD of discharge current. It is believed that these low frequency floating potential oscillations are related to interaction between the plasma and the facility. Measurements have shown that the cathode potential with respect to the chamber (GND) can fluctuate up to 20 V at low frequencies. The 62 kHz frequency matches with that of the discharge current. The peak RMS amplitude at that frequency is 122 mV. This implies very little ($\sim .001$ eV) fluctuation in electron temperature and space potential outside the channel.

6.1.2 Plume Characterization

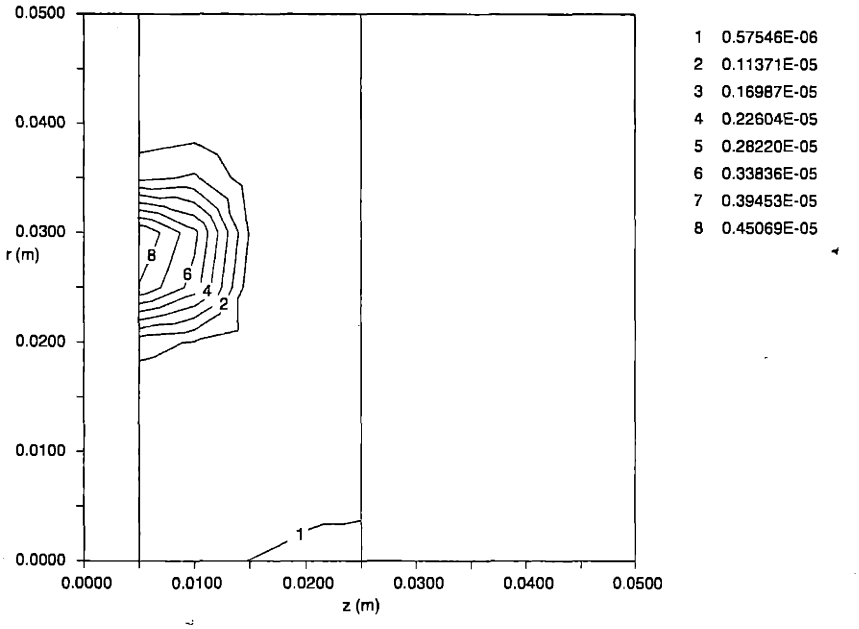

Figure 6-10: Power spectral density of V_f for the dominant mode (62.3 kHz) $[V^2/Hz]$. $\dot{m} = 2.34\ mg/s$, $V_d = 300\ V$, 80 hrs from BOL.

A two-dimensional probe scan of the plume was performed, and V_f and I_a were measured simultaneously at 2.5 $Msamples/sec$. The thruster was at 80 hrs from BOL. Figure 6-10 shows a map of the magnitude of the PSD at the dominant mode around 62 kHz. The amplitude of oscillation is highest near the exit of the channel, and increasing toward the thruster. This implies, in the case of an ionization oscillation, that the region of ionization is inside the channel.

Figures 6-11 and 6-12 show the raw data signals at a single point in the plume. A digital bandpass filter was used to eliminate high and low frequency components, and the resulting signal is shown. A correlation function was then computed as,

$$Corr(V_f, I_a) = \int_0^T V_f(t+\tau) I_a(\tau) d\tau. \tag{6.2}$$

Note that I_a and V_f represent the filtered AC components of those signals here. The resulting correlation function at $z = 1\ cm$ and $r = 2.5cm$ is shown in Figure 6-13. The phase lag, ϕ_l, between V_f and I_a was determined by applying a nonlinear curve fit of the form $A\cos(wt - \phi_l)$, parameterized in ϕ_l. This computation is performed at each point in

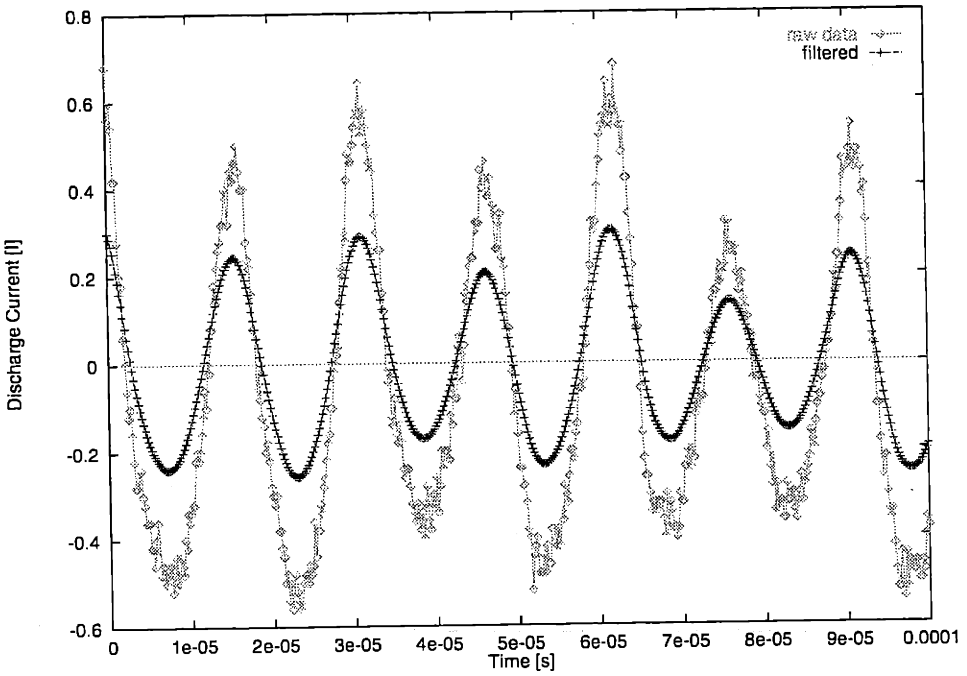

Figure 6-11: Discharge current, I_a, measured and filtered $[A]$, $\dot{m} = 2.34\ mg/s$, $V_d = 300\ V$, $z = 1\ cm$, $r = 2.5\ cm$.

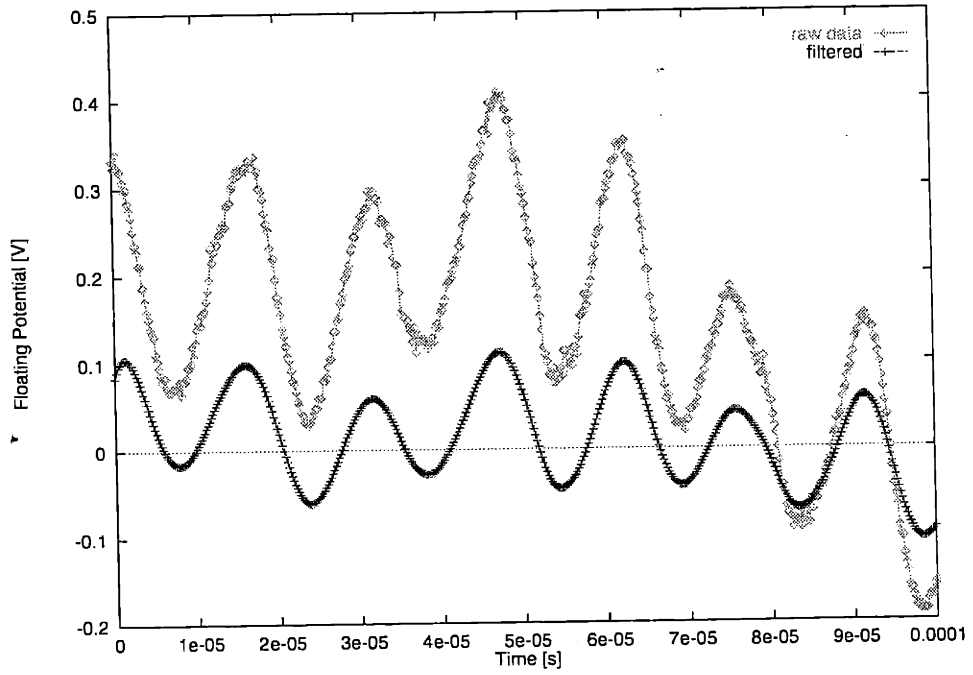

Figure 6-12: Floating potential, V_f, measured and filtered $[V]$, $\dot{m} = 2.34\ mg/s$, $V_d = 300\ V$, $z = 1\ cm$, $r = 2.5\ cm$.

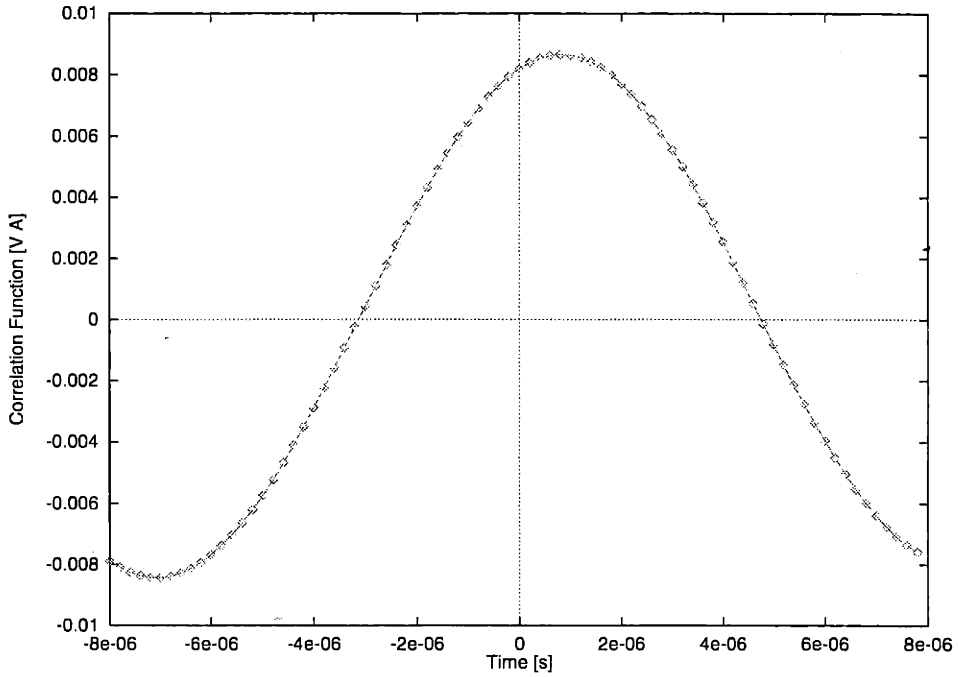

Figure 6-13: Correlation function of V_f with I_a, $[A \cdot V]$, $\dot{m} = 2.34\ mg/s$, $V_d = 300\ V$, $z = 1\ cm$, $r = 2.5\ cm$.

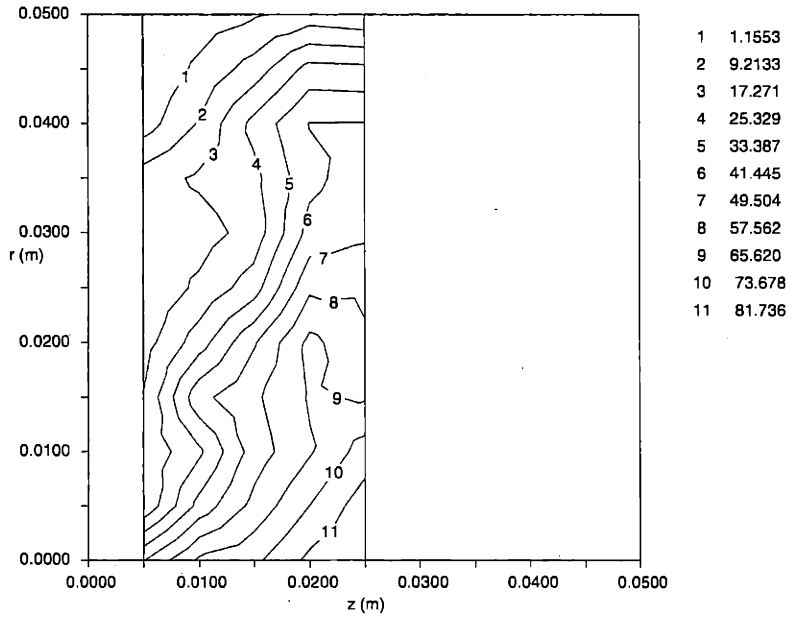

Figure 6-14: Phase lag of V_f behind I_a at 62.3 kHz $[degrees]$. $\dot{m} = 2.34\ mg/s$, $V_d = 300\ V$.

the plume and presented in Figure 6-14.

If I_a is a measure of the rate of creation of ions, all of which leave the acceleration zone at a given uniform speed, one would expect the gradient of the phase lag of V_f with I_a to be a measure of the ion velocity. Indeed, some structure can be seen in Figure 6-14. Apparently, a wave is traveling downstream, as expected. However, the phase velocity is computed to be about $10,000\ m/s$. This is roughly half of the expected value ($v_i = \sqrt{\frac{2eV_d}{m_i}} \approx 19,000\ m/s$). Some possibilities for this disparity are discussed in the next chapter.

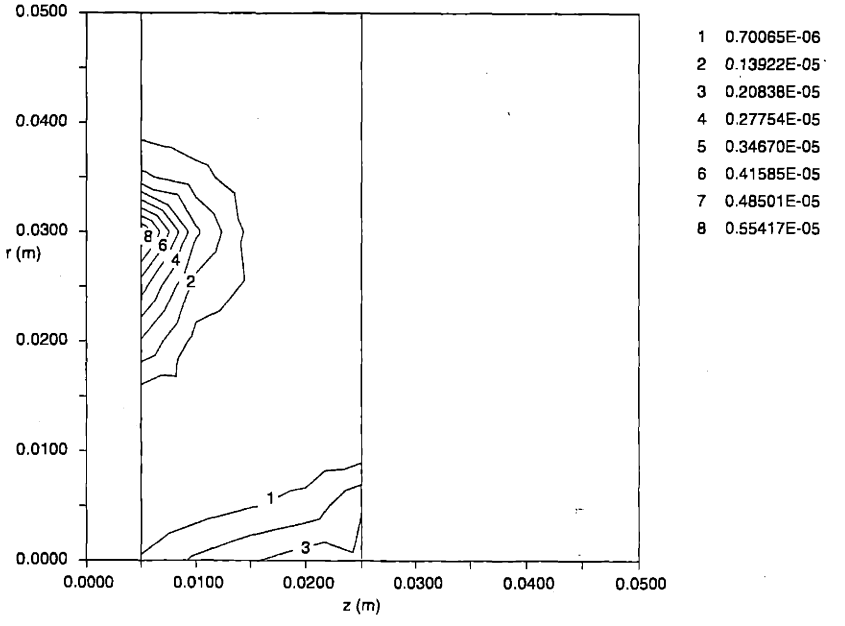

Figure 6-15: Power spectral density of V_f for the dominant mode (33.6 kHz) $[V^2/Hz]$. $\dot{m} = 1.17\ mg/s$, $V_d = 215\ V$, 80 hrs from BOL.

Figures 6-15 and 6-16 show similar results for the thruster operating at a lower power setting. The frequency of oscillation was 33 kHz. In most places, the phase velocity can be computed to be around 8000 m/s, much lower than expected ($17,000\ m/s$).

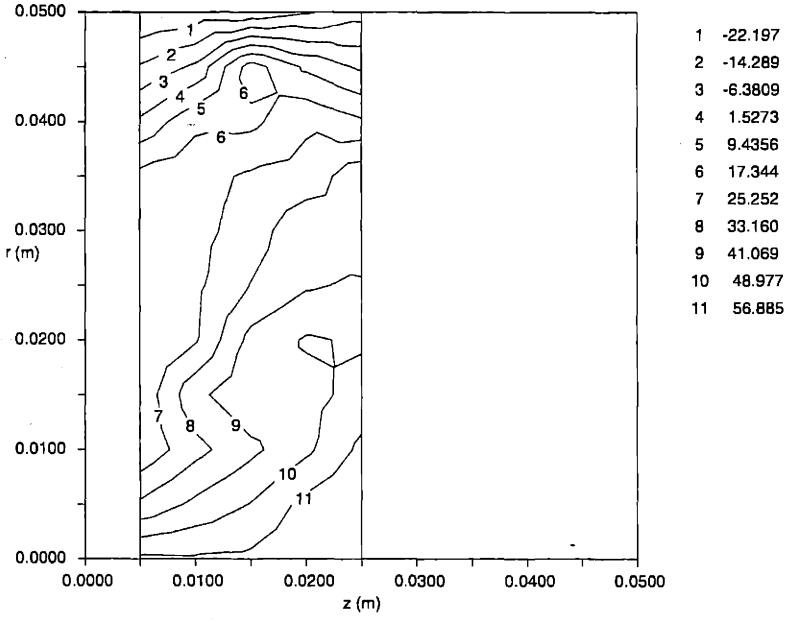

Figure 6-16: Phase lag of V_f behind I_a at 33.6 kHz [*degrees*]. $\dot{m} = 1.17\ mg/s$, $V_d = 215\ V$.

6.1.3 Azimuthal Rake

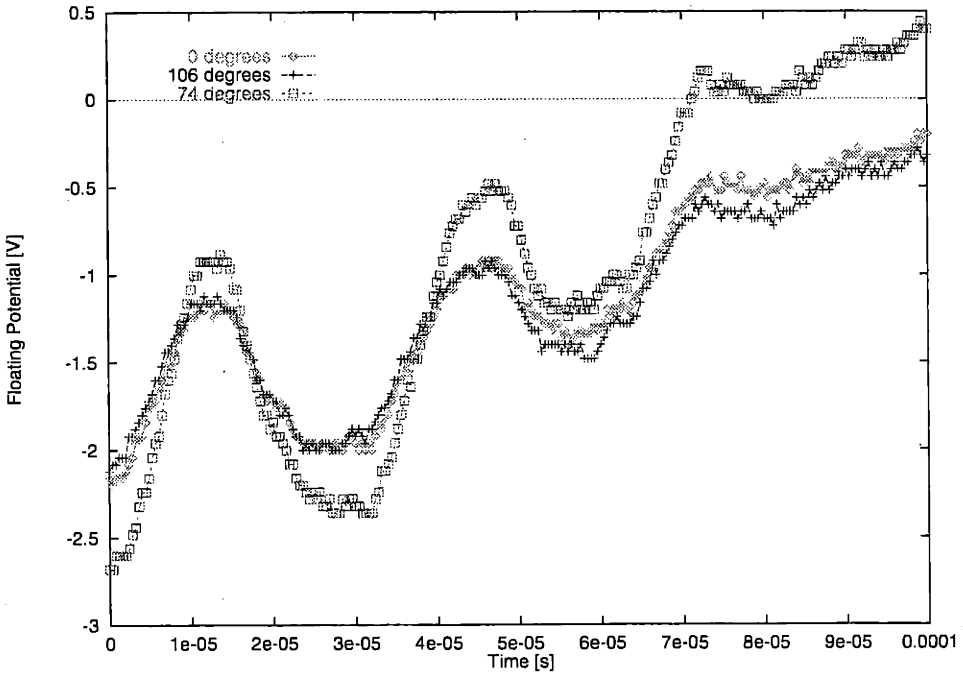

Figure 6-17: Comparison of floating potentials measured simultaneously at three circumferential locations [V], $\dot{m} = 2.93\ mg/s$, $V_d = 350\ V$, $z = 1\ cm$, $r = 2.75\ cm$.

Figures 6-17 and 6-18 show time histories of floating potentials from the three-electrode azimuthal rake, described in Section 4.4.5, for two different operating conditions. For each case, the three signals are strongly correlated, without any phase lag. Low-frequency wave motion, therefore, appears to be restricted to the $z - r$ plane.

A search throughout the rest of the spectrum revealed some other possible modes at higher frequencies, all at much less power. None of these were identified as being correlated azimuthally, however.

6.2 Numerical Model

Two modes of oscillation are observed in the numerical model: an ionization oscillation at around 15 kHz, and a transit-time instability at around 100 kHz. The first is related to local build-up of ionization, while the latter is related to growth and propagation of a plasma wave from the anode down the acceleration channel. The ionization instability is observed at almost all operating conditions. The transit-time oscillation, however, is observed only

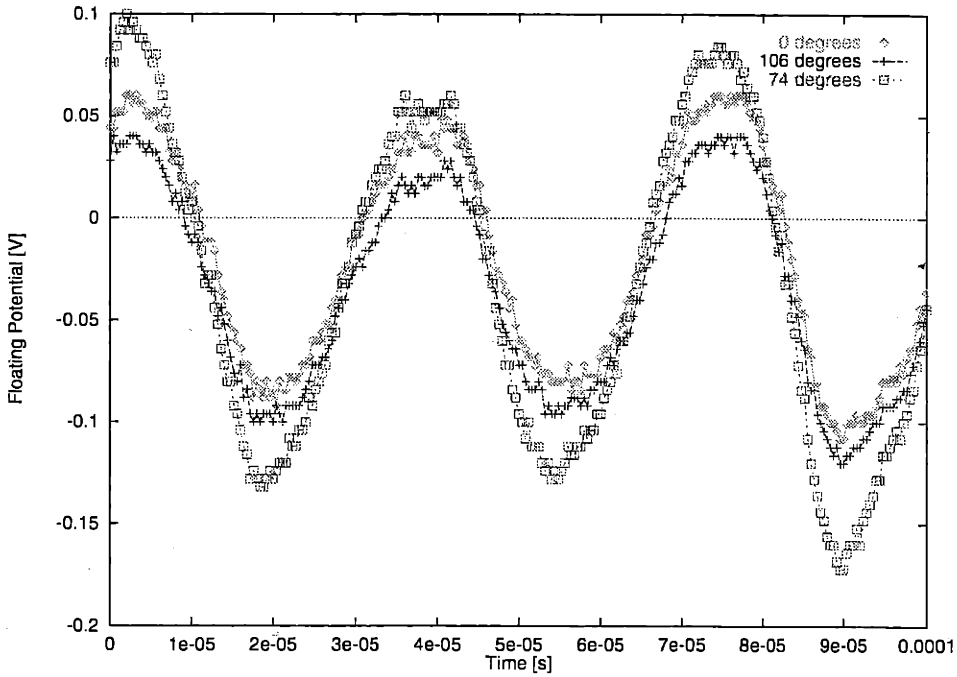

Figure 6-18: Comparison of floating potentials measured simultaneously at three circumferential locations [V], $\dot{m} = 1.17\ mg/s$, $V_d = 200\ V$, $z = 1\ cm$, $r = 2.75\ cm$.

in cases where the cross-field electron mobility near the anode was low.

To check the possibility of numerical instability causing the oscillations, additional runs were executed with one-tenth the timestep. Both oscillations were observed in their same form. Also, runs were executed with twice the number of spatial nodes. Again, oscillations were present in the same form. It is, therefore, believed that they are legitimate solutions to the governing equations. Examination of their form reinforces this belief.

6.2.1 Ionization Oscllations

An ionization oscillation is observed by numerically disturbing a converged solution. The ion particles are frozen, the electron integrator is de-activated, and the neutral particles are allowed move freely for 10 μs. Then, the ion and electron integrators are re-activated, and the solution continues, with a new spatial distribution of neutral density. A variation on this method is to erase all existing ion particles before re-activation of the integrators. The latter is analogous to actually restarting a thruster. Figure 6-19 shows a time history of oscillations resulting from a 10 μs disturbance.

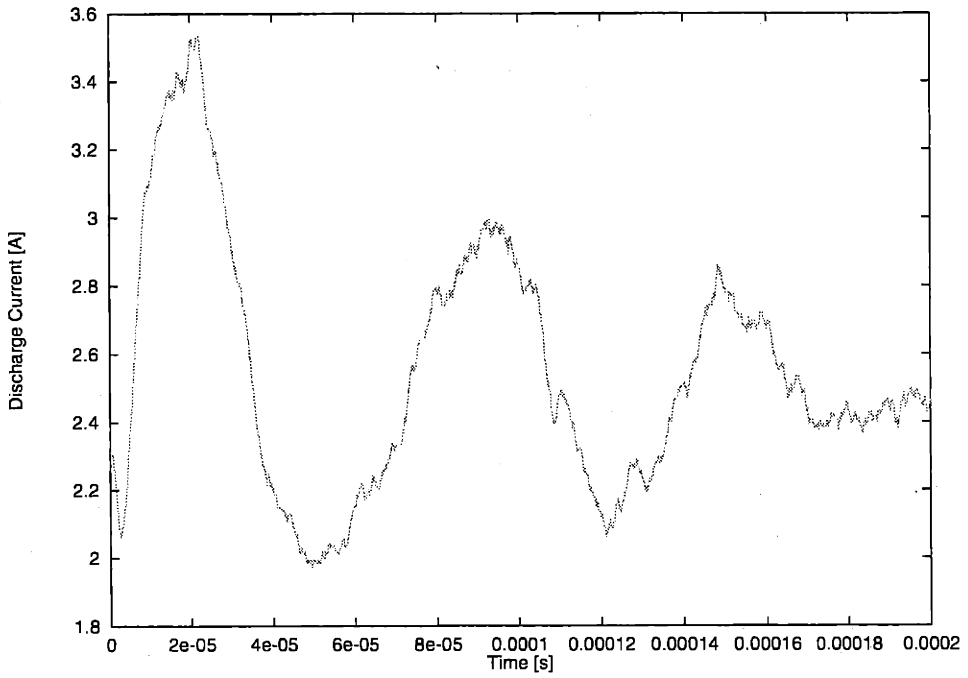

Figure 6-19: Time history of oscillations of discharge current, $[I_a]$, from numerical model, $\dot{m} = 2.34\ mg/s$, $V_d = 300\ V$, $K_B = .15$, cathode 5 mm downstream of the channel.

As can be seen from Figure 6-19, the dominant mode is approximately 13 kHz and is damped. The peaks and valleys in the I_a signal represent states of globally high and low plasma density, respectively. Figure 6-20 shows a time-progression of the mean plasma density along B-field lines, plotted against mean z coordinate. The starting point ($t = 0$) is just after the I_a cycle has reached a minimum.

To check the dependency of frequency with operating parameters, several other cases were run. Four are summarized in Table 6.2. Frequency increased slightly with discharge voltage, and slightly with propellant flow rate. For all cases, the frequency was within 18% of the mean (11.1 kHz). Both amplitude, $\hat{A}_0$, and time constant, T_c, increase with power level. At the highest power level, the oscillation is almost undamped. A comparison of these results with current theory is given in the next chapter.

6.2.2 Transit-time Oscillations

Transit-time oscillations are observed at frequencies in the neighborhood of $\frac{v_i}{l}$, where l is the length of the channel. Their appearance is limited to operating conditions where the

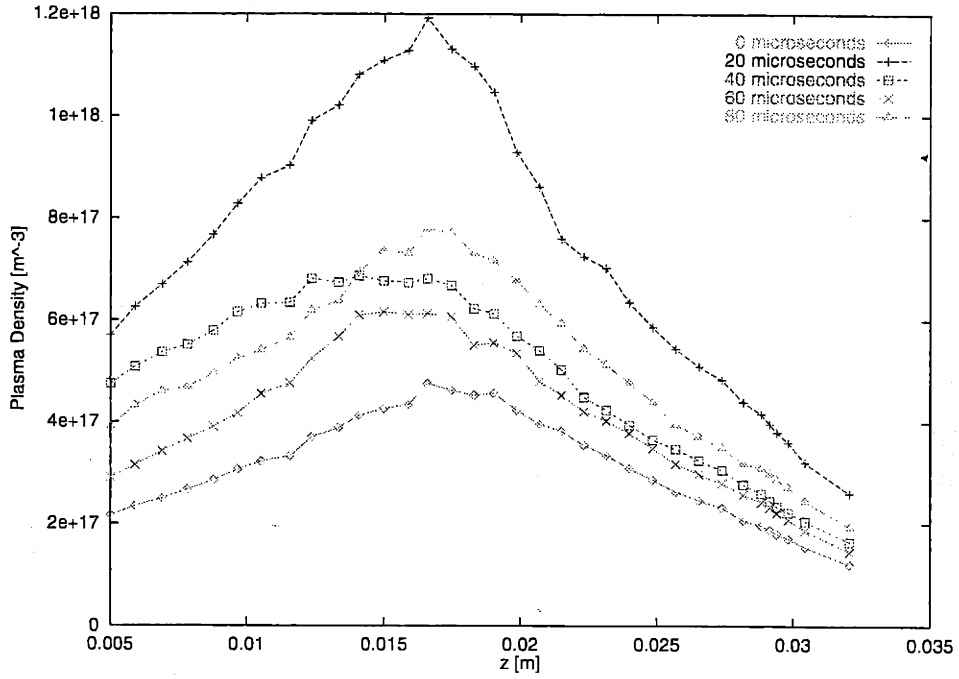

Figure 6-20: Time progression of mean plasma density, n_e, $[m^{-3}]$, versus mean axial position from the anode, for ionization oscillations from numerical model, $\dot{m} = 2.34\ mg/s$, $V_d = 300\ V$, $K_B = 0.15$, cathode 5 mm downstream of the channel.

$\dot{m}\ [mg/s]$	$V_d\ [V]$	$f_n\ [kHz]$	$\hat{A}_0\ [A]$	$T_c\ [s]$
1.17	200	9.1	.5	1.0×10^{-4}
1.17	300	12.1	.8	1.5×10^{-4}
2.34	200	11.1	.7	1.7×10^{-4}
2.34	300	12.1	2.0	1.0×10^{-3}

Table 6.2: Comparison of ionization oscillations from the numerical model for several operating conditions. $K_B = .15$, effective cathode at $z = 5\ mm$ downstream. f_n is natural frequency, $\hat{A}_0$ is maximum amplitude, and T_c is the time constant for decay.

cross-field electron mobility near the anode is low relative to near the exit of the channel. In CASE 1 through CASE 4, the radial magnitude of the electric field at the anode, B_a, was .001 T, or 5% of the peak value. Figure 6-21 shows a time history of discharge current from CASE 5 with B_a set to .005 T, 25% of the peak value.

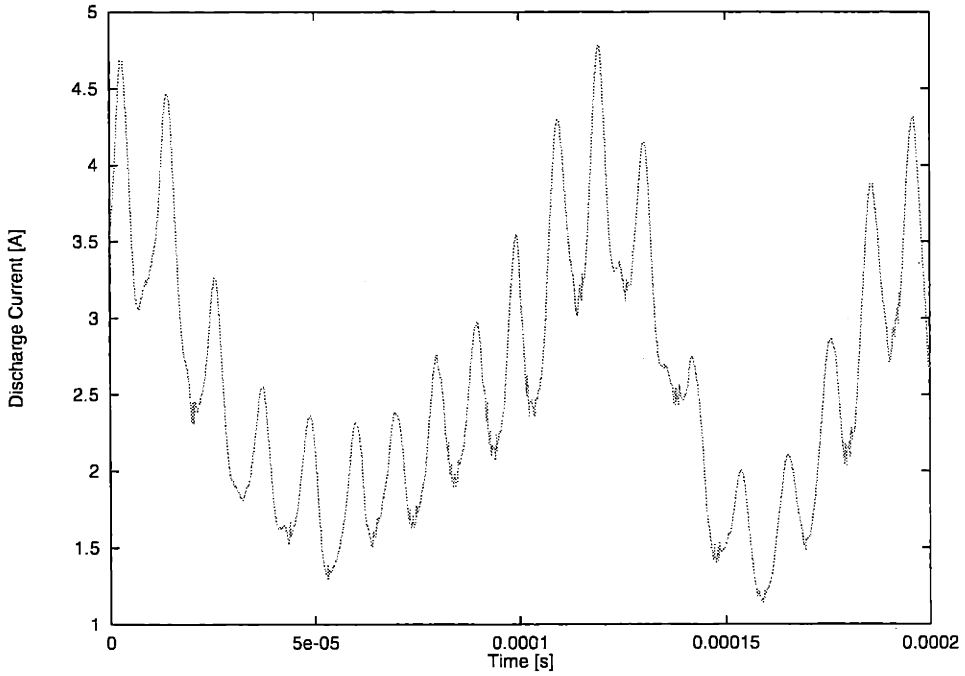

Figure 6-21: Time history of oscillations of discharge current, $[I_a]$, from numerical model CASE 5, $\dot{m} = 2.34\ mg/s$, $V_d = 300\ V$, $K_B = 0.3$, $B_a = .25B_{max}$, cathode 3 cm downstream of the channel.

The progression of events involves, first, a rise in electric field near the anode. This results in a reduction in density locally corresponding to the position of the new electric field. The lower density further increases the electric field by Ohm's Law. Limiting our discussion to the direction perpendicular to the magnetic field,

$$E = \frac{j_e}{en_e\mu_{e,\hat{n}}} - \frac{\nabla p_e}{en_e}. \tag{6.3}$$

The further growth in E promotes increases in T_e through Ohmic heating, which adds to the pressure term above. The disturbance travels downstream led by the sharp electric field, to the exit where it is mixed with other ions and exhausted. Figures 6-22 and 6-23 show the progression versus axial position, starting at a point in the cycle where I_a is a minimum.

They were constructed by computing the mean of the plasma parameters along magnetic field lines, and then presenting the results versus mean z along the line. For simulation runs with this oscillation present, considerable widening of the distribution of ion energies was observed, with half-widths of up to 200 V. The case of Figure 5-44 are attributed to this type of oscillation, which was present in that case.

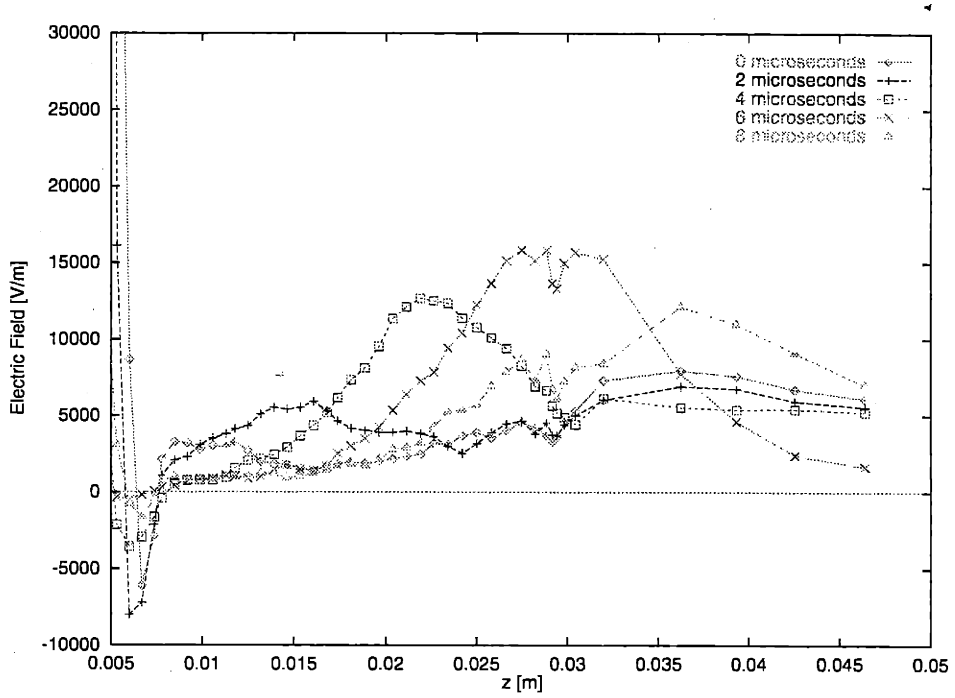

Figure 6-22: Time progression of mean electric field normal to the magnetic field, $E_{\hat{n}}$, $[V/m]$, versus mean axial position from the anode, for transit-time oscillations from numerical model CASE 5, $\dot{m} = 2.34\ mg/s$, $V_d = 300\ V$, $K_B = 0.3$, $B_a = .25B_{max}$, cathode 3 cm downstream of the channel.

A multitude of boundary conditions at the anode were tried in an attempt to suppress this behavior. In all cases, the oscillation persisted. For slightly positive electric fields throughout the near-anode region, all ions initially are moving in the positive z direction, and the point at the anode must tend to zero ion density. This triggers the disturbance by forcing local growth of the electric field by Equation 6.3.

Increasing the mobility at the anode suppresses the instability by permitting a region of reversed electric field downstream which drives a sufficient number of ions toward the anode to prevent runaway. Still, there must be a reversal point where the mean ion velocity is zero. Downstream, the plasma density is higher, and fluctuations in electric field can

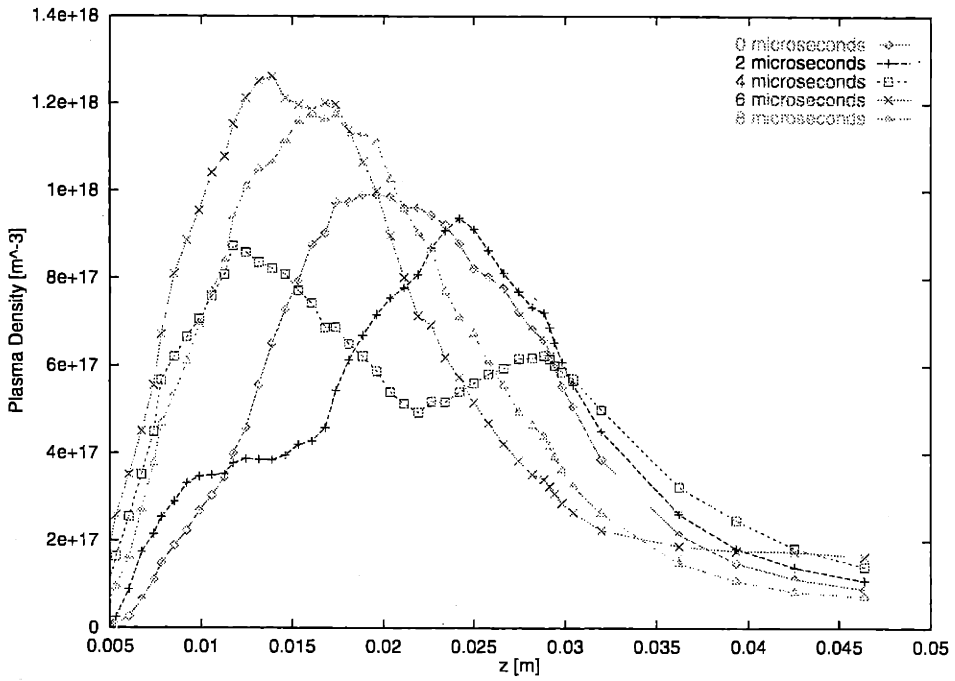

Figure 6-23: Time progression of mean plasma density, n_e, $[m^{-3}]$, versus mean axial position from the anode, for transit-time oscillations from numerical model CASE 5, $\dot{m} = 2.34\ mg/s$, $V_d = 300\ V$, $K_B = 0.3$, $B_a = .25 B_{max}$, cathode 3 cm downstream of the channel.

draw ions from both directions, so that the ion density never approaches zero. Near the anode, on the other hand, ions may only be drawn from one direction, and positive electric fields there continue to increase without bound because no ions are there to replentish those accelerated downstream. Hence, the density there tends to zero at the anode and the oscillation triggers.

By increasing K_B, $\mu_{e,\hat{n}}$ may be increased to the point where the disturbances no longer form, but at the expense of increasing I_a, thereby decreasing efficiency. Also, qualitative observations indicate increasing channel length suppresses the instability, but this may be a result of incidentally reducing the relative magnitude of the magnetic field at the anode.

Chapter 7

Discussion of Findings

This chapter discusses the results presented in the previous chapters. Some particular comparisons will be made between the experimental observations, numerical results, and current theory.

The numerical model is designed with flexible assumptions so that it may be used as a platform to test the validity of hypothetical physical processes applicable to Hall thrusters. In this way, it serves as a tool for helping to understand the physics. Places where the model fails to reproduce measured results indicate regions of inapplicability of the governing equations used, or missing relationships. This chapter will pay special attention to those places. However, since Hall thruster theory is not yet complete, some disparity is bound to remain.

7.1 Models for Cross-Field Electron Conductivity

One difference between measured values and numerical results seems to arise from the formulation of cross-field electron transport. Indeed, "anomalous" cross-field conductivity is often referenced in Hall thruster reports [42]. A brief summary of the observation is as follows.

Hall thrusters achieve high electric fields at relatively low electron currents by magnetic containment of electrons. The Hall parameter ($\beta_e = \omega_c/\nu_{en}$) is high throughout the device. Classically, collisional scattering is the mechanism by which electrons ultimately must reach the anode. In the case of the SPT-70, the electron current which must be drawn by the anode is approximately 2.2 A. Taking some sample numbers for the properties inside the

E_z	$10{,}000\ V/m$
T_e	$10\ eV$
n_n	$1 \times 10^{19} m^{-3}$
n_e	$2 \times 10^{17} m^{-3}$
B_r	$.01\ T$
β_e	415

Table 7.1: Rough mean values of plasma parameters in the SPT-70 acceleration channel at nominal operating conditions.

SPT-70 acceleration channel (Table 7.1),

$$I_{e,classical} = Aen_e \frac{e}{\nu_{en} m_e} \frac{1}{(1+\beta_e^2)} E_z = .2\ A. \tag{7.1}$$

This is smaller than the measured current by a factor of 10. Indeed, some other "anomalous" transport mechanism must be at work besides classical diffusion. Although a particular mechanism for the anomalous conductivity has not been found, microturbulence at frequencies on the order of the cyclotron frequency is generally thought to somehow aid transport. Bohm ($\frac{1}{B}$) diffusion is often attributed to such microturbulence.

The mobility model used in the numerical simulation is,

$$\mu_{e,\perp} = \frac{\mu_e}{{\beta_e}^2} + K_B \frac{1}{16B}, \tag{7.2}$$

where $K_B = .15$. It is clear from Figure 7-1 that the model for cross-field electron mobility underpredicts the measured value in both the anode and cathode regions. Near the anode the model is lower by a factor of two. Near the channel exit ($z = 4\ cm$), the model is lower by a factor of 100. The region near the exit appears to be dominated by this anomalous conductivity, while, near the anode, classical and anomalous conductivity are of the same order. Attempts to compensate with the Bohm model fail, because increasing K_B causes overprediction in the region between $z = 2.5$ and $3.5\ cm$ because of the lower magnetic field there. This indicates that the anomalous conductivity is not as simple as $K_B \frac{1}{B}$ over the entire channel. However, Section 7.3 shows, using fairly robust arguments, that transport due to wave mechanisms does go as $\frac{1}{B}$. This implies that K_B may not be constant over the entire channel, as assumed in the model. This may be due to local changes in the plasma properties which are not fully understood.

- Anomalous diffusion

The first item refers to the possibility that electrons which enter a sheath near the metallic surface find a way to cross the magnetic field unimpeded there, the net effect being a short-circuit of the magnetic impedance in the near plume. However, since the metallic face is not considered a good emitter of electrons, absorbtion and re-emission upstream is not likely. Secondary electrons may contribute, but the secondary emission coefficient of metals is generally low. Mere elastic reflection of electrons from an electrostatic sheath will not force a cross-field displacement, either.

A second possible reason for the discrepancy is that electrons are being collected by the metallic outer face of the thruster. The thruster body, in the experiments presented here, was tied to chamber GND. Electrons collected by that surface need not be returned to the plasma. They may either go to the tank walls to neutralize the ion beam, or they may go into the ground circuit and be neutralized elsewhere. This violates the assumption made in Chapter 2 that the net current to any surface (except the anode and cathode) must be zero. Since the potential drop between the plasma and the thruster face (and chamber wall) was computed to be around 135 V, however, it is not easy to see how enough electrons would be lost to make a difference.

Assuming the electrons in the center of the near-plume to be Maxwellian, the electron current lost to the wall is,

$$j_{e,w} = en_e \frac{\bar{c}}{4} e^{-\frac{e\phi}{kT_e}}. \tag{7.3}$$

Since the walls are metallic, no balance need exist between the ions and the electrons. The only condition is that the wall not emit electrons, only absorb them. Now, if the electrons are emitted at zero potential from the cathode somewhere downstream, their temperature upstream may grow at a rate of,

$$\frac{kT_e}{e} = \frac{2}{5}\phi, \tag{7.4}$$

ignoring losses. The wall then can absorb electrons at the rate,

$$j_{e,w} = en_e \sqrt{\frac{e\phi}{5\pi m_e}} e^{-\frac{5}{2}}. \tag{7.5}$$

So, higher plasma potentials in the near-plume are associated with additional electron losses to the metallic wall. We can compute the electron current expected to the wall by using

channel must be about .5 A, regardless of wall losses. According to the generalized Ohm's Law (disregarding the pressure term),

$$j_{e,\hat{n}} = \sigma_{e,\perp} E_{\hat{n}}, \tag{7.7}$$

this implies that wall losses should have no effect on $\vec{E_{\hat{n}}}$ outside the channel, since $j_{e,\hat{n}}$ is independent of them there.

The third possiblity for the discrepancy between the model and measured data in the near plume region is anomalous diffusion. As discussed in the previous section, data from an SPT-100 indicate the numerical model is underpredicting cross-field electron mobility. If the anomalous conductivity is localized outside the channel in the near plume for some reason, the electric field may be lower there, as measured. The most plausible explanation currently for anomalous transport involves azimuthal waves. Azimuthal waves with density and potential out of phase produce net drift current axially. A review of current theory on azimuthal wave transport in Hall thrusters is given in the next section.

Although the above hypotheses are difficult to test with the data available, indications are strong that anomalous electron transport is responsible for delaying the rise in potential. However, since the rise in potential begins to take place just at the metal-insulator transition surface, it is felt that the metallic wall must play some role in enhancing diffusion. Unfortunately, these experiments did not include measurement of electrical current between the thruster body and ground which would have aided in the analysis. In the papers by Bishaev, no mention is given of the electrical configuration.

7.3 Axial Transport by Azimuthal Waves

As described in the previous two sections, the discrepancies between the model and experiment may be explained by an "anomalous" electron conductivity. It is suggested by several researchers that such conductivity may be due to certain phase relationships between n_e and E_θ due to fluctuations in the azimuthal direction. This section presents a brief review those theories.

Consider a small perturbation of the plasma parameters in the azimuthal (θ) direction

only. Denoting the perturbed quantities with primes,

$$n_e(z,r,\theta,t) = n_{e,0}(z,r) + n'_e(z,r,\theta,t), \tag{7.8}$$

$$\phi(z,r,\theta,t) = \phi_{e,0}(z,r) + \phi'_e(z,r,\theta,t). \tag{7.9}$$

Now assume the perturbation is sinusoidal and the density and potential are out of phase by ψ. If the mode number (periods per circumference) is N and the azimuthal wave speed is c,

$$n'_e = \hat{n}_e \sin\left[N\left(\theta - \frac{ct}{r}\right)\right], \tag{7.10}$$

$$\phi' = \hat{\phi}\sin\left[N\left(\theta - \frac{ct}{r}\right) + \psi\right]. \tag{7.11}$$

For $\omega = N\frac{c}{r} << w_{ce}$, electrons move at the local drift velocity,

$$\bar{v_e} = \frac{\vec{E}\times\vec{B}}{B^2} = \frac{(\vec{E}+\vec{E'})\times\vec{B}}{B^2}. \tag{7.12}$$

In the z-direction (with $\vec{B} = B_r$ only),

$$v_{e,z} = -\frac{(E_{0,\theta}+E'_\theta)B}{B^2} = \frac{1}{B}\frac{d\phi'}{d(r\theta)} \tag{7.13}$$

$$= \frac{\hat{\phi}N}{Br}\cos\left[N\left(\theta - \frac{ct}{r}\right) + \psi\right]. \tag{7.14}$$

The local electron flux is then,

$$\Gamma_{e,z} = n_e v_{e,z} = (n_{e,0} + n'_e)v_{e,z} \tag{7.15}$$

$$= \frac{N\hat{\phi}}{Br}\cos\left[N\left(\theta - \frac{ct}{r}\right) + \psi\right]\left\{n_{e,0} + \hat{n}_e \sin\left[N\left(\theta - \frac{ct}{r}\right)\right]\right\}. \tag{7.16}$$

To find the net cross-field electron flux, this quantity is averaged over one period ($\Delta\theta = \frac{2\pi}{N}$):

$$\bar{\Gamma}_{e,z} = \frac{N}{2\pi}\int_0^{\frac{2\pi}{N}} \Gamma e, z d\theta. \tag{7.17}$$

After some algebra, this comes out to,

$$\bar{\Gamma}_{e,z} = -\frac{1}{2}\frac{N\hat{\phi}\hat{n}_e}{Br}\sin\psi. \tag{7.18}$$

So, for cross-field electron transport, n_e and ϕ must be nonzero and out of phase ($\psi \neq 0$). At Boltzmann equilibrium conditions, for instance, $\psi = 0$, and no transport happens. Maximum transport is given by $\psi = \pm\frac{\pi}{2}$, i.e. potential 90° out of phase with density (azimuthal electric field in-phase with density).

Equation 7.18 is independent of wave velocity, c. Therefore, the "wave" need not be traveling. It could be a standing wave or a static azimuthal non-uniformity, except that this would probably lead to Boltzmann equilibrium and no transport.

Notice equation 7.18 gives $\frac{1}{B}$ dependence as measured empirically by Bohm [12]. However, it cannot be said that $\Gamma_{e,z}$ is everywhere proportional to $\frac{1}{B}$. The amplitude and phase of azimuthal waves are, in all likelihood, very complicated functions of the local plasma properties. The other terms in Equation 7.18 may take many forms, being functions of position and $\vec{B}$, for instance. In light of this, the form of anomalous conductivity chosen for the numerical model,

$$\mu_{e,\perp} = K_B \frac{1}{16B}, \tag{7.19}$$

with K_B constant seems very crude. For this reason, the discrepancies observed between numerical and experimental results are not surprising. Other researchers have found evidence linking the anomalous transport to certain types of fluctuations which differ in various regions of the Hall thruster plasma. What follows is a brief review of literature about this subject and how it may pertain to the discrepancies observed here.

In 1973, Esipchuck and Morozov et. al. [26, 53] presented results from experiments inside the channel of a Hall thruster in which a rotating "spoke" ionization instability was identified. This wave has frequencies in the tens of kHz and appears at low discharge voltages. It extends from the exit of the channel to the anode and rotates at a speed smaller than the drift velocity by a factor of $3 - 6$. The plasma potential and density were found to be 90° out of phase in the azimuthal direction, and it was concluded that the wave is capable of enhancing axial electron transport. Also, transit-time oscillations were observed which were less coherent. By analyzing the azimuthally asymmetric turbulent properties of the transit-time oscillations, an estimate of their contribution to axial electron transport is also made. Combining the contributions from both oscillation types, they conclude that, in the channel, the anomalous conductivity may be explained to within 30%.

This may account for the discrepancy between the mobility model and the measured

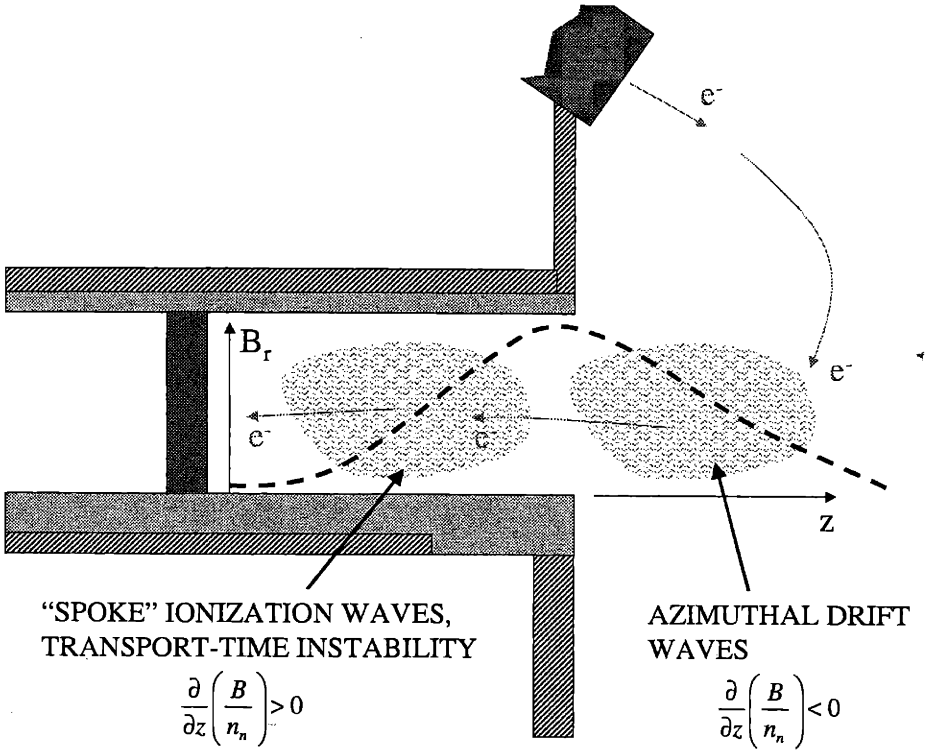

Figure 7-3: Regions of anomalously high cross-field transport with respect to the radial magnetic field strength.

mobility near the anode in Figure 7-1. However, the early measurements of Esipchuk and Morozov were performed inside the channel. Outside the channel, other mechanisms must be at work.

Later, in 1976, Esipchuk and Tilinin [25] identify azimuthal drift waves that may exist outside the channel, where the magnetic field is decreasing. These waves have frequencies of a few MHz and exist only where $\frac{\partial}{\partial z}\left(\frac{B}{n_n}\right) < 0$. However, the enhancement of cross-field electron conductivity was not quantified.

Hirakawa [35] performed numerical simulations to quantify the role of oscillations in cross-field electron transport. The simulations assumed constant axial electric field and constant radial magnetic field. Fluctuations were observed with frequency of $\frac{1}{400}$ of the plasma frequency, which correlates well with observations by Esipchuk and Tilinin. Furthermore, Hirakawa found the enhanced electron mobility to be $\frac{1}{16B}$. This is equivalent to the Bohm empirical value, which is on the order of the amount of the discrepancy between the model and experiment outside the channel.

A complete picture of the effects of azimuthally asymmetric electron transport in the SPT may now be proposed. The above information suggests two distinct regions of enhanced

conductivity, as shown in Figure 7-3. The region near the anode has increasing magnetic field. Low-frequency "spoke" ionization waves and turbulent transport-time oscillations enhance mobility in that region by a factor of 2 or so over classical. Outside the channel, where the magnetic field is decreasing, high-frequency azimuthal waves dominate, producing mobilities around 100 times greater than classical.

Substantiation of this proposal is difficult with the data available. Low frequency azimuthal waves may be ruled out, since experiments with the azimuthal rake (Figures 6-17 and 6-18) show no circumferential phase shift in floating potential at the dominant $(20 - 60\ kHz)$ mode. However, data sampling was designed primarily for detection of low-frequency signals. High-frequency modes were detected, but sampling times were not long enough to accurately determine phase relationships. A complete probe survey from the anode to well downstream of the channel exit is needed, focusing on high-frequency modes. For such an experiment to substantiate an azimuthal wave transport theory, it needs to:

- Explain why the azimuthal non-uniformity happens.
- Calculate the wave amplitudes, $\hat{n_e}$ and $\hat{\phi}$, and phase, ψ.
- Find the most likely wave number, N.

Such research is planned as an extension of this work.

7.4 Relationships Along Lines of Force

For the numerical model, electrons were assumed to be isothermal along lines of force. According to the electrostatic probe measurements, however, T_e drops off in regions of lower density and potential. This discrepancy suggests that a different law is applicable. Instead of using the momentum balance alone, with T_e set to be constant, one can use the adiabatic energy relationship (without heat conduction),

$$\frac{\partial}{\partial \hat{t}}(\frac{5}{2}\frac{kT_e}{e}) - \frac{\partial \phi}{\partial \hat{t}} = 0, \tag{7.20}$$

where, in this section, we are limiting our discussion to the direction $\hat{t}$, tangent to the magnetic field. The momentum balance is,

$$\frac{1}{n_e}\frac{\partial}{\partial \hat{t}}(n_e \frac{kT_e}{e}) - \frac{\partial \phi}{\partial \hat{t}} = 0. \tag{7.21}$$

Combining both equations, we get,

$$T_e = \tau n_e^{\frac{2}{3}}, \tag{7.22}$$

$$\phi - \frac{5}{2}\frac{kT_e}{e} = \phi^*. \tag{7.23}$$

Above, τ and ϕ^* are invariant along lines of force. Checking against the electrostatic probe data, we find that, along lines where T_e varies most, $T_e = \tau n_e^a$, where $a \approx \frac{1}{6}$, considerably less than 2/3. At other places measured, the value is much less and the distribution tends to isothermal. Apparently, heat conduction or some other mechanism needs to be included in the energy model to account for the spreading of energy. Such a model may be used in the quasi-two-dimensional electron energy equations described in Chapter 2, but would add additional complexity. That enhancement is saved for the future.

7.4.1 Computed Performance

Using the numerical model, computations of thruster performance were found to agree with measurements to within about 10% in the best case. Based on the simulation cases presented in the previous chapters, several factors are identified which influence simulated performance. This information is notable, as it may be used for thruster design, in some cases qualitatively.

Although the issue of physical processes in the near plume is not yet resolved, something may be said about the influence of that region on performance. According to the model the thrust efficiency is 16% lower in the case where acceleration is happening outside the channel versus inside. These correspond to CASE 1 and CASE 2 from Chapter 5. Indeed, according to numerical measurements, the anomalous conductivity in the near plume region actually results in an increased thrust efficiency. The conductive region delays the formation of the acceleration zone until the channel exit is reached, where the lines of force are less curved and beam divergence is reduced. The effect of floating the thruster body has not been examined experimentally, but may be an important performance determinant. Plans

are underway for further work on this topic.

Significant reductions in computed performance were also observed in cases where transit-time oscillations were pronounced. In these cases, spreading of the ion energy distribution led to poor η_e. The low-frequency ionization oscillations, however, seemed to have no observable effect on performance whatsoever.

Facility interaction has been shown to significantly affect measured performance (see Section 5.2.7). By correcting for the ingested background gas, a calibrated thrust efficiency may be determined. Such calibrations have been used before, and agree well with results from the model.

7.5 Physics in the Acceleration Zone

From the collective results presented in this paper, as well as some qualitative empirical observations, several general comments about the acceleration process and location of the acceleration zone may be made. One fundamental governing relationship is that the total integrated electric field from cathode to anode must equal the discharge voltage, V_d. (The normal mode of operation is to use a large enough capacitor across the discharge such that variations in V_d are small.) Using z as our coordinate direction, and assuming the magnetic field to be radial for simplicity,

$$\int_{z_c}^{z_a} E_z dz = V_d. \tag{7.24}$$

Using our generalized Ohm's law,

$$\int_{z_c}^{z_a} \left(\frac{j_{e,z}}{e n_e \mu_{e,z}} - \frac{1}{e n_e} \frac{\partial p_e}{\partial z} \right) dz = V_d. \tag{7.25}$$

For constant annular area,

$$\int_{z_c}^{z_a} \left(\frac{I_a - I_i}{A e n_e \mu_{e,z}} - \frac{1}{e n_e} \frac{\partial p_e}{\partial z} \right) = V_d. \tag{7.26}$$

Given an initial distribution of ions in the channel, Equation 7.26 must be be instantaneously satisfied by variation in I_a and $\frac{\partial p_e}{\partial z}$. This is the driving principle of the numerical model, which searches for values of I_a which satisfy Equation 7.26 each timestep.

For the simple case of constant plasma density and temperature, the electric field must

go as $\frac{1}{\mu_{e,z}}$, putting the peak of the acceleration zone at maximum B.

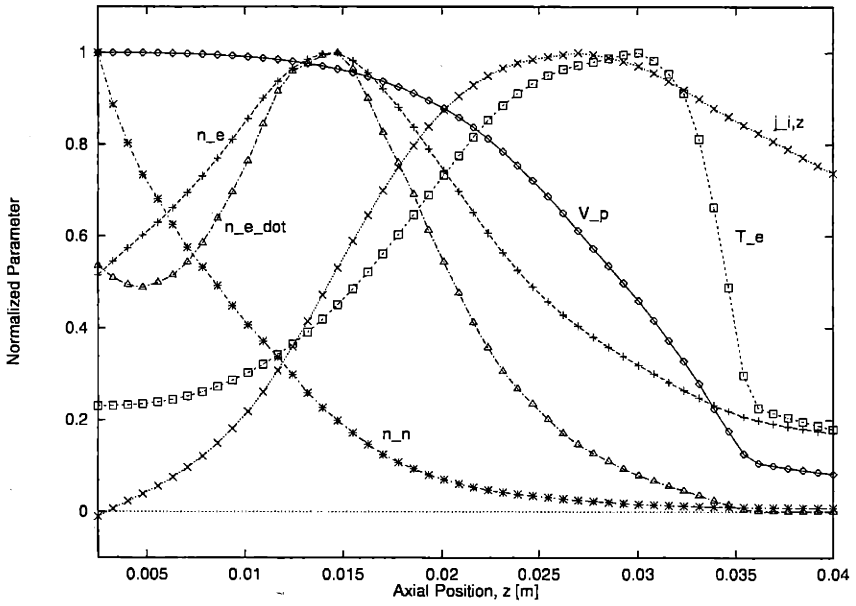

Figure 7-4: Comparison of normalized parameters along the center of the acceleration channel ($r = 2.75\ cm$), from the numerical model CASE 2. The anode is at $z = 0$ and the channel exit is at $z = 2.92\ cm$. The effective cathode is at $z = 3.6\ cm$.

The situation is more complicated when the ∇p_e term is nonzero and I_i is allowed to vary along the length of the device. This is the situation modeled. Figure 7-4 shows the 1-D results on the centerline of the acceleration channel ($r = 2.75\ cm$) taken from 2-D distributions in numerical model CASE 2. In this case, it may be said that the required transport of electrons is achieved by the sum of the effects of the electric field and the pressure gradient. Taking the other view, the electric field strength is determined by the local electron mobility and density and the pressure gradient. This pressure gradient is what gives rise to three distinct regions in the channel:

- Acceleration
- Ionization
- Diffusion

E_z can go much higher than $\frac{j_{e,z}}{en_e\mu_{e,z}}$ by balancing with a large negative pressure term. This pressure term is most negative at places where ions are being accelerated ($\nabla n_e < 0$)

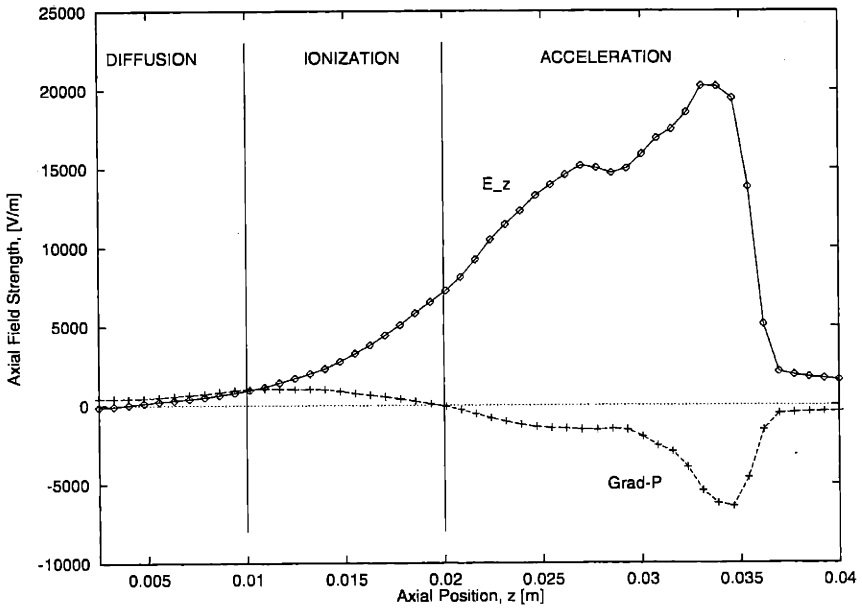

Figure 7-5: Axial electric field, E_z, and $\frac{1}{en_e}\frac{\partial p_e}{\partial z}$ $[V/m]$, along the center of the acceleration channel ($r = 2.75\ cm$), from the numerical model CASE 2. The anode is at $z = 0$ and the channel exit is at $z = 2.92\ cm$. The effective cathode is at $z = 3.6\ cm$.

and there is net heating of electrons ($\nabla T_e < 0$). This gives rise to the acceleration region, where the effects of Ohmic voltage drop and pressure gradient both reinforce the electric field. The transport term in the momentum balance becomes small at this point, compared to the E_z and $\nabla p_e/en_e$ terms.

Bulk ionization rate is given by $\varsigma(T_e)n_e n_n$. Therefore, a region of both high temperature and high density is needed. In the acceleration region, T_e is rising toward the anode. However, the density is necessarily low there, because, looking at the integrand of Equation 7.26, $E_z \sim \frac{1}{n_e}$. Therefore, the ionization zone must be separate and just upstream of the acceleration zone, where densities and T_e are high. T_e decreases toward the anode through this region as energy is lost due to ionization and inelastic excitation of atoms. Another way to see that the ionization zone and acceleration zone should be separate is to note that ionization rate and mobility should be proportionate since they are both collisional processes between electrons and ions. Therefore, regions of high ionization rate cannot support large fields without a pressure gradient to act against. Thus, ionization and acceleration are not generally coincident. The ionization region is highly collisional, and the acceleration region is not at all.

The remaining part of the acceleration channel, between the ionization region and the anode, is a region of low electric field, owing to the high cross-field electron mobility there and the high (but decreasing toward the anode) density. In that region, the momentum balance is primarily between the transport term and the pressure gradient, giving, for negligible ion current, $\mu_{e,z}\nabla p_e = I_a/A$. This is called the diffusion zone. It is also important to note that since significant cooling of electrons has taken place by the time they reach the diffusion zone, ionization there is negligible. For the electric field there to be low, the density cannot approach zero. Thus, a negative velocity of ions, coming from the ionziation zone must exist there for stability. This gives high enough density right up to the anode for smooth sonic transition through the sheath and high electron current at low electric field strength.

It should be mentioned that some 1-D models show the acceleration and ionization layers to be very thin, on the order of a few millimeters. This simulation does not predict that, due to heat conduction. A very thin ionization region would require abrupt changes in T_e which are not allowed by the energy model presented in Chapter 2. The minimum length of the ionization zone can be approximated by viewing it as a homogeneous region with constant T_e, constant n_e, and decreasing n_n. Solving the Boltzmann equation (or alternately a fluid conservation equation, which gives results within 20 % for this case) for the conditions $T_e = 25\ eV$ and $n_e = 2 \times 10^{18} m^{-3}$ the ionization layer thickness is found to be around 5 mm. The simulation predicts a region more like 15 mm due to the diffusive effects of electron energy conduction. However, the model for electron energy conduction is uncertain for the same reasons as mobility.

7.6 Effects of Secondary Emission of Electrons From the Dielectric Wall

High secondary emission coefficients increase heat loss to the wall and increase near-wall electron current, as described in Section 2.4.11. This may have important effects on the physics in the acceleration channel. For instance, long regions of high electron energy may be prohibited. For a representative density of $4 \times 10^{17}\ m^3$, and assuming electrons are at the breakpoint temperature for boron nitride (16.5 eV), the loss rate to the wall (inner and outer) is 80 W/cm. For a 2 cm length at these conditions, electrons would undergo loss of

160 W, which would decrease the total ionization rate. Given such a starting condition, it is likely that the escaping neutrals may travel downstream, to a point where the electron energy is still high, and which point complete ionization will take place. In summary, the high wall loss associated with secondary electron emission acts to shorten the zones of high electron energy.

This brings up the possiblity of tailoring the wall material to control the physics of the acceleration process. For example, if the position of the acceleration zone could be controlled, it may be placed at an optimal position for minimum beam divergence. Also, it has been suggested that the low-frequency modes observed in SPTs are actually due to movement of the position of the acceleration zone [61]. Secondary emission properties might be used to stabilize the acceleration zone position and reduce oscillation amplitude. To control the location of the acceleration zone, one possiblity is to generate an abrupt change in the secondary emission properties. Consider an acceleration channel which is made of two different materials – low secondary emission near the exit, and high secondary emission near the anode. Near the anode, losses due to secondary emission would reduce T_e and $\dot{n}_i$, forcing ionization to take place closer to the exit. A corresponding reduction in ions lost to the wall may be realized by such a geometry.

One might ask, "if the high secondary electron emission coefficient of the ceramic insulator is causing such high energy losses, why not make the channel out of metal?" There is no reason why not, as long as it is allowed to float sufficiently negative to repel electrons, and that precautions are taken to reduce the possibility of arcing. In fact, this is consistent with the TAL Hall thruster design, which has a very short "channel" on the order of 5 mm, and only a thin ceramic guard to reduce sputter erosion. One concern regarding making long metallic SPT channels would be additional ion collection and possible modification of the potential structure in the acceleration zone. These effects should be limited to scales on the order of the Debye length, however.

Cases were run with the secondary emission coefficient at the wall set (unrealistically) to zero. In these cases, the total electron wall losses were assumed to be, simply, $2kT_e$ per ion impinging. The electron power lost to the wall decreased in those cases by around 70%, and the peak T_e rose to around 50 eV. A higher ionization rate was observed, and a greater fraction of ions were lost to the walls. The net result was an increase in efficiency of around 20%.

7.7 Ions With Energies Higher Than the Discharge Potential

The numerical model predicts, and other reports have shown [3], that the plume exhaust contains ions with energies higher than the discharge potential. Figure 7-6 shows the distribution of ion energies as computed by the numerical model, with $V_d = 300\ V$. Multiply ionized atoms generally attain energies which are an integral multiple of the discharge potential, and may be seen at around 600 V in Figure 7-6. How ions attain energies just slightly higher than the discharge potential is less obvious. At first glance, conservation of energy would seem to prevent them. Since retarding potential analyzers also detect these ions, some discussion of the possible mechanisms has been circulating. Possiblities for their source include charge exchange between singly and multiply-charged ions, as well as momentum exchange collisions. Since the high-energy ions are observed with the numerical simulation, however, which does not include any of those collision processes, it is believed that time-fluctuations in the electric field are the primary cause.

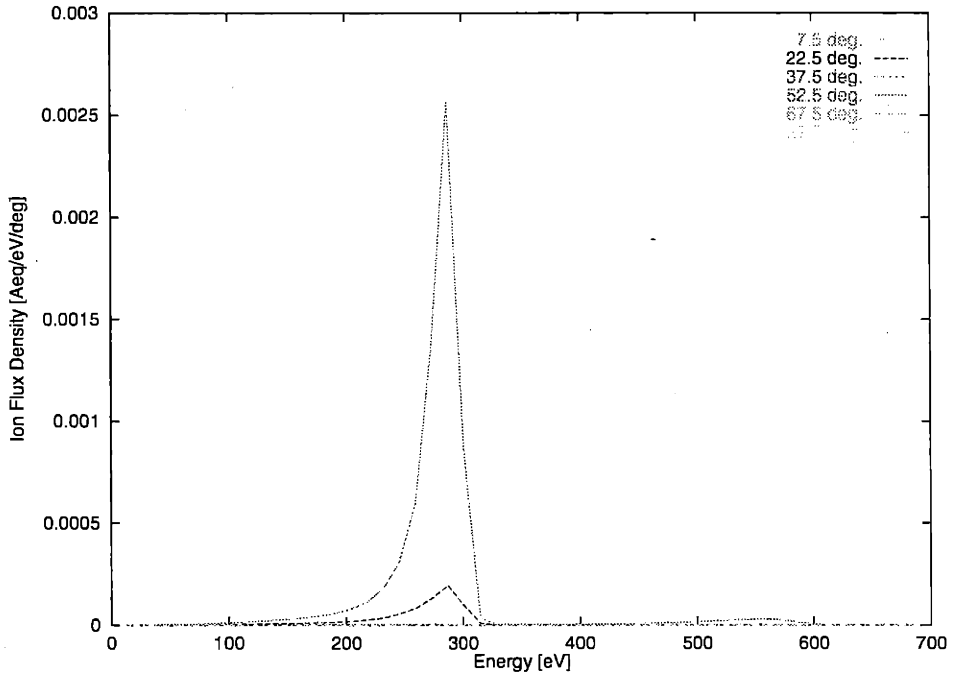

Figure 7-6: Ion distribution of energies $[A_{eq}/eV/deg]$, for CASE 2, $V_d = 300\ V$.

In one dimension, for simplicity, a particle born with zero velocity at electric potential

ϕ_0 will gain the following energy along its trajectory:

$$\frac{mv^2}{2} = \int_0^T eEdz, \tag{7.27}$$

where,

$$E = -\frac{\partial \phi}{\partial z}. \tag{7.28}$$

Normally, we would substitute and find the usual,

$$\frac{mv^2}{2} = -e(\phi - \phi_0). \tag{7.29}$$

However, ϕ may also vary in time in our case, so we need to write,

$$d\phi = \frac{\partial \phi}{\partial z}dz + \frac{\partial \phi}{\partial t}dt, \tag{7.30}$$

which gives,

$$\frac{mv^2}{2} = -e(\phi - \phi_0) + \int_0^T \frac{\partial \phi}{\partial t}dt. \tag{7.31}$$

This is counter-intuitive since one generally deals with steady electric fields that are conservative and time-invariant. For turbulent plasmas, or plasmas with oscillations, the net effect of the last term in Equation 7.31 is statistical widening of the distribution as some ions "surf" on the leading edge of electric field disturbances and others decelerate on the trailing edge. Therefore, the magnitude and type of field disturbances are important in determining the amount of widening in the distribution. In the numerical simulation, the transit-time oscillation produced the widest variation in ion energies. This was due to the fact that the wave speed was comparable to the ion velocity, so that some ions positions coincided with the leading edge for most of their path, and others with the trailing edge.

7.8 Comments on Desirable Magnetic Field Profiles

Bugrova et. al. [17] report that, for stable Hall thruster operation, the criteria,

$$\frac{d}{dz}\left(\frac{B}{n_n}\right) > 0, \tag{7.32}$$

must be enforced. Put another way, since $B/n_n \sim \beta$, the gradient of the Hall parameter must be positive (for constant T_e). This is a result of analyses by Esipchuk and Tilinin [25] in which they identify the an azimuthal drift instability that exists only for the condition $\frac{d}{dz}\left(\frac{B}{n_n}\right) < 0$. Bugrova et. al. also mention that this requirement had been experimentally verified, and that a more rigid requirement is usually imposed during design:

$$\frac{dB}{dz} > 0. \tag{7.33}$$

As mentioned in Section 7.3, Esipchuk and Tilinin [25] identified a high-frequency azimuthal drift instability that exist for the other case, where $\frac{d}{dz}\left(\frac{B}{n_n}\right) < 0$. According to the numerical simulation, which does not model azimuthal nonuniformity, there appears to be another reason for strongly positive $\frac{dB}{dz}$ near the anode.

The simulated case, CASE 5, from Section 6.2.2, had a rather flat magnetic field profile, with the magnitude of the field at the cathode 25% of the peak value. That case exhibited strong transit-time oscillations. The cases with higher magnetic field gradients, CASE 1 through CASE 4 were more stable, especially for large K_B. Another trial was executed, CASE 6, which used the form of mobility,

$$\mu_{e,\perp} = \frac{\mu_e}{{\beta_e}^2} + K_{B3}\frac{1}{B^3}, \tag{7.34}$$

with $K_{B3} = 4 \times 10^{-6}$. This, in effect, represents an increase in the gradient of B near the anode. The time-histories from CASE 6 showed no sign of the transit-time oscillation. Performance parameters were found to be slightly higher than measured for the SPT-70. Therefore, one can conclude, from the three cases, that increasing the magnetic field gradient at the anode does suppress the transit-time oscillation and increase efficiency of the thruster.

7.9 Oscillations

A multitude of oscillation modes have been observed in Hall thruster experiments [20], most of which appear at certain limited operating ranges. At nominal operating conditions, the oscillations with the highest amplitude are in the frequency range $10 - 100\ kHz$. We will concentrate here on that type.

7.9.1 Comparison of Measurements with Current Theory

The electrostatic probe measurements detected high-amplitude oscillations with spatial centering around the discharge channel. Their freqeuncies ranged from 12 to 65 kHz, and they had no detectable azimuthal component of travel. The floating potential and the discharge current were highly correlated. Since the discharge current fluctuations were high (100% of the DC value in some cases), there must have been large-scale impedance fluctuations in the channel. The most likely explanation is that plasma density in the channel was regularly varying at large amplitude. This would imply that an ionization oscillation was taking place.

Darnon et. al. [22] observed similar oscillations in an SPT-100-type thruster, and studied them with with high-speed optics. The oscillation luminosity was recorded at high speed, revealing an azimuthally uniform oscillation near the exit of the channel at the same frequency as the discharge current and with luminosity fluctuations of 70%.

For a slightly different geometry, Esipchuk [26] describes regular ionization oscillations in the range 10 to 70 kHz. By correlation of data from floating probes dispersed around the inside of the acceleration channel, Esipchuk finds that the oscillation is related to an azimuthal "spoke" wave traveling $3-6$ times slower than the electron drift velocity. In his device, the oscillation was observable mostly at low voltage, and near the anode, which is inconsistent with Darnon's oscillation. If the oscillations observed by Esipchuk are related to the ones measured by the electrostatic probe in this experiment, the azimuthal velocity of those waves would be on the order of 2×10^5 m/s, with a frequency of rotation of 1.3 MHz. Therefore, it is highly unlikely that the same mechanism is involved, unless the rotational oscillation somehow couples with a slower ionization instability.

It is also possible that some modes are acting in cooperation. For instance, ion acoustic modes, even though higher in frequency, could couple with an ionization instability. The effect should be discernable as a number possible frequencies separated by some constant Δf which is the fundamental frequency of the acoustic resonance. If this is the case, however, it is not possible to distinguish Δf in our PSD measurements.

The results by Darnon seem to compare best with observations in this experiment. The oscillation he observed was localized near the exit of the channel, high in amplitude, and produced discharge current fluctuations similar to those measured in this experiment.

However, the mechanism remains to be explained. Results from the numerical model present some possibilities.

Measurements of the AC component of floating potential in the near plume region show a regular fluctuation at the same frequency as the discharge current. However, while the discharge current amplitude was 20% of the DC value, the floating potential amplitude was only around .1 V, .3% of the DC value. At equilibrium at 5 eV, local variations in density of 20% would be expected to result in variations in plasma potential of around 1 V. In addition, the phase velocity of the wave emitted from the channel was expected to be around the mean ion velocity, but found to be around half that. Possibly, some other factors are influencing the floating potential at the same frequency, but with a different phase. However, until these experiments can be carefully repeated, and more comprehensive testing done, no conclusions regarding these observations will be ventured.

7.9.2 Ionization Oscillations

As described in the previous chapter, low-frequency, high-amplitude oscillations were observed as part of the solution to the numerical model for all cases. As can be gathered from the sequence in Figure 6-20, no detectable traveling wave is present. The oscillation observed is due to either a linear standing wave or a nonlinear limit cycle.

A standing wave pattern may be due to a resonating ionization interaction between ions and neutrals. To examine this case, we can begin by considering a region where the ionization rate is strong as a homogeneous "box" of length L. Neutrals arrive with a rate $n_n V_n$, but few leave. Ions leave at the rate $n_i V_i$, but few arrive on the upstream side. Ionization occurs inside the box at the rate $\xi(T_e) n_i n_n$. We can now write conservation equations for both species as,

$$\frac{\partial n_i}{\partial t} = \xi(T_e) n_i n_n - n_i \frac{V_i}{L}, \tag{7.35}$$

$$\frac{\partial n_n}{\partial t} = -\xi(T_e) n_i n_n + n_n \frac{V_n}{L}, \tag{7.36}$$

To determine the first-order dynamic character of the nonlinear system, we take the linear purturbation,

$$n_i = n_{i,0} + \epsilon n_i', \tag{7.37}$$

$$n_n = n_{n,0} + \epsilon n'_n. \tag{7.38}$$

To order ϵ^0,

$$\xi n_{n,0} = \frac{V_i}{L}, \tag{7.39}$$

$$\xi n_{i,0} = \frac{V_n}{L}, \tag{7.40}$$

which requires,

$$\frac{n_{i,0}}{n_{n,0}} = \frac{V_n}{V_i}. \tag{7.41}$$

From this, it can be seen that, since $V_n << V_i$, the degree of ionization must be low in this region.

To order ϵ^1, and using Equations 7.39 and 7.40,

$$\frac{\partial n'_i}{\partial t} = \xi(T_e) n_{i,0} n'_n, \tag{7.42}$$

$$\frac{\partial n'_n}{\partial t} = -\xi(T_e) n'_i n_{n,0}, \tag{7.43}$$

which can be written in the equivalent form,

$$\frac{\partial^2 n'_i}{\partial t^2} + \xi(T_e)^2 n_{i,0} n_{n,0} n'_i = 0. \tag{7.44}$$

Equation 7.44 represents an undamped harmonic oscillator with frequency, f_i, given by,

$$2\pi f_i = \omega = \sqrt{\xi(T_e)^2 n_{i,0} n_{n,0}} = \sqrt{\dot{n}_{i,0}^2 / n_{i,0} n_{n,0}}. \tag{7.45}$$

Using Equations 7.39 and 7.40 in Equation 7.45 gives,

$$2\pi f_i = \omega = \frac{1}{L}\sqrt{V_i V_n}. \tag{7.46}$$

Thus, for a fixed neutral speed, f_i is strictly a function of the length of the ionization zone and the velocity change of ions across it. We must note, however, that the length L is itself determined by the ionization rate, according to Equations 7.39 and 7.40. Notice the strong similarity of this model to the "predator-prey" dynamics, known to yield feast-famine population cycles in closed two-species habitats.

To compare this theory with results from the numerical model, we take values from the 2-D results, at the point where neutral density has been reduced to one-half its initial value. For CASE 2, this point is $z = 1.21\ cm$, $r = 2.64\ cm$. The values are $\dot{n}_{i,0} = 4.1 \times 10^{23}\ m^{-3}s^{-1}$, $n_e = 1.0 \times 10^{18} m^{-3}$, and $n_n = 1.5 \times 10^{19} m^{-3}$. This gives $f_i = 16.8\ kHz$, which is almost exactly the frequency generated by the simulation, shown in Figure 6-19. The nonlinear Equations 7.35 and 7.36 also exhibit periodic motion with nested trajectories, verified numerically. Furthermore, the nonlinear solution exhibits damping on the order seen in the numerical simulation.

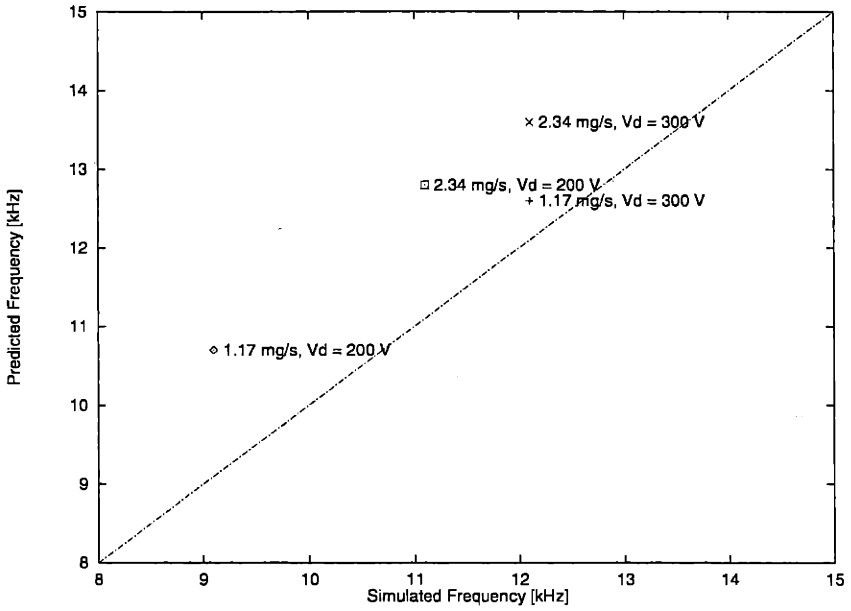

Figure 7-7: Comparison of frequency theoretically predicted, f_i, and from the numerical simulation, f_n, for several cases. $K_B = .15$, effective cathode at $z = 5\ mm$ downstream

In addition to comparison with the single nominal case, several other cases were run, and the low-frequency oscillations were analyzed. Using the same procedure for estimating the mean values in the ionization "box", theoretically predicted frequency, f_i, is determined. Figure 7-7 shows these frequencies compared with the oscillation frequency observed numerically. The agreement between the predator-prey theory and the full simulation is fairly good, considering the method of determining the "average" parameter values in the "box." What is interesting is that the frequency varies so little with operating conditions, except for a tendency to increase with V_d. This small increase is on the order of the fourth root of the ratio of voltages, as is predicted by Equation 7.46, assuming $v_i \sim \sqrt{V_d}$. Equation 7.45

implies that the frequency should increase with flow rate, assuming T_e remains constant. However, the numerical model predicted a slight drop in T_e at higher flow rates, which, due to the high sensitivity of the function $\xi(T_e)$, reduced the frequency.

Table 6.2 shows that, as power level increases, the amplitude of oscillations increases, and the damping constant decreases. Near the nominal conditions, the mode approaches a nonlinear limit cycle. The mechanism for this behavior is not yet known, but further analysis is planned for the future, when a better dynamic model of the power processing unit may be developed.

Although this simple predator-prey formulation does appear to describe the low-frequency oscillatory behavior produced in the numerical model quite well, its applicability to the real case is questionable. The frequency is much lower than that observed. However, if the ionization zone length, L, is shorter than modeled, by a factor of 3 or 4, this simple theory may explain the experimentally-observed freqency. Another difference is in the damping. While the theory here predicts a damped oscillator, some numerical cases approach a limit cycle. A mechanism for this has not been identified, but one possibility is some sort of inductive coupling with the power supply, which the simulation does not model.

7.9.3 Transit-Time Oscillations

Transit time oscillations observed in the numerical simulation may be related to those described before by Esipchuk et. al., [26], who measured inside the channel of a Hall thruster with electrostatic probes. In that research, the wave is described as a similar to a "quarter-wave standing mode," with an antinode near the anode and a node in the neighborhood of the channel exit. It was observed to have plasma potential variations of 10 to 30% of V_d. He also mentions that the wave is not very pronounced in regions where the magnetic field is small. This is consistent with the simulation results which show the instability highly amplified for CASE 5, with a higher B-field at the anode. For the SPT-70 cases (CASE 1 through CASE 4), with greatly reduced B-field near the anode, the model did not predict significant transit-time oscillations. Therefore, it is not expected that transit-time oscillations would be readily observable in the experimental data. In addition, according to Esipchuk, such oscillations would be irregular, and the oscillations observed were extremely regular.

7.9.4 Other Types of Oscillations

Many other types of oscillations are possible, and it is widely believed that some are responsible for the anomalous electron conductivity. Such oscillations near the exit of the channel would also explain the relatively low space potential growth there through induced cross-field transport, as described in Section 7.3. This has been observed before by Bishaev et. al., [10] who remark:

> "Results of oscillations study in the accelerating channel witness of their multiformity, but at optimum modes of operation, their intensity is insignificant and they should not play essential role with the exception of near-anode zone and of the zone with decreasing magnetic field at the exit."

Several previous works, including the one on oscillations by Esipchuk [26], have tried to pinpoint a single oscillation which may cause the measured electron transport, but none has succeeded. It has been supposed that this ellusive oscillation operates near the cyclotron frequency. Recent work by Baranov [6], for instance, suggests this. Also, work by Martinez-Sanchez (unpublished) shows azimuthal drift waves that are unstable, with growth rates which increase indefinitely as the wavenumber increases. The maximum wavelength is about the electron Larmor radius ($\sim 1\ mm$), where finite-orbit effects introduce damping. These extremely fast, short waves show the required phase shift between ϕ and n_e to produce axial transport, but would be hard to observe experimentally.

Chapter 8

Summary and Recommendations

The complete research project, including the numerical modeling, analysis, and experiment, yields some important gains in the understanding of the physics of the Hall thruster acceleration process. Perhaps more importantly, some new methodologies are developed which can greatly assist future research in this field.

8.1 Contributions of Methodology

The numerical model is the first of its kind to allow direct evaluation of hypothetical physical principles regarding Hall thruster operation. The nature of the method uniquely benefits research of physical phenomena observed experimentally. Also, the tool should prove extremely useful to Hall thruster designers.

Due to the particle nature of the scheme for heavy particle tracking, the effect of various modifications to the electric field on the individual ion trajectories may be studied. Particle impingement on the thruster surfaces may be used to estimate the lifetime of a particular thruster. Collisionality between ions and other particles is also easily implemented, allowing statistical computation of charge exchange and recombination in the plume. As demonstrated in the previous chapters, the distribution of ion energies is also determined. This information is considered critical to such issues as spacecraft integration.

Accurate performance estimates of various thruster geometries and magnetic field configurations suggest the numerical model to be a capable tool for design, as well. Thrust, torque, beam divergence, and efficiency can be computed for thrusters in the design phase, eliminating a portion of costly experimental testing. For various insulator wall configura-

tions, the total power lost to the walls can be estimated. Trade-offs between wall erosion rate and wall losses due to high secondary emission can then be made. In fact, for any configuration, a complete breakdown of the total power loss may be constructed, which may be extremely valuable for design purposes.

The numerical model also employs two new methodologies which may prove important for future generations of plasma simulators. The first is the technique of hybrid-PIC on a nonuniform grid. Since the spatial grid does not have a closed-form mapping to the computational grid, a scheme of integration and correction is devised to accurately move particles and track their positions in both coordinate systems with minimum computational demand. The second advance is a detachment of ions and neutrals, such that particles may have variable mass. This allows an extra degree of freedom that was used in fixing the statistical rate of particle generation at each grid point. With this method, statistical significance is automatically maintained at each cell, and computational efficiency is maximized by moving "just enough" particles.

Some advances were also made in methods of electrostatic probe disgnostics of Hall thrusters. The method of calibrating the ion collection area of the triple probe is novel. Variation of ion collection area of the measurement probe with position was calibrated with a second probe with known collecting area. Also, a technique was proven which allowed calculation of the plasma parameters for very general voltage-current models using multiple simultaneously-sampled electrodes.

8.2 Physics of the Acceleration Process

Using the results from the numerical model in comparison with experimental data from this, and other, research, several conclusions about the physics of the acceleration process in Hall thrusters can be summarized.

First, the assumption of isothermal electrons along lines of force does not exactly hold in the near-plume region. The worst-case measured deviation showed electron temperature dropping as $n_e^{\frac{1}{6}}$. This is much less than the adiabatic relationship would imply, but not quite isothermal, so it is expected that heat conduction plays a strong role along lines of force.

According to the numerical model, three distinct regions of physics exist in the acceler-

ation channel: acceleration, ionization, and diffusion. In the acceleration region, the forces on electrons are balanced between a strong electric field and opposite pressure gradient, and transport plays little role. In the ionization zone, the plasma is highly collisional, and the plasma density peaks. In the diffusion region, density trails off almost linearly to the anode through a region of almost zero electric field. This agrees with existing theory, and attests to the validity of the numerical model.

The secondary emission coefficient of the dielectric wall was found to influence the energy lost to the wall. In cases run without secondary emission from the walls, the energy loss decreased by around 70%. The remaining energy was lost due to inelastic collisions with neutrals.

As in experimental measurements, the ion energy distribution from the numerical model contained ions with energies higher than the discharge potential. These high-energy ions, it was determined, were generated as an effect of the time-varying electric field associated with oscillations.

On the issue of desirable magnetic field profiles, current design practice includes a requirement of positive magnetic field gradient from the anode to the cathode. Upon modeling two cases, with different magnetic field gradients, it was found that the case with higher field gradient was the more stable. Severe efficiency-limiting transit-time oscillations developed in one case where the magnetic field at the cathode was 25% of the peak. It is not clear at this point if the oscillations observed in the model are the same as observed experimentally. And, in fact, the basis for the requirement of positive magnetic field is said to be very high frequency (MHz) azimuthal waves, which the simulation does not model. Therefore, although the simulation predicted the same requirement on magnetic field profile, it did so for a different reason.

Plasma oscillations were observed in the numerical model as well as in the electrostatic probe experiments. According to experiment, the dominant modes were between 25 and 65 kHz for operating conditions near nominal. The numerical model, on the other hand, predicts an oscillation in the 13 kHz range. The dynamics of the oscillations predicted are related to an ionization instability, analogous to the predator-prey dynamics in a closed population. The frequency is predicted to be $\sim \frac{1}{L}$, where L is the length of the ionization zone. Since the model predicts the ionization zone to be approximately 3 times the width measured by Bishaev and Kim, the possibility exists that this mechanism could generate

frequencies on the order of 40 kHz, as measured. However, no conclusive evidence was found to this effect.

A model for increased measured efficiency with facility pressure was formulated, where the additional propellant ionized is some fraction of the mean random flux through the annular channel area. This fraction was found numerically to be 1.7, the excess over unity being from ionization taking place outside the channel, and some additional primary ionization as a result of the higher plasma density.

Disagreement persists between the model and experiment regarding the physics in the near-plume region. The model predicts large potential gradients outside the plume, and most ion acceleration happening there. Electrostatic probe experiments, on the other hand, suggest very little acceleration outside the channel, with the plasma potential going only as high as 35 V. This discrepancy has not been resolved. A possibile cause is anomalous conductivity. Azimuthally rotating oscillations just outside the channel may contribute to transport of electrons across the field lines with very little cross-field potential gradient. Another possiblity is near-wall electron transport, in which wall scattering disrupts the electron Larmor gyration. In either case, since the potential rise starts abruptly just inside the accelerator channel, it is felt that the grounded metallic wall must play some role in enhancing electron diffusion.

8.3 Recommendations

The understanding of the physics of Hall thruster discharge oscillations is still incomplete. Most measurements have been made at single operating points, limiting their usefulness. Collection of data regarding oscillations at a variety of operating points would allow better identification of the mechanisms, as well as help in comparison between different devices. Some contribution has been made here by measurement of the PSD at a variety of operating points, but such a data set with local measurements inside the channel would be extremely useful. Once a larger data set is available, more definite correlations can be made about the physics of oscillations.

The physics of the near-plume region are not well understood. The disparity between the numerical and experimental data there implies the presence of high electron diffusion for which no analytical model is available. The electrical connection to the thruster body

may influence this region. It is recommended that the 2-D near-plume surveys be repeated with the thruster body biased to various potentials while measuring the current collected by the thruster body.

The numerical model works well for most Hall thruster geometries, but the combination of the fluid and particle methods was accomplished only with great difficulty and at great computational expense. A different method, still using hybrid-PIC should be investigated which uses, perhaps, an unstructured grid which can be made more general at the boundaries and interfaces of the two systems. Also, a brute-force particle-particle method should be considered, because of the potential there to model the complete distribution function of electrons. Such a method would require increased computational power which new array and parallel processors may shortly be able to provide.

One of the gaping holes in Hall thruster research is the mechanism of anomalous electron transport. Several theories have been put forth, but none has been irrefutable. Some more basic tests to quantify this transport and diagnose its nature would be extremely valuable. One might begin with simple tests in the near plume to better quantify the total electron cross-field current in that region for various conditions. Then, a match may be found with current theory.

$\sim 40\ hrs$ from BOL

PSD of I_a

$\dot{m} = 1.17\ mg/s$

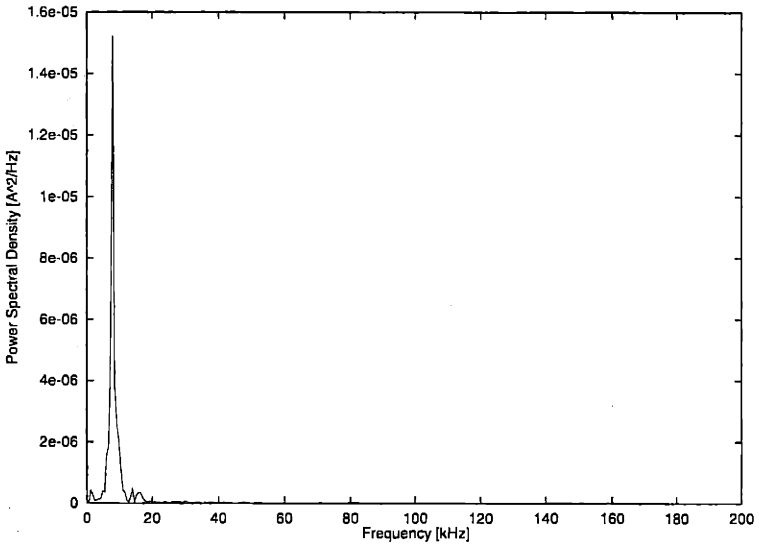

Figure A-1: Power spectral density $[A^2/Hz]$ of I_a, $\dot{m} = 1.17\ mg/s$, $V_d = 100\ V$, $\sim 40\ hrs$ from BOL.

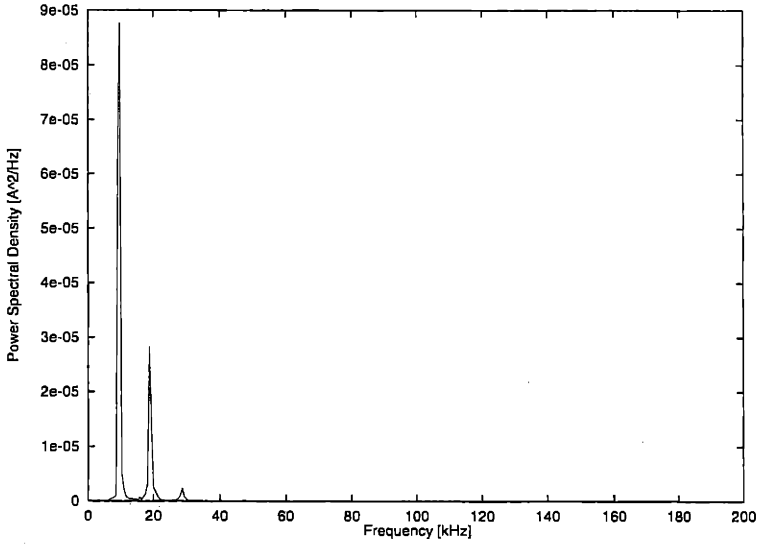

Figure A-2: Power spectral density $[A^2/Hz]$ of I_a, $\dot{m} = 1.17\ mg/s$, $V_d = 125\ V$, $\sim 40\ hrs$ from BOL.

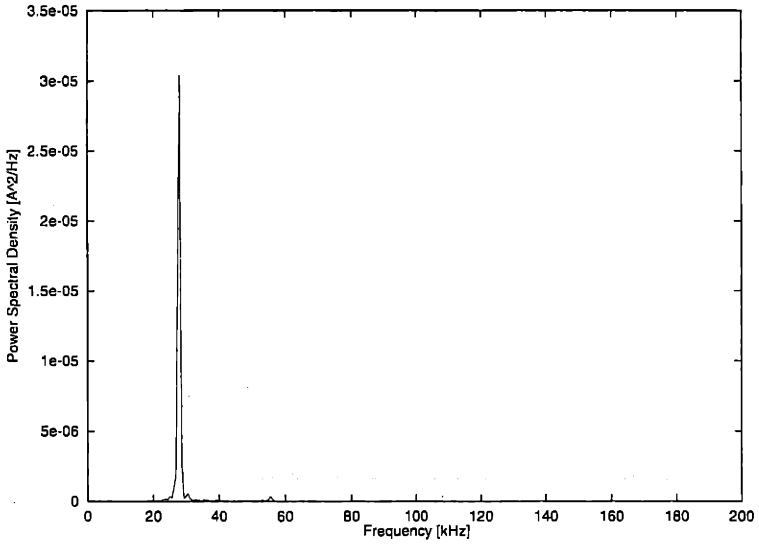

Figure A-5: Power spectral density $[A^2/Hz]$ of I_a, $\dot{m} = 1.17\ mg/s$, $V_d = 200\ V$, $\sim 40\ hrs$ from BOL.

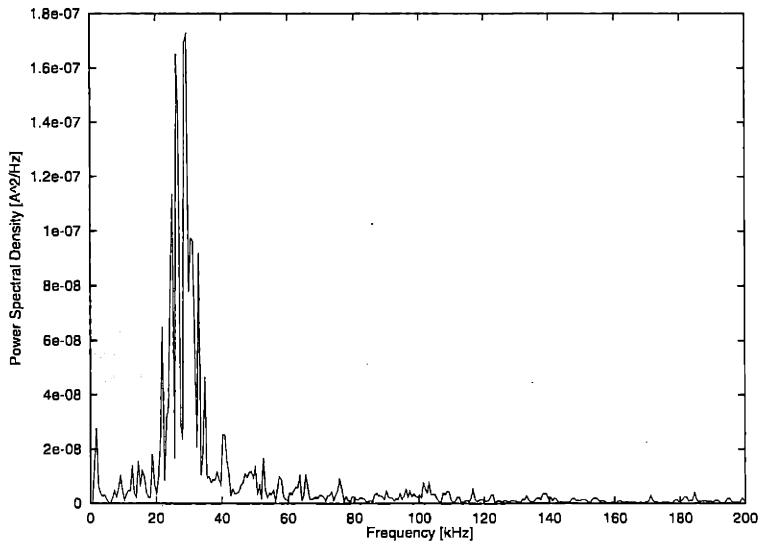

Figure A-6: Power spectral density $[A^2/Hz]$ of I_a, $\dot{m} = 1.17\ mg/s$, $V_d = 225\ V$, $\sim 40\ hrs$ from BOL.

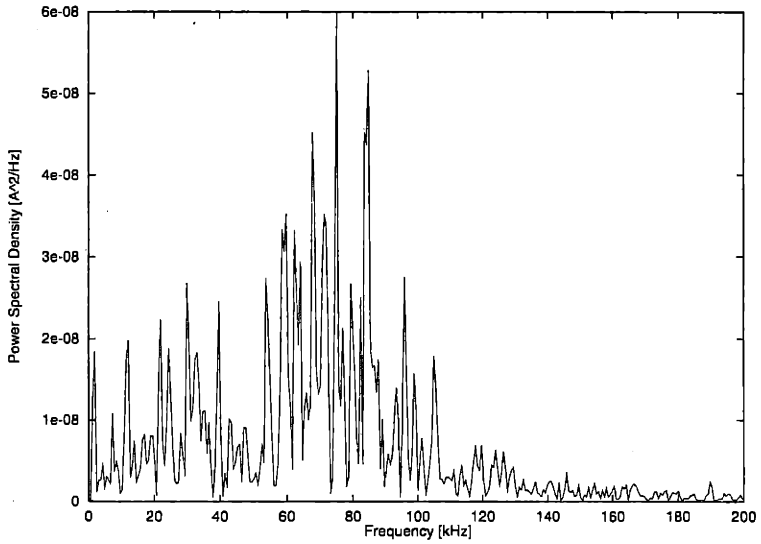

Figure A-9: Power spectral density $[A^2/Hz]$ of I_a, $\dot{m} = 1.17\ mg/s$, $V_d = 300\ V$, $\sim 40\ hrs$ from BOL.

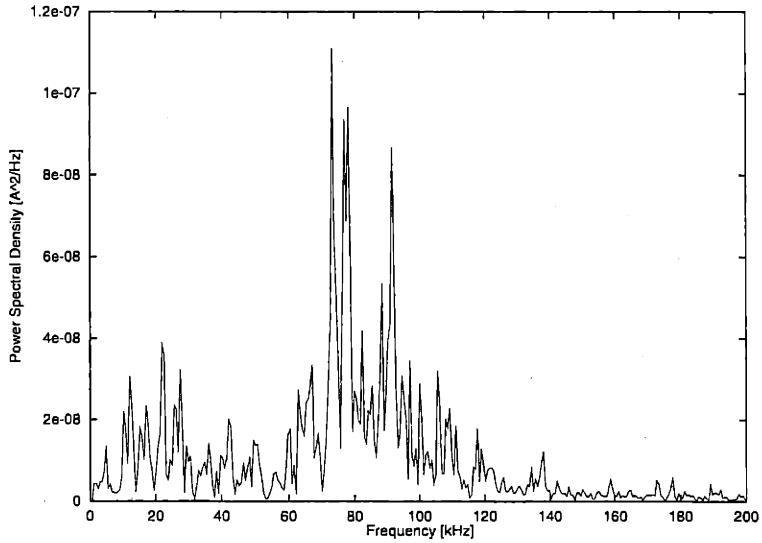

Figure A-10: Power spectral density $[A^2/Hz]$ of I_a, $\dot{m} = 1.17\ mg/s$, $V_d = 325\ V$, $\sim 40\ hrs$ from BOL.

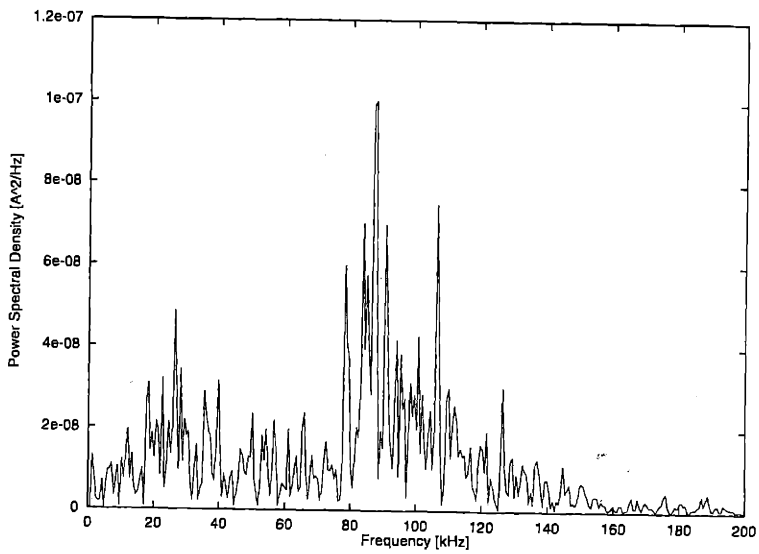

Figure A-11: Power spectral density $[A^2/Hz]$ of I_a, $\dot{m} = 1.17\ mg/s$, $V_d = 350\ V$, $\sim 40\ hrs$ from BOL.

$\sim 40\ hrs$ from BOL

PSD of I_a

$\dot{m} = 1.76\ mg/s$

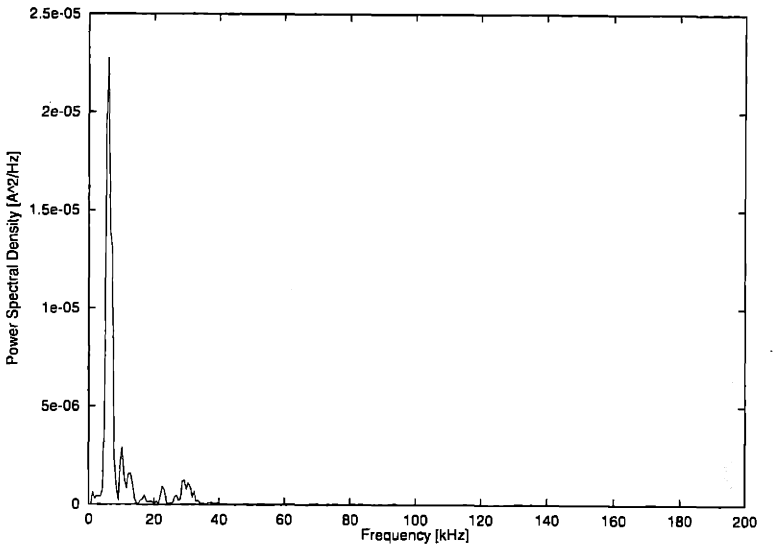

Figure A-12: Power spectral density $[A^2/Hz]$ of I_a, $\dot{m} = 1.76\ mg/s$, $V_d = 100\ V$, $\sim 40\ hrs$ from BOL.

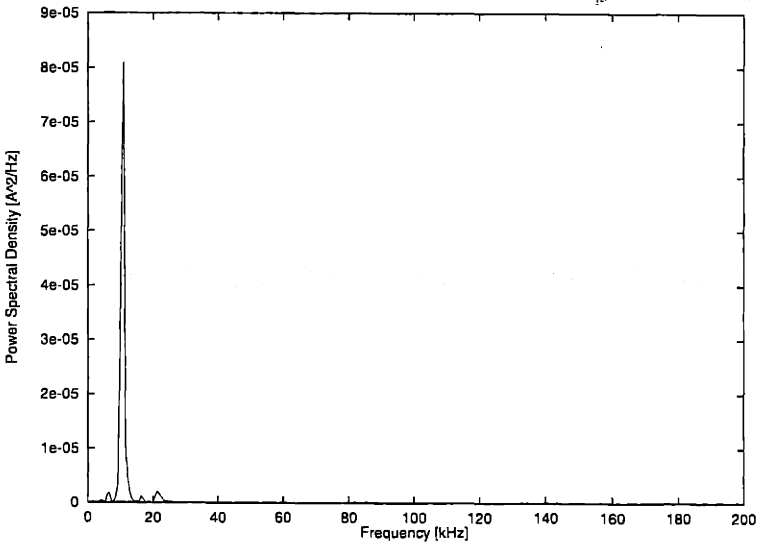

Figure A-13: Power spectral density $[A^2/Hz]$ of I_a, $\dot{m} = 1.76\ mg/s$, $V_d = 125\ V$, $\sim 40\ hrs$ from BOL.

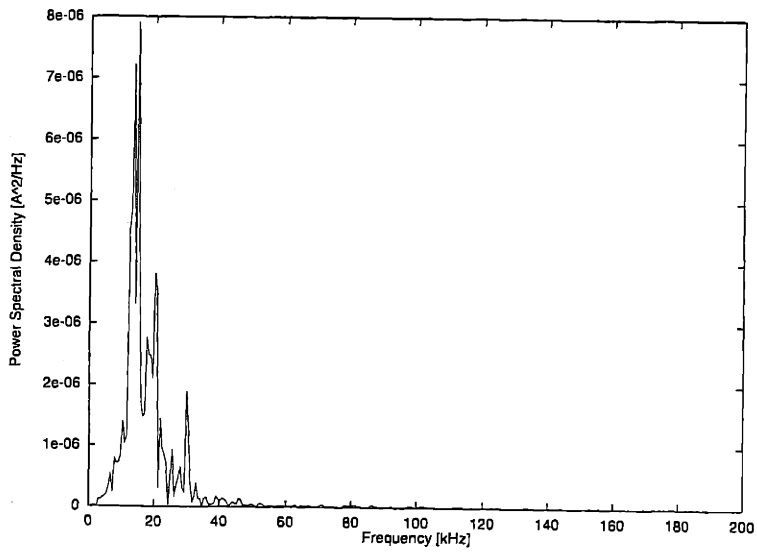

Figure A-14: Power spectral density $[A^2/Hz]$ of I_a, $\dot{m} = 1.76\ mg/s$, $V_d = 150\ V$, $\sim 40\ hrs$ from BOL.

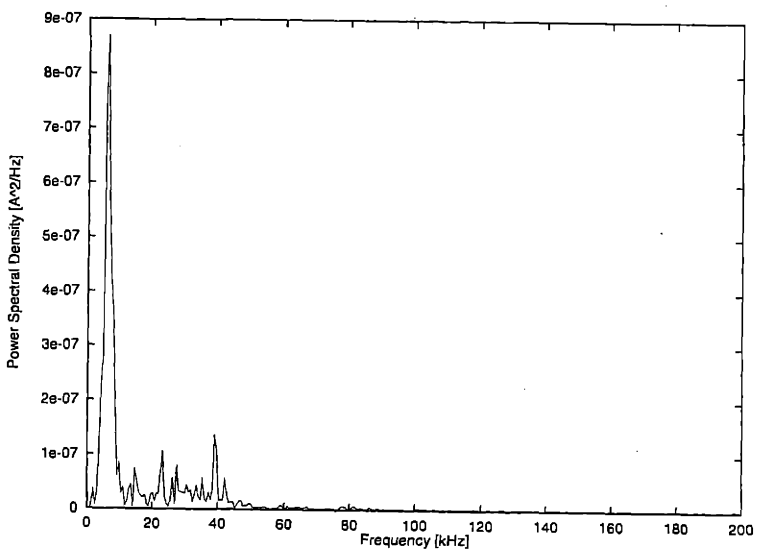

Figure A-15: Power spectral density $[A^2/Hz]$ of I_a, $\dot{m} = 1.76\ mg/s$, $V_d = 175\ V$, $\sim 40\ hrs$ from BOL.

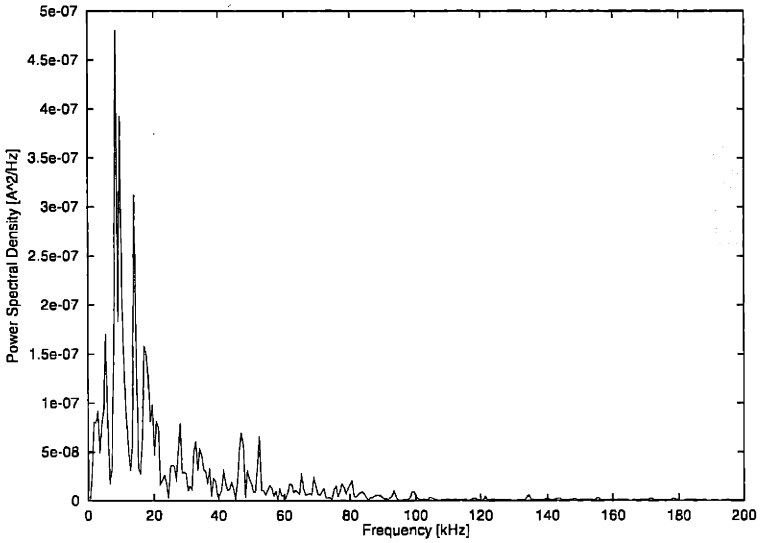

Figure A-16: Power spectral density $[A^2/Hz]$ of I_a, $\dot{m} = 1.76\ mg/s$, $V_d = 200\ V$, $\sim 40\ hrs$ from BOL.

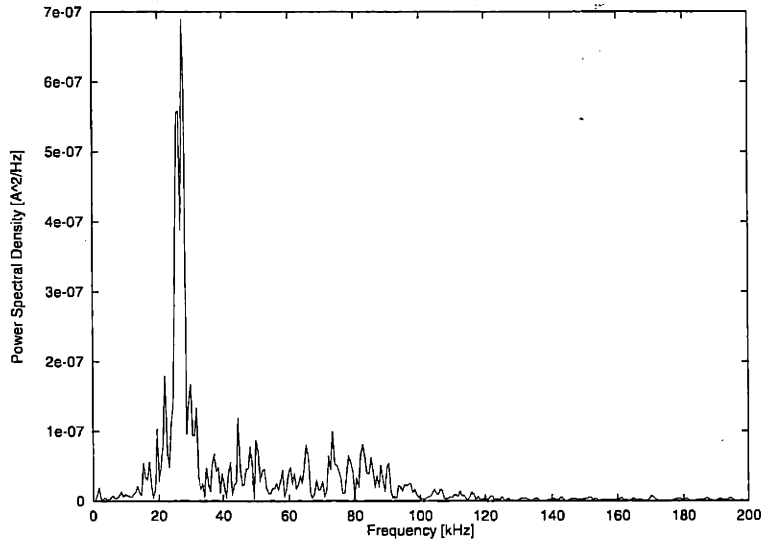

Figure A-17: Power spectral density $[A^2/Hz]$ of I_a, $\dot{m} = 1.76\ mg/s$, $V_d = 225\ V$, $\sim 40\ hrs$ from BOL.

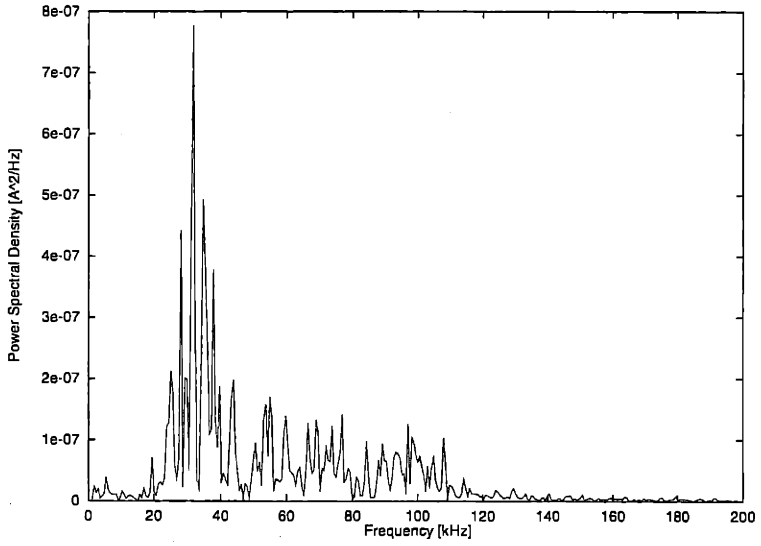

Figure A-18: Power spectral density $[A^2/Hz]$ of I_a, $\dot{m} = 1.76\ mg/s$, $V_d = 250\ V$, $\sim 40\ hrs$ from BOL.

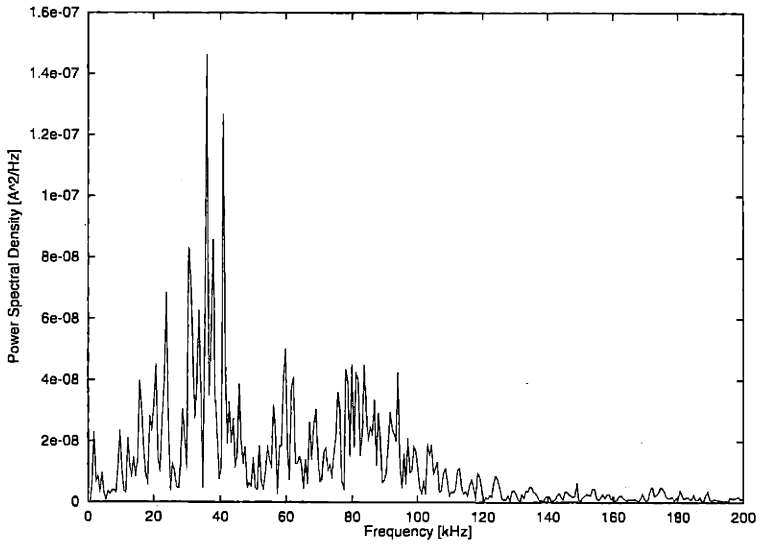

Figure A-19: Power spectral density $[A^2/Hz]$ of I_a, $\dot{m} = 1.76\ mg/s$, $V_d = 275\ V$, $\sim 40\ hrs$ from BOL.

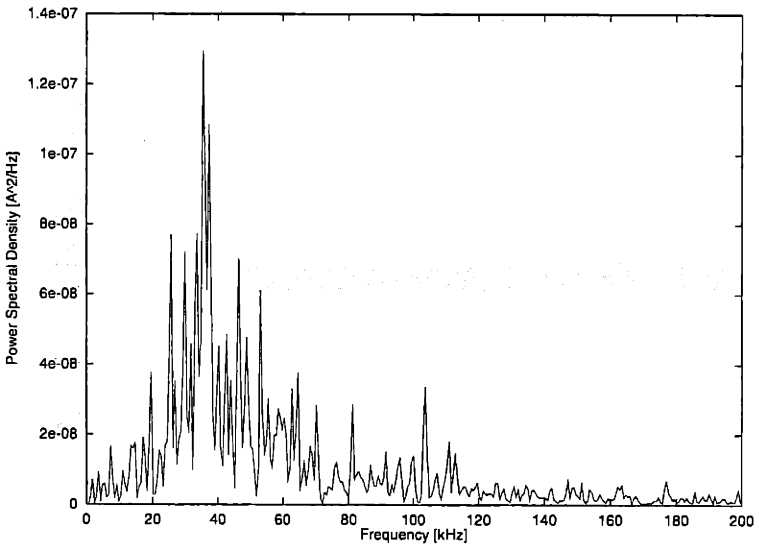

Figure A-20: Power spectral density $[A^2/Hz]$ of I_a, $\dot{m} = 1.76\ mg/s$, $V_d = 300\ V$, $\sim 40\ hrs$ from BOL.

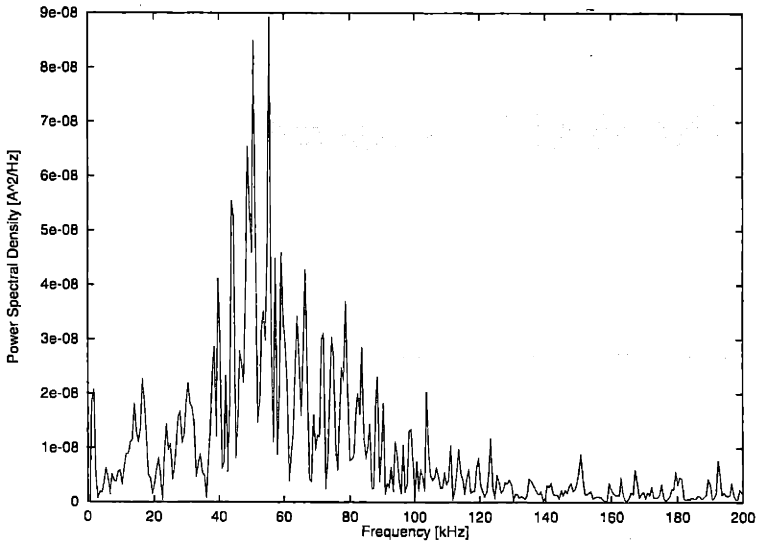

Figure A-21: Power spectral density $[A^2/Hz]$ of I_a, $\dot{m} = 1.76\ mg/s$, $V_d = 325\ V$, $\sim 40\ hrs$ from BOL.

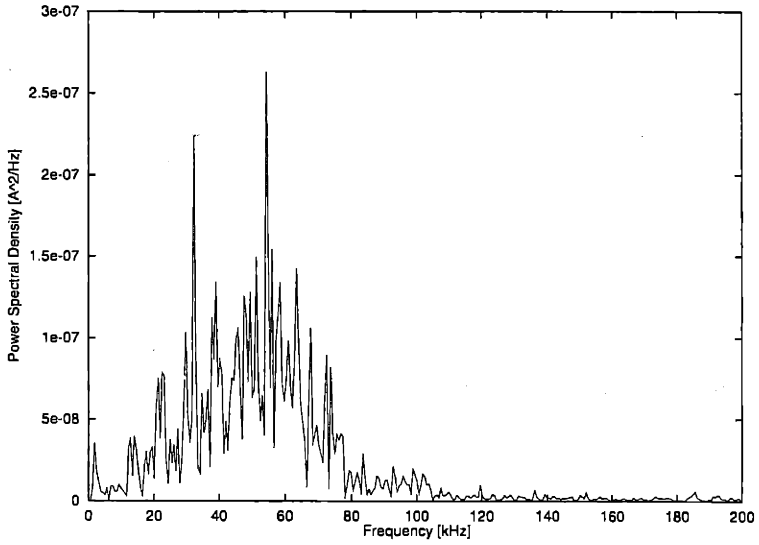

Figure A-22: Power spectral density $[A^2/Hz]$ of I_a, $\dot{m} = 1.76\ mg/s$, $V_d = 350\ V$, $\sim 40\ hrs$ from BOL.

$\sim 40\ hrs$ from BOL

PSD of I_a

$\dot{m} = 2.34\ mg/s$

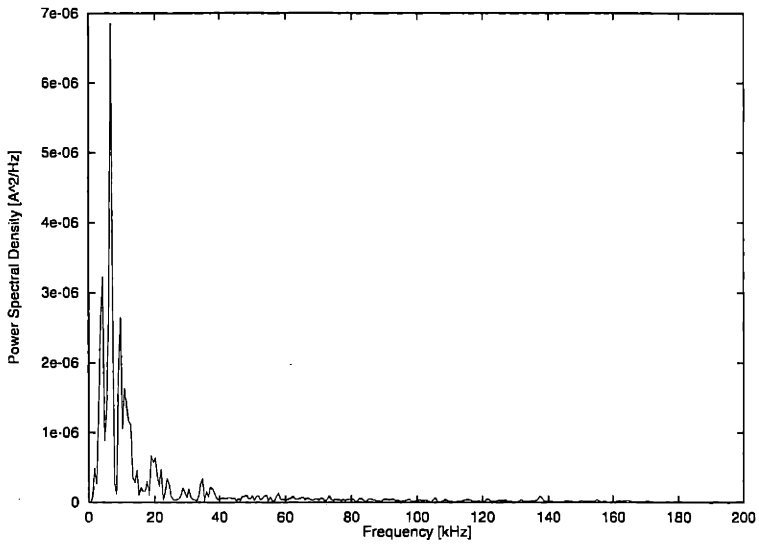

Figure A-23: Power spectral density $[A^2/Hz]$ of I_a, $\dot{m} = 2.34\ mg/s$, $V_d = 100\ V$, $\sim 40\ hrs$ from BOL.

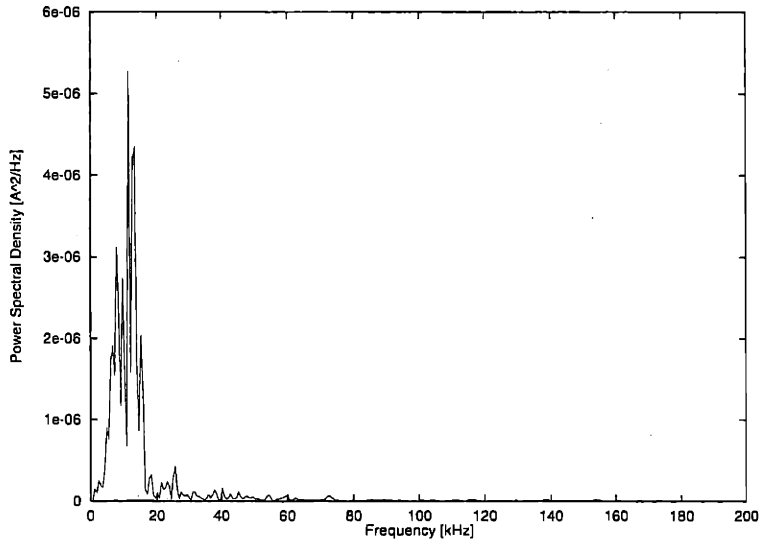

Figure A-24: Power spectral density $[A^2/Hz]$ of I_a, $\dot{m} = 2.34\ mg/s$, $V_d = 125\ V$, $\sim 40\ hrs$ from BOL.

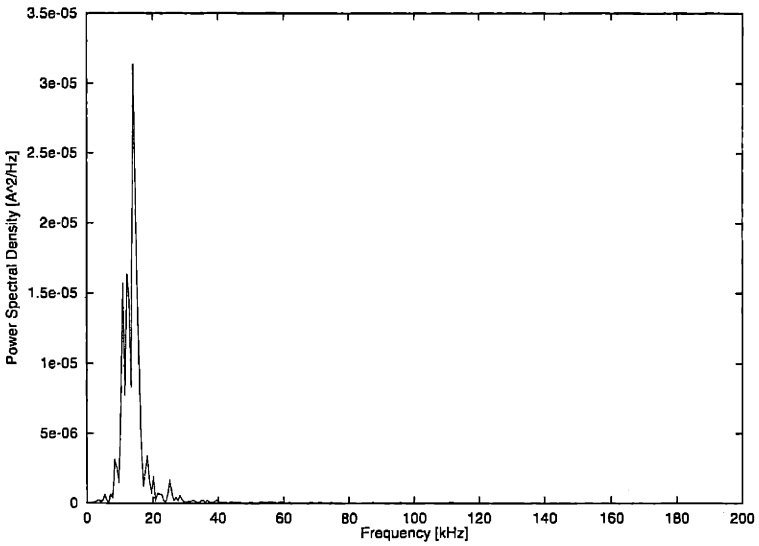

Figure A-25: Power spectral density $[A^2/Hz]$ of I_a, $\dot{m} = 2.34\ mg/s$, $V_d = 150\ V$, $\sim 40\ hrs$ from BOL.

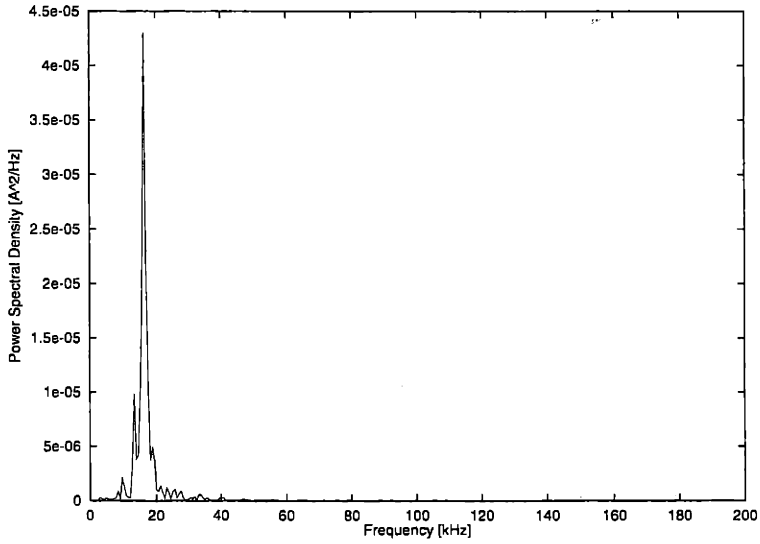

Figure A-26: Power spectral density $[A^2/Hz]$ of I_a, $\dot{m} = 2.34\ mg/s$, $V_d = 175\ V$, $\sim 40\ hrs$ from BOL.

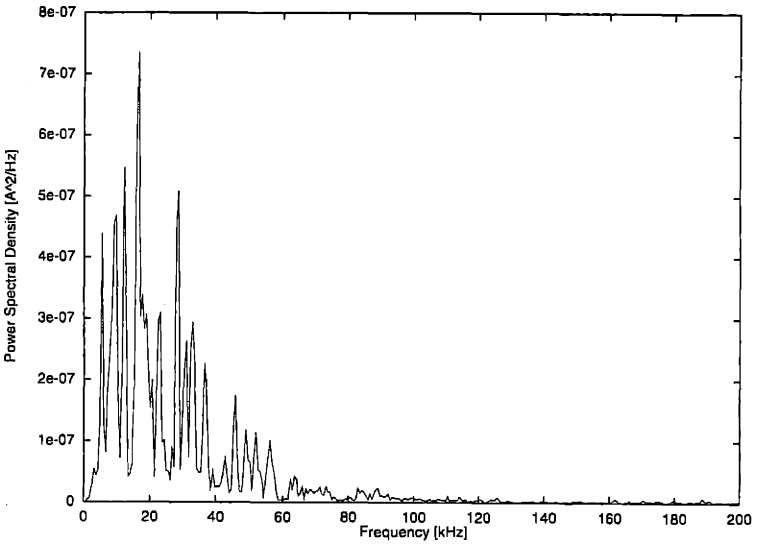

Figure A-27: Power spectral density $[A^2/Hz]$ of I_a, $\dot{m} = 2.34\ mg/s$, $V_d = 200\ V$, $\sim 40\ hrs$ from BOL.

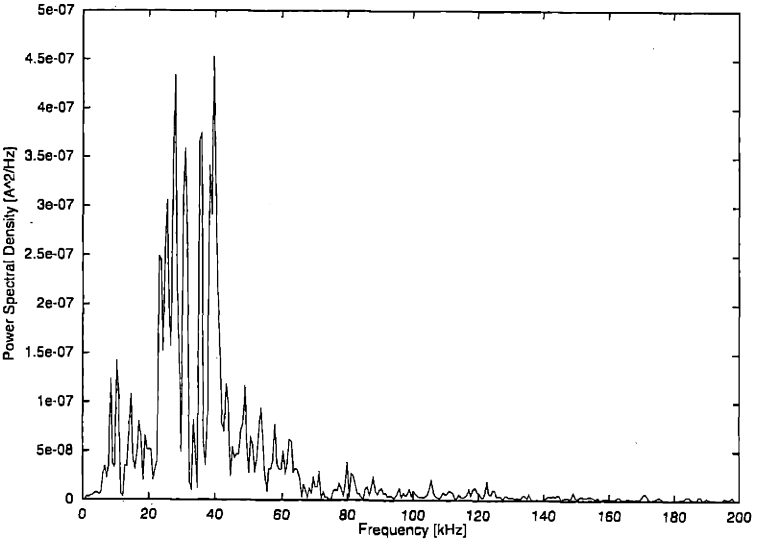

Figure A-28: Power spectral density $[A^2/Hz]$ of I_a, $\dot{m} = 2.34\ mg/s$, $V_d = 225\ V$, $\sim 40\ hrs$ from BOL.

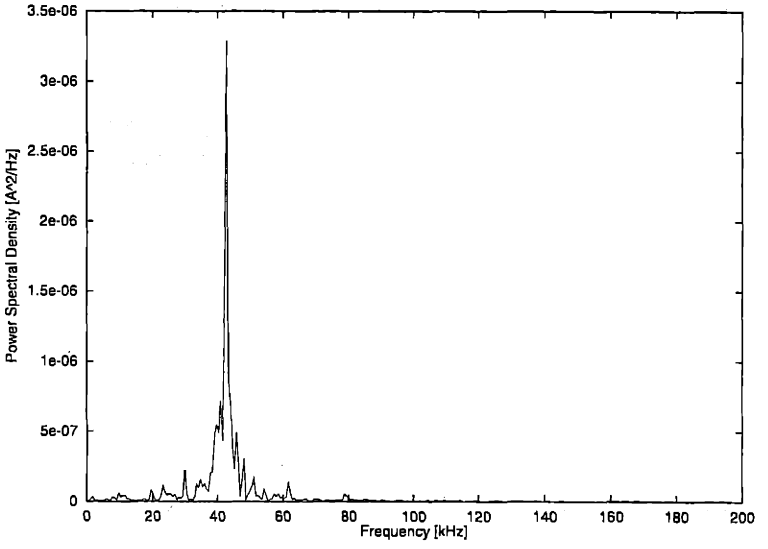

Figure A-29: Power spectral density $[A^2/Hz]$ of I_a, $\dot{m} = 2.34\ mg/s$, $V_d = 250\ V$, $\sim 40\ hrs$ from BOL.

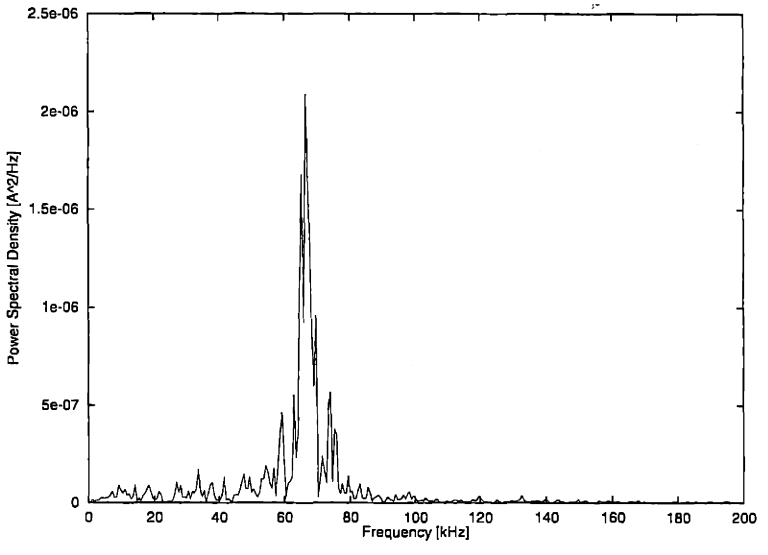

Figure A-30: Power spectral density $[A^2/Hz]$ of I_a, $\dot{m} = 2.34\ mg/s$, $V_d = 275\ V$, $\sim 40\ hrs$ from BOL.

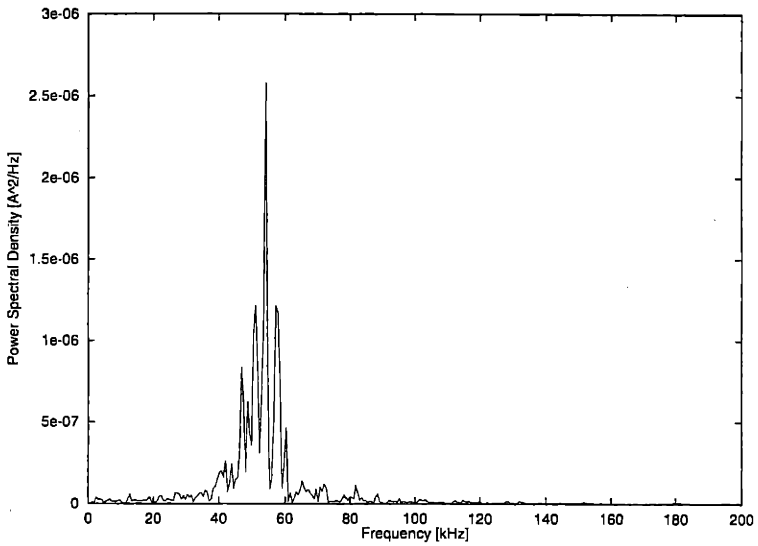

Figure A-31: Power spectral density $[A^2/Hz]$ of I_a, $\dot{m} = 2.34\ mg/s$, $V_d = 300\ V$, $\sim 40\ hrs$ from BOL.

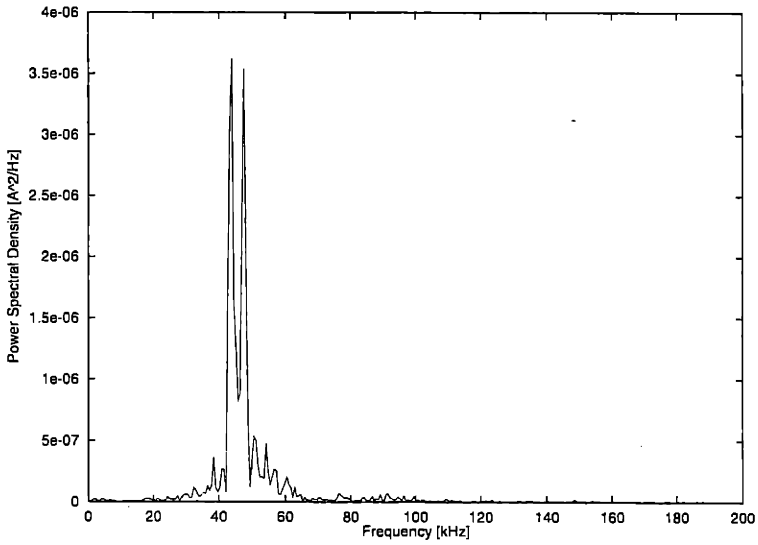

Figure A-32: Power spectral density $[A^2/Hz]$ of I_a, $\dot{m} = 2.34\ mg/s$, $V_d = 325\ V$, $\sim 40\ hrs$ from BOL.

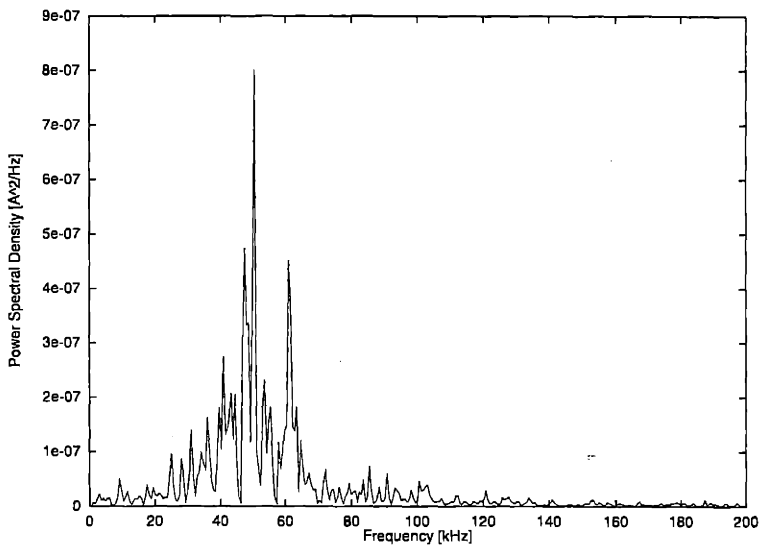

Figure A-33: Power spectral density $[A^2/Hz]$ of I_a, $\dot{m} = 2.34\ mg/s$, $V_d = 350\ V$, $\sim 40\ hrs$ from BOL.

$\sim 40\ hrs$ from BOL

PSD of I_a

$\dot{m} = 2.93\ mg/s$

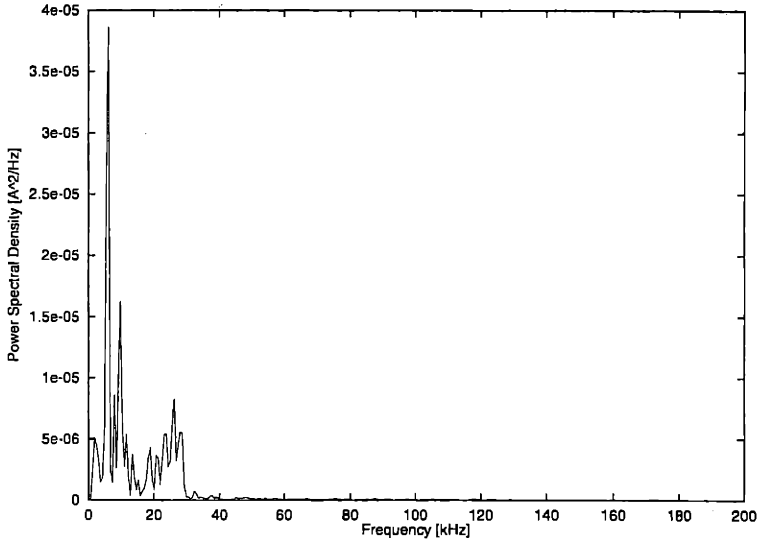

Figure A-34: Power spectral density $[A^2/Hz]$ of I_a, $\dot{m} = 2.93\ mg/s$, $V_d = 100\ V$, $\sim 40\ hrs$ from BOL.

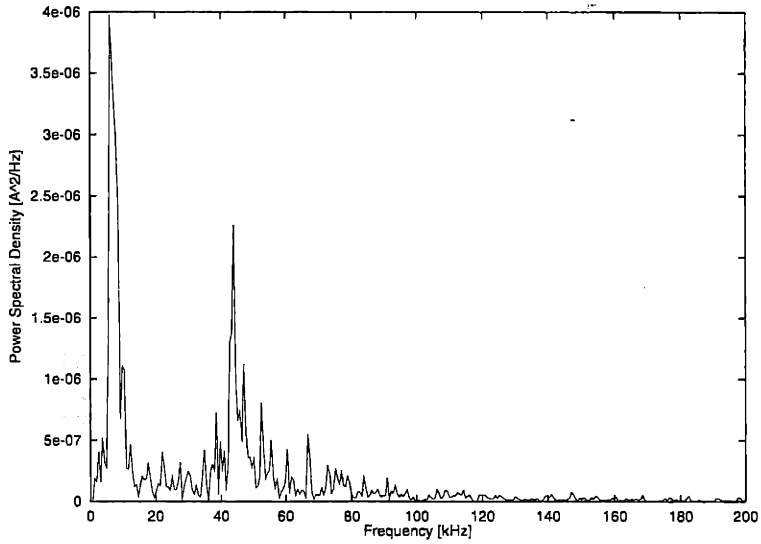

Figure A-35: Power spectral density $[A^2/Hz]$ of I_a, $\dot{m} = 2.93\ mg/s$, $V_d = 125\ V$, $\sim 40\ hrs$ from BOL.

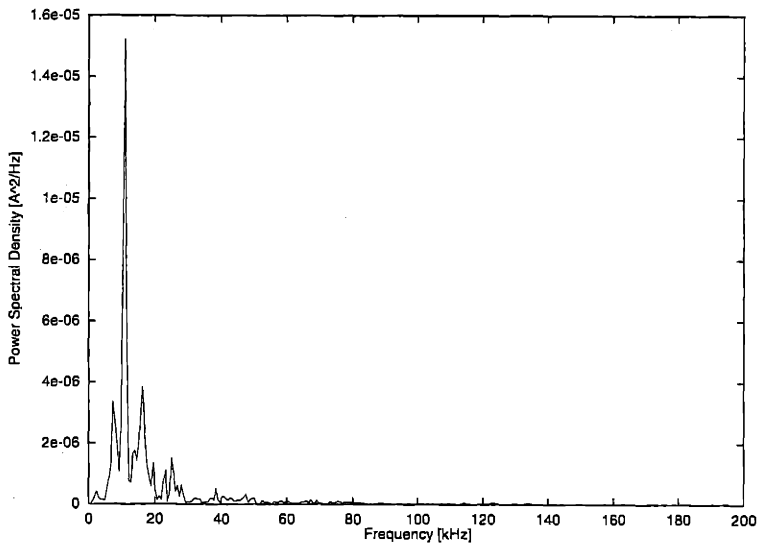

Figure A-36: Power spectral density $[A^2/Hz]$ of I_a, $\dot{m} = 2.93\ mg/s$, $V_d = 150\ V$, $\sim 40\ hrs$ from BOL.

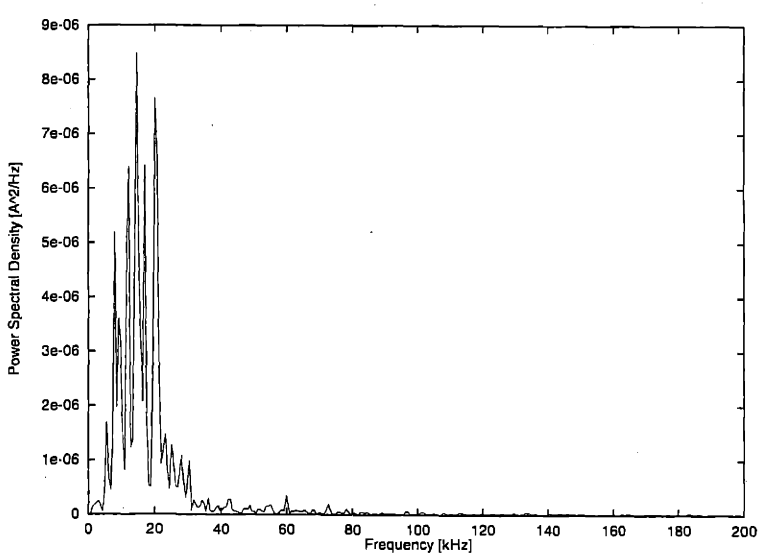

Figure A-37: Power spectral density $[A^2/Hz]$ of I_a, $\dot{m} = 2.93\ mg/s$, $V_d = 175\ V$, $\sim 40\ hrs$ from BOL.

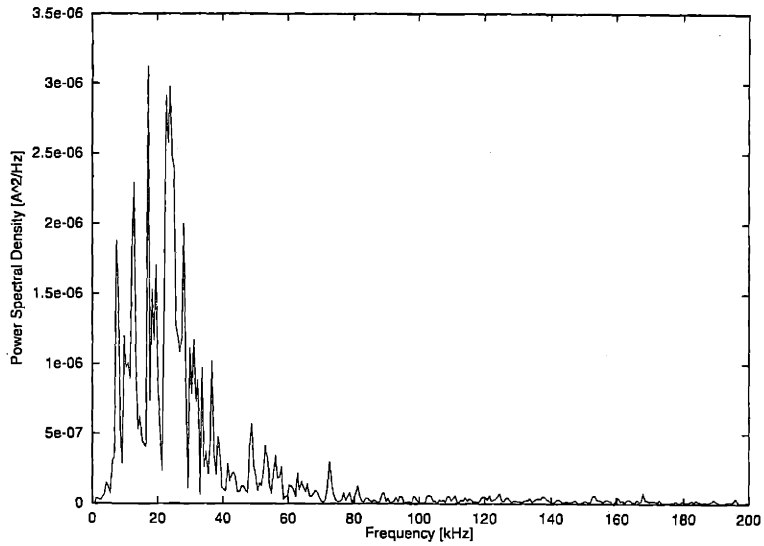

Figure A-38: Power spectral density $[A^2/Hz]$ of I_a, $\dot{m} = 2.93\ mg/s$, $V_d = 200\ V$, $\sim 40\ hrs$ from BOL.

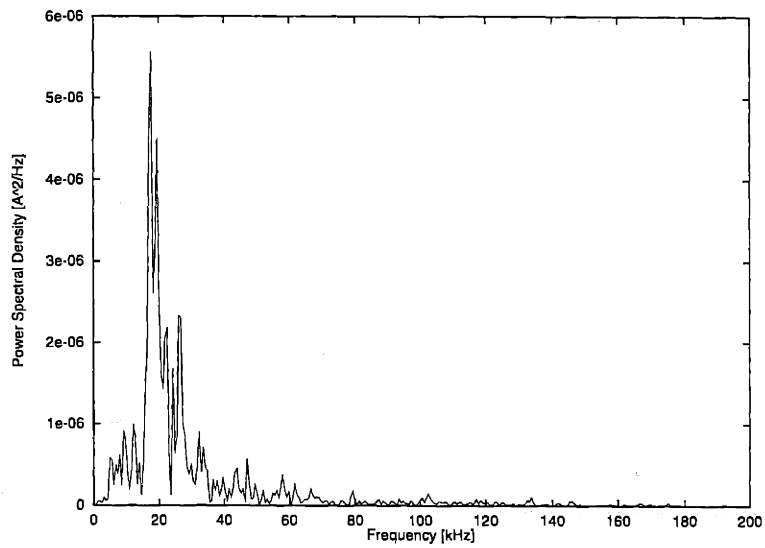

Figure A-39: Power spectral density $[A^2/Hz]$ of I_a, $\dot{m} = 2.93\ mg/s$, $V_d = 225\ V$, $\sim 40\ hrs$ from BOL.

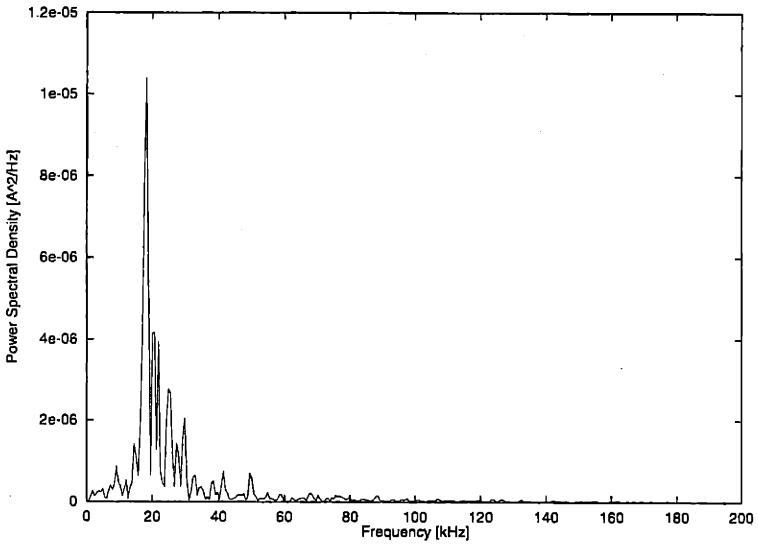

Figure A-40: Power spectral density $[A^2/Hz]$ of I_a, $\dot{m} = 2.93\ mg/s$, $V_d = 250\ V$, $\sim 40\ hrs$ from BOL.

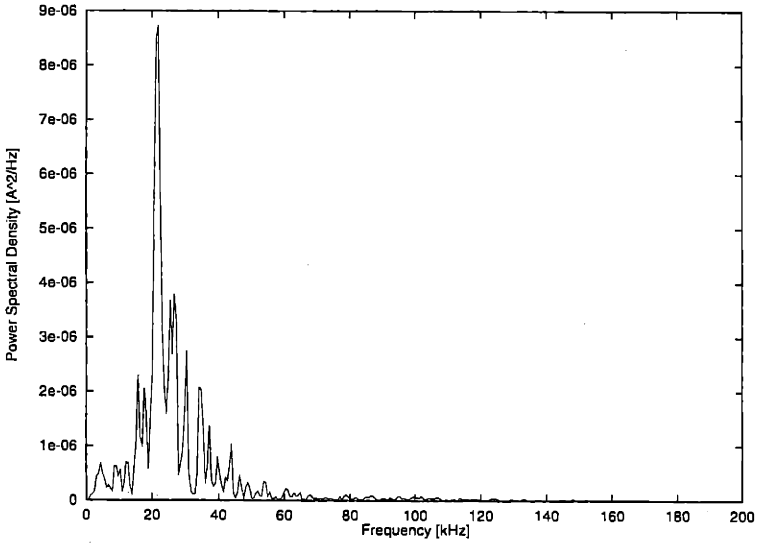

Figure A-41: Power spectral density $[A^2/Hz]$ of I_a, $\dot{m} = 2.93\ mg/s$, $V_d = 275\ V$, $\sim 40\ hrs$ from BOL.

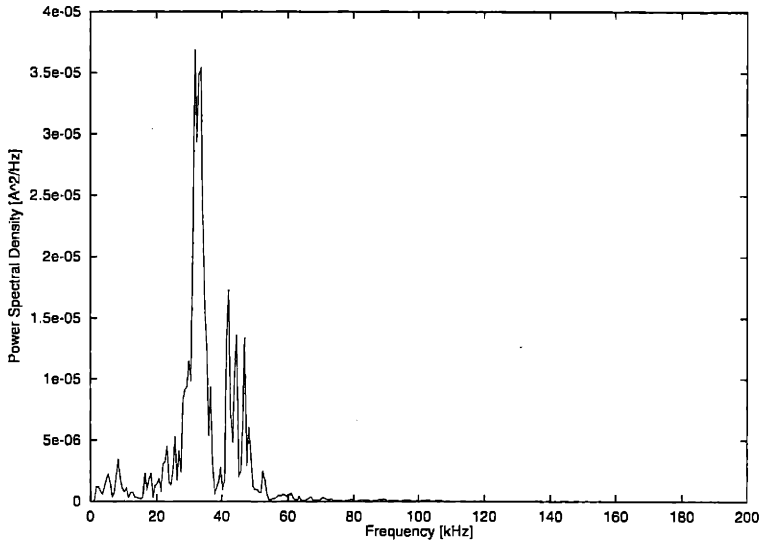

Figure A-42: Power spectral density $[A^2/Hz]$ of I_a, $\dot{m} = 2.93\ mg/s$, $V_d = 300\ V$, $\sim 40\ hrs$ from BOL.

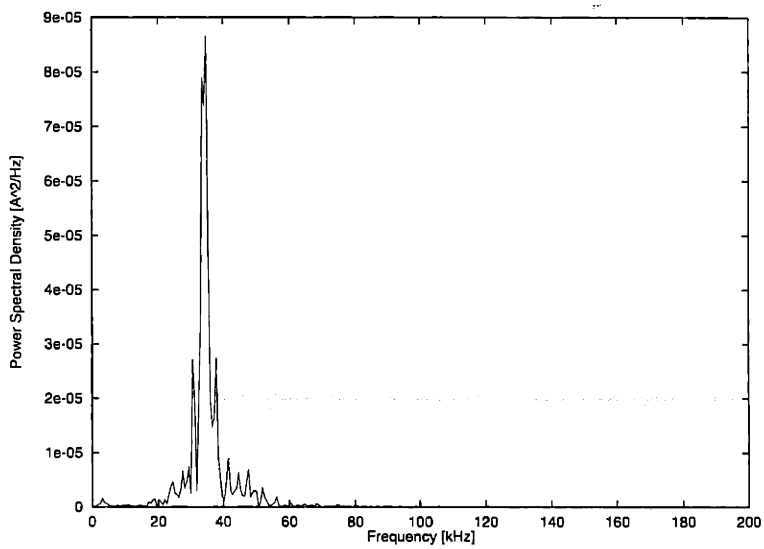

Figure A-43: Power spectral density $[A^2/Hz]$ of I_a, $\dot{m} = 2.93\ mg/s$, $V_d = 325\ V$, $\sim 40\ hrs$ from BOL.

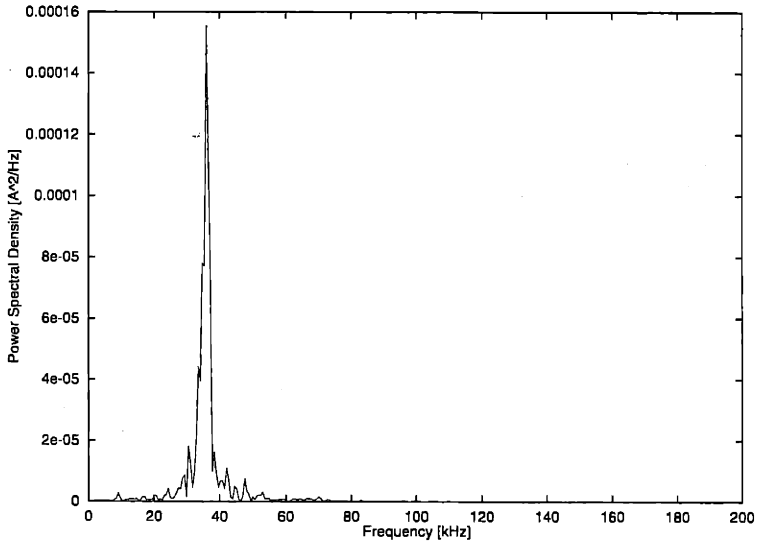

Figure A-44: Power spectral density $[A^2/Hz]$ of I_a, $\dot{m} = 2.93\ mg/s$, $V_d = 350\ V$, $\sim 40\ hrs$ from BOL.

$\sim 80\ hrs$ from BOL

PSD of I_a

$\dot{m} = 1.17\ mg/s$

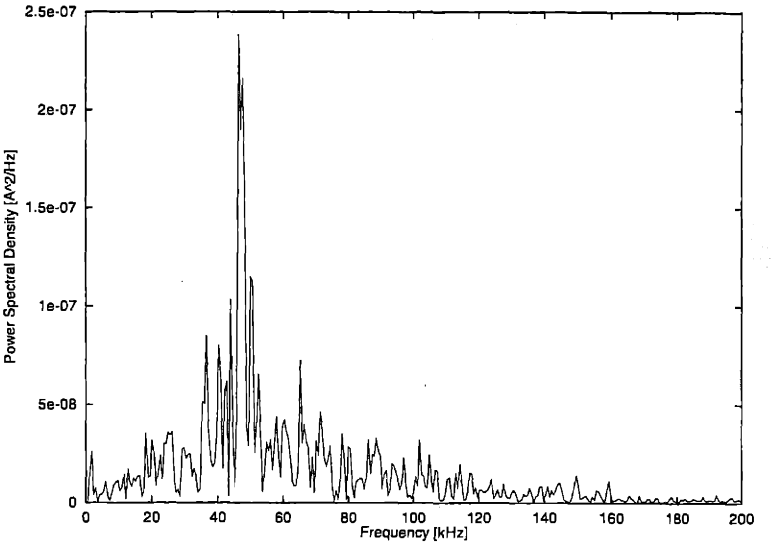

Figure A-47: Power spectral density $[A^2/Hz]$ of I_a, $\dot{m} = 1.17\ mg/s$, $V_d = 300\ V$, $\sim 80\ hrs$ from BOL.

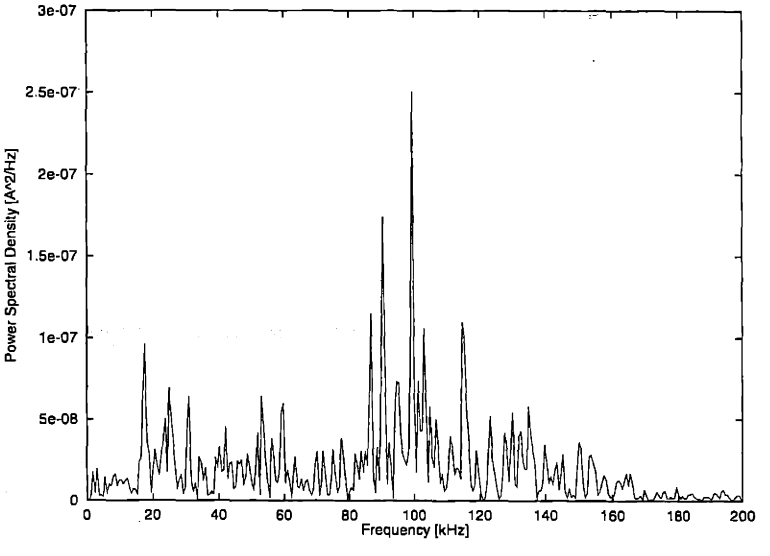

Figure A-48: Power spectral density $[A^2/Hz]$ of I_a, $\dot{m} = 1.17\ mg/s$, $V_d = 350\ V$, $\sim 80\ hrs$ from BOL.

$\sim 80\ hrs$ from BOL

PSD of I_a

$\dot{m} = 1.76\ mg/s$

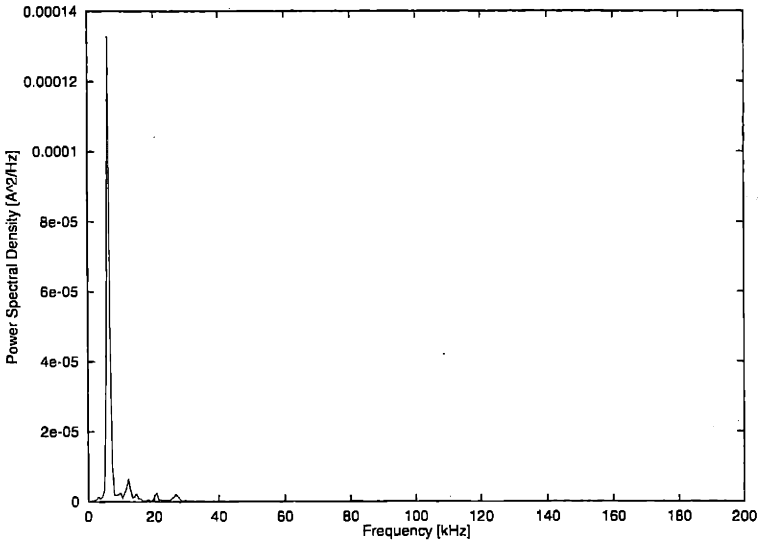

Figure A-49: Power spectral density $[A^2/Hz]$ of I_a, $\dot{m} = 1.76\ mg/s$, $V_d = 100\ V$, $\sim 80\ hrs$ from BOL.

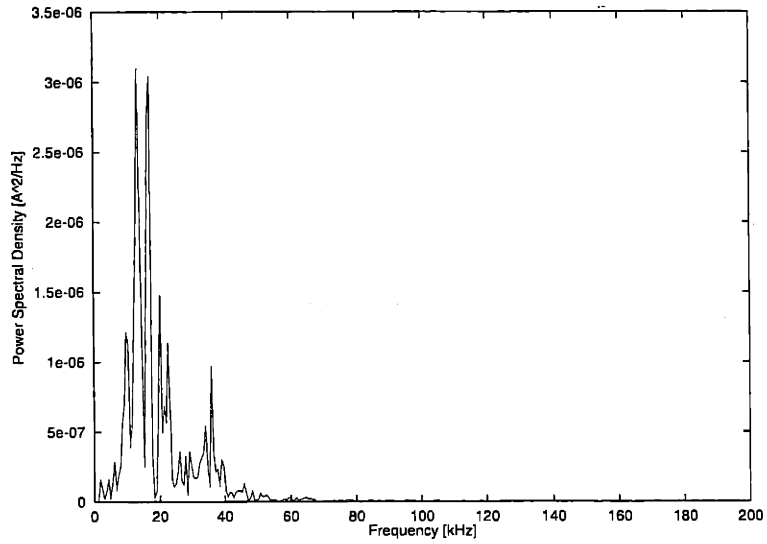

Figure A-50: Power spectral density $[A^2/Hz]$ of I_a, $\dot{m} = 1.76\ mg/s$, $V_d = 150\ V$, $\sim 80\ hrs$ from BOL.

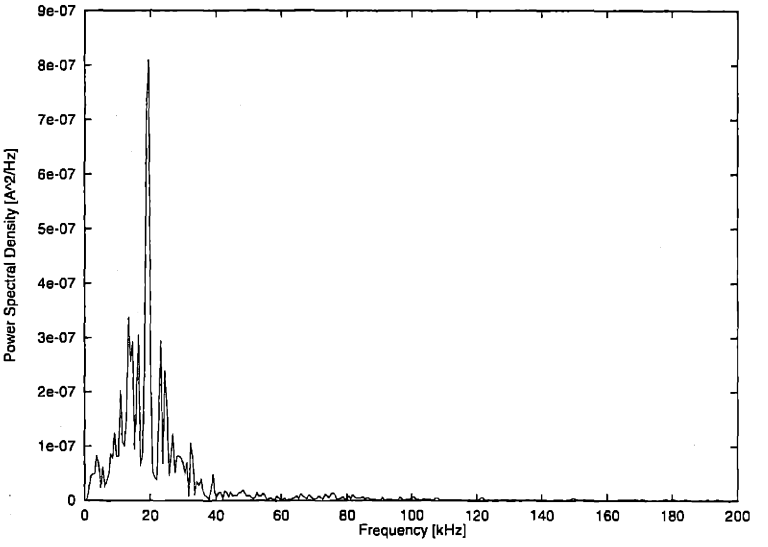

Figure A-51: Power spectral density $[A^2/Hz]$ of I_a, $\dot{m} = 1.76\ mg/s$, $V_d = 200\ V$, $\sim 80\ hrs$ from BOL.

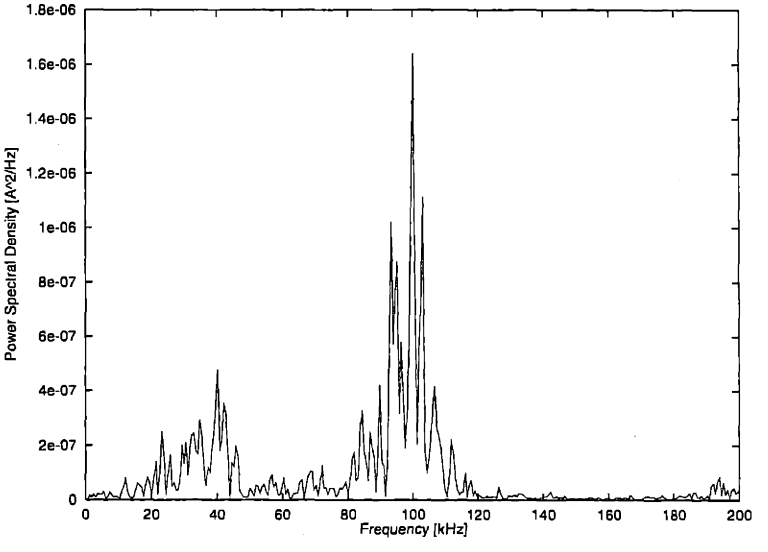

Figure A-52: Power spectral density $[A^2/Hz]$ of I_a, $\dot{m} = 1.76\ mg/s$, $V_d = 250\ V$, $\sim 80\ hrs$ from BOL.

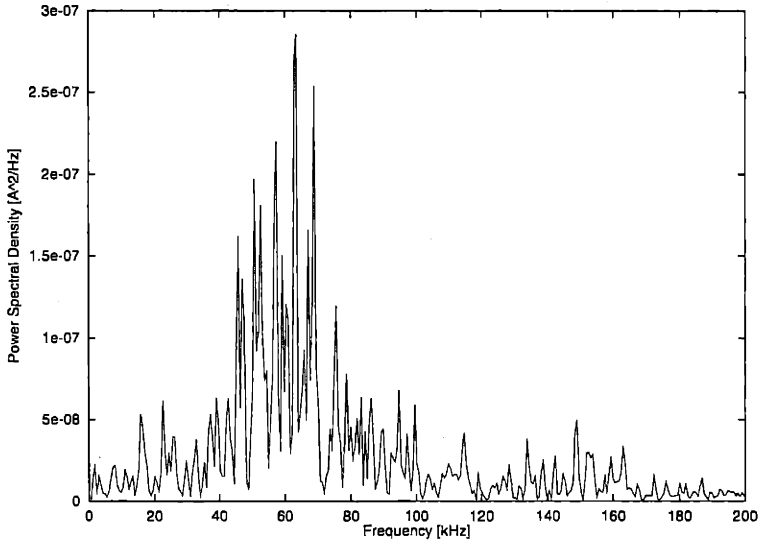

Figure A-53: Power spectral density $[A^2/Hz]$ of I_a, $\dot{m} = 1.76\ mg/s$, $V_d = 300\ V$, $\sim 80\ hrs$ from BOL.

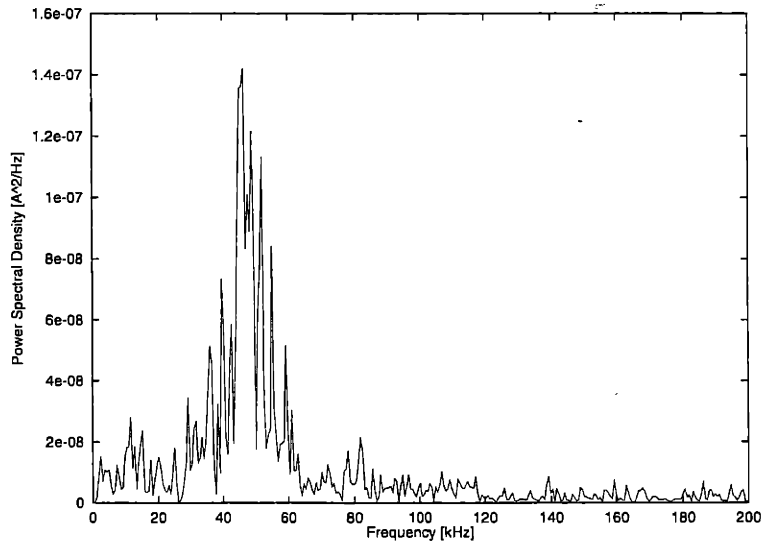

Figure A-54: Power spectral density $[A^2/Hz]$ of I_a, $\dot{m} = 1.76\ mg/s$, $V_d = 350\ V$, $\sim 80\ hrs$ from BOL.

$\sim 80\ hrs$ from BOL

PSD of I_a

$\dot{m} = 2.34\ mg/s$

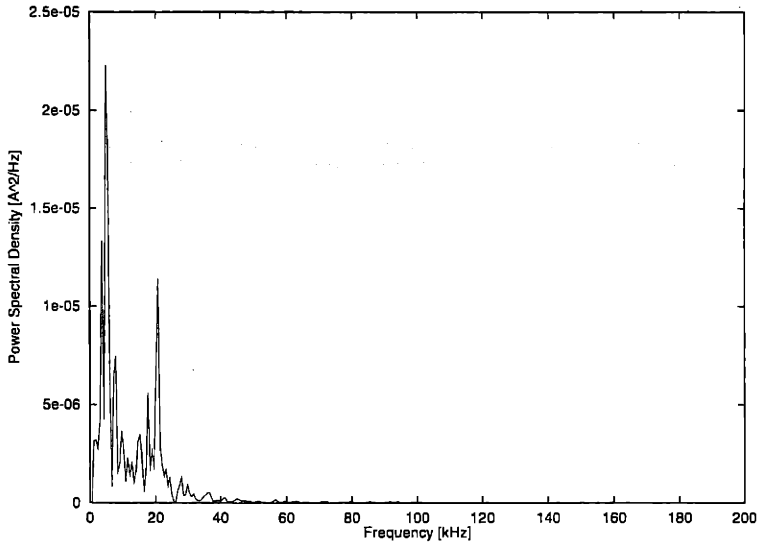

Figure A-55: Power spectral density $[A^2/Hz]$ of I_a, $\dot{m} = 2.34\ mg/s$, $V_d = 100\ V$, $\sim 80\ hrs$ from BOL.

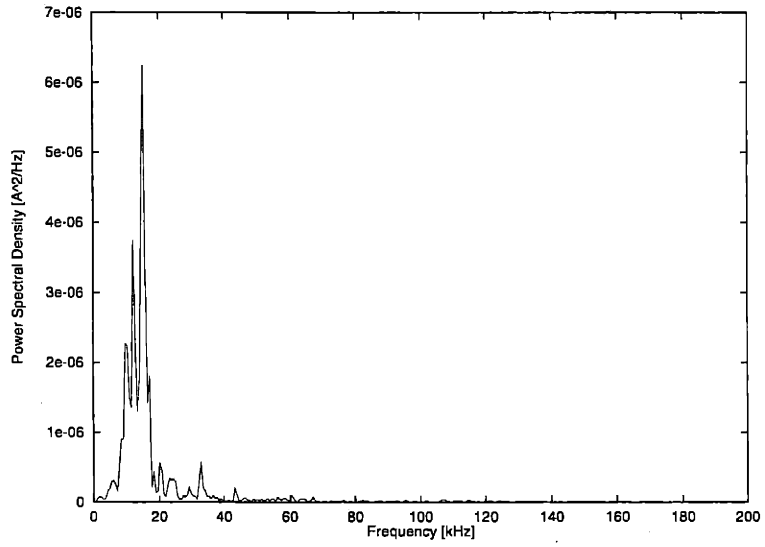

Figure A-56: Power spectral density $[A^2/Hz]$ of I_a, $\dot{m} = 2.34\ mg/s$, $V_d = 150\ V$, $\sim 80\ hrs$ from BOL.

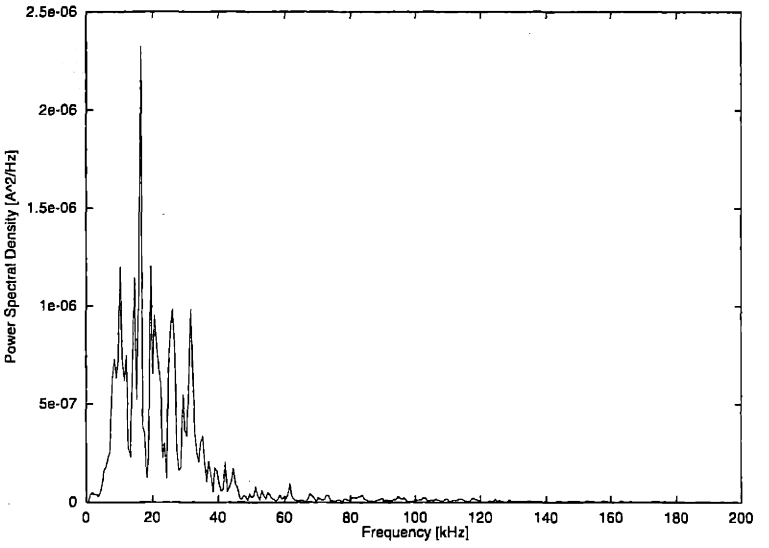

Figure A-57: Power spectral density $[A^2/Hz]$ of I_a, $\dot{m} = 2.34\ mg/s$, $V_d = 200\ V$, $\sim 80\ hrs$ from BOL.

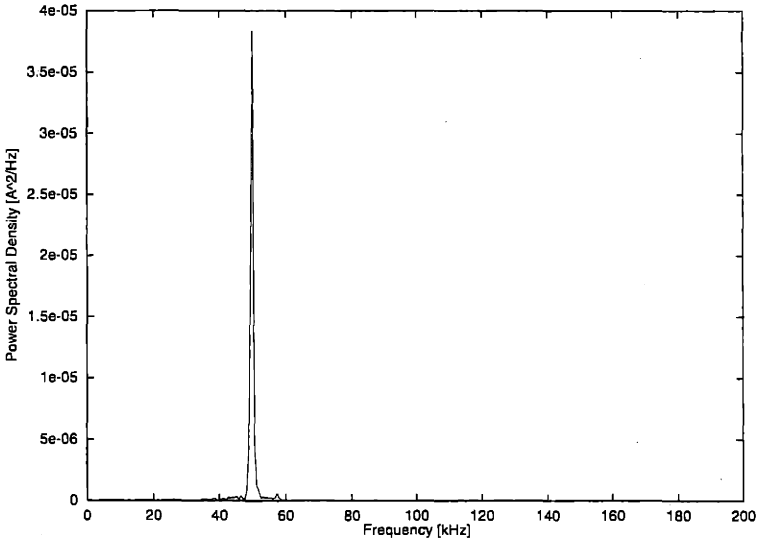

Figure A-58: Power spectral density $[A^2/Hz]$ of I_a, $\dot{m} = 2.34\ mg/s$, $V_d = 250\ V$, $\sim 80\ hrs$ from BOL.

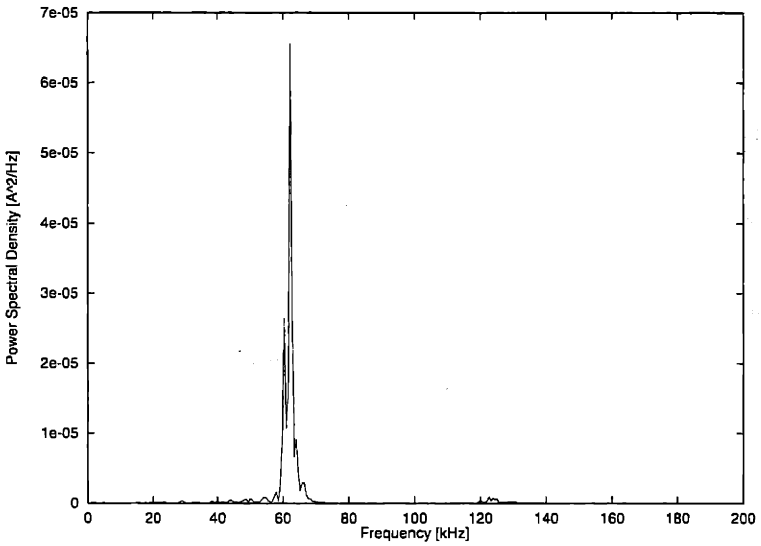

Figure A-59: Power spectral density $[A^2/Hz]$ of I_a, $\dot{m} = 2.34\ mg/s$, $V_d = 300\ V$, $\sim 80\ hrs$ from BOL.

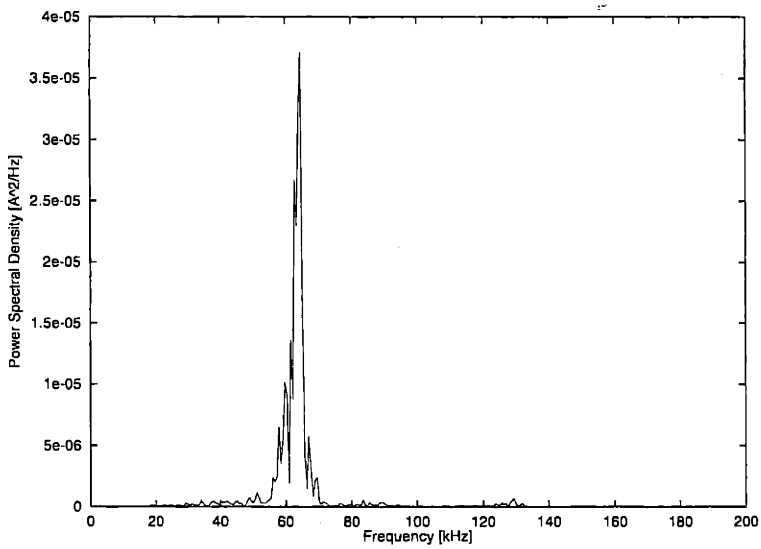

Figure A-60: Power spectral density $[A^2/Hz]$ of I_a, $\dot{m} = 2.34\ mg/s$, $V_d = 350\ V$, $\sim 80\ hrs$ from BOL.

$\sim 80\ hrs$ from BOL

PSD of I_a

$\dot{m} = 2.93\ mg/s$

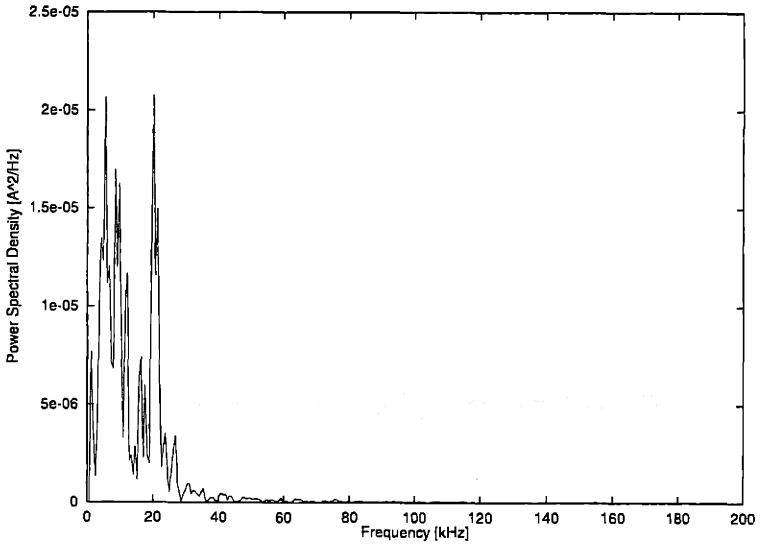

Figure A-61: Power spectral density $[A^2/Hz]$ of I_a, $\dot{m} = 2.93\ mg/s$, $V_d = 100\ V$, $\sim 80\ hrs$ from BOL.

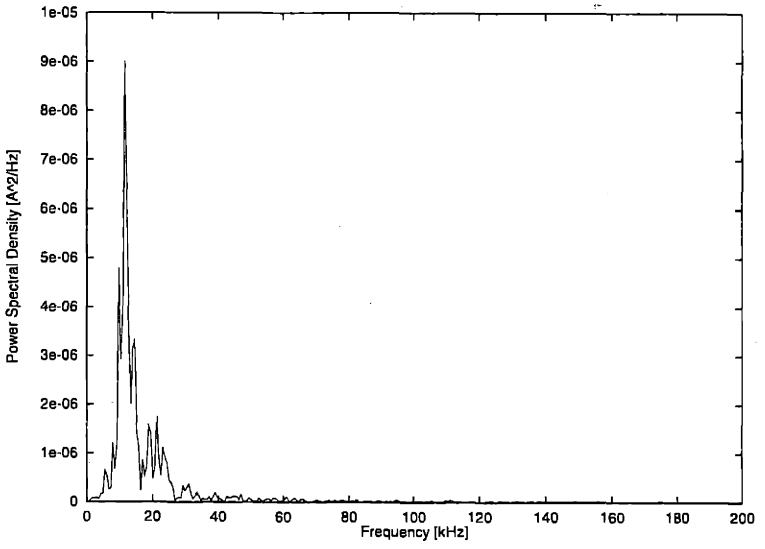

Figure A-62: Power spectral density $[A^2/Hz]$ of I_a, $\dot{m} = 2.93\ mg/s$, $V_d = 150\ V$, $\sim 80\ hrs$ from BOL.

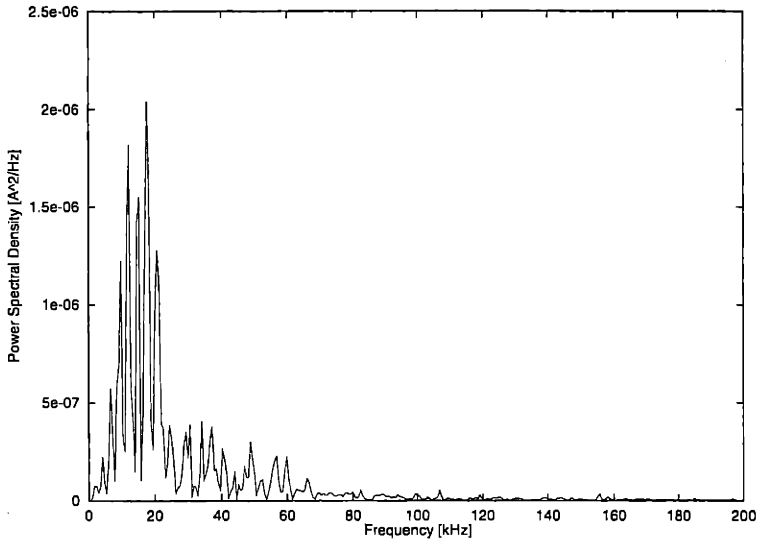

Figure A-63: Power spectral density $[A^2/Hz]$ of I_a, $\dot{m} = 2.93\ mg/s$, $V_d = 200\ V$, $\sim 80\ hrs$ from BOL.

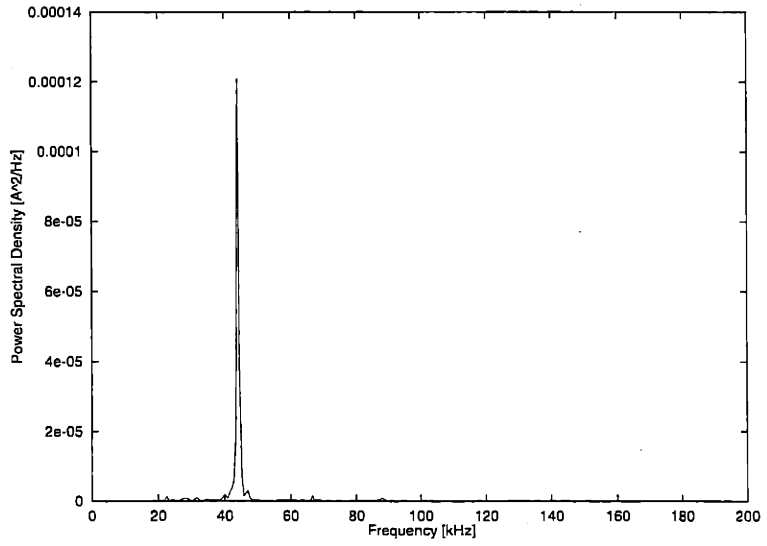

Figure A-64: Power spectral density $[A^2/Hz]$ of I_a, $\dot{m} = 2.93\ mg/s$, $V_d = 250\ V$, $\sim 80\ hrs$ from BOL.

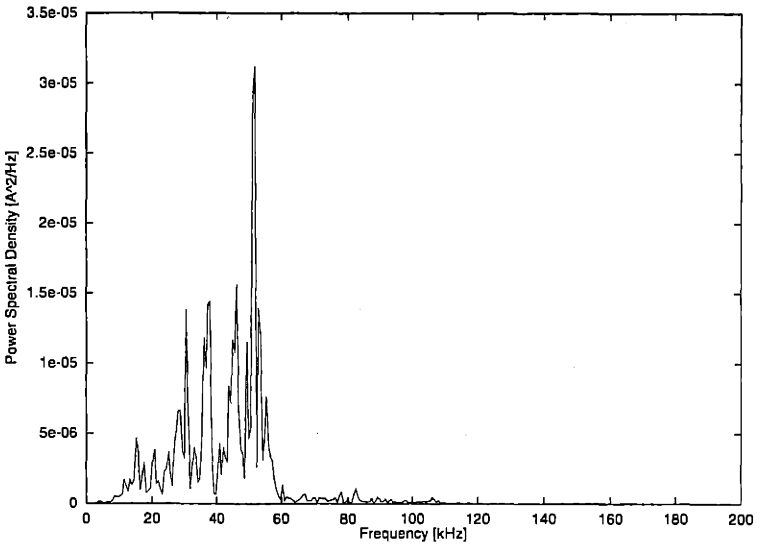

Figure A-65: Power spectral density $[A^2/Hz]$ of I_a, $\dot{m} = 2.93\ mg/s$, $V_d = 300\ V$, $\sim 80\ hrs$ from BOL.

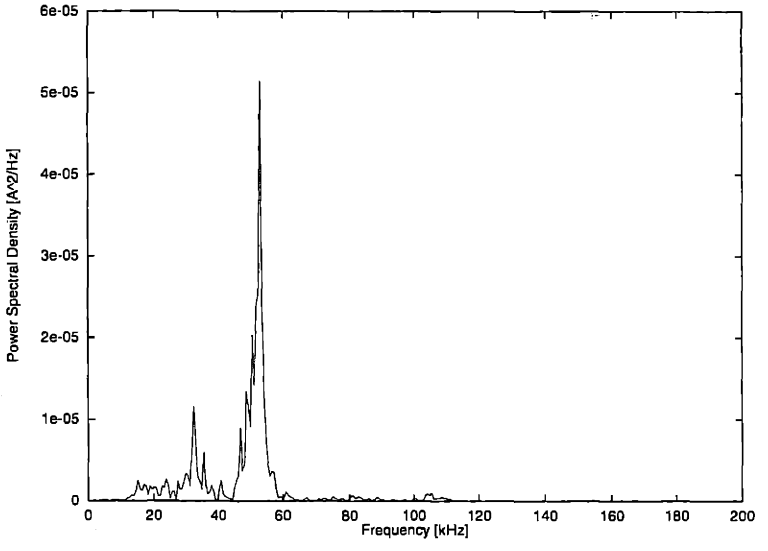

Figure A-66: Power spectral density $[A^2/Hz]$ of I_a, $\dot{m} = 2.93\ mg/s$, $V_d = 350\ V$, $\sim 80\ hrs$ from BOL.

$\sim 80\ hrs$ from BOL

PSD of V_f

$\dot{m} = 1.17\ mg/s$

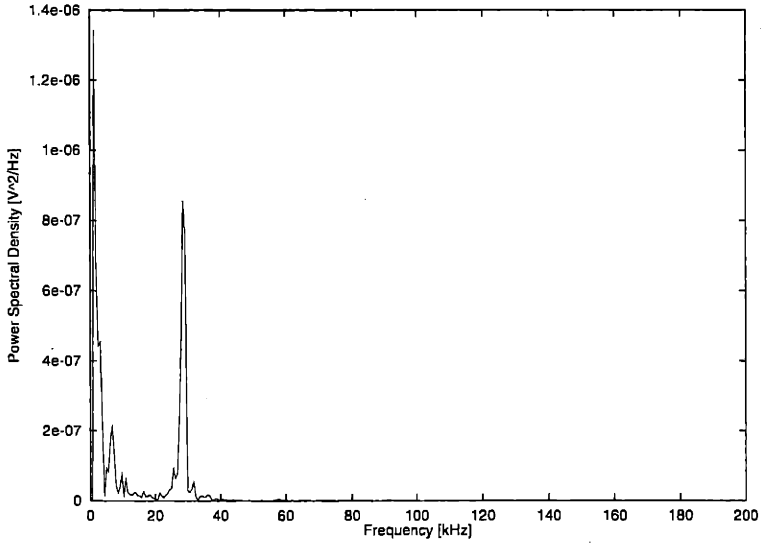

Figure A-67: Power spectral density $[V^2/Hz]$ of V_f, $\dot{m} = 1.17\ mg/s$, $V_d = 200\ V$, $\sim 80\ hrs$ from BOL.

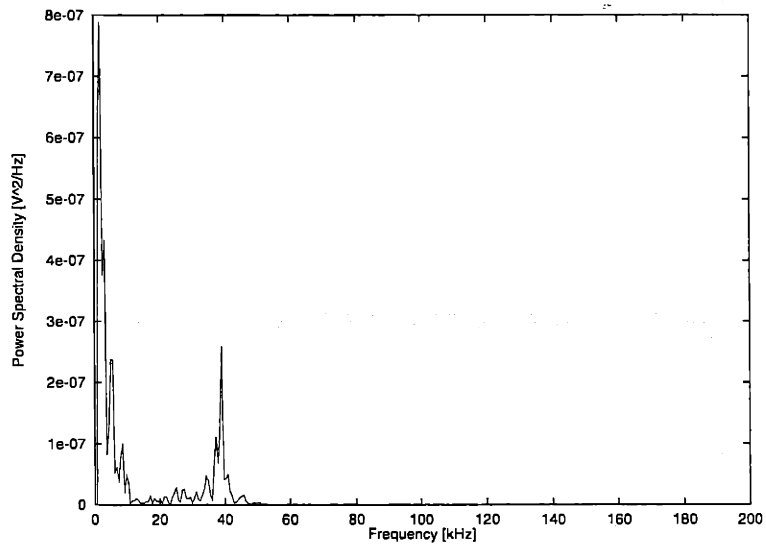

Figure A-68: Power spectral density $[V^2/Hz]$ of V_f, $\dot{m} = 1.17\ mg/s$, $V_d = 250\ V$, $\sim 80\ hrs$ from BOL.

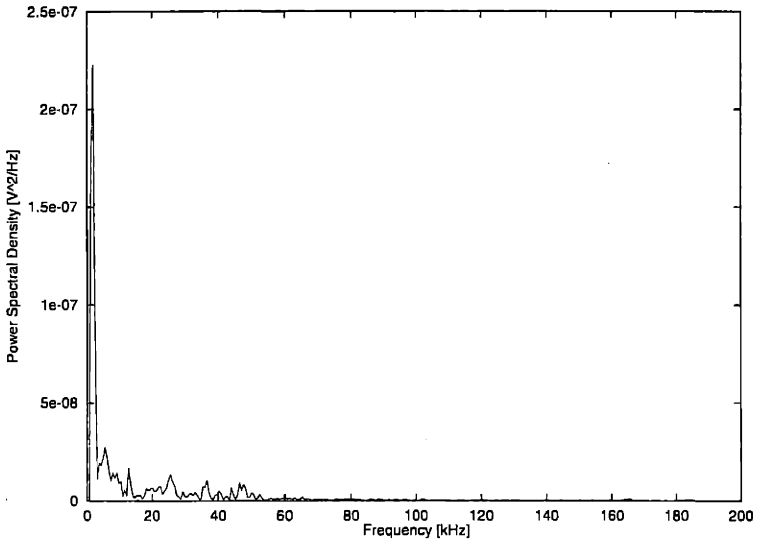

Figure A-69: Power spectral density $[V^2/Hz]$ of V_f, $\dot{m} = 1.17\ mg/s$, $V_d = 300\ V$, $\sim 80\ hrs$ from BOL.

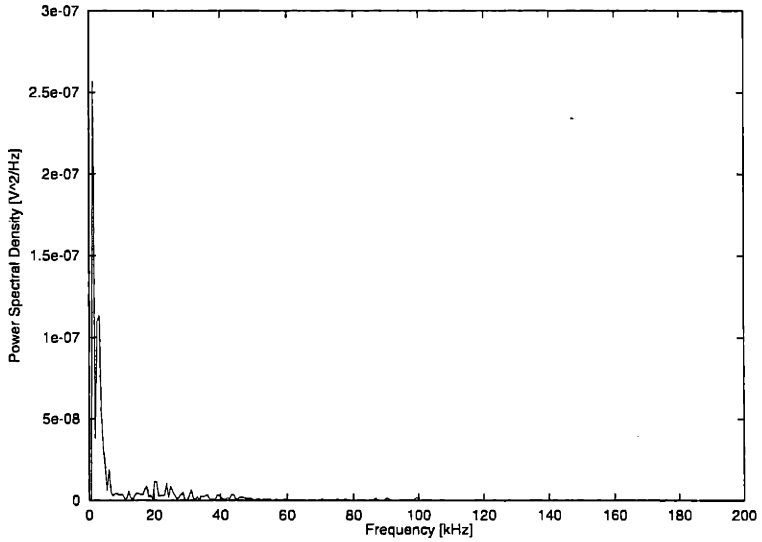

Figure A-70: Power spectral density $[V^2/Hz]$ of V_f, $\dot{m} = 1.17\ mg/s$, $V_d = 350\ V$, $\sim 80\ hrs$ from BOL.

$\sim 80\ hrs$ from BOL

PSD of V_f

$\dot{m} = 1.76\ mg/s$

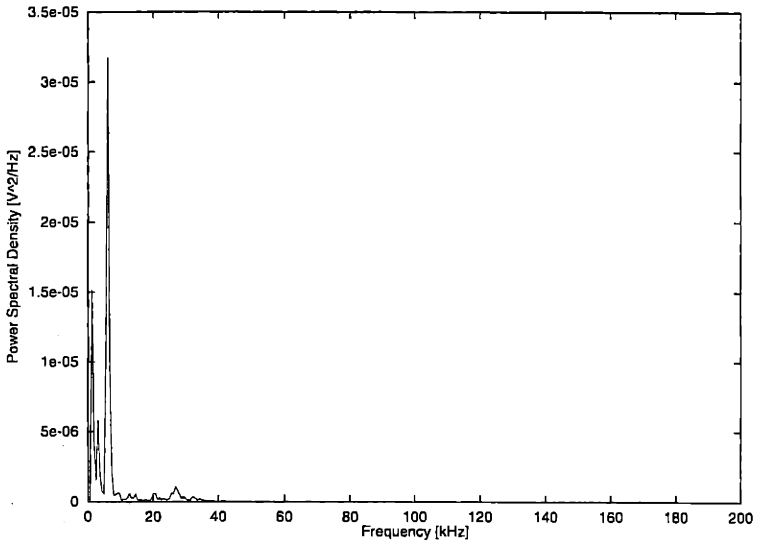

Figure A-71: Power spectral density $[V^2/Hz]$ of V_f, $\dot{m} = 1.76\ mg/s$, $V_d = 100\ V$, $\sim 80\ hrs$ from BOL.

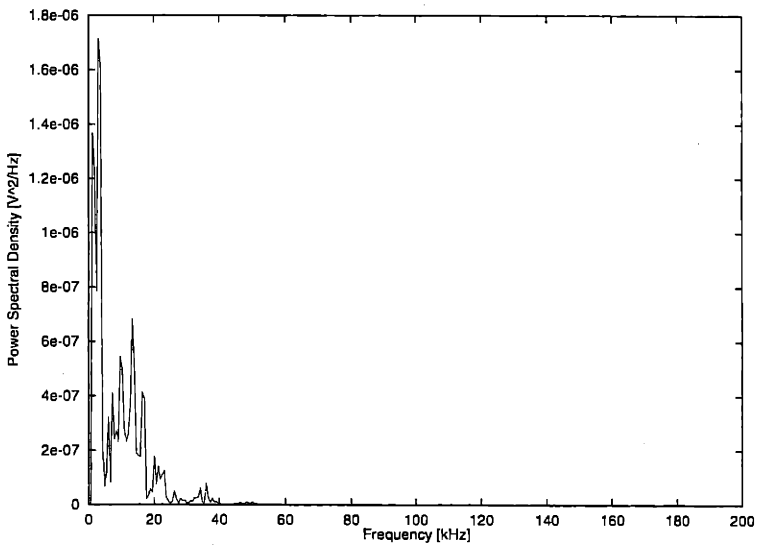

Figure A-72: Power spectral density $[V^2/Hz]$ of V_f, $\dot{m} = 1.76\ mg/s$, $V_d = 150\ V$, $\sim 80\ hrs$ from BOL.

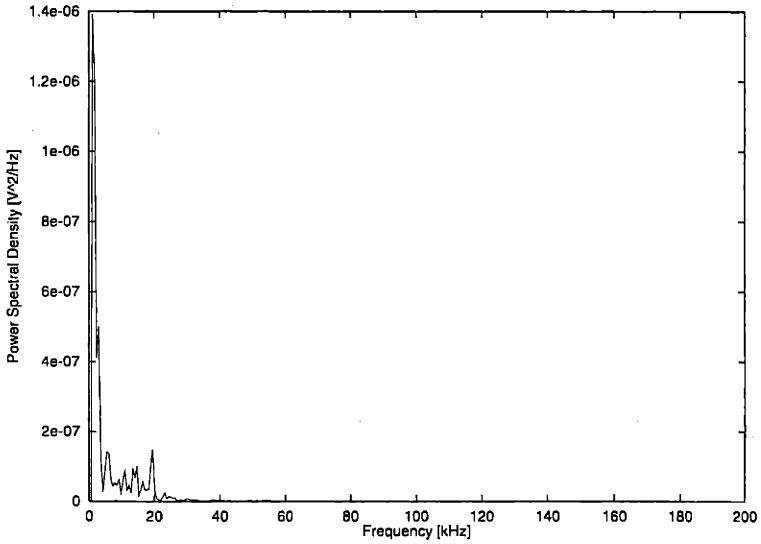

Figure A-73: Power spectral density $[V^2/Hz]$ of V_f, $\dot{m} = 1.76\ mg/s$, $V_d = 200\ V$, $\sim 80\ hrs$ from BOL.

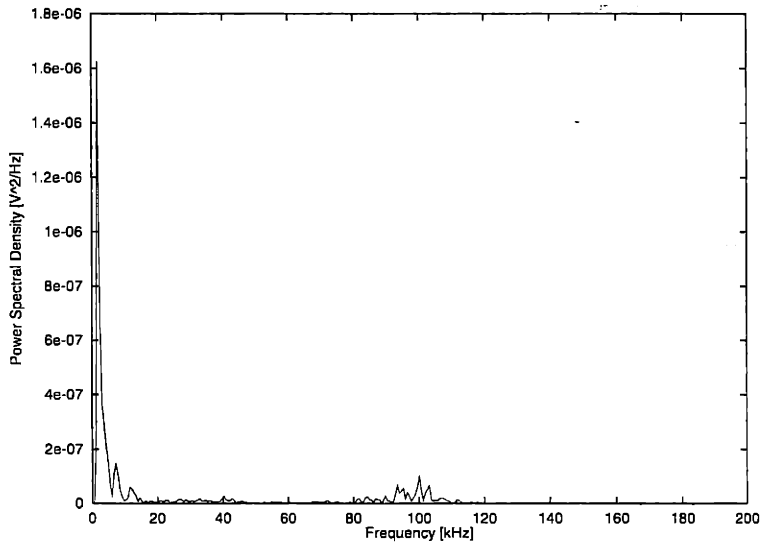

Figure A-74: Power spectral density $[V^2/Hz]$ of V_f, $\dot{m} = 1.76\ mg/s$, $V_d = 250\ V$, $\sim 80\ hrs$ from BOL.

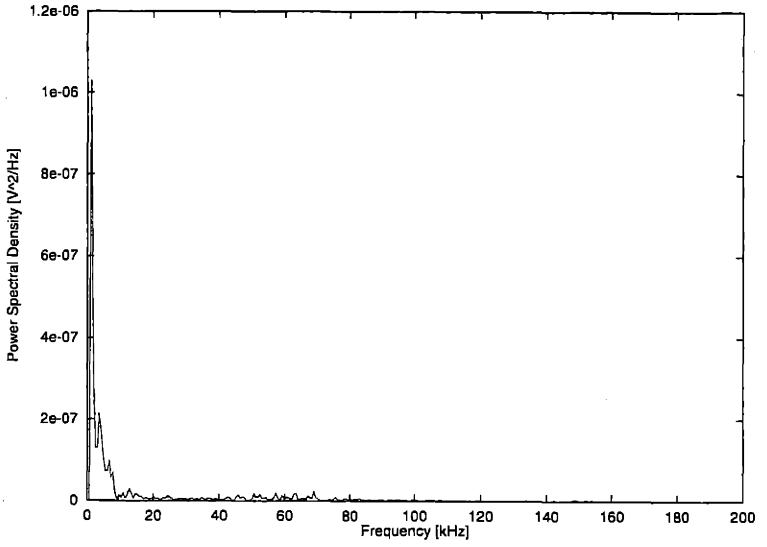

Figure A-75: Power spectral density $[V^2/Hz]$ of V_f, $\dot{m} = 1.76\ mg/s$, $V_d = 300\ V$, $\sim 80\ hrs$ from BOL.

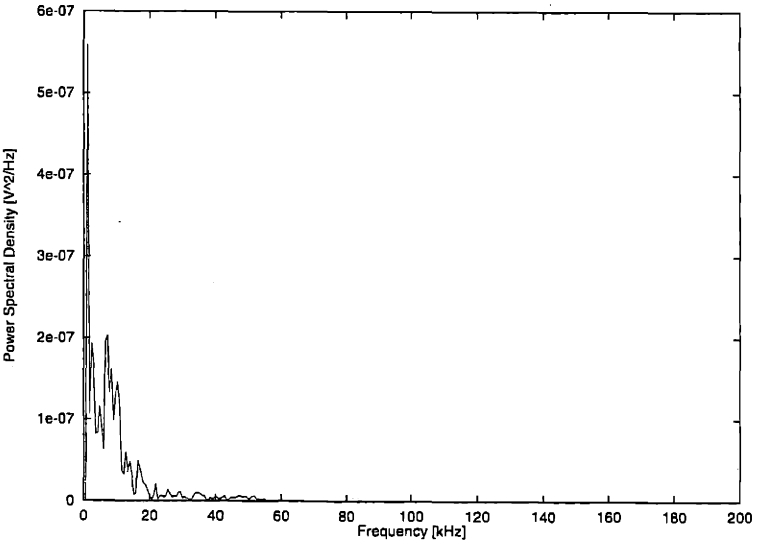

Figure A-76: Power spectral density $[V^2/Hz]$ of V_f, $\dot{m} = 1.76\ mg/s$, $V_d = 350\ V$, $\sim 80\ hrs$ from BOL.

$\sim 80\ hrs$ from BOL

PSD of V_f

$\dot{m} = 2.34\ mg/s$

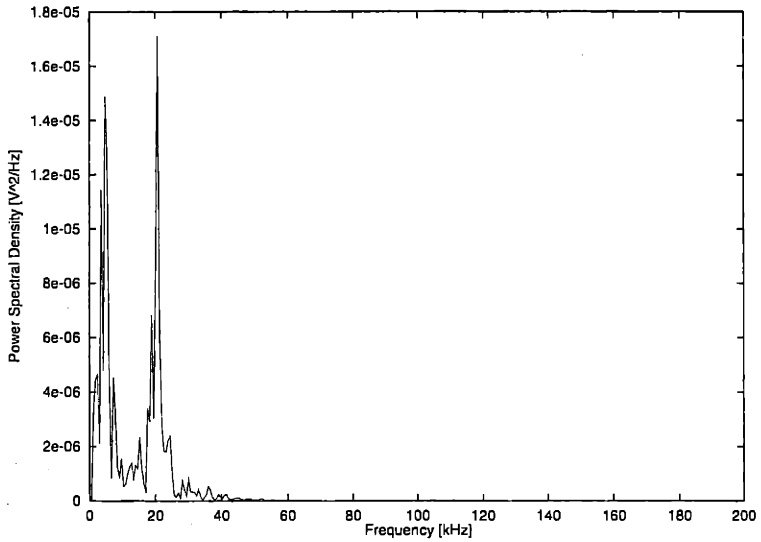

Figure A-77: Power spectral density $[V^2/Hz]$ of V_f, $\dot{m} = 2.34\ mg/s$, $V_d = 100\ V$, $\sim 80\ hrs$ from BOL.

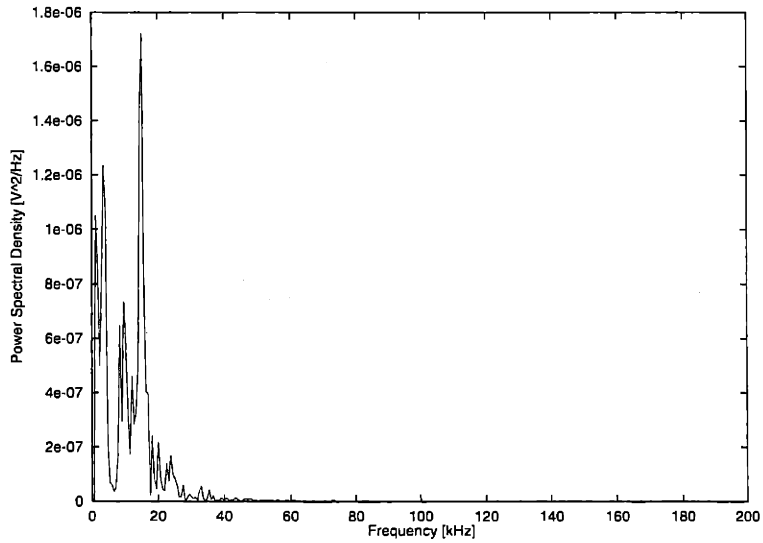

Figure A-78: Power spectral density $[V^2/Hz]$ of V_f, $\dot{m} = 2.34\ mg/s$, $V_d = 150\ V$, $\sim 80\ hrs$ from BOL.

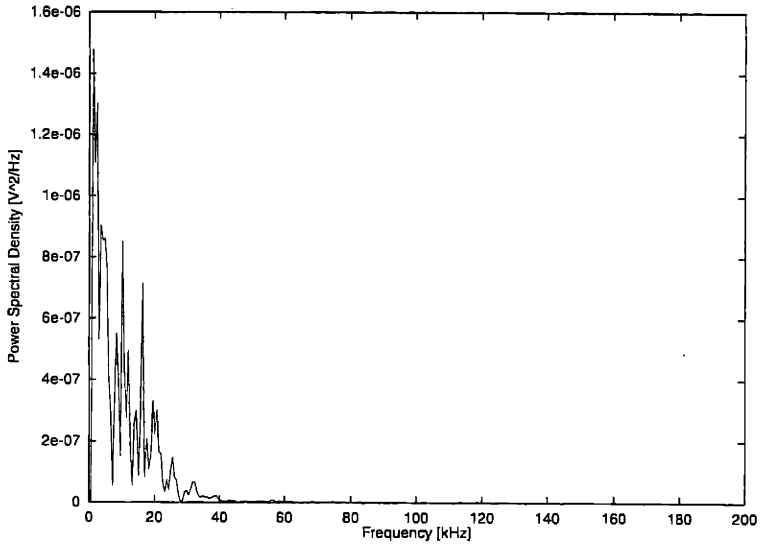

Figure A-79: Power spectral density $[V^2/Hz]$ of V_f, $\dot{m} = 2.34\ mg/s$, $V_d = 200\ V$, $\sim 80\ hrs$ from BOL.

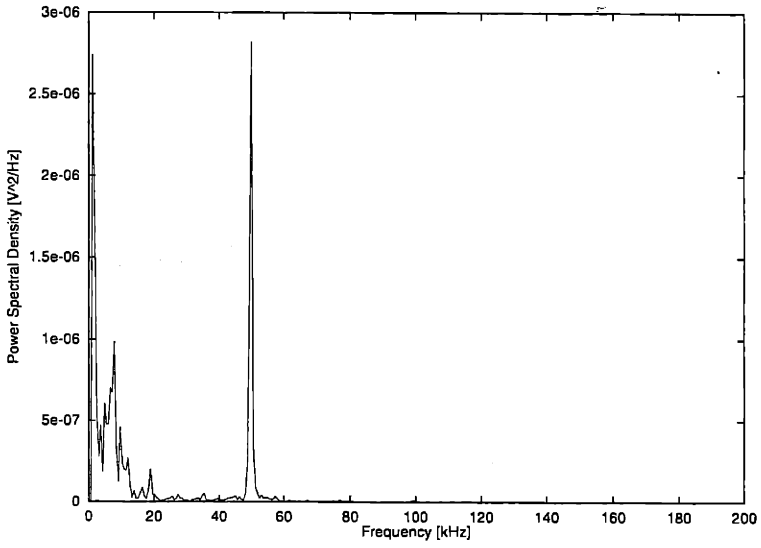

Figure A-80: Power spectral density $[V^2/Hz]$ of V_f, $\dot{m} = 2.34\ mg/s$, $V_d = 250\ V$, $\sim 80\ hrs$ from BOL.

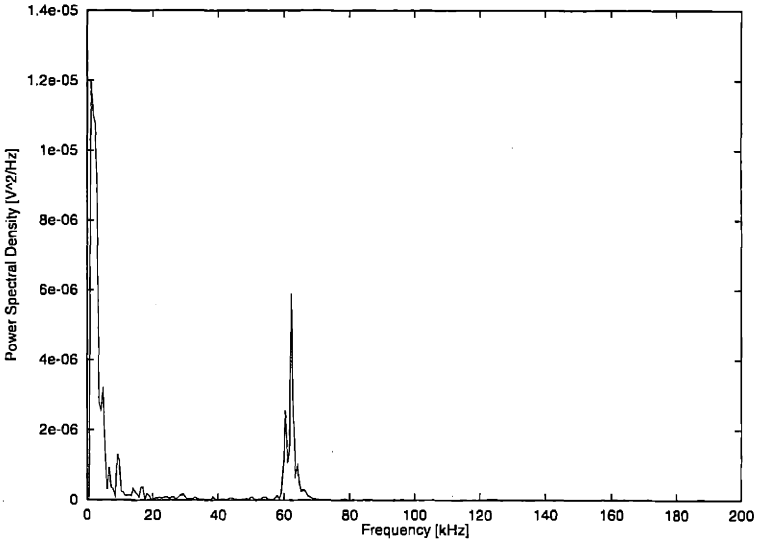

Figure A-81: Power spectral density $[V^2/Hz]$ of V_f, $\dot{m} = 2.34\ mg/s$, $V_d = 300\ V$, $\sim 80\ hrs$ from BOL.

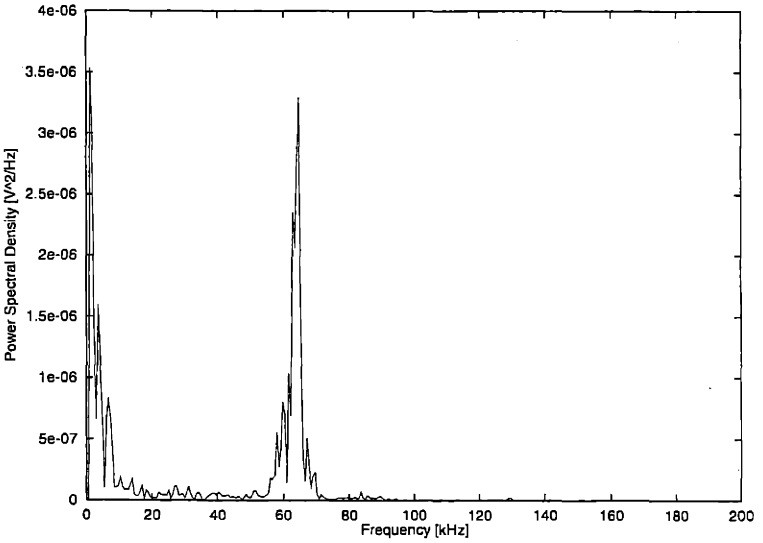

Figure A-82: Power spectral density $[V^2/Hz]$ of V_f, $\dot{m} = 2.34\ mg/s$, $V_d = 350\ V$, $\sim 80\ hrs$ from BOL.

$\sim 80\ hrs$ from BOL

PSD of V_f

$\dot{m} = 2.93\ mg/s$

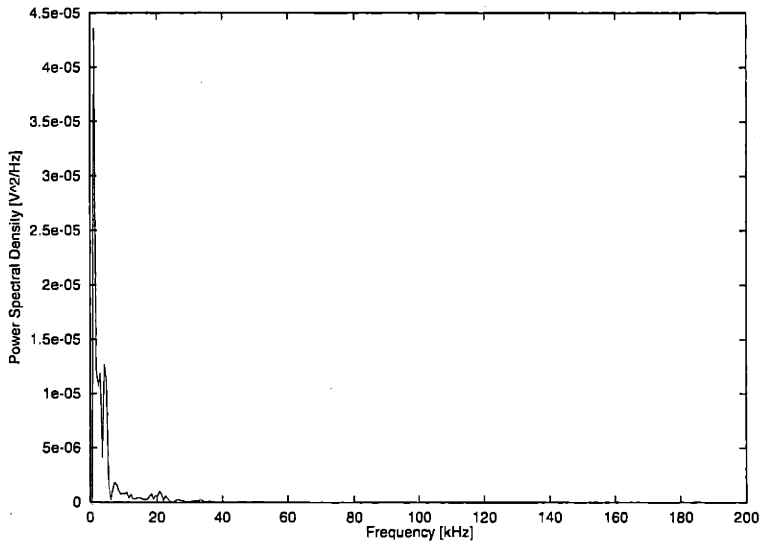

Figure A-83: Power spectral density $[V^2/Hz]$ of V_f, $\dot{m} = 2.93\ mg/s$, $V_d = 100\ V$, $\sim 80\ hrs$ from BOL.

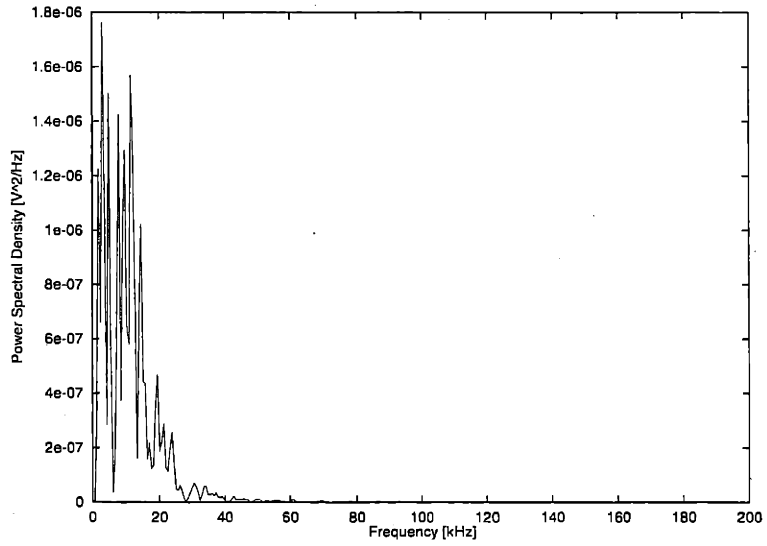

Figure A-84: Power spectral density $[V^2/Hz]$ of V_f, $\dot{m} = 2.93\ mg/s$, $V_d = 150\ V$, $\sim 80\ hrs$ from BOL.

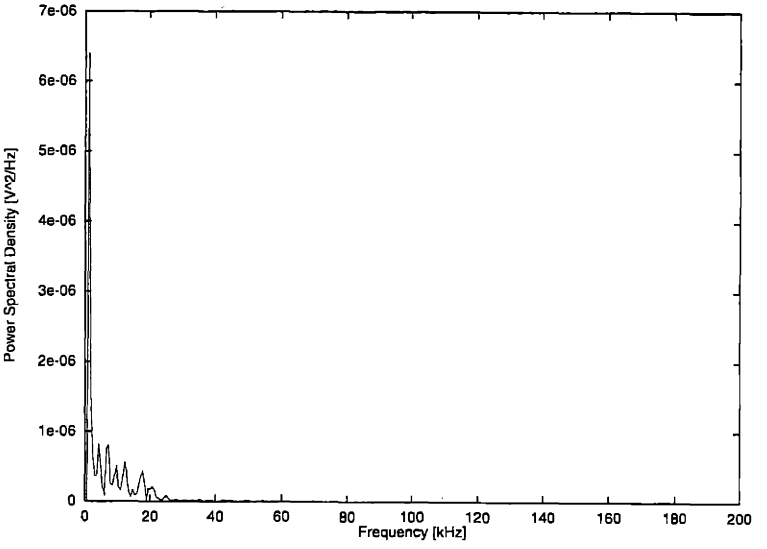

Figure A-85: Power spectral density $[V^2/Hz]$ of V_f, $\dot{m} = 2.93\ mg/s$, $V_d = 200\ V$, $\sim 80\ hrs$ from BOL.

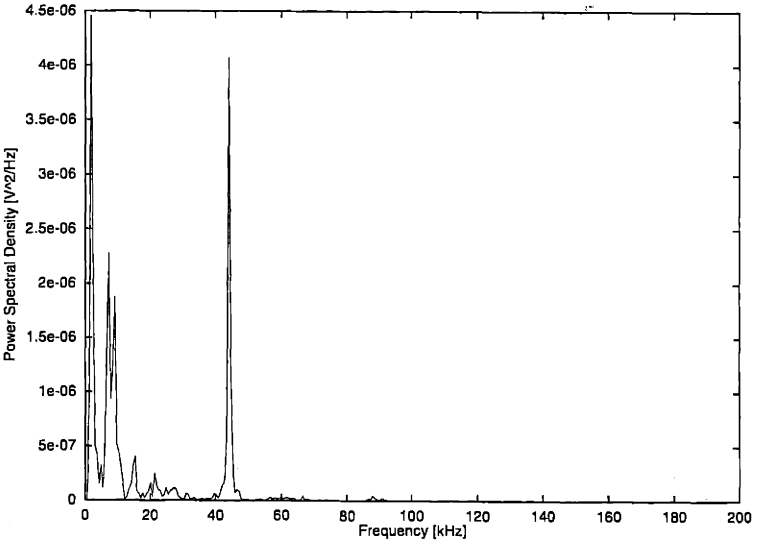

Figure A-86: Power spectral density $[V^2/Hz]$ of V_f, $\dot{m} = 2.93\ mg/s$, $V_d = 250\ V$, $\sim 80\ hrs$ from BOL.

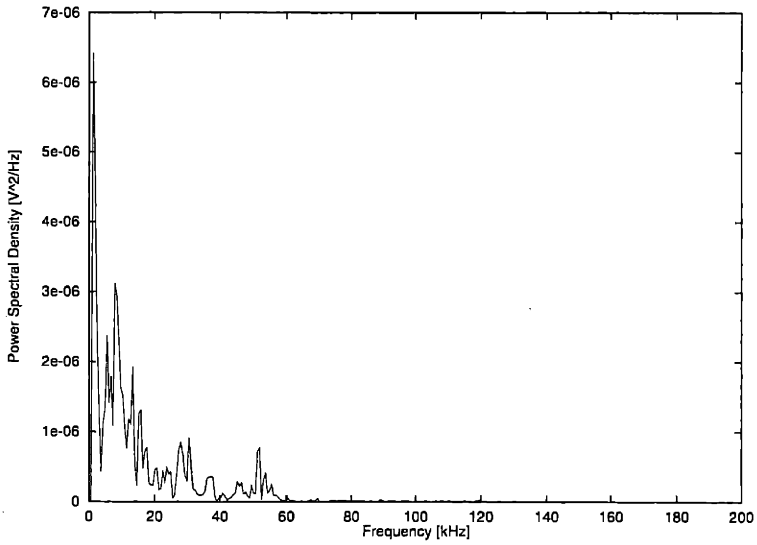

Figure A-87: Power spectral density $[V^2/Hz]$ of V_f, $\dot{m} = 2.93\ mg/s$, $V_d = 300\ V$, $\sim 80\ hrs$ from BOL.

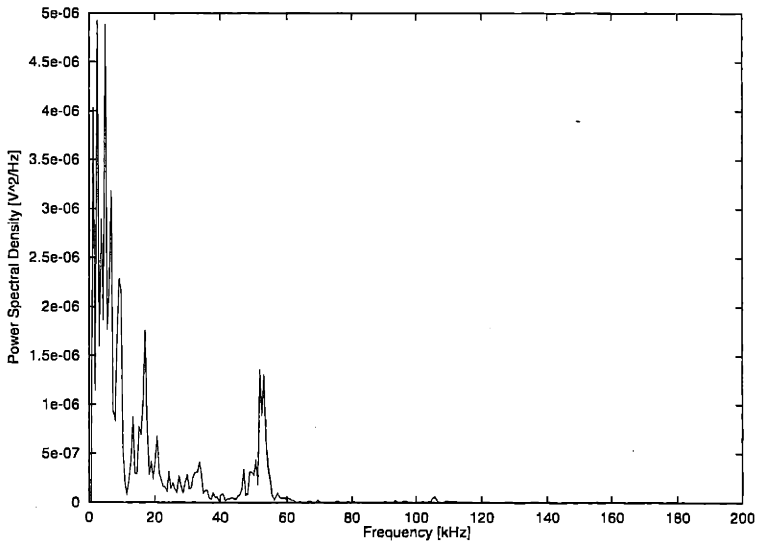

Figure A-88: Power spectral density $[V^2/Hz]$ of V_f, $\dot{m} = 2.93\ mg/s$, $V_d = 350\ V$, $\sim 80\ hrs$ from BOL.

Bibliography

[1] Ahedo, E., Martinez-Sanchez, M., "One-Dimensional Plasma Structure in Hall Thrusters", Joint Propulsion Conference, Cleveland, Ohio, 1998.

[2] Abgaryan, V., et. al., "Calculation Analysis of the Erosion of the Discharge Chamber Walls and Their Contamination During Prolonged SPT Operation," 30th Joint Propulsion Conference and Exhibit, Indianapolis, Indiana, June 1994.

[3] Absalamov, S. K., et. al., "Measurement of Plasma Parameters in the Stationary Plasma Thruster (SPT-100) Plume and it's Effect on Spacecraft Components," AIAA/SAE/ASME/ASEE 28th Joint Propulsion Conference and Exhibit, Nashville, TN, 1992.

[4] Anderson, D. A., Tannehill, J. C., and Pletcher, R. H., Computational Fluid Mechanics and Heat Transfer, Hemisphere Publishing Corporation, New York, 1984.

[5] Baranov, V. I., et. al., "Energy Balance and Role of Walls in ACDE," IEPC-97-060, 24th International Electric Propulsion Conference, Cleveland, Ohio, August 24-28, 1997.

[6] Baranov, V. I., et. al., "Electron Drift Oscillations Outside the Acceleration Zone of Accelerator with Closed Electron Drift," IEPC-95-42, AIDAA/AIAA/DGLR/JSASS 24th International Electric Propulsion Conference, Moscow, Russia, October, 1995.

[7] Bird, G. A., Molecular Gas Dynamics and the Direct Simulation of Gas Flows, Clarendon Press, Oxford, 1994.

[8] Birdsall, C. K., and Langdon, A. B., Plasma Physics via Computer Simulation, IOP Publishing Ltd., Bristol, England, 1991.

[9] Bishaev, A. M., and Kim, V., "Local Plasma Properties in a Hall-Current Accelerator with an Extended Acceleration Zone," Soviet Physics, Technical Physics, 23(9):1055-1057, 1978.

[10] Bishaev, A. M., et al., "The Experimental Investigations of Physical Processes and Characteristics of Stationary Plasma Thrusters With Closed Electron Drift," First Russian-German Conference on Electric Propulsion Engines and their Technical Applications, Giessen, Germany, 1992. RGC-EP 92-06.

[11] Bittencourt, J. A., Fundamentals of Plasma Physics, Pergamon Press, New York, 1988

[12] Bohm, D., Burhop, E.H.S., and Massey, H.S.W., in "Characteristics of Electrical Discharges in Magnetic Fields," A. Guthrie and R. K. Waterling, Eds., McGraw-Hill, New York, 1949.

[13] Brophy, J. R., et. al., "Performance of the Stationary Plasma Thruster: SPT-100," AIAA/SAE/ASME/ASEE 28th Joint Propulsion Conference and Exhibit, Nashville, TN, 1992.

[14] Brophy, J. R., "Stationary Plasma Thruster Evaluation in Russia: Summary Report," Strategic Defense Initiative Organization/Innovative Science and Technology Office, March 15, 1992, JPL Publication 92-4.

[15] Brown, Clyde O. and Pinsley, Edward A., "Further Experimental Investigations of a Cesium Hall-Current Accelerator," AIAA Journal Vol 3, No. 5, May 1965.

[16] Bugeat, J.P., Koppel, C., "Development of a Second Generation of SPT", IEPC-95-240, 24th International Electric Propulsion Conference, Moscow, Russia, September 12-23, 1995.

[17] Bugrova, A. I., Kim, V., Maslennikov, N. A. and Morozov, A. I., "Physical Process and Characterisics of Stationary Plasma Thrusters with Closed Electron Drift", IEPC-91-079, AIDAA/AIAA/DGLR/JSASS 22nd International Electric Propulsion Conference, Viareggio, Italy, Oct. 1991.

[18] Bugrova, A. I., Morozov, A. I. and Kharchevnikov, V. K., "Probe Measurements of Drift Current in a Hall Accelerator," Sov. Phys. - Tech. Phys., 30, P. 610, 1985.

[19] Chen, Sin-Li and T. Sekiguchi, "Instantaneous Direct-Display System of Plasma Parameters by Means of a Triple Probe", Journal, of Applied Physics, Vol. 36, No. 8, August 1965.

[20] Choueiri, E. Y., "Characterization of Oscillations in Closed Drift Thrusters," 30th AIAA/ASME/SAE/-ASEE Joint Propulsion Conference, Indianapolis, IN, June 27-29, 1994.

[21] Chung, Paul M., et. al., Electric Probes in Stationary and Flowing Plasmas: Theory and Application, Springer-Verlag, New York, 1975.

[22] Darnon, F. et. al., "Optical Investigation on Plasma OScillations of SPT Thrusters," 33rd Joint Propulsion Conference, Seattle, WA, July 6-9, 1997.

[23] de Boer, P. C. T., "Electric Probe Measurements in the Plume of an Ion Thruster", AIAA Journal of Propulsion and Power, Vol. 12, No. 1., January-February 1996.

[24] Dugan, John V. and Sovie, Ronald J., "Volume Ion Production Costs in Tenuous Plasmas: A General Atom Theory and Detailed Results for Helium, Argon and Cesium," NASA TN D-4150.

[25] Esipchuk, Yu. V. and Tilinin, G. N., "Drift Instability in a Hall-Current Plasma Accelerator," Sov. Phys. - Tech. Phys., 21, P.419, 1976.

[26] Esipchuck, Y. B., A. I. Morozov, G. N. Tilinin, and A. V. Trofimov, "Plasma Oscillations in Closed-Drift Accelerators with an Extended Acceleration Zone," Soviet Physics Technical Physics, 18(7):928-932, 1974.

[27] Fife, John M., and Manuel Martinez-Sanchez, "Comparison of Results from a Two-Dimensional Numerical SPT Model with Experiment," 32nd AIAA/ASME/-SAE/ASEE Joint Propulsion Conference, Lake Buena Vista, FL, 1996.

[28] Fife, J. M., Martinez-Sanchez, "Measurements of the AC Components of Discharge Current and Floating Potential in an SPT-70 Hall Thruster," Massachusetts Institute of Technology Space Systems Laboratory Internal Report, MIT Aeronautics and Astronautics Library, August 1998.

[29] Fife, J. M., Martinez-Sanchez, M., and Szabo, J., "A Numerical Study of Low-Frequency Discharge Oscillations in Hall Thrusters," 33rd AIAA/ASMA/SAE/ASEE Joint Propulsion Conference, Seattle, Washington, July 1997.

[30] Fife, John M., Two-Dimensonal Hybrid Particle-In-Cell Modeling of Hall Thrusters, Master's Thesis, Massachusetts Institute of Technology, May 1995.

[31] Fife, J. M., and Manuel Martinez-Sanchez, "Two-Dimensional Hybrid Particle-In-Cell (PIC) Modeling of Hall Thrusters," 24th International Electric Propulsion Conference, Moscow, Russia, September 1995

[32] Garner, C. E., et. al., "Cyclic Endurance Test of a SPT-100 Stationery Plasma Thruster," 3rd Russian-German Conference on Electric Propulsion Engines and Their Technical Applications, Stuttgart, Germany, July 1994.

[33] Grishin, S. D., and L. V. Leskov, Electrical Rocket Engines of Space Vehicles, A partially-edited machine translation of Elektricheskikh Raketnyye Dvigateli Kosmicheskikh Apparatov, Publishing House "Mash-inostroyeniye", Moscow, 1989, pp.1-216.

[34] Haag, Thomas W., "Design of a Thrust Stand for High Power Electric Propulsion Devices," AIAA-89-2829, Joint Propulsion Conference, Monterrey, California. July 1989.

[35] Hirakawa, M., "Electron Transport Mechanism in a Hall Thruster", 25th International Electric Propulsion Conference, Cleveland, Ohio, August 24-28, 1997.

[36] Hirakawa, M., and Y. Arakawa, "Particle Simulation of Plasma Phenomena in Hall Thrusters," 24th International Electric Propulsion Conference, Moscow, Russia, 1995.

[37] Hastings, Daniel, and Henry Garrett, Spacecraft-Environment Interactions, Cambridge University Press, 1996.

[38] Hutchinson, I. H., Principles of Plasma Diagnostics, Cambridge University Press, Cambridge, 1990.

[39] Jahn, Robert G., Physics of Electric Propulsion, McGraw Hill Series in Missile and Space Technology, New York, 1968.

[40] Janes, G. S. and Lowder, R. S., "Anomalous Electron Diffusion and Ion Acceleration in a Low-Density Plasma," Physics of Fluids, 9. P. 1115, 1966.

[41] Katz, Ira., et. al., "The Importance of Accurate Secondary Electron Yields in Modeling Spacecraft Charging," Journal of Geophysical Research, V. 91, No. A12, December 1, 1986.

[42] Kaufman, H. R., "Technology of ClosedDrift Thrusters," 19th Joint Propulstion Conference, Seattle, Washington, June 1983.

[43] Kim, Sang-Wook, Foster, J. E., and Alec Gallimore, "Very-Near-Field Plume Study of a 1.35 kW SPT-100," 32nd Joint Propulsion Conference, Lake Buena Vista, Florida, July 1-3, 1996.

[44] Komurasaki, K., Hirakawa, M. and Arakawa, Y., "Plasma Acceleration Process in a Hall-Current Thruster", IEPC-91-078, AIDAA/AIAA/DGLR/JSASS 22nd International Electric Propulsion Conference, Viareggio, Italy. Oct. 1991.

[45] Laframboise, James G., "Theory of Spherical and Cylindrical Langmuir Probes in a Collisionless, Maxwellian Plasma at Rest," University of Toronto Institute of Aerospace Studies Report 100, 1966. Also in Rarefied Gas Dynamics (J. H. De Leeuw, ed.), Vol. II, page 22, Academic Press, New York.

[46] Lawless, J. L., J. R. Wetch, "A High Performance Closed Drift Hall Thruster", AIP, 1991, pp. 507-510.

[47] Lentz, C. A., "Transient One Dimensional Numerical Simulation of Hall Thrusters", Massachusetts Institute of Technology, S.M. Thesis, 1993.

[48] Liberman, M. A. and Velikovich, Physics of Shock Waves and Gasses, Springer Series in Electrophysics, vol. 19, Springer-Verlag, New York, 1986.

[49] Manzella, D. H., "Stationary Plasma Thruster Plume Emissions", 23rd International Electric Propulsion Conference, Seattle, WA, 1993.

[50] Manzella, D. H., "Stationary Plasma Thruster Ion Velocity Distribution", 30th AIAA Joint Propulsion Conference, Indianapolis, IN, June 27-29, 1994.

[51] Marthur, D. and C. Badrinathan, "Ionization of Xenon by Electrons: Partial Cross Sections for Single, Double, and Triple Ionization," Physical Review A, Vol.35, No.3, February 1, 1987.

[52] Mitchner and Kruger, Partially Ionized Gasses, John Wiley & Sons, New York, 1973.

[53] Morozov, A. I., Esipchuk, Yu. V. and Kapulkin, A. M., "Azimuthally Asymmetric Modes and Anomalous Conductivity in Closed Electron Drift Accelerators," Sov. Phys. - Tech. Phys., 18, P. 615, 1973.

[54] Morozov, A. I. and V. V. Savelyev, "The Electron Dynamics in SPT-Channel and the Problem of Anomalous Erosion," International Electric Propulsion Conference, 1995.

[55] Morozov, A. I., Esipchuk, Yu. V., Kapulkin, A. M., Nevrovskii, V. A. and Smirnov, V. A., "Effect of the Magnetic Field on a Closed-Electron-Drift Accelerator," Sov. Phys. - Tech. Phys., 17, P. 482, 1972.

[56] Morozov, A. I., Esipchuk, Yu. V., Tilinin, G. N., Trofimov, A. V., Sharov, Yu. A. and Shchepkin, G. Ya., "Plasma Accelerator With Closed Electron Drift and Extended Acceleration Zone", Soviet Phys. - Tech. Phys., 17, P. 38, 1972.

[57] Randolph, T., et. al., "The Mitigation of Discharge Oscillations in the Stationary Plasma Thruster," 30th AIAA Joint Propulsion Conference, Indianapolis, IN, June 27-29, 1994.

[58] Rapp, D. and Francis, W. E., "Charge Exchange Between Gaseous Ions and Atoms," Journal of Chemical Physics, Vol. 37, No. 11, 1962, pp. 2631-2645.

[59] Smirnov, V. A., "Electron Energy Balance in a Hall-current Accelerator with an Extended Acceleration Zone", Soviet J. Plasma Phys., 5, P. 202, 1979.

[60] Valentian, D. and J. P. Bugeat, "Theoretical and Experimental Analysis of Stationary Plasma Thruster Operation," IEPC-93-226, 23rd International Electric Propulsion Conference, Seattle, Washington, September 1993.

[61] Zhurin, V., et. al., "Dynamic Characteristics of Closed Drift Thrusters," 23rd International Electric Propulsion Conference, Seattle, Washington, September 1993.

[62] Zubkov, I. P., Kislov, A. Ya. and Morozov, A. I., "Experimental Study of a Two-Lens Accelerator," Sov. Phys. - Tech. Phys., 15, P.1796, 1971.

4536 - 39